Urban Climate and Energy Demand in Buildings

Jonas Allegrini

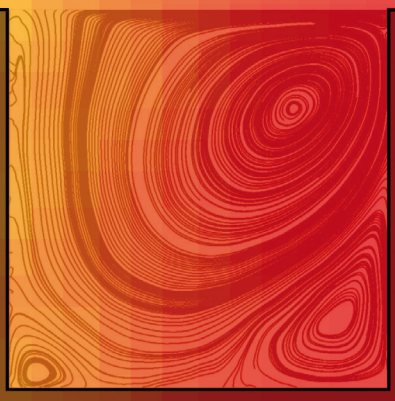

Diss. ETH No. 20848

DISS. ETH NO. 20848

Urban Climate and Energy Demand in Buildings

A dissertation submitted to

ETH Zurich

for the degree of

Doctor of Sciences

presented by

Jonas Allegrini

MSc in Mechanical Engineering, ETH Zurich

born August 18, 1983
citizen of Ins BE (Switzerland)

accepted on the recommendation of

Prof. Dr. Jan Carmeliet, examiner
Viktor Dorer, co-examiner
Prof. Dr. Jan Hensen, co-examiner

2012

Cover: Measured turbulent kinetic energies and streamlines inside a scaled street canyon (by Jonas Allegrini and Andreas Rubin)

Acknowledgment

This thesis was conducted at the Laboratory for Building Science and Technology of the Swiss Federal Laboratories for Materials Science and Technology (Empa). I am deeply grateful to Prof. Dr. Jan Carmeliet, who gave me the opportunity to work on this challenging research project. I would like to thank him for the fruitful discussions, the valuable advises and his encouragement. Viktor Dorer was my co-supervisor and project leader. I would like to express my gratitude to him for the numerous discussions during the development of the different modelling approaches and wind tunnel setups. Especially, I want to thank him for his help to improve the quality of the papers, which we wrote during this project. Both Jan and Viktor guided and supported me during my studies and gave me constructive remarks and suggestions.

Further, I would like to thank Robert Weber and Beat Lehmann for the discussions and explanations that helped me to get familiarized with the building energy simulation models. I am also indebted to Beat Margelisch for his support during the design and the construction of the wind tunnel model. Thanks go to all my colleagues at Empa and ETH Zürich, especially to the members of the Urban Physics Group: Saba Saneinejad, Peter Moonen, Thijs Defraeye, Enrico Paterna, Parham Mirzaei, Aytac Kubilay and Jaebong Lee.

I would also like to thank Prof. Dr. Jan Hensen and Prof. Dr. Georgios Anagnostou for being in the examination committee.

This research was funded by the Swiss Federal Office of Energy (SFOE) (Project Number: 154 143, Project Title: Urban climate and energy demand in buildings). Their contribution is gratefully acknowledged.

Finally, I want to thank my family and my friends for their support.

Abstract

In the past decades the portion of the population living in urban areas has continuously increased. Due to the high building density, the microclimate in urban areas changed significantly compared to rural areas. The temperatures measured in urban areas are, due to the urban heat island (UHI) effect, higher compared to the rural temperatures. The UHI intensities are increasing with higher building densities and growing cities. Space cooling and heating demands of buildings are strongly affected by the local microclimate at the building sites. Due to the climate change and the limited energy resources, energy saving and sustainability are nowadays important issues. A significant part of the global energy consumption is used for space cooling and heating of buildings. Thus its minimization for buildings in urban areas has great energy saving potential. The aim of this thesis is to investigate the impact of the urban microclimate on the energy demand of buildings in an urban context by conducting detail building energy simulations (BESs). Most BES models were developed for stand-alone buildings and therefore do not consider effects of the urban microclimate. For this thesis a BES model is adjusted in such a way that it can account for the urban microclimate. The three main aspects of the urban microclimate are (in order of importance): (i) the radiation exchange between neighbouring buildings, (ii) the UHI effect and (iii) the reduced convective heat transfer due to wind sheltering. Diurnal UHI intensity schedules are developed based on measured data of Basel (Switzerland). For the determination of the convective heat transfer at the building façades, computational fluid dynamic (CFD) simulations are conducted. The convective heat transfer is strongly dependent on the flow in the boundary layer at the building surfaces. There exist mainly two approaches to model the boundary layers at walls using Reynolds-averaged Navier-Stokes (RANS) CFD simulations. The first approach is to resolve the boundary layers with low-Reynolds number modelling (LRNM) using a fine mesh in the near-wall region. Because LRNM is computationally expensive, for a wide range of applications wall functions (WFs) are preferred, which model part of the boundary layer with empirical equations. With WFs computational power can be saved using coarser meshes. However, standard wall functions may show important errors predicting the wall heat fluxes. Therefore, in a first part of this thesis a new temperature wall function is proposed improving substantially the heat transfer predictions of RANS CFD simulations. In a following part correlations for convective heat transfer coefficients (CHTCs) are derived as a function of the wind speed for different stand-alone and urban geometric building configurations. Street canyons are chosen as a generic urban configuration. In street canyons building façades are heated by solar radiation inducing buoyancy, which has to be considered in the CFD simulations. To validate the CFD simulations of buoyant flows in street canyons, wind tunnel measurements of a street canyon with heated surfaces are conducted. For the validation the velocities and turbulent kinetic energies of the CFD simulations are compared with the values of the measured flow fields.

With CFD the general flow structure can be captured. Differences in the detailed flow fields between the CFD and the measurements may originate from errors in the predictions of the wind velocities at the top plane of the street canyon. A last aspect of the urban microclimate considered this thesis for BESs, is the longwave and solar radiation exchange between neighbouring buildings. The radiation model in the BES model was originally developed only for interior spaces. To be able, to use this radiation model for outdoor spaces, the street canyons are modelled as outside "atria" with open ceiling. The radiation model accounts for multiple reflections of longwave and solar radiation between buildings. In the last part of this thesis, BESs for the climate of Basel are conducted for different stand-alone and street canyon configurations. In addition to simulations using the established CHTC correlations, also coupled BES-CFD simulations are conducted, where at each BES time step a CFD simulation is conducted and the results are transferred to the BES, to determine the convective heat flux at the building façades. With coupled simulations the BES results can be improved, especially for cases where no case specific CHTC correlations are available. A strong influence of the urban microclimate on the space cooling and space heating demands of buildings can be observed. The changes of building energy demands for different local microclimates may be in the same order of magnitude as the demands themselves. This shows the importance of accounting for the local microclimate, when predicting the energy demands for buildings in urban areas with BESs. Finally BESs are conducted for different climates. The general trends, of how the local microclimate influences the space cooling and space heating demands, are similar for different climates. With the approach, proposed in this thesis, most of the thermal effects of the urban microclimate can be captured and quantified on street canyon scale.

Zusammenfassung

In den vergangenen Jahrzehnten hat sich der Anteil der Bevölkerung, welche in städtischen Gebieten lebt, kontinuierlich vergrössert. Durch die grosse Gebäudedichte ist das Mikroklima in städtischen Gebieten deutlich verändert im Vergleich zu ländlichen Gebieten. In städtischen Gebieten werden, aufgrund des städtischen Wärmeinsel Effekts, höhere Temperaturen gemessen als in ländlichen Gebieten. Die Intensität des städtischen Wärmeinsel Effekts nimmt mit höheren Gebäudedichten und wachsenden Städten zu. Der Klimakälte- und der Heizwärmebedarf von Gebäuden werden stark vom lokalen Mikroklima um das Gebäude beeinflusst. Aufgrund der Klimaerwärmung und den beschränkten Energieressourcen sind Energiesparen und Nachhaltigkeit heutzutage wichtige Themen. Ein wesentlicher Anteil des weltweiten Energieverbrauchs wird durch Kühlen und Heizen von Gebäuden verursacht. Deshalb hat dessen Minimierung für Gebäude in städtischen Gebieten grosses Energiesparpotential. Das Ziel dieser Thesis ist es, den Einfluss vom städtischen Mikroklima auf den Energiebedarf von Gebäuden, mit Hilfe von detaillierten Gebäudesimulationen, zu untersuchen. Die meisten Gebäudesimulationsmodelle wurden für freistehende Gebäude entwickelt und berücksichtigen deshalb die Effekte des städtischen Mikroklimas nicht. Für diese Thesis wurde ein Gebäudesimulationsmodell so angepasst, dass es das städtische Mikroklima berücksichtigen kann. Die drei Hauptaspekte des städtischen Mikroklimas sind (geordnet nach deren Wichtigkeit): (i) der Strahlungsaustausch zwischen benachbarten Gebäuden, (ii) der städtische Wärmeinsel Effekt und (iii) der reduzierte konvektive Wärmeübergang infolge kleinere Windgeschwindigkeiten. Tagesgänge der Intensität des städtischen Wärmeinsel Effekts werden basierend auf Messdaten von Basel (Schweiz) entwickelt. Für die Berechnung des konvektiven Wärmeübergangs an den Gebäudefassaden werden CFD (computational fluid dynamics) Simulationen durchgeführt. Der konvektive Wärmeübergang ist stark von den Strömungen in den Grenzschichten an den Gebäudefassaden abhängig. Es gibt, für RANS (Reynolds-averaged Navier Stokes) CFD Simulationen, hauptsächlich zwei Ansätze, um die Grenzschicht an Wänden zu modellieren. Der erste Ansatz besteht darin, die Grenzschicht mit LRNM (low-Reynolds number modelling) aufzulösen, indem in der Wandnähe ein feines Rechengitter verwendet wird. Weil LRNM rechenintensiv ist, werden für eine Vielzahl von Anwendungen WFs (wall functions) bevorzugt, welche einen Teil der Grenzschicht mit empirischen Gleichungen modellieren. Mit WFs kann, durch gröbere Rechengitter, Rechenkapazität gespart werden. Allerdings kann die Verwendung von SWFs (standard wall functions) zu Fehler in der Vorhersage des Wärmestroms an Wänden führen. Deshalb wird in einem ersten Teil dieser Thesis eine neue WF für die Temperatur entwickelt, um die Wärmeübergangsvorhersagen für RANS CFD Simulationen zu verbessern. Im anschliessenden Teil werden Korrelationen von Wärmeübergangskoeffizienten als eine Funktion der Windgeschwindigkeit für verschiedene Konfigurationen freistehenden und städtischen Gebäuden hergeleitet. Strassenschluchten werden als typische städtische Kon-

figurationen verwendet. In Strassenschluchten werden Gebäudefassaden durch Solarstrahlung erwärmt und verursachen Auftriebskräfte in der wandnahen Luft, welche in CFD Simulationen berücksichtigt werden müssen. Für die Validierung von CFD Simulationen mit auftriebsbehafteten Strömungen in Strassenschluchten, werden Windkanalversuche einer Strassenschlucht mit beheizten Oberflächen durchgeführt. Zur Validierung werden die Geschwindigkeiten und turbulenten kinetischen Energien aus den CFD Simulationen mit den gemessenen Strömungsfeldern verglichen. Mit CFD können die generellen Strömungsstrukturen erfasst werden. Unterschiede in den detaillierten Strömungsfeldern stammen wahrscheinlich von Fehlern in der Vorhersage der Windgeschwindigkeiten in der Dachhöhe der Strassenschluchten. Der letzte Aspekt des städtischen Mikroklimas, welcher in den Gebäudesimulationen dieser Thesis berücksichtig wird, ist der langwellige und solare Strahlungsaustausch zwischen benachbarten Gebäuden. Das Strahlungsmodell im Gebäudesimulationsmodell wurde ursprünglich nur für Innenräume entwickelt. Um in der Lage zu sein, dieses Strahlungsmodell auch für Aussenräume zu verwenden, werden die Strassenschluchten als Atrien modelliert. Das Strahlungsmodell berücksichtigt mehrfache Reflexionen der langwilligen und solaren Strahlung zwischen Gebäuden. Im letzten Teil dieser Thesis werden Gebäudesimulationen für das Klima von Basel für verschiedene Konfigurationen von freistehenden Gebäuden und Strassenschluchten durchgeführt. Zusätzlich zu den Simulationen, welche die erstellten Korrelationen von Wärmeübergangskoeffizienten verwenden, werden auch gekoppelte Gebäudesimulations-CFD Simulationen durchgeführt, bei welchen, für jeden Gebäudesimulationszeitschritt, eine CFD Simulation durchgeführt wird und die Resultate zur Berechnung des konvektiven Wärmestroms an den Gebäudefassaden an das Gebäudesimulationsmodell weitergegeben werden. Mit gekoppelten Simulationen können die Resultate der Gebäudesimulationen verbessert werden, im Speziellen für Fälle für welche keine fallspezifischen Korrelationen von Wärmeübergangskoeffizienten vorhanden sind. Ein starker Einfluss des städtischen Mikroklimas auf den Klimakälte- und den Heizwärmebedarf von Gebäuden kann festgestellt werden. Die Änderungen des Energiebedarfs für verschiedene lokale Mikroklimas können in derselben Grössenordnung sein, wie der Energiebedarf selbst. Dies zeigt die Wichtigkeit auf, das lokale Mikroklima zu berücksichtigen, wenn der Energiebedarf von Gebäuden in städtischen Gebieten vorausgesagt werden muss. Abschliessend werden Gebäudesimulationen für verschiedene Klimas durchgeführt. Der generelle Trend, wie das lokale Mikroklima den Klimakälte- und den Heizwärmebedarf beeinflusst, ist sehr ähnlich für verschiedene Klimas. Mit dem Ansatz, welcher in dieser Thesis präsentiert wird, können die meisten thermischen Effekten des städtischen Mikroklimas, in der Grössenordnung von Strassenschluchten, erfasst und quantifiziert werden.

Nomenclature

Roman Symbols

ΔT_0	base temperature for regional air temperature variation
$\Delta T_{a,solar}$	solar radiation contribution
ΔT_{NLWR}	net longwave radiation contribution
A	surface area
a	thermal diffusivity
B	wetness parameter
C	heat capacity
C_f	skin friction coefficient
C_H	transfer coefficient
C_i	thermal capacity of a thermal zone
c_p	specific heat capacity
C_μ	turbulent viscosity constant
c_{cover}	cloudiness factor
d	zero plane displacement
E	wall function constant
F	view factor matrix
f_i	external forces in direction i
f_{sky}	fraction of the sky seen by a surface
Fr	Froude number
G	Gebhart factor matrix
g	gravitational acceleration
H	building height

h	convective heat transfer coefficient
h	reference height
H_B	building height
h_c	convective heat transfer coefficient
H_{Fl}	floor height
I	identity matrix
I_b	beam solar radiation
I_d	diffuse solar radiation
I_l	longwave radiation
I_s	solar radiation flux
k	conductivity
k	turbulent kinetic energy
L	building length
L	characteristic length
l	latent heat of evaporization
L_{ref}	reference length
M	number of pixels in x direction
m	pixelshift in y direction
N	cloudiness
N	number of pixels in y direction
n	pixelshift in x direction
Nu	Nusselt number
P	population
p	pressure
p_0	local air pressure
P_i	heating/cooling power
P_J	wall function constant

p_{atm}	atmospheric pressure
Pr	molecular Prandtl number
Pr_t	turbulent Prandtl number
q	specific humidity
Q_A	net heat advection
q_A	specific humidity of the air
Q_E	sensible heat
Q_i	net heat gain
Q_L	latent heat
Q_l	longwave radiation flux
Q_r	net radiative flux
Q_s	solar radiation flux
Q_s	stored energy
q_S	saturated specific humidity at the surface
Q_T	anthropogenic heat
$q_{c,w}$	convective heat flux normal to the wall
Re	Reynolds number
Re^*	turbulent Reynolds number
Ri	Richardson number
Ri_{lo}	local Richardson number
s_{ij}	rate-of-strain tensor
T	surface temperature
T	temperature
T	time period
t	time
T^*	dimensionless temperature
T_P^*	dimensionless temperature at the centre point P of the wall-adjacent cell

T_0	amplitude of the temperature fluctuations at the surface
T_0	reference temperature
T_A	air temperature
T_a	ambient temperature
T_i	temperature of thermal zone
T_m	average yearly temperature
T_P	temperature at the centre point P of the wall-adjacent cell
T_S	surface temperature
T_w	wall temperature
T_{amb}	ambient air temperature
T_{Gr}	ground temperature
T_{in}	indoor air temperature
T_{ref}	reference temperature
T_{sat}	dew point temperature
T_{sky}	fictive sky temperature
T_{u-r}	UHI intensity
T_{vent}	incoming air temperature
U	velocity
U^*	dimensionless velocity
u^*	frictional velocity
U_p^*	dimensionless velocity at the centre point P of the wall-adjacent cell
u_{ABL}^*	ABL friction velocity
U^+	dimensionless velocity
U_0	reference wind speed
u_i	velocity in direction i
u_P	velocity at the centre point P of the wall-adjacent cell
U_{10}	wind speed at 10m above the ground

U_{FS}	freestream velocity
U_{ref}	reference velocity
v	velocity
V_{AVG}	averaged velocity
V_{RMS}	root mean square velocity
W	building width
W	street canyon width
W_1	subwindow in the first PIV image
W_2	subwindow in the second PIV image
x	horizontal coordinate
x_i	coordinate in direction i
Y	lapse rate
y	vertical coordinate
y^*	dimensionless wall distance
y_P^*	dimensionless wall distance of the centre point P of the wall-adjacent cell
y^+	dimensionless wall distance
y_P^+	dimensionless wall distance at the centre point P of the wall-adjacent cell
y_{sky}	sky view factor
z	distance from the surface
Z_0	reference height
z_0	aerodynamic roughness length

Greek Symbols

α	albedo
α	thermal diffusivity
β	volumetric thermal expansion coefficient
η_{HRV}	efficiency of the heat recovery system

κ	von Karman constant
λ	thermal conductivity
μ	dynamic viscosity
μ	thermal inertia
ν	kinematic viscosity
ν_t	eddy-viscosity
ϕ^D	dissipation function
ρ	cross-correlation
ρ	density
ρ_0	reference density
σ	Stefan-Boltzmann constant
σ	reflectivity
τ_w	wall shear stress
Θ	orientation
ε	emissivity
ε	turbulent dissipation rate

Subscripts

$_P$	centre point of wall-adjacent cell

Abbreviations

ABL	atmospheric boundary layer
AFW	adaptive wall function
BES	building energy simulation
CFD	computational fluid dynamics
$CHTC$	convective heat transfer coefficient
$CTTC$	cluster thermal time constant

$DEHS$	Di-Ethyl-Hexyl-Sebacat
EST	excess surface temperature
LES	large eddy simulation
LIF	laser-induced fluorescence
$LRNM$	low-Reynolds number modelling
LW	leeward
$NEWF$	non-equilibrium wall function
PIV	particle image velocimetry
POD	proper orthogonal decomposition
$RANS$	Reynolds averaged Navier-Stokes equations
SA	stand-alone
SC	street canyon
SWF	standard wall function
TKE	turbulent kinetic energy
TMY	typical meteorological year
UHI	urban heat island
$URANS$	unsteady RANS
WF	wall function
WW	windward
NEWF1	non-equilibrium wall function

Table of contents

1 Introduction

1.1 Background and motivation

Residential and commercial buildings consume roughly respectively 25 % and 15 % of the final energy consumption in the EU, including all energy delivered to the final consumers (excluding deliveries for transformation and network losses). Heating represents almost 70 % of the residential energy consumption [1]. Therefore there is a great energy saving potential by minimizing the energy demand for space cooling and heating of buildings. There is a global trend towards urbanization. In 1800 only 3 % of the world's population lived in urban areas, whereas today this number is up to 50 %. By 2050, this proportion will have risen to 70 %, resulting in larger cities. In Central Europe, urbanization is even more pronounced [2]. The microclimate in urban areas differs significantly from the climate in rural areas. The air temperatures are higher due to the urban heat island (UHI) effect [3] and the wind speeds are lower due to wind sheltering by buildings. Global warming and respective heat waves [4, 5] may further increase the temperatures in urban areas. The increased temperatures in urban areas, due to the strengthened UHI effect caused by urbanization, climate change and heat waves, have an impact on the thermal comfort and health of the people living in urban areas as well as on the energy demand for space cooling and space heating of buildings. The space cooling demand of buildings is not only increasing due to the higher outdoor air temperatures, but also due to higher comfort expectations of the occupants, higher solar gains for the increasing number of highly glazed buildings and higher internal gains from electrical appliance and artificial lightning. Added to the increasing need for space cooling in future, the increasing temperatures in urban areas will reduce the potential for passive night ventilation cooling significantly. Both effects cause higher space cooling demands.

Building energy simulation (BES) models are commonly used to predict space cooling and heating demands of buildings [6]. Most BES models, used today, were developed for stand-alone buildings. The question remains, whether these BESs are adequate for predicting the energy demand of buildings in urban areas. It is known that the radiation exchange between neighbouring buildings has a major impact on the energy demand of buildings. Commonly only shadowing is modelled in BESs. However, to correctly solve the energy balance, also multiple reflections of solar radiation between buildings and the longwave radiation exchange between them, has to be accounted for. To model the convective heat transfer at the building envelope, convective heat transfer coefficients (CHTCs) are commonly used. The CHTC relations, used in BESs, are usually based on measurements at façades of stand-alone buildings. Therefore, these CHTC correlations as a function of wind speed and surface temperature are not sufficiently correct for buildings in urban areas, since the flow field and as such also the convective heat transfer is strongly

influenced by the neighbouring buildings. In built areas the CHTCs are also influenced by buoyancy effects caused by the higher building surface temperatures, especially due to solar radiation. A third important urban aspect that has to be considered for a correct analysis of energy demand of buildings in urban areas is the UHI effect. Mostly meteorological data are not available for a specific urban area, or only for a very few locations. Therefore UHI models or additional temperature measurements are needed to account for the UHI effect.

Due to the limited energy resources, there is a need to reduce the global energy demand. Further the CO_2 production has to be reduced, to mitigate the global climate change. Therefore there is a need to build sustainable buildings. To design and optimize sustainable buildings, reliable BES models are needed, to be able to accurately predict the demands of buildings (especially in urban areas).

Using field measurements to derive CHTC correlations for buildings in urban areas is practically not feasible. Conducting a measurement campaign for each building that has to be simulated with BESs is very time-consuming and often not possible, e.g. because the buildings are not built yet. Computational fluid dynamics (CFD) is a solution to overcome this problem. CFD has a number of advantages for the determination of the CHTCs in urban areas: neighbouring buildings can be considered, geometries can be adapted, detailed information on the flow fields are known, the boundary conditions can be controlled (e.g. wind directions, wind speeds, boundary layer types) and therefore the effects of changed boundary conditions on the heat transfer can be investigated. The disadvantage of using CFD simulations for convective heat transfer predictions is that CFD simulations are computationally rather expensive. For convective heat transfer predictions with CFD it is of great importance that the thermal boundary layer at the analysed surfaces is physically accurately modelled. Resolving the whole boundary layer leads to the most accurate results, but is computationally expensive. The computational costs can be significantly reduced by using wall functions, which model, instead of resolve, the region between the wall and the fully turbulent regions. The disadvantage of wall functions is that they can introduce large errors for the prediction of the convective heat transfer.

In CFD codes a large number of different physical models are available that introduce certain assumptions. Therefore for each simulation the appropriate models need to be chosen, which is a task that is often not straightforward. To confirm that the chosen model predict a physically correct flow field, the CFD simulations have to be validated. For validation purposes commonly wind tunnel measurements are conducted. Urban street canyons are often chosen for validation as they are the most generic elements a city is composed of. In urban street canyons buoyancy plays an important role. During the day the building façades are heated by solar radiation. The heated walls induce buoyancy, what significantly affects the flow field in the street canyons. The effect of buoyancy in street canyons has been studied in wind tunnels (e.g. [7, 8]), but not yet enough data are available for a detailed validation of CFD simulations. Therefore the existing CFD codes need to be further validated for buoyant flows in urban areas.

CFD simulations in urban areas are not only useful for convective heat transfer predictions, but also to predict the urban microclimate and to investigate UHI mitigation strategies. Further CFD is important for pollutant dispersion studies in urban areas.

1.2 Scope and methodology

This thesis aims at a better understanding of the urban microclimate in street canyons taking in particular combined effects of wind and solar radiation into account. On the street canyon scale the microclimatic processes are analysed from the point of view of energy demand in buildings.

Because this thesis focuses on the street canyon scale, larger scale (mesoscale) processes are not investigated. The UHI effect for example is not predicted by simulations, but modelled based on measurements. Small scale processes, which are only relevant for the building scale, are not taken into consideration (e.g. dimensioning of HVAC systems). The geometries of the buildings and street canyons are strongly simplified. No real existing buildings or street canyons are studied. Because the aim of this study is to investigate the impact of the urban microclimate on the energy demand of buildings, the pedestrian comfort and pollutant dispersion inside the street canyons are not studied. Further the indoor comfort situation of the studied buildings is not evaluated, but considered as a boundary condition.

This study is conducted for the moderate European climate (Basel in Switzerland). Basel was chosen, because there exists a large number of measured climatic data for the urban areas and the surrounding rural areas [9]. The space cooling demand for stand-alone buildings in the rural areas surrounding the city of Basel is rather low. Space cooling becomes only important for buildings in the urban areas.

In a first part of the thesis the convective heat transfer at the building façades is studied. This part is conducted by means of CFD simulations. To limit the computational costs, steady RANS simulations with a $k - \varepsilon$ turbulence model are used. Resolving the whole thermal boundary layer to determine the wall heat fluxes is too time-consuming for the simulations in this thesis. On the other hand using existing wall functions leads to not sufficiently accurate results. Thus first the existing temperature wall functions are improved, to be able to use wall functions for the convective heat transfer studies within this thesis.

CFD is used to establish CHTC correlations for different stand-alone and street canyon geometries. For low wind speeds buoyancy is considered. Buoyancy has an important influence on the flow structure in urban street canyons. Only little relevant research is conducted for thermal flows in urban street canyons yet. For validation purposes wind tunnel experiments are conducted for isothermal street canyons and street canyons with heated surfaces. The flow field (velocities and turbulence) is measured with a high resolution measurement equipment.

In a second part of the thesis, the influence of the urban microclimate on the space cooling and space heating demands of buildings in urban areas is studied by performing BESs. The three main influencing mechanisms of an urban microclimate are considered: (i) the radiation exchange between neighbouring buildings, (ii) the UHI effect and (iii) the reduced convective heat transfer due to wind sheltering. To account for the radiation exchange between buildings, the radiation models, implemented in the BES model, are used. These models consider shadowing by neighbouring buildings as well as the longwave and solar radiation exchange between buildings. As outlined above, the UHI effect is modelled with UHI intensity schedules that are based on measurements. For the convective

heat transfer first the above mentioned CHTC correlations are used and later the BES model is coupled with CFD simulations. For each BES time step of a coupled simulation, a CFD simulation is performed in order to determine the CHTCs for the current urban microclimate.

1.3 Outline

This thesis consists of 6 chapters. In chapter 2 the urban microclimate and its influence on the energy demand in buildings is discussed. Further an outline of the state of the art in numerical and experimental modelling approaches for the applications used in this thesis are given. In chapter 3 the numerical models that are applied in this thesis, are described in more detail. In this chapter also the newly developed temperature wall function and the in this thesis established CHTC correlations are explained. In chapter 4 the wind tunnel measurements and the results are presented. In the second part of this chapter, a validation study is conducted. The results of the BESs are given in chapter 5. Results for the space heating and space cooling demands are presented as well as results for the radiative fluxes and temperatures at the surfaces. In the last chapter the conclusions of this thesis and an outlook for possible future research are given.

2 Urban microclimate and energy demand in buildings

In this chapter an introduction to the urban microclimate and its impact on the building energy demands is given. Further the state of the art numerical and experimental modelling approaches, that are relevant for this thesis, are presented.

2.1 Energy budget

The microclimate in urban areas differs significantly from the climate in rural areas. The air temperature is increasing from the rural to the densely built urban areas (Figures 2.1 and 2.2). This phenomenon is called the urban heat island (UHI) effect. The UHI effect is mainly caused by the following phenomena [10]:

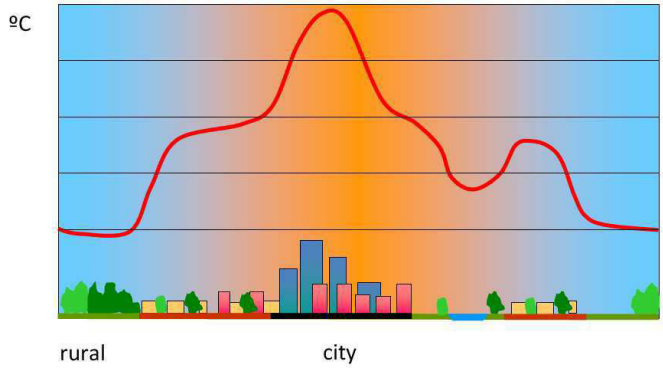

Figure 2.1: Sketch of an UHI profile (after [10]).

- Reduced sky view factors. Due to the high building density in urban areas, the sky view factors of the individual surfaces are reduced. Thus less longwave radiation can be radiated to the cold sky and the surface temperatures are higher in urban compared to the rural areas. Due to the high surface temperatures the convective heat flux from the surfaces to the air is increased leading to increased air temperatures.
- Materials with high heat capacities. The materials used in built environment can store more sensible heat than the natural soil. This sensible heat is again released at night-times and causes increased air temperatures.
- Anthropogenic heat. In urban areas large amount of anthropogenic heat is released by transportation, industry, animal metabolism etc.

- Urban greenhouse effect. More pollutants are produced in urban areas (transportation, industry etc.). Therefore the pollutant concentration is higher, which leads to an increase in incoming longwave radiation.
- Multiple reflections of radiation between buildings. In urban areas incoming solar and longwave radiation cannot be directly reflected back to the environment. The radiation gets entrapped between the buildings by multiple reflections and causes higher surface temperatures.
- Lack of evapotranspiration. Because there is less vegetation in urban areas, more absorbed radiation is transformed into sensible heat and less into latent heat.
- Reduced turbulent convective transfer. Due to the buildings that block the wind the turbulent convective transfer is reduced and less heat can be transported out of the cities by convection.

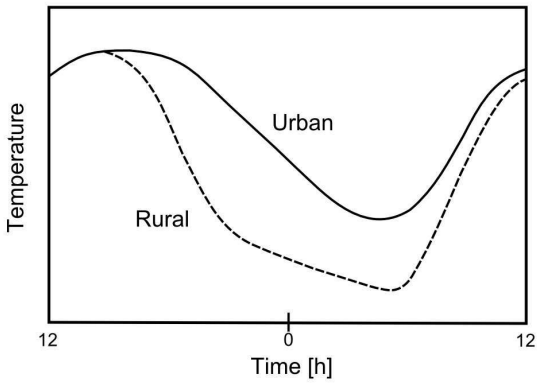

Figure 2.2: Sketch of diurnal temperatures in urban and rural areas (after [10]).

In Figure 2.1 a sketch of the spatial variation of the UHI profile is given. The UHI intensity is increasing with the building density and decreasing for vegetated areas. Due to the different morphologies these profiles are different for different urban areas. A sketch of diurnal temperatures in urban and rural areas is given in Figure 2.2. The highest temperature differences between urban and rural areas can be found during the night, when the materials in the urban areas cool down faster than the material in urban areas. This slower temperature decrease of the materials in urban areas is mainly caused by higher heat capacity of the materials and reduced sky view factors. At day-times the materials in rural areas heat up faster and the temperature difference is smaller. Due to this faster temperature increase in rural areas, for some cases also negative UHI intensities (temperature difference between rural and urban areas) can be found in the morning. The intensity of the UHI effect for a specific city depends on wide range of parameters (e.g. density of buildings, building materials, population, density of vegetation), what makes it difficult to predict the UHI intensities at a certain location in a specific city. UHI intensities up to 12 $°C$ can be measured. An overview of the UHI intensities that can be found in literature is given in Table 2.1 (summarized by Santamouris et al. 2001 [10] and

City	UHI intensity [°C]	Author
America		
Atlanta, USA	1.2	Hafner et al. 1999 [11]
Edmonton, Canada	6.5	Hage 1972 [12]
Fairbanks, USA	1	Magee et al. 1999 [13]
Montreal, Canada	10.5	Oke et al. 1971 [14]
New York City, USA	2.2	Holt et al. 2006 [15]
Phoenix, USA	1.5	Hartz et al. 2006 [16]
Asia		
Bangkok, Thailand	8	Tran et al. 2006 [17]
Beijing, China	10	Tran et al. 2006 [17]
Bombay, India	9.5	Padmanabhamurty 1986 [18]
Calcutta, India	4	Padmanabhamurty 1986 [18]
Ho Chi Minh, Vietnam	5	Tran et al. 2006 [17]
Hong Kong, China	3.4	Giridharam 2007 [19]
Kuala Lumpur, Malaysia	7	Sani 1990 [20]
Madras, India	4	Padmanabhamurty 1986 [18]
Manila, Philippines	7	Tran et al. 2006 [17]
New Delhi, India	6	Padmanabhamurty 1986 [18]
Pyongyang, North Korea	4	Tran et al. 2006 [17]
Seoul, South Korea	8	Tran et al. 2006 [17]
Shanghai, China	7	Tran et al. 2006 [17]
Tokyo, Japan	8	Saito et al. 1996 [21]
Africa		
Cairo, Egypt	4	Fouli 1994 [22]
Johannesburg South, Africa	2	Goldreich 1985 [23]
Lagos, Nigeria	4	Oguntoyinbo 1986 [24]
South America		
Buenos Aires, Argentina	7.4	Mazzeo et al. 1990 [25]
Europe		
Athens, Greece	10	Santamouris et al. 2001 [26]
Basel, Switzerland	6	Wanner et al. 1983 [27]
Biel, Switzerland	5	Wanner et al. 1983 [27]
Budapest ,Hungary	2.3	Pongracz et al. 2006 [28]
Freiburg, Germany	10	Nuebler 1979 [29]
Fribourg, Switzerland	5	Wanner et al. 1983 [27]
Goteborg, Sweden	5	Eliasson 1996 [30]
Lodz, Poland	12	Klysik et al. 1999 [31]
London, England	7	Watkins et al. 2003 [32]
Paris, France	8	Lemonsu et al. 2002 [33]
Zürich, Switzerland	7	Wanner et al. 1983 [27]

Table 2.1: UHI intensity for different cities.

Memon et al. 2009 [34]). Two types of UHI intensities can be studied: (i) air temperature based UHI intensities and (ii) surface temperature based UHI intensities [34]. Surface temperature based UHI intensities are mostly measured with satellites. For building energy simulations the air temperature based UHI intensities are important and therefore only this kind of UHI intensity is discussed in this thesis. There are large differences between the qualities of the different UHI studies in literature. Stewart et al. 2011 [35] used the following criteria to evaluate the quality of 190 UHI studies in literature:

- Operational test and conceptual model are aligned
- Operational definitions are explicitly stated
- Instrument specifications are explicitly stated
- Site metadata are appropriately detailed
- Field sites are representative of the local-scale surroundings
- Number of replicate observations is sufficiently large
- Weather effects are passively controlled
- Surface effects are passively controlled
- Temperatures are measured synchronously

They conclude that "overall, the quality of the UHI literature and its empirical content is low at best". For most of the studies there is information missing to evaluate the quality of the measurements. The large number of UHI studies were mostly not conducted following a widely accepted guideline. Therefore it is very difficult, if not impossible, to compare the results of the different studies. Aguilar et al. 2003 [36] and Oke 2004 [37] proposed guidelines to measure and report temperatures in urban and rural areas. Further there is no consistent definition of the UHI intensity. Mostly it is defined as the temperature difference between an "urban" and a "rural" area. But there also exists no consistent definition for these two terms. Therefore the areas called "urban" or "rural" differ significantly for the different studies. To solve the problem of the missing definitions, Stewart et al. 2009 [38] proposed a system for classifying UHI measurement sites. They suggest to report "inter-zone" temperature differences for standardized zones instead of UHI intensities.

The thermal balance in urban areas is strongly modified compared to rural areas, what causes the microclimatic differences. The energy gains in urban areas are the sum of the longwave and solar radiative fluxes (Q_r) and the anthropogenic heat (Q_T). This energy is either stored (Q_s), lost in form of sensible (Q_E) or latent heat (Q_L) or transferred from the system through advection (Q_A). The energy balance of the surface-air system is given in Equation 2.1 [10] and illustrated in Figure 2.3:

$$Q_r + Q_T = Q_E + Q_L + Q_s + Q_A \tag{2.1}$$

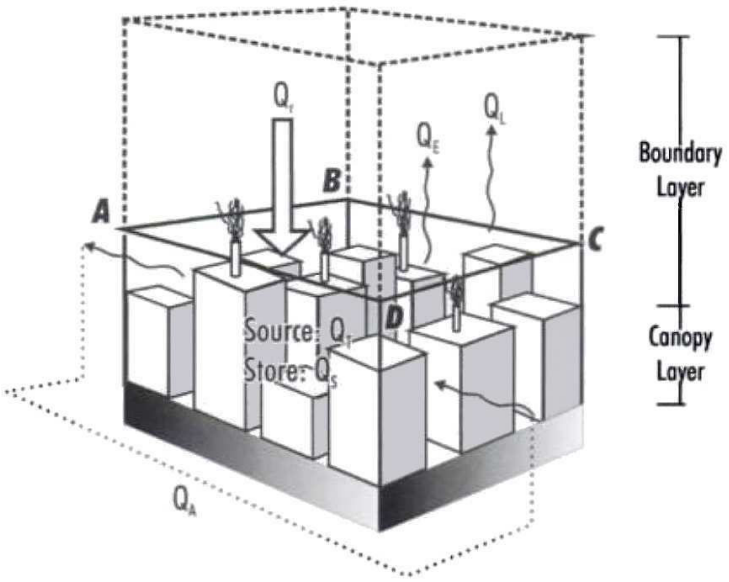

Figure 2.3: Schematic presentation of the energy fluxes in the urban environment (taken from [10], after [3]).

Here the different heat fluxes of Equation 2.1 are described. The net radiative flux Q_r is the difference between the sum of the incoming absorbed longwave and solar radiation and the emitted longwave radiation [10]:

$$Q_r = (I_b + I_d)(1 - \alpha) - I_l \tag{2.2}$$

where I_b is the beam solar radiation, I_d is the diffuse solar radiation, α is the albedo of the city and I_l is the longwave radiation (positive values for emitted and negative values for absorbed longwave radiation).
The longwave radiation emitted by the surfaces in urban areas is given by the Stefan-Boltzmann law:

$$I_l = \varepsilon \sigma T^4 \tag{2.3}$$

where ε is the emissivity, σ is the Stefan-Boltzmann constant and T is the surface temperature.
The longwave radiation from the sky that is absorbed in the cities cannot directly be determined with the Stefan-Boltzmann law. A fictive sky temperature (T_{sky}) is introduced, which is defined as the black-body temperature that gives the same spectral distribution as the sky. This fictive sky temperature is needed to determine the longwave radiation exchange with the sky. The sky temperature is mostly defined as a function of the ambient air temperature. The sky temperature is further influenced by the cloudiness, humidity, the pollutant concentration in the air and other parameters. With the sky temperature the incoming longwave radiation can be determined as follows:

$$I_l = \sigma T_{sky}^4 \tag{2.4}$$

The anthropogenic heat Q_T is mainly caused by transportation, industry, heating and power generation systems. The amount of anthropogenic heat by area varies strongly between different cities. A summary of the anthropogenic heat from literature is given in Table 2.2 (summarized by [10] and [39]).

City	Anthropogenic heat $[W/m^2]$	Author
Basel Switzerland	5-20	Christen et al. 2004 [40]
Lodz Poland	32	Offerle et al. 2005 [41]
Reykjavik Iceland	35	Steinecke 1999 [42]
Tokyo Japan	200-1590	Ichinose et al. 1999 [43]
Chicago USA	53	Taha 1997 [44]
Los Angeles USA	21	Taha 1997 [44]
New York City USA	117-159	Taha 1997 [44]
Moscow Russia	127	Taha 1997 [44]
Budapest Hungary	43	Taha 1997 [44]
Vancouver Canada	19	Taha 1997 [44]
Berlin Germany	21	Taha 1997 [44]

Table 2.2: Reported anthropogenic heats in various parts of the world.

The anthropogenic heat causes an increase of the air temperatures in urban areas. Different estimates of the impact of the anthropogenic heat on the air temperatures can be found in literature (summarized by [10]). Taha et al. 1992 [45] found that the anthropogenic heat can cause an increase of the air temperature in a large city of $2-3\ ^\circ C$. Oke et al. 1991 [46] estimated an air temperature increase of $2-8\ ^\circ C$ due to heat originating from heating systems of buildings. Gutman and Torrance 1975 [47] determined an heat island intensity of 2.9 $^\circ C$ for a theoretical city with an anthropogenic heat flux of 125 W/m^2.

The radiative heat absorbed by the surfaces in urban areas is either stored in the materials or transferred into latent or sensible heat. In urban areas sensible heat Q_E is more important than latent heat due to low vegetation percentages. The sensible heat flux is mostly approximated as a function of the temperature difference between the surface and air $(T_S - T_A)$.

$$Q_E = h\,(T_S - T_A) \tag{2.5}$$

where h is the convective heat transfer coefficient (CHTC).
The treatment of the latent heat Q_L is usually modelled in a similar way as for the sensible heat. For example the Monin-Obukhov similarity can be applied [48]:

$$Q_L = l\rho BC_H U\,(q_S - q_A) \tag{2.6}$$

where l is the latent heat of evaporization, B is the wetness parameter, C_H is the transfer coefficient, U is the wind speed, q_A is the specific humidity of the air and q_S is the saturated specific humidity at the surface.

The amount of heat that is stored Q_s in the building materials and the soil is almost impossible to measure [40]. To estimate the stored heat, usually the heat balance (Equation 2.1) needs to be solved [39].

The amount of heat Q_A that can be transported from the urban to the rural areas and the convective heat transfer at the urban surfaces are strongly dependent on the wind patterns in the built environment. The interaction of the wind flow with the urban canopy is very complex. The wind speed close to ground is decreased due to the roughness of the terrain. Thus an atmospheric boundary layer (ABL) develops with high velocity and turbulent kinetic energy gradients. A common way to model the ABL is to divide the ABL into two sublayers: the free surface layer (above roof top) and the obstructed sublayer [3]. A logarithmic law is usually applied to approximate the free surface layer [49]:

$$U(z) = \frac{u^*}{\kappa} ln \left(\frac{z + d + z_0}{z_0} \right) \tag{2.7}$$

where z is the height above the ground, u^* is the frictional velocity, κ is the von Karman constant, d is the zero plane displacement and z_0 is the roughness length.
For the obstructed sublayer an exponential law is mostly used to describe the boundary layer [49]:

$$U(z) = U_0 e^{z/Z_0} \tag{2.8}$$

where U_0 is a constant reference wind speed and Z_0 a reference height.
In Figure 2.4 a sketch of the ABL of an urban area is given.

In this thesis the flows around buildings immersed in an ABL are studied. Buildings are mostly bluff bodies with sharp edges. For sharp edged bluff bodies the separation points are predefined and are at the edges of the bodies. In Figure 2.5 a sketch of the flow around a cube is given. The flow approaching the cube is guided partly over and partly around the cube. Close to the cube a complex vortex structure is formed. The air hitting the windward wall is not only directed over and around the cube, but a part is also directed towards the ground. This air creates a standing vortex near the ground in front of the cube. This standing vortex wraps around the corner and is called horseshoe vortex. At the top and the two sides of the cube recirculation zones that are formed due to separation, can be found. At the leeward wall of the cube there is a large standing vortex and behind this vortex the flow reattaches again. For wind directions that are not normal to the cube, the flow structures are completely different, but the separation points are still predefined by the edges.

For flows in urban areas it is not sufficient to study the flow around a single bluff body, but one has to account for the interaction of a number of bluff bodies. The flow in passages between buildings can be strongly accelerated due to pressure differences or can be completely blocked. Therefore it is important to consider the neighbouring

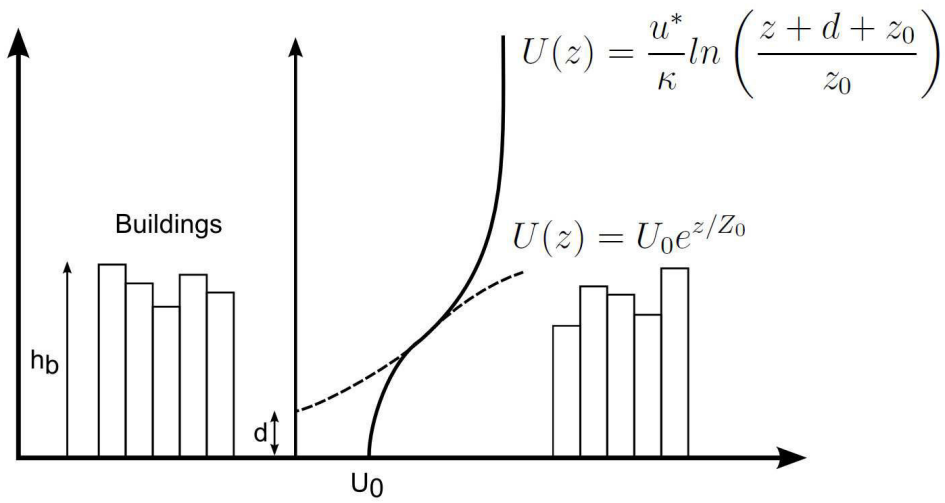

Figure 2.4: Sketch of an urban boundary layer (after [49]).

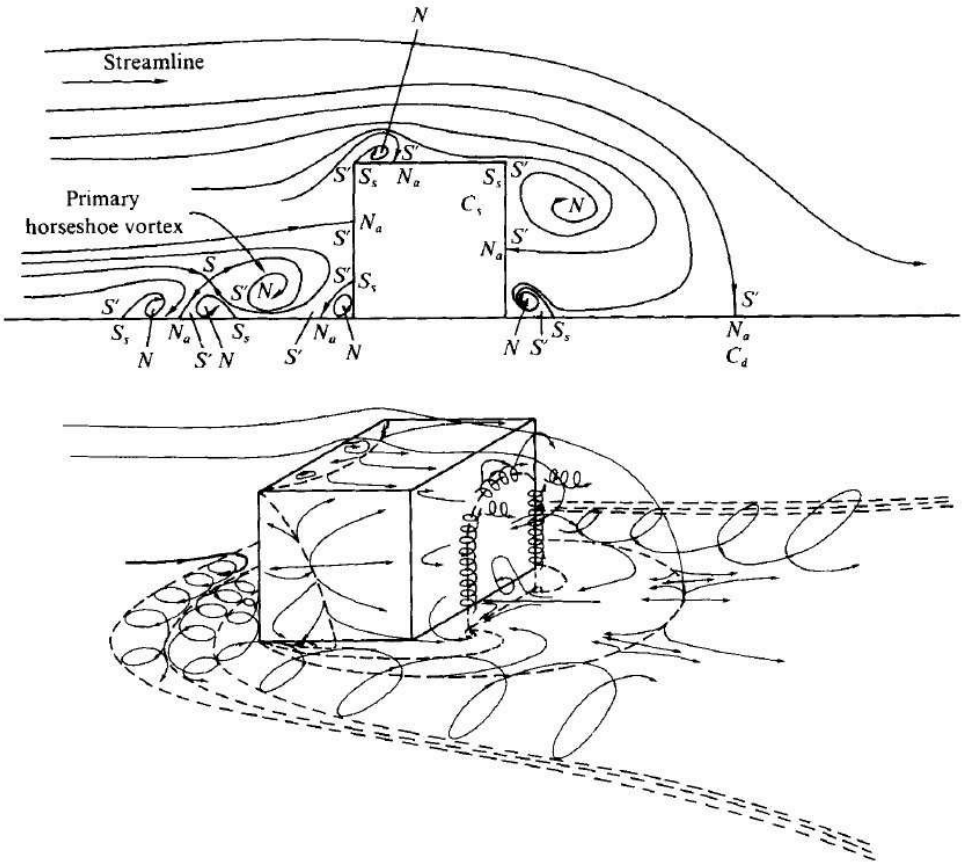

Figure 2.5: Sketch of the flow around a cube (taken from [50]).

buildings, when for example the convective heat transfer at a building façade needs to be determined. In Figure 2.6 the flows around different building configurations are shown. The wind speeds are mainly increased around the corners (corner streams) and between the buildings. Comparing the results of the two columns in the figure, it can be noticed that already small changes in the building configuration, have a large impact on flow field around the individual buildings. Further case b_1 can be regarded as a superposition of case a_1 and c_1. On the other hand for case b_2 the flow field cannot be considered as a superposition of the flows of cases a_2 and c_2. Therefore the flow in urban areas cannot be predicted by superimposing the flows fields around individual buildings or small building groups. An example of a complex flow field in an urban area is given in Figure 2.7

In this thesis mostly urban street canyons are chosen being the most generic elements a city is composed of. Here the flow in urban street canyons is discussed in more detail. In literature a large number of studies for urban street canyons have been conducted. Results of numerical studies (e.g. [53–55]), experimental studies (e.g. [7, 56–62]) in wind tunnels and field measurements (e.g. [63, 64]) can be found in literature. Urban street canyons are characterized by the length (L) and the height of the buildings (H) and the width of the street canyon (W) (see Figure 2.8). The ratio H/W is called the aspect ratio of the street canyon. For most studies it was assumed that the approach flow direction is normal to the street canyon axis. Oke et al. 1988 [65] described three different flow regimes dependent on the street canyon aspect ratio (Figure 2.9). For very small aspect ratios ($H/W < 0.05$) there is no interaction of the flows around the individual buildings. With smaller spacing first the wakes get disturbed by the neighbouring buildings. This flow regime is known as the "isolated roughness" flow regime (Figure 2.9a). For "wake interference flows" (Figure 2.9b) the standing vortices at the windward and leeward walls of the neighbouring buildings start to interact. The vortices at the leeward sides of the buildings are reinforced by the downwards motion at the windward wall of the next building. For large aspect ratios a stable standing vortex in the centre of the street canyon is formed. The flow for such flow regimes is called "skimming flow". In this thesis only flows in the skimming flow regime have been analysed. In this case there is a coupling between the wind speed above and inside a street canyon. The relation between the two wind speeds is linear. For an aspect ratio of 1 the wind speed inside the street canyon is about 0.66-0.75 times slower than above the street canyon [66]. For low wind speeds this coupling is lost. In deep street canyons more than one vortex can exist. For wind directions parallel to the street canyon the wind speeds inside the street canyon are also a linear function of the wind speed above the street canyon. The wind speed inside the street canyon is decreased due to friction. With oblique flow directions a helical vortex is formed inside the street canyon.

The microclimate inside street canyons is not only dependent on the wind flow but also strongly influenced by radiation exchange between buildings. As for the flow also for the radiation exchange the aspect ratio of the street canyon plays an important role, because it affects the sky view factors of the surfaces inside the street canyon. Narrow street canyons have small sky view factors, what means that less heat can be radiated by longwave radiation to the cold sky. Therefore narrower street canyons cool down at a lower rate at night-times and therefore experience higher surface temperatures. At day-times less solar radiation can enter narrow street canyons and therefore the surfaces heat

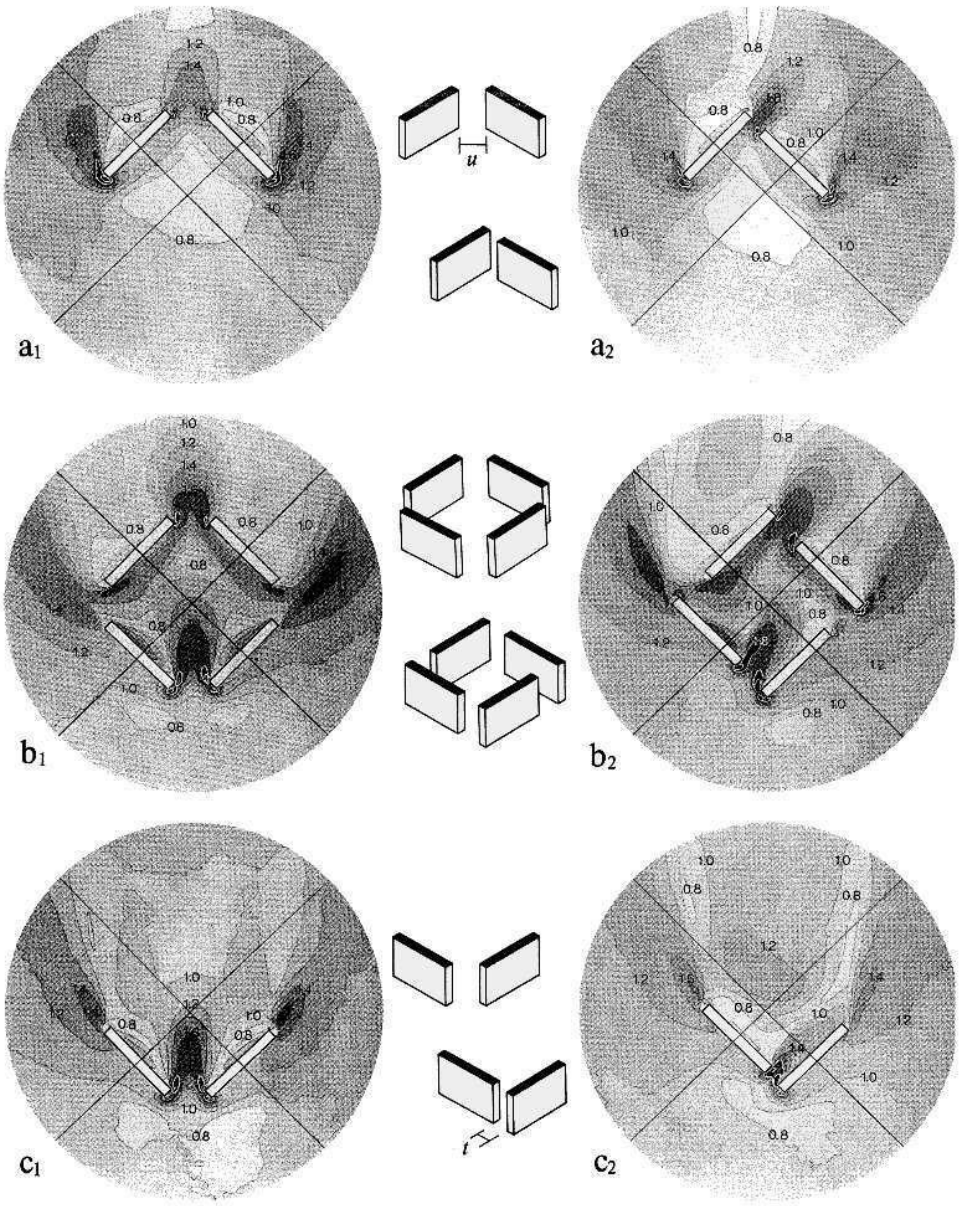

Figure 2.6: Flow around groups of buildings (taken from [51]).

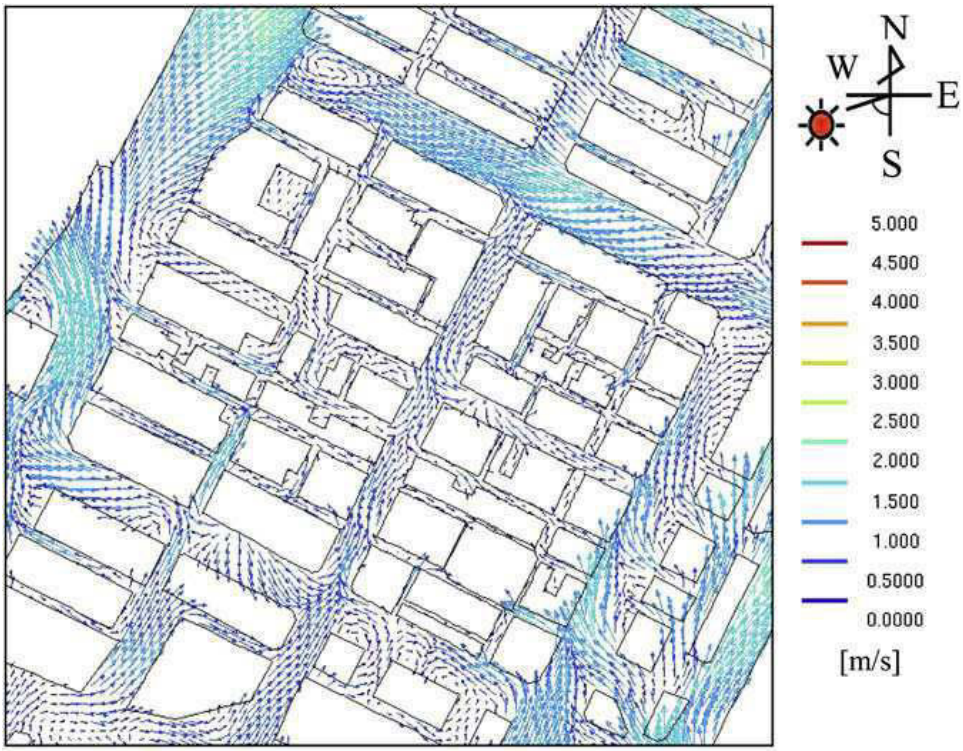

Figure 2.7: Horizontal distribution of the wind velocity in Kyobashi. (taken from [52]).

up less compared to wide street canyons. The air temperature inside the street canyons increases by convection from the heated surfaces. The increased surface temperatures not only increase the UHI effect, but also induce buoyancy, what has an impact on the flow field inside the street canyon. For high surface temperatures at the windward wall and low wind speeds the flow field can be significantly different from the flow fields described above. The effect of buoyancy inside street canyons is discussed in more detail in the following sections of the thesis.

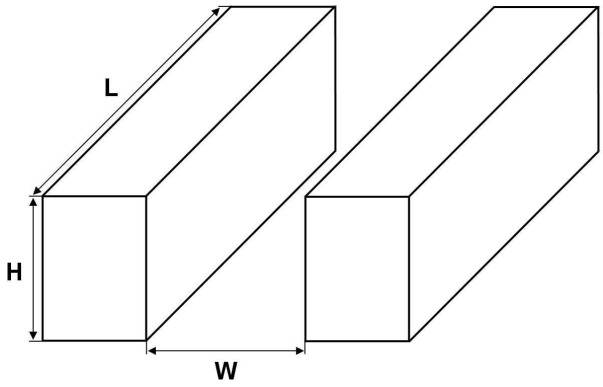

Figure 2.8: Sketch of an urban street canyon.

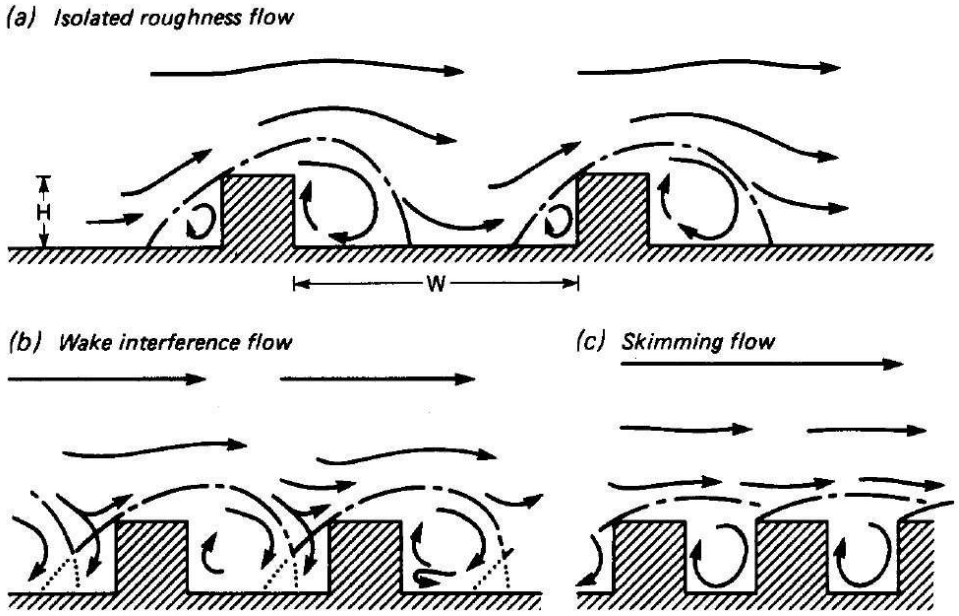

Figure 2.9: The flow regimes associated with air flow over building arrays of increasing H/W (taken from [65]).

2.2 Impact of urban microclimate on building energy demand

The energy demand for space cooling and heating of buildings is strongly dependent on the climate that it is exposed to. To accurately predict the energy demand of a specific building, the detailed local microclimate has to be known. The climate at the mesoscale can only be used to determine a general trend of e.g. the space cooling and heating demands. Buildings in the same region can have very different energy demands due to different local microclimates. The microclimate gets especially important when the energy demands of buildings in urban areas are compared with the demands of buildings in rural areas. The UHI effect causes a different thermal behaviour of buildings. The higher ambient air temperatures increase the space cooling demands and decrease the space heating demand. Akbari et al. 1992 [67] reported that for US cities the peak electricity loads increase by $1.5 - 2$ % for a temperature increase of 1 $°F$. Several studies have been conducted to investigate the impact of the UHI effect on the space cooling demand of buildings (e.g. Athens [26]; London [68, 69]; Kassel [70]; Tokyo [71]). All studies show a significant impact of the UHI on the energy consumption of buildings. Due to the higher ambient temperatures in general natural ventilation potential and especially the night cooling potential decrease. Reasons are the higher air temperatures and the lower wind speeds in urban areas. Due to the high building density, the wind is blocked in urban areas, what causes a lower air exchange and therefore lower ventilation potential of the outdoor spaces [72, 73]. The lower wind speeds also affect the convective heat transfer at the building surfaces. The heat exchange is reduced due to the reduced local wind speeds. Therefore the energy losses from the building to the environment are

lower in urban areas, what has an additional impact on the space cooling and heating demands [74, 75]. The façades temperatures of buildings are for almost all instance in time higher than the ambient air temperatures [76] due to the entrapment of the solar radiation. The higher temperature of the building mass cause a higher space cooling and a lower space heating demand compared to buildings in rural areas [77–80]. To mitigate this effect, it is proposed to use high albedo colours for the building façades and roofs to reflect the solar radiation [44, 81–83]. This strategy is only working, if the solar radiation can be reflected back to the environment and is not entrapped between the buildings due to multiple reflections. Neighbouring buildings affect not only the radiation balance at the façades, but also cause shading effects that influence the demand for artificial lighting and therefore the energy consumption of buildings in urban areas [84].

There is not only an influence of the urban microclimate on the buildings, but also the buildings strongly influence the urban microclimate. The surface temperatures of the buildings have a strong impact on the UHI effect. By minimizing the surface temperatures not only the building mass temperature can be reduced but also the air temperatures in the urban area are reduced. Further the building geometries have a large impact on the wind flows in urban areas and therefore also on the ventilation of those areas and on the convective heat transfer at the building surfaces. In hot cities the UHI effect can be reduced by choosing a heat rejection system for the air conditioners that releases the heat at a location where the heat can be transported out of the city by wind [85].

A number of studies have been conducted to investigate the influence of the urban microclimate on the energy demand of buildings. This influence is commonly modelled at different degrees of complexity. A first step is to account for the UHI effect by using meteorological data measured at a specific location instead of data from a meteorological station. Schneider et al. 2010 [70] found a significant change of the predicted energy demand by using different meteorological data for their simulations. Kolokotroni et al. 2010 [68] and Santamouris et al. 2001 [26] reported a significant reduction of the night ventilation potential for London and Athens due to the UHI effect. A second step consists in taking into account more correctly radiative heat fluxes. Stupka et al. 2010 [86] accounted for shadowing and reduced ground reflectance and found a lower heating demand with increasing density of the neighbourhood. Stromann et al. 2011 [84] found an increase of the total energy consumption of buildings due the effect of urban density on daylight availability and passive solar gains. The third step is to take the local air flow field into account. Bouyer et al. 2011 [87] coupled a BES (building energy simulation) model with CFD (computational fluid dynamics) simulations. The authors reported that the solar irradiance is the most important parameter for the energy demand of the studied building, followed by the convective fluxes. Ooka 2007 [88] proposed a similar coupling method for evaluating the energy demand and the thermal comfort inside buildings. It is known that for modelling the microclimate around a building accurately, effects at different scales have to be accounted for. These scales are the meso-meteorological scale, the city scale, the city quarter scale, the street canyon scale and the building scale. The computational costs for taking all these scales into account in BESs are still far too high. Therefore Rasheed 2009 [89] proposed a method to convert the complex geometry of a real urban area into a simplified geometry consisting of a regular grid of blocks. It can be concluded that most of these studies focused only on the influence of one single aspect of the urban

microclimate on energy demands or that urban microclimate physical mechanisms are strongly simplified.

2.3 Numerical modelling

2.3.1 Computational fluid dynamics (CFD)

Fluid flows play an important role at a large number of different scales from large scale atmospheric flows to small scale channel flows for example. Further a large number of different fluids exist, whereof air and water are the most studied fluids. For all fluid flows one of the most important characterizations is the distinction between laminar and turbulent flows. For laminar flow the fluid flows in layers that are not mixed and no swirl can be found in the flow. If the boundary conditions do not change over time the flow is stationary. Even if the flow is accelerated over time, the flow can be instationary but still remain laminar. Turbulent flows on the other hand are always instationary and always have swirls. The turbulent flows have a chaotic behaviour and are therefore difficult to simulate. As a criterion to decide whether a flow is laminar or turbulent the Reynolds number is commonly used:

$$Re = \frac{U_{ref} L_{ref}}{\nu} \tag{2.9}$$

where U_{ref} is a reference velocity, L_{ref} is a reference length and ν is the kinematic viscosity. For low Reynolds numbers flows are laminar, with increasing Reynolds numbers the flows get unstable and reach, above a critical Reynolds number, a fully turbulent state. The value of the critical Reynolds number depends on a number of parameters and is different for different configurations.

Laminar as well as turbulent fluid flows can be described with the Navier-Stokes equations. The Navier-Stokes equations are conservation equations for mass, momentum and energy. For incompressible flows the conservation equations are given below:
Conservation of mass:

$$\frac{\partial u_l}{\partial x_l} = 0 \tag{2.10}$$

Conservation of momentum:

$$\frac{\partial u_i}{\partial t} + u_l \frac{\partial u_i}{\partial x_l} = -\frac{1}{\rho} \frac{p}{x_i} + \nu \frac{\partial^2 u_i}{\partial x_l \partial x_l} + f_i \tag{2.11}$$

Conservation of energy:

$$\frac{\partial T}{\partial t} + u_l \frac{\partial T}{\partial x_l} = \frac{\lambda}{\rho c_p} \frac{\partial^2 T}{\partial x_l \partial x_l} + \frac{1}{\rho c_p} \phi^D \tag{2.12}$$

with the dissipation function ϕ^D:

$$\phi^D = 2\mu s_{lm} s_{lm} \tag{2.13}$$

and the rate-of-strain tensor:

$$s_{ij} = \frac{1}{2}\left(\frac{\partial u_i}{\partial x_j} + \frac{\partial u_j}{\partial x_i}\right) \tag{2.14}$$

where u_i is the velocity, x_i is the coordinate in direction i, t is the time, ρ is the density, p is the pressure, f_i are external forces in direction i, T is the temperature, λ is the thermal conductivity, c_p is the specific heat capacity, ϕ^D is the dissipation function, μ is the dynamic viscosity and s_{ij} is the rate-of-strain tensor.

The Navier-Stokes equations can only be solved analytically for a very limited number of flows. For most flow configurations the Navier-Stokes equations have to be solved numerically, what is called computational fluid dynamics (CFD). For turbulent flows, solving the Navier-Stokes equations gets computationally very expensive and is with the today's computer for most cases not feasible. To be able to simulate complex turbulent flows, turbulence models are commonly used. One of the most used turbulence model is based on the decomposition of the flow quantities into mean and fluctuating components, what is called Reynolds averaging. The velocity for example is decomposed as follows:

$$\underline{u}\left(\underline{x}, t\right) = \overline{\underline{u}\left(\underline{x}, t\right)} + u'\left(\underline{x}, t\right) \tag{2.15}$$

where $\overline{\underline{u}\left(\underline{x}, t\right)}$ is the time averaged and $u'\left(\underline{x}, t\right)$ is the fluctuating velocity.

Reynolds averaging of the Navier-Stokes equations results in equations for the time averaged quantities. These equations are called Reynolds averaged Navier-Stokes (RANS) equations and are given below.
Mass:

$$\frac{\partial \overline{u}_l}{\partial x_l} = 0 \tag{2.16}$$

Momentum:

$$\frac{\partial \overline{u}_i}{\partial t} + \overline{u}_l \frac{\partial \overline{u}_i}{\partial x_l} = -\frac{1}{\rho}\frac{\partial \overline{p}}{\partial x_i} + \nu \frac{\partial^2 \overline{u}_i}{\partial x_l \partial x_l} - \frac{\partial}{\partial x_l}\left(\overline{u_i' u_l'}\right) + \overline{f_i} \tag{2.17}$$

Energy:

$$\frac{\partial \overline{T}}{\partial t} + \overline{u_l}\frac{\partial \overline{T}}{\partial x_l} = \frac{\lambda}{\rho c_p}\frac{\partial^2 \overline{T}}{\partial x_l \partial x_l} - \frac{\partial}{\partial x_l}\left(\overline{u_l' T'}\right) + \overline{\phi^D}\frac{1}{\rho c_p} \tag{2.18}$$

with the averaged dissipation function $\overline{\phi^D}$:

$$\overline{\phi^D} = 2\mu \overline{s}_{lm} \overline{s}_{lm} + 2\mu \overline{s_{lm}' s_{lm}'} \tag{2.19}$$

Compared to the Navier-Stokes equations the RANS equations contain nine additional

unknowns: the Reynolds stress tensor $\overline{u_i' u_j'}$ and the Reynolds (turbulent) heat flux $\overline{u_l' T'}$. Therefore the RANS equations have more unknowns (14) than equations (5) and are therefore not closed. Turbulence modelling is needed to close and therefore solve the RANS equations. Eddy-viscosity models are most commonly used to close the RANS equations. The Reynolds stresses are modelled by the Boussinesq eddy-viscosity approximation:

$$-\overline{u_i' u_j'} + \frac{1}{3}\overline{u_l' u_l'}\delta_{ij} = 2\nu_t \overline{s_{ij}} \tag{2.20}$$

where ν_t is the eddy-viscosity.
With the eddy-viscosity hypothesis the number of unknowns of the Reynolds stress tensor in the momentum equation (Equation 2.17) of the RANS equations can be reduced from six to one. The eddy-viscosity is not a fluid property, but a model variable of the eddy-viscosity model. There are a number of different models for the eddy-viscosity. For a wide range of application the $k-\varepsilon$ model is often used, which relates the eddy-viscosity to the turbulent kinetic energy k and the turbulent dissipation rate ε:

$$\nu_t = C_\mu \frac{k^2}{\varepsilon} \tag{2.21}$$

where C_μ is a model constant.

Additional to the RANS equations, transport equations for the turbulent kinetic energy and the turbulent dissipation rate have to be solved. There exist different versions of these transport equations.

Besides the eddy-viscosity model there exists also more advance RANS turbulence models. For the Reynold-Stress transport model, the transport equations for all Reynolds stresses and the turbulent dissipation rate are solved. This has the advantage that this model can account for anisotropy, what is not possible with the eddy-viscosity models.

All the described RANS models solve for time averaged flow quantities. To solve transient flow phenomena other models exist (e.g. direct numerical simulations, large eddy simulations, unsteady RANS). For more details on turbulence modelling it is referred to [90].

In this study mainly atmospheric boundary layer flows are studied by CFD. These flows are caused by large-scale pressure systems. In the boundary layers the flow is turbulent due to the large roughness of the earth's surface (especially in urban areas) and due to turbulence induced by buoyancy. In atmospheric flow the very large scale turbulence as well as the very small scale turbulence are important. This makes it computationally expensive to simulate atmospheric boundary layer flows. Therefore in practice often RANS simulations with a $k-\varepsilon$ turbulence model are used to limit the computational costs of the CFD simulations.

2.3.2 Building energy simulation (BES)

Building energy simulation (BES) models are commonly used to predict space cooling and heating demands and to optimize buildings in terms of energy efficiency. In this thesis BESs are conducted to predict and compare the energy demands of buildings in urban areas with buildings in rural areas. There exists a large number of BES models (e.g. TRNSYS, EnergyPlus, DOE, IDA-ICE, ESP-r), which use different numerical approaches. In this study TRNSYS [91] is used. Therefore in this section mainly the models that are implemented in TRNSYS are discussed. For more information on other BES model it is referred to Crawley et al. 2008 [92]. This paper gives an overview of the 20 major BES programs and compares their features and capabilities. TRNSYS is a transient 3D mulitzone BES model. This means that the buildings are modelled in 3D and are divided into different thermal zones. A thermal zone can consist of a single room, a storey or even a whole building. For each thermal zone the boundaries (walls, windows, ground, roof etc.) need to be modelled and the heat fluxes (by conduction, convection, radiation etc.) through the boundaries need to be determined to solve the energy balance for the thermal zone. Sink and source terms (e.g. internal gains, ventilation, cooling, heating etc.) are also to be accounted for in the energy balance. In the following subsections it is described, how the different building components and the energy fluxes are modelled.

2.3.2.1 Opaque surfaces

A large part of a building consists of opaque surfaces (internal and external walls, ground, roof, etc.). These elements strongly influence the thermal behaviour of a building. The opaque surfaces are mostly together with the transparent surfaces (windows) the boundaries of a thermal zone. Opaque surfaces usually consist of multiple layers (insulation, load-bearing materials, plaster etc.). To determine the heat conduction through these surfaces and the energy stored inside the materials, the following material properties need to be defined: thermal conductivity, heat capacity and material density. Further to determine the radiation exchange with the environment and other surfaces, the solar absorptance and the longwave emission coefficients need to be given. Usually CHTCs are used to determine the convective heat transfer at the surfaces. In some cases the boundary conditions (e.g. temperature or heat flux) at one side of a opaque material are known and can directly be imposed. For more complex constructions heat sources inside the opaque materials can be defined.

2.3.2.2 Transparent surfaces

For transparent surfaces (windows) not only the heat conduction, convection and the absorption of longwave and solar radiation has to be modelled, but also the transmission of solar radiation into and out of the thermal zone. Windows can be modelled in different ways. Here the description is limited to windows in TRNSYS. A window consists of a number of window panes (glazing), where the cavity between the panes can be filled by different gases. At each window pane the absorption, the reflection and the transmission of solar radiation is determined separately. The longwave radiation exchange between the different window panes as well as the heat conduction and convection in the gas are

considered. Because the amount of absorbed, reflected and transmitted solar radiation is strongly dependent on the incidence angle of the solar beam, different solar absorptances and reflectivities are given for different incidence angles. In TRNSYS the solar absorptances, the reflectivities, the solar transmisivities, the emissivities and the conductivity of the gas fillings are precalculated and used as an input file. For the determination of the convective heat transfer at the outer and inner surfaces of the windows mostly CHTCs are used.

2.3.2.3 Solar protection

Radiation through windows lead to high solar gains, therefore shading devices are installed to protect the buildings from too high solar gains. These shading devices can be modelled with different degrees of complexity. The simplest way is to define a shading factor and to assume that the incident solar radiation is reduced by this factor. A next step is to account for the additional thermal resistance caused by the shading device that reduces the heat losses of the windows to the environment. This model neglects the solar radiation exchange between the shading device and the window panes and the solar heat gains of the shading device that increases the air temperature by convection. For more complex shading device models this effect can be taken into account by defining the reflectivity of the shading devices and the amount of solar radiation that is absorbed by the shading device and increases the air temperature by convection. For this thesis the shading devices were modelled with constant reduction factor and an additional thermal resistance was considered.

2.3.2.4 Soil

At the lowest storey, buildings are in contact with the soil. At the ground floor a temperature boundary condition has to be imposed. A part of the soil is modelled and a temperature is imposed following a schedule for a period of one year. This schedule is obtained by modelling the soil at the location of the simulated building with appropriate thermal properties (thermal diffusivity, yearly averaged temperature, temperature amplitude).

2.3.2.5 Weather

At most boundaries, of the buildings modelled with BESs, meteorological data have to be imposed. The meteorological data are usually given as input files and contain the data of a typical meteorological year (e.g. TMY) of a specific location. For the determination of the convective heat transfer at the building envelope the wind speed and wind direction are needed. Further the ambient air temperature is used for the convective heat transfer calculations, but also for heat transfer by ventilation, infiltration etc. To model the solar radiation in BESs, the solar angle and the fluxes of direct and diffuse solar radiation on each surface orientation are needed. For the longwave radiation balances often a fictive sky temperature is used to compute the amount of radiation that is radiated from the building surface to the sky. The fictive sky temperature is a function of the ambient temperature, air humidity, cloudiness factor of the sky, and the local air pressure.

2.3.2.6 Internal gains

Internal gains refer to the heat that is produced inside the buildings. The most important sources for the internal gains are persons, devices (e.g. computers) and artificial lighting. The heat transfer is for most gains partly convective and partly radiative. Because the internal gains are not constant over time, utilization and occupancy schedules define the heat flux, due to the internal gains, over time. Mostly hourly schedules for each day of the week and daily schedules for a week are defined.

2.3.2.7 Ventilation and infiltration

To model ventilation and infiltration in BESs, the air change rate or the mass flow rates can be defined. For the air entering the thermal zone, the air temperature and the humidity can be specified. In this study for all simulations it is assumed that mechanical ventilation systems are installed in the buildings. Night ventilation is used for passive cooling of the buildings. Buildings can be ventilated also by natural ventilation. For natural ventilation the flow into the building and inside the building is driven by pressure differences caused by wind or buoyancy. In TRNSYS these flow can be considered using the air flow model TRNFLOW. TRNFLOW is basically the air flow model COMIS (Conjunction Of Multizone Infiltration Specialists) integrated into the BES model TRNSYS. COMIS models the air flow in building and can account for the influence of cracks, ducts, duct fittings, fans, flow controllers, vertical large openings (windows and/or doors), kitchen hoods and passive stacks [93].

2.3.2.8 Radiation

The radiative heat flux is one of the most important heat fluxes for buildings. The radiative flux can be divided into three parts: (1) the direct solar radiation, (2) the diffuse solar radiation and (3) the longwave radiation. Most BES models were developed for stand-alone buildings. Therefore at the outside surfaces absorption coefficients are used to determine the part of the incoming solar radiation that is absorbed at the building surfaces. For the longwave radiation the amount of longwave radiation radiated from the building to the environment is determined. In these BES models, no radiation exchanges with other buildings or the environment is considered. Neighbouring buildings are only modelled for shadowing effects. In this thesis the radiation exchange between buildings in urban areas is considered and modelled (for more details see section 3.1.1). For interior surfaces the radiation exchange between the surfaces is considered for 3D geometries by using e.g. view factors or if no 3D geometries are used by using predefined factors that distribute the radiation over the different surfaces of a thermal zone.

2.3.2.9 Convection

To model the convective heat transfer at interior and outside surfaces CHTCs (for more information see section 3.1.2) are used. The CHTCs relate the convective heat flux to the temperature difference between the surface temperature and the temperature of the air

close to the surface. These CHTCs are for outside surfaces often a function of the wind speed.

2.3.2.10 Conduction

A large part of heat is transported from inside the buildings to the environment by conduction through the walls. In TRNSYS wall transfer function are used to solve the Fourier equation. For a detailed derivation it is referred to [94].

2.3.2.11 Space cooling and heating

For the control of space cooling and space heating two set temperatures have to be given. If the temperature in a thermal zone is below the set temperature for heating, heating is used to keep the temperature at the set temperature. The second set temperature is for the cooling. The thermal zone is cooled to keep the temperature at the set temperature for cooling. Between these two temperatures the air temperature in the thermal zone is free floating. To determine the air temperature in a thermal zone in case of a free floating temperature the following equation is used:

$$C_i \frac{d}{dt} T_i = \dot{Q}_i \tag{2.22}$$

where C_i is thermal capacity of the thermal zone, T_i is the air temperature of the thermal zone and Q_i is net heat gain of the zone.

The net heat gain of the zone is the sum of all gains to the air in the zone (individually discussed above). These gains are the convective wall heat fluxes from the walls, radiative gains, the heat gains from the ventilation and the infiltration and internal gains. If a thermal zone needs to be heated or cooled, the heating or cooling power (P_i) is subtracted from the net heat gains in Equation 2.22:

$$C_i \frac{d}{dt} T_i = \dot{Q}_i - P_i \tag{2.23}$$

If P_i has a negative value, the thermal zone needs to be cooled and if it has a positive value it needs to be heated. For this study no limit for the cooling or heating power was defined and therefore the set temperatures for the air temperatures could always be reached.

2.3.3 Urban heat island modelling

For building energy simulations the local ambient air temperatures are needed. For urban areas the air temperatures can change very strongly within small areas due to the UHI effect. In most cities there exist only very few meteorological stations, which are often even located at airports outside of the city (e.g. Zürich). Therefore to predict the thermal behaviour of buildings in urban areas by BESs, models are needed that can predicted the

UHI intensity. A wide range of spatial and temporal scales are relevant for the UHI intensity. To resolve all the important physical effects, simulations for the flow, the longwave and solar radiation, the anthropogenic heat release, the buildings, vegetation, moisture, soil etc. need to be conducted in a coupled form from the mesoscale down to the buildings scale. The computational costs for taking all these scales and physical phenomena into account are still far too high. Therefore in literature a number of strongly simplified models are proposed to predict the urban heat island intensities based on measurements.

One of the first simplified attempt to model the UHI was proposed by Oke 1973 [95]. He determined the maximum UHI intensity as a function of the population of the urban area for calm wind and clear sky conditions. Because measurements of the UHI intensity showed differences between European and North American cities, he derived two different functions for the two continents. The UHI intensities are in general higher for North American cities, because of the higher building densities and taller buildings in the North American cities. The two functions are given below:

- North America:

$$T_{u-r} = 2.96 \log P - 6.41 \tag{2.24}$$

- Europe:

$$T_{u-r} = 2.01 \log P - 4.06 \tag{2.25}$$

where T_{u-r} is the UHI intensity and P is the population (number of people).

Further Oke 1982 [96] developed a model for North American cities, where the UHI intensity is not only a function of the population but also a function of the wind speed:

$$T_{u-r} = P^{0.25} / \left(4U\right)^{0.5} \tag{2.26}$$

The above described models predict only one value for the UHI intensity for the whole city. This is not accurate enough to study for example the microclimates and its influence on the energy demand of buildings at a specific location in an urban area. The UHI intensity is strongly varying within an urban area. The building density is for example an important parameter for the UHI intensity. Because the UHI intensity is strongly dependent on the longwave and solar radiation exchange, Oke 1981 [97] related the UHI intensity for an urban street canyon to the aspect ratio (H/W) or the sky view factor in the middle of the street canyon (Y_{sky}):

$$T_{u-r} = 7.45 + 3.97 \ln \left(H/W\right) \tag{2.27}$$

$$T_{u-r} = 15.27 - 13.88 Y_{sky} \tag{2.28}$$

This model can account for the local building density, but at the same time this model

does not account for the total size of the urban area, what makes it difficult to use this model to predict the air temperature for BESs.

There exist also other UHI models, where the intensities are based on the mesoscale weather conditions and not on the density or the city size. Based on measurements Ludwig 1970 [98] developed a model, where he determines the UHI intensity as a function of the corresponding lapse rate (decrease of the temperature with height above the ground level; K/millibar) over the rural area (Y):

$$T_{u-r} = 1.85 - 7.4Y \tag{2.29}$$

Bornstein 1986 [99] suggested a model for Uppsala (Sweden), where the UHI intensity is based on the cloudiness (N), wind speed, temperature and specific humidity (q):

$$T_{u-r} = 2.8 - 0.1N - 0.38U - 0.02T + 0.03q \tag{2.30}$$

As for the model of Ludwig, this UHI intensity model does not account for the building density of the urban area and has therefore to be modified to be used for other cities than Uppsala. A similar model was developed by Moreno 1994 [100], who related the UHI intensity to the cloudiness and the wind speed or the cloudiness and the air pressure at sea-level (p) for Barcelona (Spain):

$$T_{u-r} = -0.583N - 0.077U + 6.443 \tag{2.31}$$

$$T_{u-r} = -0.612N + 0.044p - 39.772 \tag{2.32}$$

More advanced models exist, where not only the geometry of street canyons but also the properties of the building materials and the ground are taken into account for the determination of the UHI intensity. Montavez et al. 2008 [101] based their model on the model of Oke 1981 [97] (Equation 2.27):

$$T_{u-r} = a + bY_{sky} \tag{2.33}$$

As for Okes model the sky view Y_{sky} factor is a function of the aspect ratio of the street canyon. The model constants a and b are a function of the thermal inertia ($\mu = \sqrt{kC}$, where k is the conductivity and C the heat capacity) of the walls and the ground. Additionally their model can account for the effect of pollution on the sky radiation.

More complex UHI intensity models are the analytical CTTC model and the improved analytical CTTC model [102–104]. These former models account for the contribution of the longwave and solar radiation, while the improved model additionally account for the effect of vegetation and anthropogenic heat. With the CTTC model the temperature in an urban area is determined as follows:

$$T_a = T_0 + \Delta T_{a,solar} - \Delta T_{NLWR} \tag{2.34}$$

where T_a is urban air temperature , T_0 is the base temperature for regional air temperature

variation, $\Delta T_{a,solar}$ is the solar radiation contribution and ΔT_{NLWR} is the net longwave radiation contribution.
The solar contribution is determined as a function of the incoming direct solar radiation, the convective heat transfer coefficient and the cluster thermal time constant (CTTC). The CTTC expresses the thermal inertia of the urban landscapes and is a material property. The net longwave radiation contribution is a function of the air temperature, the Brunt number (ratio of radiant energy emitted by the air to the energy emitted by a black-body at the same temperature), the CHTC and the sky view factor (geometry). Therefore the CTTC models account for the material properties and building geometries in a limited zone of urban area. It does not consider the size of the whole city and does not account for advection of the heat by wind.

Mihalakakou et al. 2002 [105] developed an artificial neutral network model that predicts the temperature at discrete locations within an UHI dependent on the temperature at one measurement location. For this model historical temperature measurements at the discrete locations are needed to train the artificial neutral network to the studied city. Kolokotroni et al. 2010 [68] developed and validated such a model for the city of London.

All the above described UHI intensity models aim at quantifying the UHI intensity for cities, where the UHI intensity is not known. The different models account for different effects. The most simple models are based on correlations between the UHI intensity and some typical parameters of urban areas or weather conditions (population, street canyon aspect ratios, wind speeds, cloudiness etc.). For more complex models the heat exchange and storage at the buildings is determined with heat balance equations. But to the authors knowledge no UHI intensity model exists that can account for the detailed morphology of a specific city and the detailed weather conditions. Because the UHI intensity is very sensitive to small changes in the urban morphology (e.g. green spaces in a densely built area), the described models cannot predict the UHI intensity for a specific place in a specific city in an accurate way. Thus, these models can give an estimate of the UHI intensity for a city, but to run accurate BESs, more accurate UHI intensity predictions are needed at the street canyon or neighbourhood scale. Recently attempts have been made to simulate large urban areas with CFD. Such CFD simulations are computationally very expensive, but are capable of simulating the UHI. Ashie et al. 2011 [106] used CFD to simulate the UHI effect in Tokyo. As boundary conditions they impose results from mesoscale models. The resolution of the mesh is 5 m, what is still rather coarse to capture detailed flow fields. Further the model to determine the surface temperatures is strongly simplified. Finally it is not feasible to run this kind of simulations to predict the UHI intensity for BESs, because these simulations are too time consuming.

Beside the urban area itself also the surrounding areas have an impact on the urban microclimate. Urban areas at lakes, close to mountains or valleys are strongly influenced by wind systems caused by complex topography. These wind systems are very difficult to include in a general UHI intensity model. The studies within this thesis are conducted for Swiss cities. Most Swiss cities are strongly influenced by this kind of wind systems [107]. There are no reliable UHI intensity models that predict the UHI intensities for Swiss cities. Therefore in this thesis no UHI intensity model is used, but the UHI intensities are based on statistical analysis of measured data (see section 3.1.3).

2.3.4 Urban microclimate and energy impact modelling

For several applications, it is not sufficient to only consider the UHI effect of the urban microclimate. For the evaluation of the thermal comfort of pedestrians, besides the local temperature also the radiation balances, the wind speed and the humidity need to be known. To determine the pollutant dispersion in an urban area, the precise wind flow structures have to be known. Due to buoyancy these structures are dependent on the air temperatures, which are influenced by the radiation absorbed at the surfaces. Especially for BESs it is necessary to know the detailed urban microclimate to predict the thermal behaviour of buildings. Mainly two types of models are needed to model the urban microclimate: (i) a radiation model for longwave and solar radiation and (ii) a flow model that can predict the wind flow structures, and can for example also account for pollutant dispersion or moisture transport. There exist two general approaches to model the urban microclimate. The first approach is to use a large scale climate model and to refine the model and the resolution to be able to capture all the smaller scale phenomena that are important for the urban microclimate. A second approach is to apply models that were developed for smaller scales at larger scales and simplify them in such a way that still all important phenomena are captured.

The first approach is for example applied for the software ENVI-met [108]. ENVI-met was developed to study the microclimate in urban areas. Typical spatial resolutions are $0.5-10m$. For the flow the 3D Navier-Stokes equations are solved with a $k-\varepsilon$ turbulence model. The spatial resolution is relatively low, therefore no boundary layer is resolved at surfaces, what makes it for example not possible to determine the wall heat fluxes at building façades from the flow simulations. Instead CHTCs are used. To account for the radiative fluxes (solar and thermal radiation) the concept of flux reduction coefficients is used [109]. These coefficients describe how much the incoming radiation is reduced by buildings and plants. Therefore also for radiation a strongly simplified model is used. In this thesis the flow and the radiation exchange is studied in more detail and therefore ENVI-met is too simplified for this use. Other models using similar approaches are for example AMSUS or FITNAH 3D [110].

When the second approach is applied, the wind flow and the radiation are modelled by separate programs. Then, these programs are coupled to account for the combined effect of radiation and flow. These models are further coupled with BESs, if detailed results for buildings in urban areas are needed. Radiation models with different degree of complexity exist. One of the most complex radiation models is RADIANCE [111]. RADIANCE was developed to predicted light levels in buildings. It uses a hybrid approach of Monte Carlo and deterministic ray tracing and accounts for direct, specular reflected and diffuse radiation. Ray tracing is a computationally expensive method and is therefore mostly not applied for the prediction of radiation in urban areas. Solene [112] is a radiation model that applies simplified algorithms to determine radiative fluxes. For the incoming direct and diffuse solar radiation, the sky vault is divided into patches. The sun is modelled as a point source and its position is determined for each time step. For the diffuse solar radiation, each patch of the sky vault is given a source of diffuse energy. To consider different weather conditions (from overcast to clear sky) the Perez model [113] is commonly applied. All surfaces within the computational domain are meshed. The total absorbed

solar radiation from the sky is determined for each cell of the surfaces by computing the absorbed solar radiation originating from each patch (that is not obstructed) and integrating over all patches. This is done separately for the diffuse and the direct solar radiation. The reflections of the solar radiation between the buildings are modelled using a radiosity approach. The same radiosity model is as well used for the longwave radiation. In the CitySim model [114] this approach is further simplified. As in Solene, in CitySim the sky vault is divided into patches and determines the solar radiation from each patch to each cell of the surfaces. For the reflected solar radiation, a simplified radiosity algorithm (SRA) [115] is applied. Using this algorithm, for the patches of the sky vaults that are obstructed, the solar radiation reflected by the obstruction is used instead of the solar radiation from the patch of the sky vault. This method may also be used for longwave radiation.

As mentioned in section 2.2, Bouyer et al. 2011 [87] coupled a combined radiation-BES model with a CFD model. For the radiation they used Solene, which includes also a building model. With Fluent [116] they simulated the flow field and the moisture transport in the outdoor spaces. For each time step they computed once the flow field and then iterated between the radiation-BESs and the CFD to resolve the transport equations for energy and moisture. They could not use the predicted wall heat fluxes from CFD to compute the CHTCs, since wall functions do not accurately predict the wall heat fluxes at building façades (see section 3.2.2). For the determination of the CHTCs they applied convective heat transfer correlations as a function of the wind speed, which were determined with CFD. Mochida et al. 2006 [117] developed a similar coupling method, where they coupled TRNSYS (which is the BES model used within this thesis) with CFD. The aim of their study was to investigate the effect of the microclimate around a building on cross-ventilation. Also climatic models have been coupled with BES models. One example is the approach of Kikegawa et al. 2003 [118]. They coupled different climatic models with different scales to refine the simulations and coupled the climatic model with the smallest scale with a BES model.

2.3.5 Summary

To conduct a numerical study on the impact of the urban microclimate on the building energy demands in urban areas, a number of numerical models are needed to solve the different physical phenomena. For the modelling of the building behaviour, there exist a number BES models. The flow can be simulated with existing and validated CFD programs. There do still not exist accurate enough microclimate models to simulate the UHI for a whole urban area. Therefore the main task, for studies on the impact of the urban microclimate on buildings, is to find an efficient and accurate approach to couple the different existing models. In literature work (aiming on understanding the interaction between the urban microclimate and the buildings) can be found, but there are still further developments and investigations needed to enhance the understanding of the relevant physical phenomena.

2.4 Experimental modelling

2.4.1 Flow measurement

Validation of CFD simulations is an important task, when the flow around buildings is studied. Mostly wind tunnel measurements are used for this purpose. There is a wide range of measurement techniques to measure flow velocities and turbulent kinetic energies. Two types of measurement techniques exist: intrusive and non-intrusive techniques. Non-intrusive measurement techniques have the advantage that they don't disturb the flow field, but it is mostly required that the flow is seeded with some kind of particles. Because the velocity cannot directly be measured, other physical quantities have to be measured and correlated to the velocity. Such quantities are e.g. pressure, forces, time of flight or frequency shifts caused by the Doppler effect.

2.4.1.1 Mechanical anemometers

Mechanical anemometers convert aerodynamic forces into rotational frequencies. Mechanical anemometers are relatively simple to use, but have the disadvantage that they disturb the flow field and the wind speed can be measured in only one direction. Further due to the inertia of the rotating head only time averaged velocities can be measured. Therefore turbulence quantities cannot be measured.

2.4.1.2 Hot-wire anemometers

Hot-wire anemometers relate the convective cooling of a hot wire to the wind speed of the flow. A single hot-wire can only measure the flow velocity in one direction. Therefore hot-wire anemometers with a number of different hot-wires to measure different velocity components exist.

2.4.1.3 Pitot tubes

Pitot tubes measure the pressure difference between the stagnation and the static pressure to determine the flow speed. For the determination of the wind speed the Bernoulli equation is used.

2.4.1.4 Acoustic and laser Doppler velocimetry

The frequency of a wave is shifted, when the wave is scattered by a moving object. This (Doppler) effect can be used to measure flow speeds. Acoustic Doppler velocimetry is mostly used for liquid flows, while laser Doppler velocimetry is used for both gaseous and liquid flows.

2.4.1.5 Time-of-flight sensors

Time-of-flight sensors use e.g. two laser beams and particles in the flow to measure the time needed for the particle to flow from the first to the second laser beam.

2.4.1.6 Particle tracking velocimetry

For particle tracking velocimetry the flow is seeded with particles that follow the flow field. The flow is illuminated with a two-dimensional light sheet in one plane that is parallel to the flow field. Multiple images separated by a known time are taken. Single particles are tracked and the velocities (v) are computed as follows:

$$\begin{aligned} \vec{v}(\vec{x},t) &= \frac{1}{t_2-t_1}\left(\vec{x_2}-\vec{x_1}\right) \\ \vec{x} &= \frac{1}{2}\left(\vec{x_2}+\vec{x_1}\right) \\ t &= \frac{1}{2}\left(t_1+t_2\right) \end{aligned} \tag{2.35}$$

By using at least three cameras and illuminating a volume, this technique can be extended to a three-dimensional measurement technique.

2.4.1.7 Particle image velocimetry

Particle image velocimetry (PIV) is a non-intrusive flow measurement technique and similar to particle tracking velocimetry, but instead of tracking single particles, constellations of particle are tracked. For the measurements the flow is seeded with small particles (mostly oil particles) (Figure 2.10). The particles have to follow the flow and therefore they need to be non-buoyant and have a low inertia. With a pulsed laser a thin light sheet is created that illuminates the particles in a 2D plane. The particles in the illuminated plane scatter the laser light, while the other particles remain invisible. With a camera two images are taken within a short time interval. Constellations of particles are tracked in the two images and the velocity is determined with the following relationship:

$$\vec{v} = \frac{\Delta\vec{x}}{\Delta t} \tag{2.36}$$

For the determination of the flow field, the first image is divided into subwindows (Figure 2.11). The windows are then shifted in x and y direction and compared with the second image. For each position of the subwindow the cross-correlation is computed. Δx in Equation 2.36 is the shift of the subwindow to the position, where the cross-correlation has the highest value. The cross-correlation is computed with the following equations:

$$\begin{aligned} \rho &= \frac{Cov\left(W_1,W_2\right)}{\sqrt{Var\left(W_1\right)Var\left(W_2\right)}} \\ Cov\left(W_1,W_2\right) &= \frac{1}{MN}\sum_{k=1}^{M}\sum_{l=1}^{N} W_1\left(x_k,y_l\right)W_2\left(x_{k+m},y_{l+n}\right) \\ Var\left(W_i\right) &= Cov\left(W_i,W_i\right) \end{aligned} \tag{2.37}$$

where ρ is the cross-correlation, W_1 and W_2 are the subwindows of the first and second image, M and N are the number of pixels in x and y direction of the subwindows and n and m are the pixelshifts between the two subwindows.

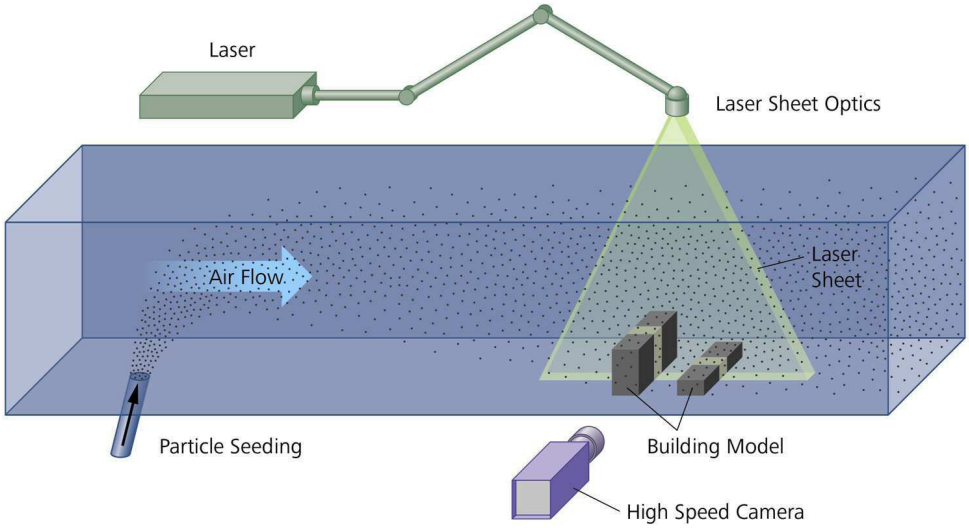

Figure 2.10: Sketch of the measurement equipment.

For each subwindow one two-dimensional vector is computed. To have a finer resolution of the flow field, subwindows with an overlap can be used. With the here described method the out of plane velocity components cannot be computed. To compute this velocity component, stereo or volumetric PIV setups with two and more cameras have to be used.

The advantages of PIV are that it is a non-intrusive method and the flow fields can be measured with a high spatial and temporal resolution. Because the flow field in a whole area can be measured at the same time, vortex structures can be tracked in space and time. Disadvantages are the following: strong laser reflection may occur at the surfaces that could damage the camera sensors, and due to high light intensities by the reflections it is difficult to measure the flow field close to these surfaces. Further no complex geometries can be used, because no object, that could block the view, should be located between the camera and the light sheet. The wind tunnel models can also cause shadowing effects. In shaded areas the particles cannot be seen on the images and therefore the velocity cannot be measured.

There are different sources of errors for PIV measurements as listed below [119]:

- Random errors: there are different causes for random errors. Noise is introduced by a mismatch of the recorded and effective particle size, what causes an error in the measured location of the centre of the particles. This mismatch can occur, when the particle size is similar to the pixel size of the camera and the shape of the particle is not resolved. Further particles move in and out the illuminated plane in the time interval between the two images are taken.

- Tracking errors: due to the inertia the particles do not exactly follow the streamlines of the flow.

- Gradient errors: the deformation and rotation of the flow within a subwindow causes a loss in correlation.
- Acceleration errors: if the streamlines are curved, the particle displacements do not exactly represent the velocity vectors.
- Bias errors: using sub-pixel accuracy for small particles the displacement can be biased to integer pixel values, what is called pixel locking.
- Systematic errors: those errors can occur due to errors in the calibration and due to the fact that only two-dimensional vector fields are measured.

All those errors can be limited by using particles with an appropriate size, subwindows with an appropriate size and appropriate time intervals between the to images.

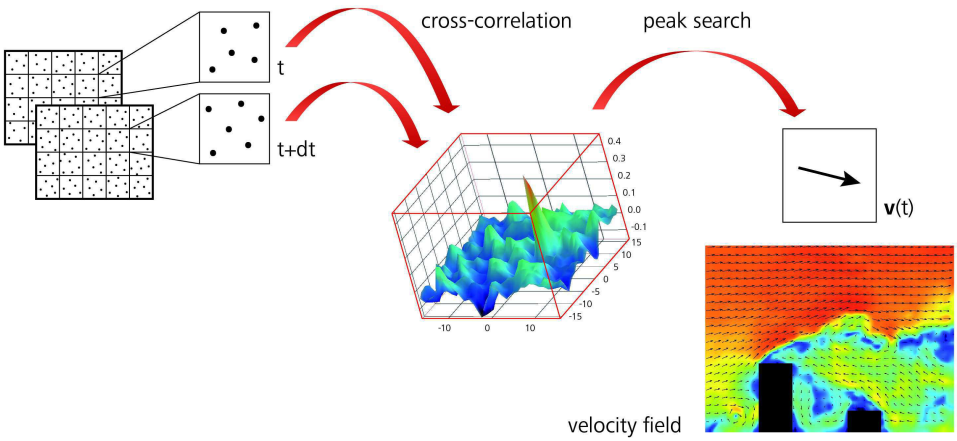

Figure 2.11: PIV measurement principle (LaVision GmbH).

2.4.2 Temperature measurement

To measure the temperatures of a fluid less measurement techniques exist, than for the measurement of the velocities. As for the velocities, there exist intrusive and non-intrusive techniques.

2.4.2.1 Thermocouple

A thermocouple is a intrusive temperature measurement device. Thermocouples consist of two metal conductors that are only in contact at the position, where the temperature is measured. If the two ends of a conductor have a different temperature, a voltage can be measured between the two ends due to the Seebeck effect. Two different metal conductors are needed for thermocouples, because the voltage is measured between the two ends that

have the same temperature. No voltage could be measured, if the two conductors would be made out of the same material. The measured voltage is a function of the temperature at the connected ends and dependent on the material of the two conductors. Because this measurement technique is intrusive, it disturbs the flow field, what is a disadvantage. Further the measurement error is $1 - 2°C$, what is rather high for some applications.

2.4.2.2 Laser-induced fluorescence (LIF)

LIF is a non-intrusive measurement technique, which can be combined with PIV. To measure the temperature of the flow, a fluorescence tracer gas is added to the flow. The tracer gas is excited with a laser light sheet (as for PIV). The fluorescence emission is then detected with a camera. The level of fluorescence is dependent on the temperature. LIF can also be used for concentration measurements, because the level of fluorescence varies with the concentration of the tracer gas. Ketones (e.g. Acetone) are used as tracer gas in gas phase flows. Because ketones are hazardous and flammable, LIF can in most large wind tunnels not be applied to measure temperatures and concentrations.

2.4.3 Summary

There exist a large number of measurement techniques to measure wind velocities. For this thesis PIV was chosen, because it is a non-intrusive technique and does not disturb the flow field. Further it has the advantage that the wind velocities and turbulent kinetic energies can be measured in the area of a 2D plane at the same time. Only a limited number of measurement techniques exist for temperature measurements. The ideal technique would be LIV, because it can be combined with PIV. Nevertheless thermocouples were chosen for the temperature measurements of this thesis, because the fluorescent particles needed for LIV are hazardous and flammable.

3 Numerical modelling

In the previous chapter the state of the art modelling approaches were presented. In this chapter the numerical models that are developed and used in this thesis are discussed. In a first part the models for describing the urban microclimate in BESs are presented. These models are the radiation model, the modelling of the convective heat transfer at the building façades and the urban heat island model. Further a method to couple the BESs with CFD is explained. The coupling can be used as an alternative to the use of precalculated convective heat transfer coefficients. In a second part of this chapter the CFD simulation models applied to predict the convective heat transfer at the building façades are discussed. First, different ways to model the thermal boundary layer are explained and then CFD simulations are used to establish convective heat transfer coefficients for buildings in urban areas that are used in chapter 5 for the BESs.

3.1 Building energy simulation (BES)

3.1.1 Radiation

In classical building energy simulations (BESs) of stand-alone buildings, solar irradiation on façade elements is considered as a gain, and longwave radiation as a heat loss to the cold sky. In street canyon configurations, however, the solar direct and diffuse irradiation is characterized by multiple diffuse and specular reflections at the building surfaces. Similarly, the multiple longwave reflections and radiative exchange with neighbouring building surfaces and the sky have to be considered. In TRNSYS 17 [91], the 3D radiation model is only used for interior zones. Therefore, in this thesis, the outdoor space between buildings is modelled as an atrium with an open ceiling (see section 3.1.5). In this way, the shadowing by the neighbouring buildings and the exchange of longwave and solar radiation between the different buildings is considered. TRNSYS 17 determines which surfaces are sunlit and which are shaded, dependent on the position of the sun and the orientation of the studied building. At opaque surfaces a part of the direct solar radiation is absorbed and the remaining part is reflected in a diffuse way. Thus, specular reflection of direct solar irradiation is not considered. If direct solar radiation hits a transparent surface (window), a part of the solar radiation is absorbed at the window panes, a second part is transmitted through the window into the building, and the rest is reflected diffusely. The sum of all diffuse solar radiation, consisting of diffuse solar radiation and the diffuse reflection of direct solar radiation, is distributed over all the surfaces in the street canyon (including a surface that represents the sky) using Gebhart factors [120, 121]. Gebhart factors are basically view factors, corrected to include the effect of multiple (diffuse) reflections:

$$G_{i,k} = \left(I - F_{i,k}\sigma_k\right)^{-1} F_{i,k}(I - \sigma_k) \tag{3.1}$$

where G is the Gebhart factor matrix, i is any surface that exchanges radiation with surface k, I is the identity matrix, F is the view factor matrix and σ is the reflectivity. The solar radiation fluxes in closed volumes are calculated as:

$$Q_{s,k} = A_k(1-\alpha_k)I_{s,k} + \sum_{i=1}^{n} A_i G_{i,k}\alpha_i I_{s,i} \tag{3.2}$$

where n is the number of surfaces, Q_s is the solar radiation flux, A is the surface area, α is the surface albedo and I_s is the solar radiation flux on surface k.
The part of the diffuse solar radiation that is distributed onto transparent surfaces is again reflected, absorbed and transmitted by the window panes. As for the diffuse solar radiation, the longwave radiation in closed volumes is distributed using Gebhart factors:

$$Q_{l,k} = A_k\varepsilon_k\sigma T_k^4 - \sum_{i=1}^{n} A_i\varepsilon_i\sigma T_i^4 G_{i,k} \tag{3.3}$$

$$G_{i,k} = (I - F_{i,k}\sigma_k)^{-1}F_{i,k}\varepsilon_k \tag{3.4}$$

where Q_l is the longwave radiation flux, ε is the emissivity, σ is the Stefan-Boltzmann constant and T is the surfaces temperatures.
For the sky a fictive sky temperature as a function of the ambient temperature (T_a), dew point temperature (T_{sat}), cloudiness factor of the sky (c_{cover}), and the local air pressure (p_0) is used for the calculations of the longwave radiation (Equations 3.7 and 3.8) [91]. For surfaces that are not in a closed volume the longwave radiation to the sky and the environment is computed as follows:

$$Q_{l,k} = A_k\varepsilon_k\sigma(T_k^4 - T_{fsky}^4) \tag{3.5}$$

$$T_{fsky} = (1-f_{sky})T_a + f_{sky}T_{sky} \tag{3.6}$$

$$T_{sky} = T_a\left(\epsilon_0 + 0.8\left(1-\epsilon_0\right)c_{conver}\right)^{0.25} \tag{3.7}$$

$$\epsilon_0 = 0.711 + 0.005T_{sat} + 0.013\cos\left(2\pi\frac{time}{24}\right) + 12\cdot 10^{-5}\left(p_{atm} - p_0\right) \tag{3.8}$$

where f_{sky} is the fraction of the sky seen by surface k and p_{atm} the atmospheric pressure. All surfaces are considered to be opaque for longwave radiation. Therefore no longwave radiation is transmitted through windows.

3.1.2 Convection

In BES the convective heat transfer at interior and exterior surfaces are modelled. The convective heat transfer is driven by the flow close to the surfaces. The convective heat transfer has to be determined in a simplified way, because most BESs do not resolve

the flow inside and around the buildings. Mostly the convective heat transfer is quantified using convective heat transfer coefficients (CHTCs), which relate the convective heat transfer to a temperature difference of the surface temperature (T_s) and a reference temperature (T_{ref}):

$$h_c = \frac{q_{c,w}}{T_s - T_{ref}} \tag{3.9}$$

where h_c is the convective heat transfer coefficient and $q_{c,w}$ is the convective heat flux normal to the wall.

In BES models, the CHTCs are usually given as a function of a reference wind speed. Equation 3.9 is not a representation of a physical law, but a simplification of a complex phenomenon. Therefore there is no clear rule, which temperature and wind speed has to be used as reference value. For BESs usually the measured data from a meteorological station are used as reference. Those values are, especially for buildings in urban areas, not representative for modelling the flow close to the studied buildings using Equation 3.9. Therefore the values can lead to a source for inaccurate predictions of convective heat transfer close to the wall.

There are different ways to estimate CHTCs. For strongly simplified geometries, it is possible to analytically derive CHTCs. For flat-plate flows, one of these methods is based on the assumption that a similarity of the structure and development rate between the thermal and the momentum boundary layer can be found. Therefore CHTCs can be described based on the empirical information of the momentum boundary layer. Due to the viscosity effect, the velocity of the fluid in the momentum boundary layer decrease towards the heated surfaces having a zero value at the surface itself (no motion of the fluid). In the laminar boundary layer, close to the surface, the heat transfer from the surface to the fluid is caused by conduction. However, the temperature outside the laminar thermal boundary layer does not change linearly and with increasing distance from the wall, mixing caused by the fluid motion, becomes the dominant phenomenon for the heat transfer. To derive the similarity between the momentum and thermal boundary layer, the Navier-Stokes equations (see section 2.3) have to be simplified. By analysing the order of magnitude of the terms in the Navier-Stokes equations (Equations 2.10-2.12), a number of terms can be neglected for boundary layer flows:

$$\frac{\partial u}{\partial x} + \frac{\partial v}{\partial y} = 0 \tag{3.10}$$

$$u\frac{\partial u}{\partial x} + v\frac{\partial u}{\partial y} = -\frac{1}{\rho}\frac{\partial p}{\partial x} + \nu\frac{\partial^2 u}{\partial y^2} \tag{3.11}$$

$$u\frac{\partial T}{\partial x} + v\frac{\partial T}{\partial y} = \alpha\frac{\partial^2 T}{\partial y^2} + \frac{\nu}{c_p}\left(\frac{\partial u}{\partial y}\right)^2 \tag{3.12}$$

Further the Navier-Stokes equations are non-dimensionalised introducing the following variables:

$$x^* = \frac{x}{L}, \qquad y^* = \frac{y}{L}, \qquad u^* = \frac{u}{u_{ref}}, \qquad v^* = \frac{v}{u_{ref}}, \qquad T^* = \frac{T - T_s}{T_{ref} - T_s}$$

where L is a characteristic length and u_{ref} is a reference wind speed (here the freestream velocity).
Using the non-dimensional variables in Equations 3.10-3.12, the simplified Navier-Stokes equations can be written as:

$$\frac{\partial u^*}{\partial x^*} + \frac{\partial v^*}{\partial y^*} = 0 \tag{3.13}$$

$$u^* \frac{\partial u^*}{\partial x^*} + v^* \frac{\partial u^*}{\partial y^*} = -\frac{\partial p^*}{\partial x^*} + \frac{\nu}{u_{ref} L} \frac{\partial^2 u^*}{\partial y^{*2}} \tag{3.14}$$

$$u^* \frac{\partial T^*}{\partial x^*} + v^* \frac{\partial T^*}{\partial y^*} = \frac{\alpha}{u_{ref} L} \frac{\partial^2 T^*}{\partial y^{*2}} \tag{3.15}$$

Using the Reynolds (Re) and the Prandtl (Pr) number, the equations can be further simplified as:

$$\frac{\partial u^*}{\partial x^*} + \frac{\partial v^*}{\partial y^*} = 0 \tag{3.16}$$

$$u^* \frac{\partial u^*}{\partial x^*} + v^* \frac{\partial u^*}{\partial y^*} = -\frac{\partial P^*}{\partial x^*} + \frac{1}{Re} \frac{\partial^2 u^*}{\partial y^{*2}} \tag{3.17}$$

$$u^* \frac{\partial T^*}{\partial x^*} + v^* \frac{\partial T^*}{\partial y^*} = \frac{1}{Re \cdot Pr} \frac{\partial^2 T^*}{\partial y^{*2}} \tag{3.18}$$

The Prandtl number is defined as:

$$Pr = \frac{\nu}{\alpha} \tag{3.19}$$

where α is the thermal diffusivity.
The Prandtl number is defined as the ratio of the momentum diffusivity to the thermal diffusivity and also represents the thickness ratio of momentum to thermal boundary layer.
Further for boundary flows the skin friction coefficient C_f can be written as:

$$C_f = \frac{2}{Re} \frac{\partial u^*}{\partial y^*}\bigg|_{y^*=0} \tag{3.20}$$

The Nusselt number (Nu) is defined as:

$$Nu = \frac{h_c L}{\lambda} \tag{3.21}$$

C_f, Nu, T^* and u^* can be written as a function of x^*, y^*, Re, Pr, and $\frac{\partial P^*}{\partial x^*}$:

$$\begin{aligned} u^* &= u^*\left(x^*, y^*, Re, \frac{\partial P^*}{\partial x^*}\right) \\ T^* &= T^*\left(x^*, y^*, Re, Pr, \frac{\partial P^*}{\partial x^*}\right) \\ C_f &= C_f\left(x^*, Re, \frac{\partial P^*}{\partial x^*}\right) \\ Nu &= Nu\left(x^*, Re, Pr, \frac{\partial P^*}{\partial x^*}\right) \end{aligned}$$

Using the Reynolds-Colburn analogy, a relation between the above mention dimensionless parameters (C_f, Pr, Re and Nu) can be derived:

$$\frac{Nu}{RePr} Pr^{2/3} = \frac{C_f}{2} \tag{3.22}$$

The skin friction coefficient C_f can be eliminated by using empirical models. Finally the Nusselt number can be written as a function of the Reynolds and Prandtl numbers:

$$Nu = aRe^b Pr^c \tag{3.23}$$

where a, b and c are empirical parameters. Therefore the CHTC can be determined as follows:

$$h_c = \frac{\lambda a Re^b Pr^c}{L} \tag{3.24}$$

The CHTCs for the heat transfer at flat-plates can be used adapted for a lot of different applications. For the determination of the heat transfer at building façades this becomes somewhat difficult. The geometry of building surfaces can be quiet complex. Moreover, the exact characteristics of the approach flow are mostly unknown. As stated above, for most BESs the weather data are taken from a meteorological station, and those values do not match the values for which Equation 3.24 is valid to describe the heat transfer problem.

Therefore for BESs CHTC correlations as a function of the wind speed, based on measurements of stand-alone buildings, are usually used. A large amount of measurements of the convective heat transfer at building façades were made by field tests, such as by Ito et al. 1972 [122], Nicol 1977 [123], Jayamaha et al. 1996 [124], Sharples 1984 [125], Hagishima and Tanimoto 2003 [126], Liu and Harris 2007 [127], and in wind tunnels,

mostly on isolated cube models, e.g. by Nakamura et al. 2001 [128]. Overviews are given by Hagishima et al. 2005 [129], Defraeye et al. 2011 [130], and for building envelope energy systems by Palyvos 2008 [131]. Significant differences between the measured data can be found [130], because these data are very case specific and thus not general, which is however a prerequisite to use them as standard values. Especially for simulations of buildings in urban areas CHTC correlations based on measurements at building façades of stand-alone buildings can lead to large errors in terms of convective heat transfer predictions.

Wind tunnel measurements have been conducted to study the convective heat transfer at surfaces of bluff bodies. Wind tunnel experiments have the advantage that the approach flow can be controlled. Further the CHTCs for different geometries can be measured. However, most of the convective heat transfer measurements were not conducted in the context of building engineering. Due to scaling problems the measured CHTC correlations cannot directly be used for BES, especially when buoyancy plays an important role.

Wind tunnel measurements are useful for the validation of CFD simulations. CFD simulations have the advantage that CHTC correlations for complex geometries can be predicted with controlled approach flow conditions. A number of CFD studies for the determination of CHTC correlations can be found in literature (e.g. [74, 130, 132–134]). In this thesis CHTC correlations for flows in urban street canyons are precalculated using CFD (section 3.2.4) and then further used in BESs (chapter 5).

3.1.3 Urban heat island effect

For the BESs meteorological data of a typical meteorological year (TMY) are used instead of measured data of a specific year. Therefore also for the urban heat island effect typical values need to be used instead of hourly measured values. The hourly measured values of a specific year would not correspond to the weather conditions of the typical meteorological year and therefore the results would not be improved by using hourly measured data. To model the urban heat island (UHI), a UHI intensity approximation is developed for the city of Basel (Switzerland). This approximation is based on measured data of the BUBBLE project [9] from Basel. The idea is to get a diurnal schedule of the air temperature difference between a rural and urban meteorological station. Here Basel-Binningen is chosen as the rural station, because for most BES the climatic data of this station are used for the simulations. Climatic data measured at the Spalenring are chosen to represent the urban area. The Spalenring is an urban street canyon in the centre of the city of Basel with an aspect ratio of about one and 3-5 storey building blocks. For each month, the hourly temperature differences between these two stations are determined and then averaged for a time period from 1.9.1994 - 31.12.2001. These obtained temperature profiles are given in Figure 3.1.

The schedules show that the UHI intensity is higher at night-times than at day-times. Further it can be seen that the UHI intensity at night-times is more pronounced in summer and spring and less in winter and fall. At day-times the opposite is the case. The UHI intensities presented in Figure 3.1 are averaged intensities, for extreme weather cases much higher intensities can be found in Basel. The UHI intensities for Basel are rather moderate compared with e.g. Athens where UHI intensities of up to 10K can be found [26]. For

the BESs of the buildings surrounded by street canyons for each time step the actual temperature difference is added to the air temperature of the rural station.

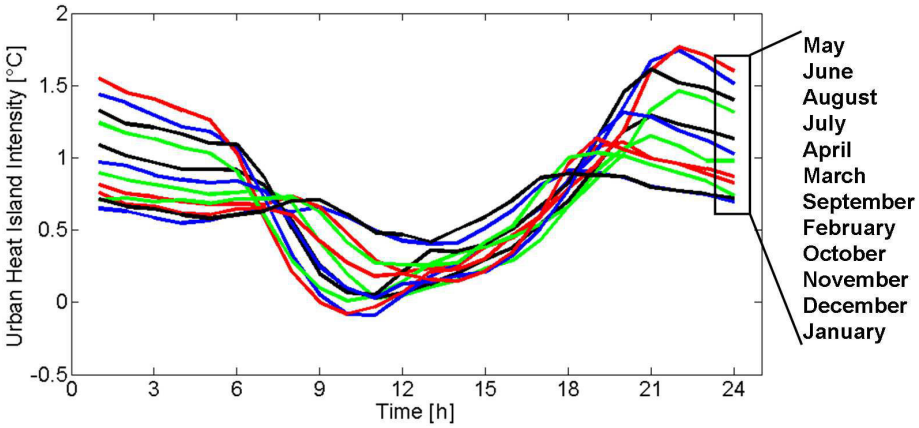

Figure 3.1: Average diurnal UHI intensity schedules for each month of a year.

3.1.4 BES-CFD coupling

Especially for buoyant flow fields, CHTC correlations only as function of the freestream velocity cannot predict the convective heat transfer in an accurate way (see also section 3.2.4). For buoyant flow fields, the CHTCs are not only dependent on the local temperature of the surface of interest, but also depend on the temperatures of the surrounding surfaces within the domain. The surfaces may induce strong buoyant flows, which in turn increase the convective heat transfer at the studied surface. The increased air velocities close to the surface due to buoyancy cannot be represented by the freestream velocity that is used as a measure of the wind speed close to the studied surface. To accurately account for buoyant flows in street canyons, a very high number of precalculated CHTC correlations would be required. In this case it might be more efficient to run coupled BES-CFD simulations. In this section the coupling method that is used in this thesis, is explained.

A schematic representation of the external coupling method is given in Figure 3.2. The masterprogram of the externally coupled simulation is the BES model. The CFD program is called by the BES and integrated in the framework of the BES software (TRNSYS 17.0). The coupling methods are written in Fortran. At the beginning of the simulation all required input data (geometries, weather data, building materials, occupancy etc.; see section 5.2) are read by the BES model. For the CFD simulation only the geometry of the street canyon has to be specified as an input (dimensions of the computational domain). In this thesis the street canyon in the CFD simulations is modelled as a cavity (Figure 3.3a). The leeward and windward walls are divided into three parts (one part per floor) and one temperature boundary condition is used for each part. For the BESs the geometry is slightly different, as a building surrounded by two street canyons is used (Figure 3.3b). After the initialization a number of uncoupled BES time steps (1 hour) are run with precalculated CHTC correlations (Figure 3.4). After n time steps it is assumed that the

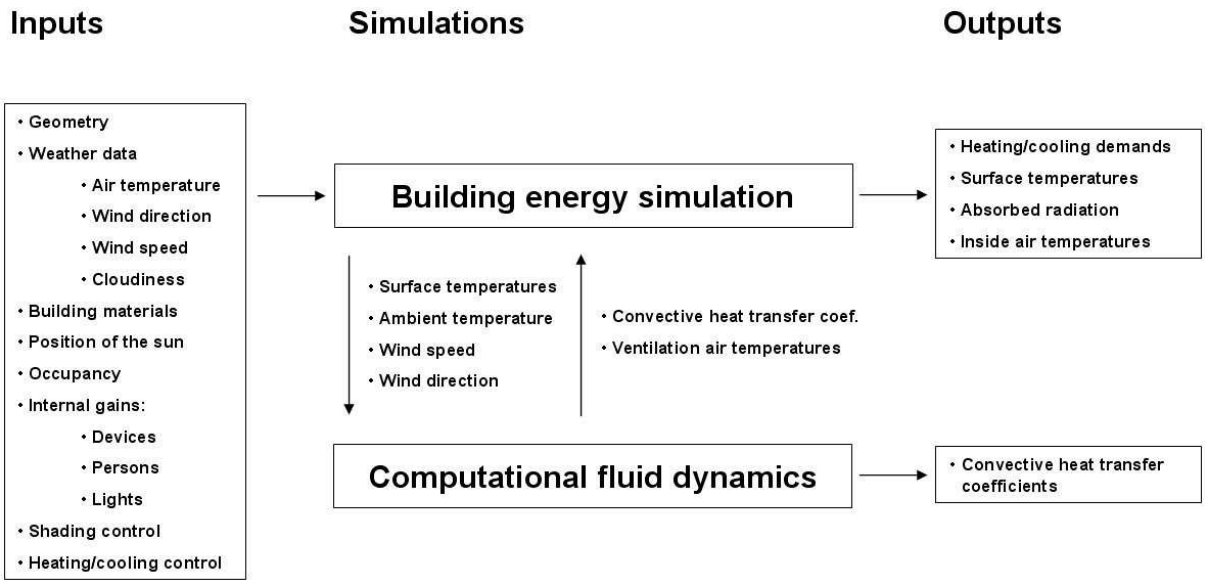

Figure 3.2: Schematic representation of the coupled model.

building is in a realistic initial state. Then, the CFD simulation is initialized and called by the BES. All the required boundary condition parameters for the CFD simulation are transferred from the BES to the CFD simulation. These boundary condition parameters are the area averaged surface temperatures for each floor of both façades and for the street surface, the ambient air temperature (using the UHI schedules), the wind speed and the wind direction. Only 2D CFD simulations are conducted for the coupled simulations, in order to limit the computational costs. The wind direction is used to determine, which façade is the windward façade and which is the leeward façade. The windward wall is defined as the wall, on which the velocity component normal to the wall is pointing towards the wall. Because the computational costs of the CFD simulations is a critical issue for the coupled simulations, steady RANS simulations with a realizable $k - \varepsilon$ turbulence model are conducted, and adaptive wall functions (see section 3.2.3) [135] are used instead of low-Reynolds number modelling. The run time of the CFD simulations are much higher compared to the BES and therefore more time can be saved by efficiently minimizing the run time of the CFD simulations compared to the BES. The CFD simulations are launched by using a journal file that contains all information of the boundary conditions. As convergence criterion a limit of $5 \cdot 10^{-7}$ is used for all residuals in CFD. Once the CFD simulation is converged, the CHTCs are transferred to the BES model. The air temperatures at a distance 0.1 m from the façade of each floor are used to determine the intake air temperature for the ventilation system in BES. For each floor, the average of the air temperatures close to the two façades is used. The results of the CFD simulations are used for the following time step of the BES. No iterations are performed between the BES and the CFD simulation within an individual time step. Thus a one step static coupling according to Zhai et al. 2002 [136] is employed. The CFD simulation is only initialized, when it is called for the first time, for consecutive calls the flow field of the previous time step is used as the initial flow field. For each time step of the coupled simulations, the

outputs of the BESs are: space cooling and heating demands that are needed to maintain the air temperatures inside a given temperature range, room air temperatures, surface temperatures of the façades and the street surface and the absorbed radiation on the building façades. The outputs produced by the CFD simulations are the CHTCs.

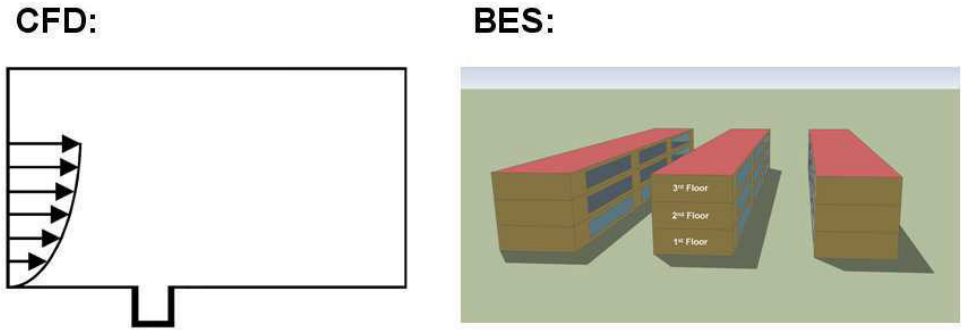

Figure 3.3: Geometries used in CFD and BES.

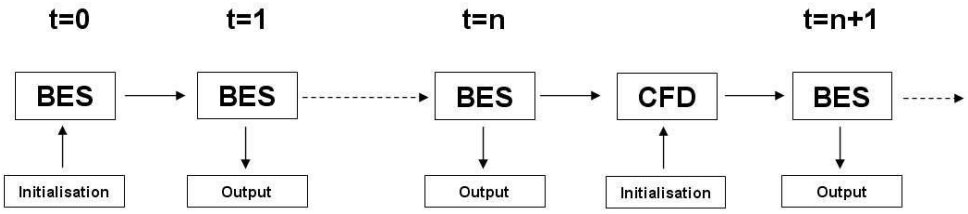

Figure 3.4: Schematic representation of the coupled model.

3.1.5 Street canyon

In the previous sections the models used for the BESs were presented. In this section it is described, how the street canyon space is modelled for coupled and uncoupled simulations. In Figure 3.5 a schematic representation of the street canyon space is given for uncoupled BESs (left) and coupled BES-CFD simulations (right). For both simulation types the street canyon space is modelled as an atrium. At the top of the street canyon a window is used to have a closed volume for the street canyon space. This window transmits all incoming and outgoing solar radiation and has the temperature of the sky (T_{sky}). The longwave and solar radiative fluxes are both determined within the BES model. For the uncoupled BESs the air temperature above and inside the street canyon is the sum of the ambient air temperature (T_{amb}) and the UHI intensity (T_{u-r}) from the UHI schedules. The same temperature is also used for the incoming air temperature of the ventilation system (T_{vent}) assuming that the air intake is located at the roof level. To determine the convective heat transfer, the CHTC correlations from Figure 3.25 are used. These correlations consider the increased temperatures inside the street canyon, because they are established with CFD, where the increased temperatures inside the street canyon are determined and where thus, due to the higher temperatures, the convective heat transfer

is decreased. For the coupled simulations the CHTCs are determined for each BES time step by running a CFD simulation. Also the intake air temperatures for the ventilation system are directly taken from CFD as separate values for each floor.

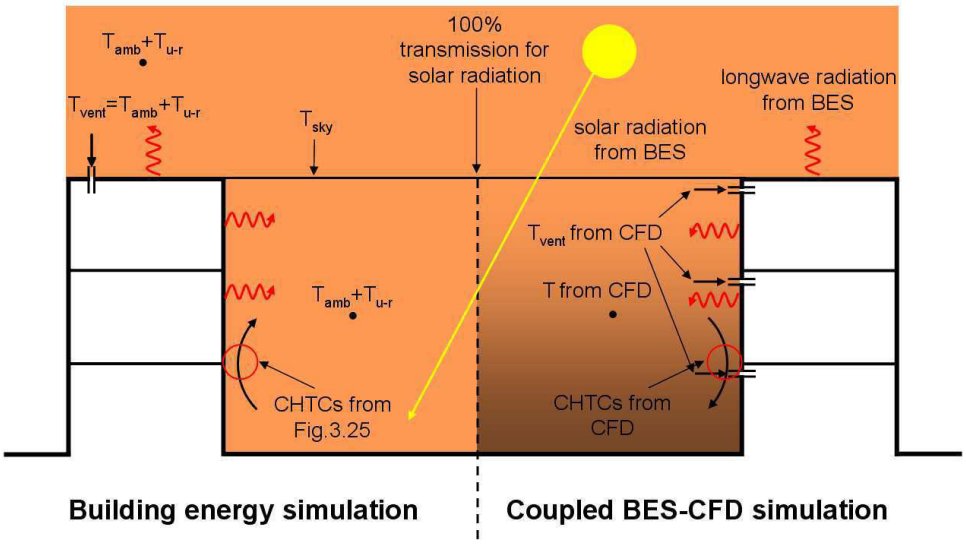

Figure 3.5: Schematic representation of the street canyon space.

3.2 Computational fluid dynamics (CFD)

3.2.1 Methods

In this section the CFD models used in this thesis are presented. All CFD simulations are conducted using ANSYS Fluent 12.0 [116]. Fluent uses a control volume method to solve for the flow field. Steady 2D and 3D incompressible RANS simulations are performed. To model turbulence the realizable $k-\varepsilon$ model [137] is used. In the commonly used standard $k-\varepsilon$ model isotropic turbulence is assumed. However for flows around bluff bodies the turbulence is not always isotropic. This can lead for example to an overestimation of the turbulent kinetic energy close to windward wall surfaces of bluff bodies. Further the standard $k-\varepsilon$ model does not predict the vortex shedding and therefore underestimates the lateral mixing at the leeward wall and predicts too large recirculation zones. The realizable $k-\varepsilon$ model was developed to mitigate these deficiencies. It uses a variable instead of a constant C_μ (Equation 2.21) and uses a different transport equation for the turbulent dissipation rate ε compared to the standard $k-\varepsilon$ model [138, 139].

The near-wall regions are either resolved with low-Reynolds number modelling (LRNM) as described in section 3.2.2.3 or modelled with a wall function approach. Structured grids are used and are build based on the guidelines of Franke et al. 2007 [140]. The grids are refined towards the walls to resolve the boundary layers. At the inlet of the domain vertical profiles of the mean horizontal wind speed U (logarithmic law), turbulent kinetic energy (k) and rate of dissipation of turbulent kinetic energy (ε) are imposed according to Richards and Hoxey 1993 [141]. Richards and Hoxey derived these boundary layer profiles

for the standard $k-\varepsilon$ model. These profiles represent a neutral atmospheric boundary layer (ABL), where the turbulence originates only from friction and shear:

$$\begin{aligned} U(y) &= \frac{u^*_{ABL}}{\kappa}\ln(\frac{y+z_0}{z_0}) \\ k &= \frac{{u^*_{ABL}}^2}{\sqrt{C_\mu}} \\ \varepsilon &= \frac{{u^*_{ABL}}^3}{\kappa(y+z_0)} \end{aligned} \tag{3.25}$$

where u^*_{ABL} is the ABL friction velocity, y is the height above the ground, z_0 is the aerodynamic roughness length (here assumed to be 0.03 m).

To account for buoyancy the Boussinesq approximation is applied. With the Boussinesq approximation a constant value for the density is used for all equations except for the buoyancy term in the momentum equation, where the following formulation is used:

$$\rho = \rho_0(1-\beta(T-T_0)) \tag{3.26}$$

where ρ_0 is a reference density, β is the volumetric thermal expansion coefficient, T is the temperature of the flow and T_0 is the reference temperature.
The Boussinesq approximation is only valid for small density changes in the flow field ($\beta(T-T_0) << 1$).

For all simulations the PRESTO! spatial discretization scheme is used for the pressure interpolation and second order spatial discretization schemes are used for the convection term in the governing equations. Radiation is not directly considered in the CFD simulations, but is accounted for by applying increased surface temperatures as obtained from the BESs.

3.2.2 Near-wall treatment

3.2.2.1 Background

Convective heat transfer can have a significant effect on the heat exchange at exterior building surfaces and thus also on the surface temperatures. For some cases the convective part of the total heat flux at the surface can be up 2 to 7 times larger than the radiative component [142], and thus can be important for the thermal behaviour of a building. Convective heat transfer is especially important for glazed façade elements such as windows or double-skin façades [143], where the contribution of convective heat transfer to the overall thermal conductance of the building component is high due to its lower thermal resistance. Convection is also important, when the heat fluxes at the surface is large due to high surface temperatures caused by solar irradiation. Accurate convective heat transfer predictions also become increasingly important for renewable energy system components mounted on or integrated into building roofs and façades, such as solar

chimneys [144], solar collectors [145], and ventilated or building integrated photovoltaic panels [131, 146].

Local heat transfer predictions at building surfaces in general, including radiative fluxes, are not only of interest for the performance of the buildings but also for studying the effects on urban climate [88] and for thermal comfort assessment of urban outdoor spaces [147]. Modelling sensible heat fluxes from building surfaces is also important for urban canopy layer parameterizations in urban micro- and mesoscale models [148,149]. Such models are employed to study UHI effects, which in return affect the building energy demand. Here, sunlit building façades with surface temperatures higher than the outside air temperature have a distinct influence on the local air flow patterns and the outdoor air temperature distribution due to buoyancy effects.

Recently, convective heat transfer at building façades was investigated by numerical methods using CFD (e.g. [133, 150]). Compared to wind-tunnel experiments, numerical methods offer many advantages, such as larger flexibility in geometry and boundary conditions, a larger Re range, etc. However some limitations have to be emphasized. In order to limit the computational efforts for CFD simulations, (steady) RANS methods are often applied, especially for complex building configurations, larger urban studies, combined indoor-outdoor air flow studies [151] or coupled BES-CFD simulations [52]. Even though e.g. large eddy simulations (LES) give more accurate results for flows in urban areas, RANS simulations are still used where LES are considered too calculation intensive. For example, correct average flow quantities can be obtained by LES only by considering very large numbers of time steps [152]. In addition, to simulate one year with a coupled BES-CFD simulation, preferably one CFD simulation for each BES time step (often 1 hour) has to be run. Therefore RANS simulations are often the preferred choice to get results within reasonable time. Here the boundary layer flow close to the surface is usually not resolved but modelled using wall functions (WFs) in order to reduce the computational cost. Alternatively, the boundary layer flow can be explicitly resolved by LRNM, where the near-wall region is resolved down to the viscous sublayer (see section 3.2.2.2). LRNM however requires an extremely high grid resolution at high Re. The standard formulation for WFs [139], referred to as standard wall functions (SWFs), however has two main limitations: (i) the cell centre point P of the wall-adjacent cell has to be located outside of the viscosity-affected region (viscous sublayer and buffer layer) (i.e. $y_P^+ > 30$), but on the other hand close enough to the wall in order to be within the logarithmic layer, (i.e. $y_P^+ < 500$) [116, 140]; (ii) SWFs are derived for wall-attached boundary layers under equilibrium conditions, i.e. small pressure gradients, local equilibrium between generation and dissipation of turbulent energy and a constant (uniform) shear stress and heat flux in the near-wall region. For flow with regions of separation, as is normally the case for flows around buildings, the SWF concept does not hold anymore. Although the overall flow field may not differ much from that calculated by more sophisticated approaches like LRNM, SWFs often lead to inaccurate predictions of wall friction and convective heat transfer [134]. Therefore a number of adjusted WFs were proposed for non-equilibrium boundary layer flow, mainly in respect to velocity [153–155]. Defraeye et al. 2011 [156] proposed and validated an adjusted temperature WF for non-equilibrium forced-convective flows around buildings using LRNM. However, for the investigation of flow and heat transport in street canyons, at façades and building integrated solar com-

ponents, accurate WFs for mixed convection are needed, which consider buoyancy effects and their impact on the turbulence levels.

The aim of studying the thermal boundary layer is to determine improved thermal WFs for flows including buoyancy at exterior building surfaces, to apply them to a 2D street canyon case and to compare these results with LRNM. For the first part of this thesis it is assumed that with LRNM correct flow fields and convective heat fluxes can be predicted. This assumption is based on the validation study of Defraeye et al. 2010 [134], who conducted the validation for the geometry of a cube. In chapter 4 simulations using LRNM are validated for the flow inside a street canyon. Here the validation study focuses on the flow field, while Defraeye et al. also validated the convective heat fluxes. The 2D street canyon is a rather academic geometry that was chosen to develop a methodology how WF can be adapted for buoyant flows in urban areas. It is possible to extend this methodology to other (more complex) geometries. First the temperature profiles in the near-wall region are studied for different Ri. It is found that the temperature profiles correspond well to the temperature profiles of SWFs if the flow is in a forced convective flow regime and to the temperature profiles of the adjusted WF of Defraeye et al. 2011 [156] if it is in the mixed convective flow regime. Based on these results an adaptive temperature wall function (AWF) is derived that varies dynamically between the two types of temperature WFs. The AWF is implemented in such a way that the temperature WF regime is chosen separately (individually) for each wall adjacent cell of the computational grid. This AWF is used to model both forced and mixed convection in a 2D street canyon.

3.2.2.2 Turbulent boundary layer

In the near-wall regions at surfaces boundary layers develop. Turbulent boundary layers in equilibrium (local equilibrium between generation and dissipation of turbulent kinetic energy) have a characteristic shape of the velocity profile [90]. An example of such a boundary layer from a experimental study of Hussain and Reynolds 1975 [157] is given in Figure 3.6. The profiles are presented with dimensionless wall units:

$$y^+ = \frac{u^* y}{\nu} \tag{3.27}$$

$$U^+ = \frac{u}{u^*} \tag{3.28}$$

The region close to the wall can be divided into three sublayers. At the wall there is the viscous sublayer. In this layer, momentum and heat transport occur mainly by diffusion. Further away from the wall the logarithmic layer can be found. Here the momentum and heat transport is mainly driven by turbulence. Between the viscous sublayer and the logarithmic layer, there is the buffer layer. In this layer the two velocity profiles of the other layers blend.

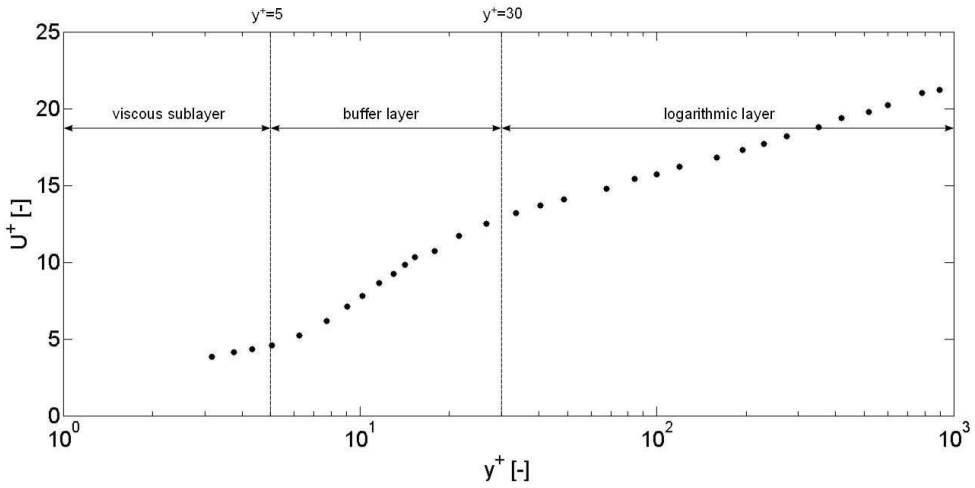

Figure 3.6: Dimensionless velocity (U^+) boundary layer profile as a function of y^+ (experimental data of Hussain and Reynolds 1975 [157]).

3.2.2.3 Low-Reynolds number modelling

Low-Reynolds number modelling (LRNM) is a method to model the flow in the boundary layer close to a wall surface. With LRNM, the near-wall region is resolved down to the viscous sublayer. Defraeye et al. 2010 [134] demonstrated that for the case of a cube immersed in a turbulent boundary layer the convective heat transfer predictions obtained with LRNM (steady RANS with realizable $k-\varepsilon$ turbulence model) show a satisfactory agreement with the experimental data of Meinders et al. 1999 [158]. LRNM performs well in terms of convective heat transfer determination, because the flow field (turbulent kinetic energy, velocity, temperature etc.) close to the walls is explicitly resolved. Based on detailed convective heat transfer measurements around the cube in a turbulent boundary layer reported by Meinders et al. 1999 [158], Defraeye et al. 2010 [134] performed a detailed validation of their CFD model. However, for buoyant flows in street canyons the data provided by the available experimental studies on convective heat transfer in street canyons are mostly not of sufficiently high spatial resolution for CFD validation purposes, or information relevant to CFD validation are lacking. In section 4.3 of this thesis a validation study for the flow field is conducted. The convective heat transfer is not validated, because it is not measured.

With the LRNM a two layer approach for the turbulent dissipation rate (ε) and the turbulent viscosity is used. In this study, in the fully-turbulent region the flow is resolved with the $k-\varepsilon$ model, and in the viscosity-affected region the one-equation Wolfshtein model [159] is employed to compute ε and the turbulent viscosity. For distinction between the fully-turbulent and the viscosity-affected region the turbulent Reynolds number Re^* is used:

$$Re^* = \frac{\sqrt{k}y}{\nu} \tag{3.29}$$

where y is the normal distance from the wall.
For $Re^* < 200$ the Wolfshtein model and for $R^* > 200$ the $k - \varepsilon$ model is employed to calculate ε and the turbulent viscosity. The disadvantage of LRNM is that a very fine cell grid is required close to the wall to resolve the entire boundary layer, which leads to an increased computing time. Therefore, for CFD simulations of buildings in urban areas, WFs are mostly used to cope with the complexity of the geometries and the size of computational domain. Another disadvantage is that no surface roughness can be used with LRNM. Here, it is assumed that CFD simulations using LRNM are sufficiently accurate and can be used as reference solutions for evaluating results from different wall function approaches. The validation study of this thesis (see section 4.3) shows better flow field results for the simulations using WFs compared with the simulations using LRNM. It is assumed that the better results with WFs are due to the more accurate prediction of the wind speed at the top plane of the street canyon and that using LRNM leads to better results for the convective heat fluxes.

3.2.2.4 Standard wall function

Standard wall functions (SWFs) are used to save computing time by not resolving but modelling the flow in the viscous sublayer, the buffer layer and a part of the logarithmic layer. SWFs were derived for flows with a local equilibrium between the generation and dissipation of the turbulent kinetic energy, e.g. flat plate flow. The assumptions on which SWFs are based are usually not valid for complex flows, such as flows around bluff bodies, buoyancy driven flows or flows with large pressure gradients. Therefore SWFs can lead to inaccurate flow predictions for such non-equilibrium boundary layer flows.

For SWFs the centre point P of the wall-adjacent cell is placed inside the logarithmic layer and the flow parameters in the wall-adjacent cell centre are modelled by the law-of-the-wall. The profiles of dimensionless velocity U^* and the dimensionless temperature T^* as a function of the dimensionless wall distance y^* are universal in the near-wall region for equilibrium boundary layer flows and can be described by the law-of-the-wall. These dimensionless parameters are related to the turbulent kinetic energy k:

$$y^* = \frac{\rho C_\mu^{1/4} k^{1/2} y}{\mu} \tag{3.30}$$

$$U^* = \frac{\rho C_\mu^{1/4} k^{1/2} U}{\tau_w} \tag{3.31}$$

$$T^* = \frac{\rho C_\mu^{1/4} k^{1/2} (T_w - T) c_p}{q_{c,w}} \tag{3.32}$$

where ρ is the air density, C_μ is the turbulent viscosity constant, μ is the dynamic viscosity, U is a velocity, τ_w is the wall shear stress, T_w is the wall temperature, T is the considered temperature to be made dimensionless, c_p is the specific heat capacity and $q_{c,w}$ is the

convective heat flux at the wall.
The law-of-the-wall for the velocity, derived for equilibrium boundary layer flows and used by the SWFs, is linear in the viscous sublayer and logarithmic in the logarithmic layer:

$$U_p^* = y_P^* \quad y_P^* < 11.225 \tag{3.33}$$

$$U_p^* = \frac{1}{\kappa} \ln(E y_P^*) \quad y_P^* > 11.225 \tag{3.34}$$

where the subscript P refers to the point P, E is an empirical constant (9.793) and κ is the von Karman constant (0.4187).
The temperature law-of-the-wall for incompressible flows has a similar form:

$$T_p^* = Pr\, y_P^* \quad y_P^* > 11.639 \tag{3.35}$$

$$T_p^* = Pr_t(\frac{1}{\kappa} \ln(E y_P^*) + P_J) \quad y_P^* > 11.639 \tag{3.36}$$

where Pr and Pr_t are the molecular and turbulent Prandtl numbers and P_J is an empirically-determined coefficient, which is a function of Pr and Pr_t (here -1.12 for air).

All the previously mentioned numerical values in Equations 3.34-3.36 are default values in ANSYS Fluent [116]. In ANSYS Fluent Pr_t is called the Wall Prandtl number and can be specified for the wall independently from the turbulent Prandtl number used in the energy equation. The default Wall Prandtl Number in ANSYS Fluent is 0.85, and is used by the SWFs.

3.2.2.5 Non-equilibrium wall function

Defraeye et al. 2010 [134] studied the heat transfer at the surface of a cube immersed in a turbulent boundary layer. They found that the temperature law-of-the-wall of the SWFs is not valid for the bluff body cases they studied, due to non-equilibrium conditions of the flow (e.g. separation). They also found that although the law-of-the-wall for the velocity was not valid, the impact on the global flow field was however limited.

For their cases, Defraeye et al. 2011 [156] observed a universal behaviour of the dimensionless temperature in the boundary layer. In Figure 3.7 dimensionless temperature profiles of LRNM simulations are given for flows in street canyons (from CFD simulations of this study; compare with Figure 3.12), which correspond to the universal behaviour Defraeye et al. 2011 [156] observed. The results of their simulations with LRNM showed that for this type of non-equilibrium flow the temperature in the boundary layer also shows a logarithmic-like behaviour, consisting of two parts following line A and line B in Figure 3.7. Therefore they were able to derive a customized temperature WF, here called non-equilibrium wall function (NEWF). This NEWF is based on fitting a logarithmic law, similar to Equation 3.36, to the LRNM data. Defraeye et al. 2010 [134] proposed a way to

implement the adjusted logarithmic law in ANSYS Fluent. Because it is only possible to adjust one parameter in Equation 3.36 in this code, namely Pr_t, an exact approximation of the data (line A and B) could not be implemented. Therefore this NEWF can only be applied for y_P^* larger than 50. The best approximation with LRNM data was found for $Pr_t = 1.95$. With this NEWF for non-equilibrium boundary layer flows Defraeye et al. 2011 [156] improved the convective heat transfer at the walls significantly.

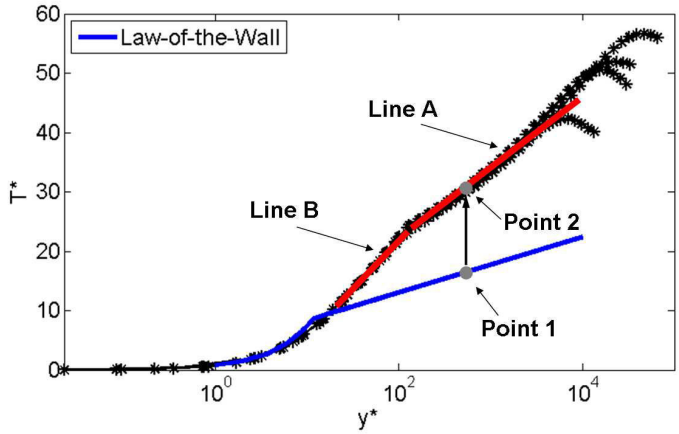

Figure 3.7: Dimensionless temperature profiles of LRNM simulations of non-equilibrium flows in street canyons (from CFD simulations of this study; compare with Figure 3.12) as a function of the y^* value; Blue: temperature law-of-the-wall; Red: logarithmic approximations.

3.2.3 Adaptive wall function

3.2.3.1 Importance of buoyancy

The NEWF by Defraeye et al. 2011 [156] was derived for bluff bodies in forced-convective turbulent boundary layers not considering buoyancy effects. In this study, the flow and heat transfer inside a street canyon is investigated. In Figure 3.8, three characteristic flow types for two-dimensional street canyons can be distinguished. For forced convective flow (e.g. in a quasi-isothermal case) mainly one vortex (and small corner vortices) is formed in a street canyon with flow normal to the street axis, as illustrated in Figure 3.8a. Buoyancy can however become important, e.g. during a sunny day with low wind speeds. The flow field in an urban street canyon can change completely due to buoyancy induced by high surface temperatures at the building façades, compared to the forced convective case. A second vortex (or even multiple vortices) can be formed due to buoyancy effects (e.g. [7] or [160]). Here, this case is denoted as mixed convection (Figure 3.8c). There exists also intermediate states, where the flow pattern mainly resembles that of the forced convective case but where the influence of buoyancy on the local flow field can already be noticed (growing corner vortex in Figure 3.8b), here denoted as the intermediate convective case. Buoyancy thus has a strong impact on the specific microclimate that develops in a street canyon and on the convective heat transport at the building façades. Due to buoyancy

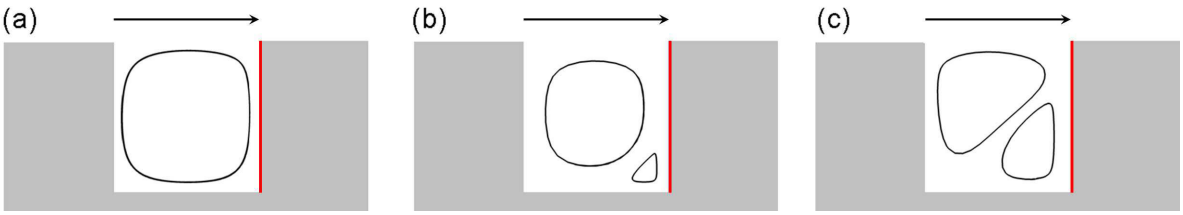

Figure 3.8: Streamlines of forced convective (a), intermediate convective (b) and mixed convective (c) cases (red walls are heated).

also the turbulence in the street canyon is increased, which enhances the convective heat transport at the walls. The increase of the turbulence due to buoyancy is shown in section 4.1 for flows in street canyon measured in the wind tunnel.

3.2.3.2 Numerical model

First a 2D street canyon in an ABL is analysed and extended later to the three dimensional case. The size of the computational domain (Figure 3.9) is determined according to the guidelines of Franke et al. 2007 [140]. The street canyon is modelled as a cavity of 10 m width (W) and 10 m (H) height, thus with an aspect ratio (H/W) of 1.

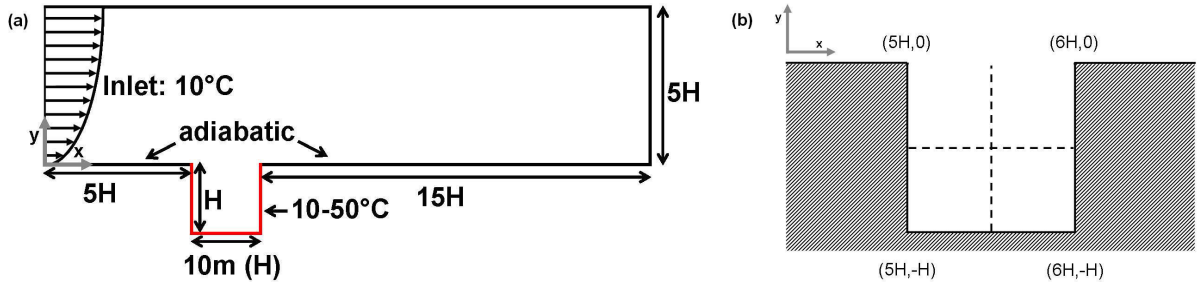

Figure 3.9: Computational domain (a); Horizontal and vertical centrelines in the street canyon (b). In all Figures y* ranges from the surface to the intersection of the horizontal and the vertical centrelines.

At the inlet of the domain vertical profiles of the mean horizontal wind speed, turbulent kinetic energy and rate of dissipation of turbulent kinetic energy are imposed according to Richards and Hoxey 1993 [141] (see section 3.2.1). By imposing this type of approach flow, the street canyon is modelled as a cavity within an ABL with low approach flow roughness, instead of as a repeated street canyon. The approach flow conditions for the latter are often obtained by employing periodic boundary conditions. The choice for the type of approach flow was made with the perspective on wind-tunnel tests on buoyancy effects presented in section 4.2. For these tests approach flow conditions for repeated street canyon configurations could not be obtained in the wind tunnel. The methodology developed in this section could however easily be extended to more complex geometries like a row of street canyons. Note that the applied roughness is chosen rather low to limit the gradient in the vertical profiles of the mean horizontal wind speed, as for LRNM

simulation in general no roughness can be specified. For this study the ABL friction velocity is determined with the logarithmic law (Equation 3.25) for different reference wind speeds U_{10} between 0.5 m/s and 5 m/s. U_{10} is the mean approach flow wind speed at $10m$ above the ground ($y = 10\ m$). At the inlet a constant temperature of 10 $°C$ is imposed. At the ground surface a no-slip boundary condition with zero roughness is used, because no surface roughness can be specified for LRNM in ANSYS Fluent [116]. In order to correctly compare the simulations using WF with the simulations using LRNM, also for the simulations with WF no roughness is specified. Therefore a gradient in the vertical profiles of the mean horizontal wind speed, k and ε cannot be avoided. This gradient is rather limited, because a short upstream fetch is considered [161]. By conducting CFD simulations with WFs and roughness, it was found that this change in the ABL causes only small differences of the flow inside the street canyon and therefore also of the wall heat fluxes at the building façades. The ground outside the street canyon is modelled adiabatic. At the ground of the street canyon different constant temperatures ranging from 10.5 to 50 $°C$ are imposed. For the building walls in the street canyon a no-slip boundary condition with zero roughness is used. Different constant temperatures between $10.5 - 50\ °C$ are imposed at the walls. Surface temperatures of ground and walls are always identical. So, it is important to remark that the surface temperatures in the street canyon are assumed to remain constant over space and time. At the top boundary, a symmetry boundary condition is applied, assuming that there are no normal velocities or normal gradients at this boundary. At the outlet an outflow boundary condition is used, which assumes that there are quasi no streamwise gradients at the outlet.

A 2D structured grid is build based on a grid sensitivity analysis and the guidelines of Franke et al. 2007 [140]. The grid consists of 17300 cells for the simulations with LRNM and of 4900 cells for the simulations with wall function modelling. The grids are refined towards the wall to resolve the boundary layers. For the LRNM simulations the highest y_P^+ (Equation 3.27) values, i.e. at the highest wind speed, are < 4 and for the simulations with WFs, they are < 300. According to user's guide of Fluent 2009 [116] the y_P^+ has to be < 5 for the LRNM and < 300 (and > 30) for WFs.

3.2.3.3 Numerical simulation

As mentioned, simulations with different WFs are compared with LRNM, which are considered as reference results. Xie et al. 2006 [53] validated their CFD model for a street canyon with the experimental data from Uehara et al. 2000 [162]. In this study, the CFD model of the street canyon is similar to the one of Xie et al. 2006 [53]. They used ANSYS Fluent to run 2D RANS simulation with the realizable $k - \varepsilon$ turbulence model and used the Boussinesq approximation to account for buoyancy. LRNM was used to resolve the near-wall region. They found that the temperature and horizontal velocity profiles along the vertical centreline of the CFD simulations were comparable with the wind tunnel measurements of Uehara et al. 2000 [162]. Above the roof level the horizontal velocities of the CFD simulations were higher than the velocities from the measurements. They claim that the reason for this were the inflow profiles, which were slightly different from the profiles of the experiment. In the validation study of this thesis (see section 4.3) the velocities inside the street canyon were overestimated with the here used numerical models. This

Velocity (U_{10})	5 m/s	1 m/s	3 m/s	1 m/s	2 m/s	1 m/s	0.5 m/s	1 m/s	0.5 m/s	1 m/s
Temp. difference	10 K	1 K	10 K	2 K	10 K	5 K	2 K	10 K	10 K	40 K
Ri	0.14	0.34	0.38	0.68	0.86	1.7	2.7	3.4	13.7	13.7

Table 3.1: Reference velocities at 10m above the ground, temperature difference between the inflow and the wall surfaces and the global Richardson number for the studied cases.

overestimation is assumed to be caused by overestimated velocities in the top plane of the street canyon. Because the flow inside the boundary layer could not be measured detailed enough, it could not be evaluated, if LRNM accurately resolves the boundary layer. Further also convective heat fluxes were not measured and therefore were not validated. Based on the validation of Defraeye et al. 2011 [156] it is here considered that the LRNM simulations can accurately predict the heat transfer for the case considered in this study, and as such the LRNM results can be considered as sufficiently accurate to be used as reference solutions. The focus of this study is not on the detailed flow field and therefore the errors, found for the flow field in the validation study, can be accepted.

In this study the buoyancy forces are induced by air density changes due to the heated building façades. To decide whether buoyancy forces have to be accounted for, a 'global' Richardson number (Ri) is used:

$$Ri = \frac{g\beta(T_w - T_0)h}{U^2} \tag{3.37}$$

where g is the gravitational acceleration, h is a reference height (here the building height H) , U is a reference velocity (here the reference velocity U_{10}) and T_0 is a reference temperature (here the temperature at the inlet boundary).

The inverse of the Ri is the Froude number. For the experimental study of this thesis, the Froude number is used for better comparison with experimental studies in literature. For very low Ri (forced convection) the buoyancy forces can be neglected. For Ri around 1 (mixed convection) the mechanical and the buoyancy forces are both important. For very high Ri (natural convection) the mechanical forces can be neglected. In this study CFD simulations with Ri from 0.14 to 13.7 were conducted, for different combinations of wind velocity and temperature difference (Table 3.1).

3.2.3.4 Results with different near-wall modelling approaches

3.2.3.4.1 Dimensionless temperature profiles in the near-wall region

In this section, results of the LRNM simulations for global Ri from 0.14 to 13.7 (Table 3.1) are presented. In Figure 3.10, the profiles for the dimensionless temperature (a,b) and turbulent kinetic energies (c,d) along a horizontal centreline for two different global Ri (0.34 and 3.4) are given for the leeward (a,c) and the windward wall (b,d) in a street canyon. Mainly two types of dimensionless temperature profiles were found close to the wall. For the simulation with global $Ri = 0.34$ the dimensionless temperature profiles follow the law-of-the-wall of the SWFs for both leeward and windward wall. The dimensionless

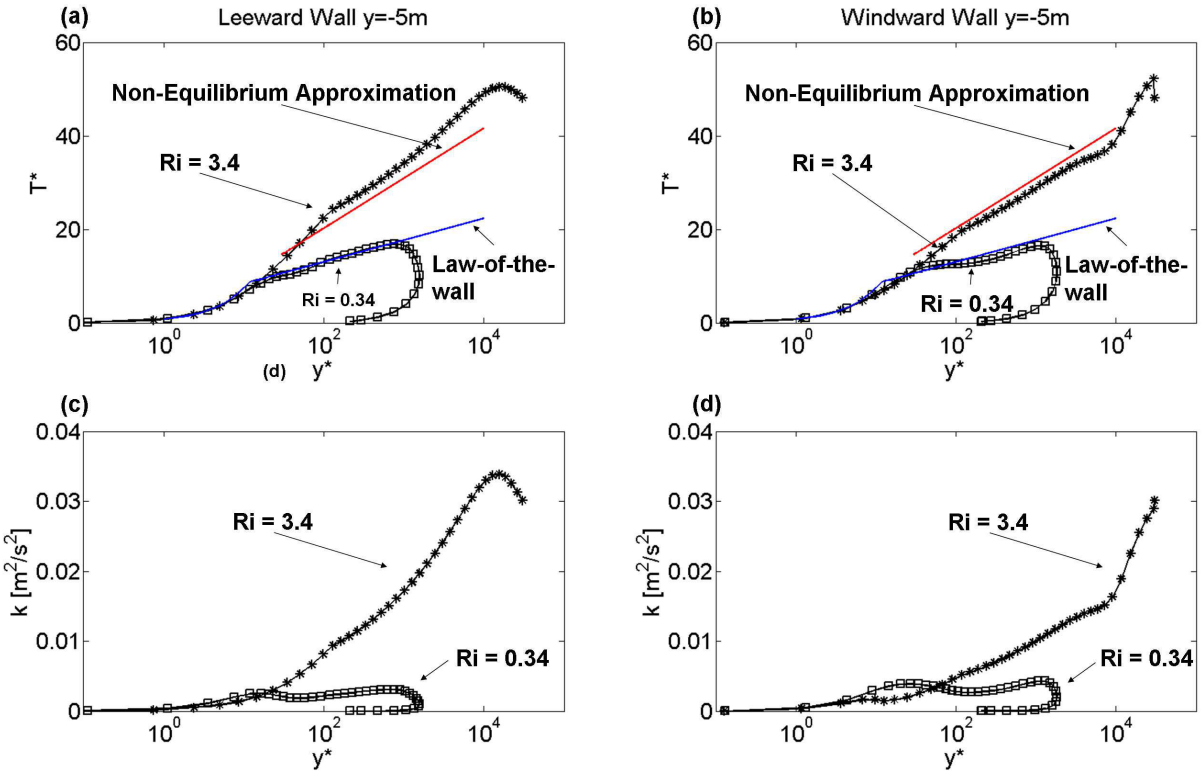

Figure 3.10: Dimensionless temperature profiles and turbulent kinetic energy profiles as a function of the y^* value on the horizontal centreline (see Figure 3.9b) of a street canyon for two simulations with different global Ri numbers (0.34 and 3.4).

temperature profiles of the simulation with global $Ri = 3.4$ follows the non-equilibrium approximation derived by Defraeye et al. 2011 [156]. It is remarked that for some flow fields y^* decreases after some distance from the wall, which can be explained by the fact that the square root of k in Equation 3.30 is decreasing faster than y is increasing.

Further it can be observed that the shape of the turbulent kinetic energy profiles in the boundary layer is different for the two global Ri numbers. For the flow with low global Ri the turbulent kinetic energy is increasing in the viscous sublayer ($y^* < 100$) due to the velocity gradient. Further away from the wall the turbulent kinetic energy is decreasing again. This behaviour is similar to the behaviour of a flat plate flow (Figure 3.11), for which the SWFs were originally derived. In Figure 3.10c and 3.10d the turbulent kinetic energy is moderately increasing at higher distance from the wall due to the higher turbulent kinetic energies in the centre of the street canyon. Because the flow inside the street canyon with low global Ri is similar to a flat plate flow and the law-of-the-wall was derived for a flat plate flow, the dimensionless temperatures are approximately similar to the law-of-the-wall. Therefore also the wall heat fluxes calculated with the SWFs correspond to the wall heat fluxes simulated with LRNM, as will be shown further below.

For the simulation with the higher global Ri, the turbulent kinetic energy is monotonically increasing in the boundary layer. This monotonic increase of turbulent kinetic

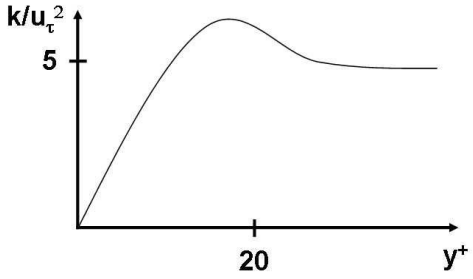

Figure 3.11: Schematic representation of the turbulent kinetic energy, scaled with the friction velocity as a function of the y+ value for flat plate flow [163].

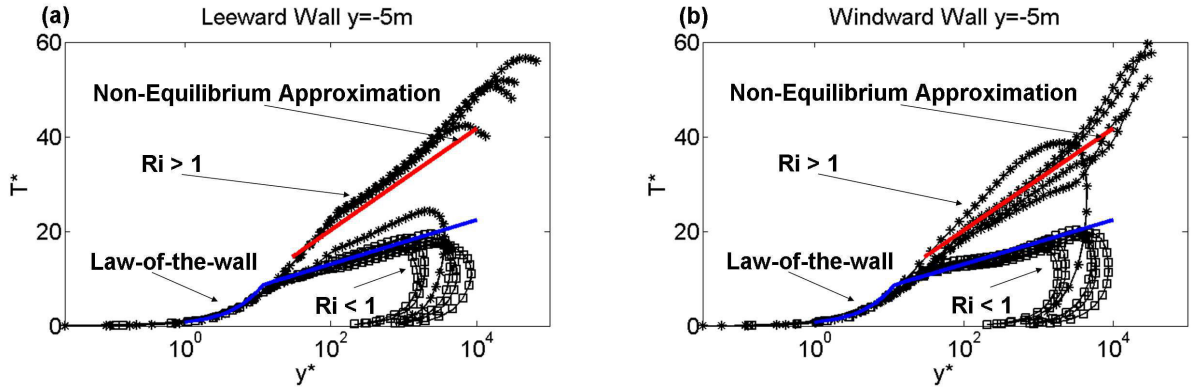

Figure 3.12: Dimensionless temperature profiles as a function of the y^* value along the horizontal centreline (see Figure 3.9b) of a street canyon for simulations with different global Ri numbers.

energy is caused by the high turbulence level further away from the walls inside the street canyon due to buoyancy. In an urban street canyon with mixed convection (global $Ri > 1$) an important part of the turbulent kinetic energy is produced by buoyancy and therefore the law-of-the-wall derived for equilibrium boundary layer flows is not applicable anymore. For this type of non-equilibrium boundary layer flows a quasi universality of the dimensionless temperature profiles can be found, as shown below, which can be used to determine a NEWF as described in section 3.2.2. Such dimensionless temperature profiles are described by Defraeye et al. 2011 [156], who determined a NEWF that improves the results for non-equilibrium boundary layer flows especially in terms of the wall heat fluxes.

Figure 3.12 shows the dimensionless temperature profiles along the horizontal centreline of different simulations with global Ri numbers from 0.14 to 13.7. For almost all the simulations with global $Ri < 1$ the dimensionless temperature profiles follow the law-of-the-wall and for almost all the simulations with global $Ri > 1$ the dimensionless temperature profiles follow non-equilibrium approximation.

It can be concluded that, for a flow in a street canyon with constant surface temperatures in space and time, two extreme types of dimensionless temperature profiles exist for the whole range of global Ri. The two extreme cases can be described by either SWFs or NEWFs. The global Ri number can be used be to distinguish between these two types.

3.2.3.4.2 Forced convection case

For forced convection or equilibrium flows the SWFs performs better, because of the reasons explained above. In Figure 3.13 the CHTCs, are given for simulations with global $Ri = 0.14$ and for LRNM, SWF and NEWF. In this case the results with the SWFs agree better with the LRNM results than, as expected, with the results using NEWF. The NEWF underestimates the CHTCs.

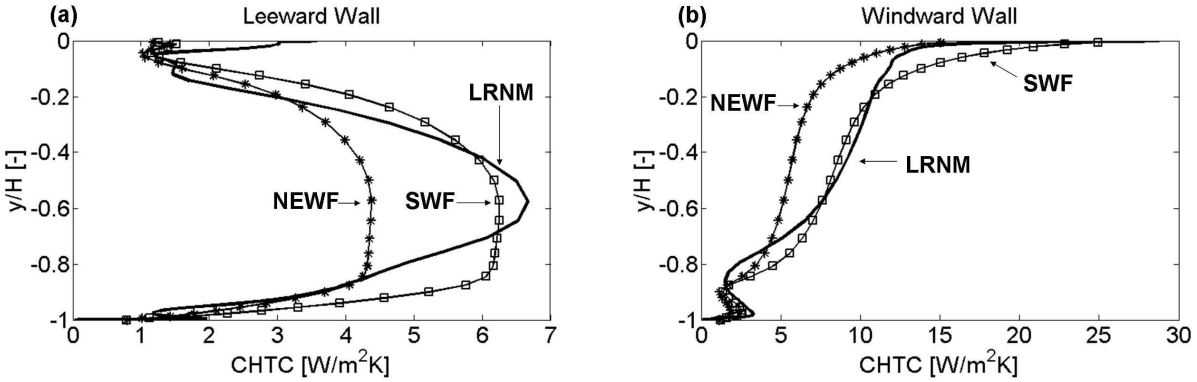

Figure 3.13: CHTC as a function of the vertical position y/H for a simulation with global $Ri = 0.14$. Results from SWF and NEWF are compared with LRNM.

3.2.3.4.3 Mixed convection case

In Figure 3.14, the CHTCs at the leeward and windward wall for SWFs and NEWF are compared with LRNM for a global $Ri = 3.4$. It can clearly be noticed that the results with the NEWF show a much better agreement with the LRNM results than the results with the SWFs. This is what was expected by the analysis of the dimensionless temperature profiles for the same boundary conditions in the section 3.2.3.4.1. In Figure 3.15 profiles of the

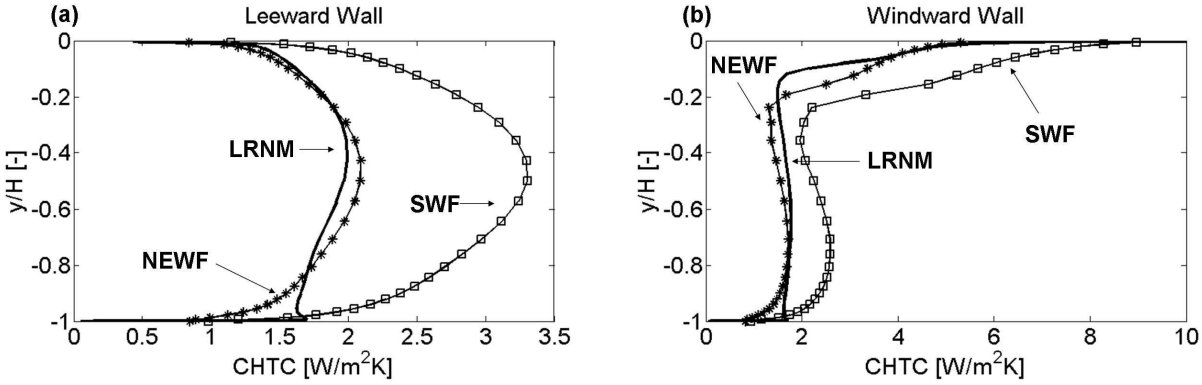

Figure 3.14: CHTC as a function of the vertical position y/H for a simulation with global $Ri = 3.4$. Results from SWF and NEWF are compared with LRNM.

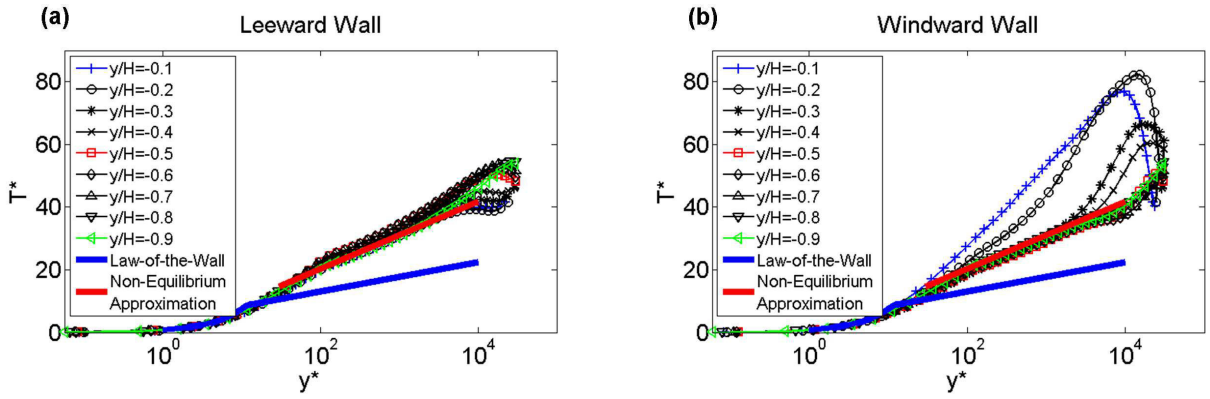

Figure 3.15: Dimensionless temperature profiles as a function of the y^* value on horizontal lines at different vertical positions y/H.

dimensionless temperature for different heights above the ground of the street canyon are given. These profiles do correspond to the non-equilibrium approximation for all heights, and not only for the centreline given in Figure 3.12. There is however an underestimation of the wall heat flux close to the ground ($y/H < -0.8$). This underestimation is caused by the interaction with the ground surface and cannot be avoided because the flow fields with the WFs and the LRNM are different here.

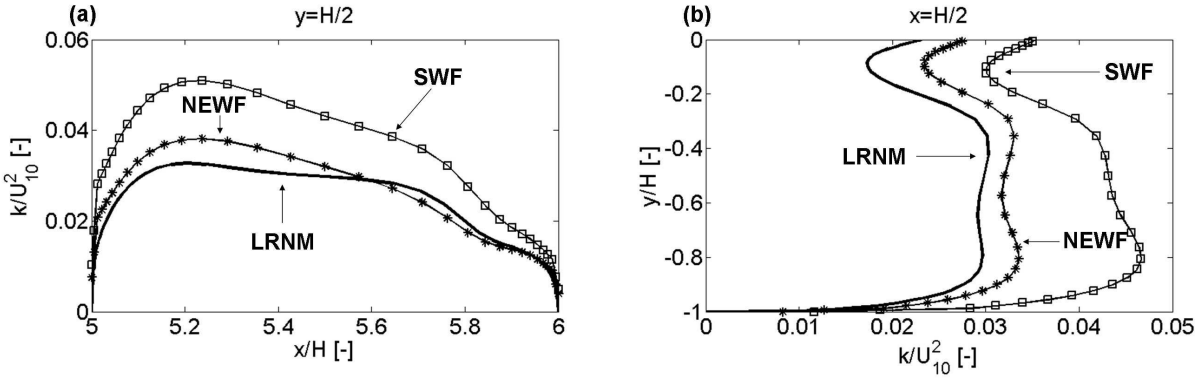

Figure 3.16: Turbulent kinetic energy profiles normalised by the square of the reference velocity as a function of the x or y position along the horizontal (a) and vertical centreline (b) (see Figure 3.9b). Results from simulations with SWF and NEWF are compared with result of a simulation with LRNM.

Figure 3.16 shows the turbulent kinetic energy profiles along the horizontal (a) and the vertical centreline (b) for the three near-wall modelling approaches. It can be noticed that for the SWFs the turbulent kinetic energies are too high in the street canyon. The turbulent kinetic energy profiles with the NEWF agree better with the LRNM results than the ones with the SWFs. Therefore with the NEWF not only the temperature field and the calculation of the wall heat fluxes can be improved, but also the flow field characteristics. For the study of Defraeye et al. 2011 [156] the use of the NEWF did not have any influence on the flow field, because buoyancy was neglected. In this study

buoyancy is accounted for and therefore the thermal field predictions also influence the turbulent kinetic energies and the velocities inside the street canyon.

3.2.3.4.4 Intermediate convection case

For intermediate convection cases (Figure 3.8) the dimensionless temperature profiles correspond in a part of the street canyon to the law-of-the-wall and in other parts to non-equilibrium approximation. As an example results for a simulation with a global $Ri = 0.38$ are shown in Figure 3.17. Here the profiles of the dimensionless temperature are given for different heights above the ground of the street canyon for the leeward (a) and the windward wall (b). Close to the ground the profiles correspond to the non-equilibrium approximation. Above $y/H = -0.8$ the profiles correspond to the law-of-the-wall. For this convection case it is not possible to choose one single temperature WF for the whole domain. The temperature WF has to be chosen locally, namely dependent on the local flow field characteristics. To solve this problem an adaptive WF is proposed in this thesis.

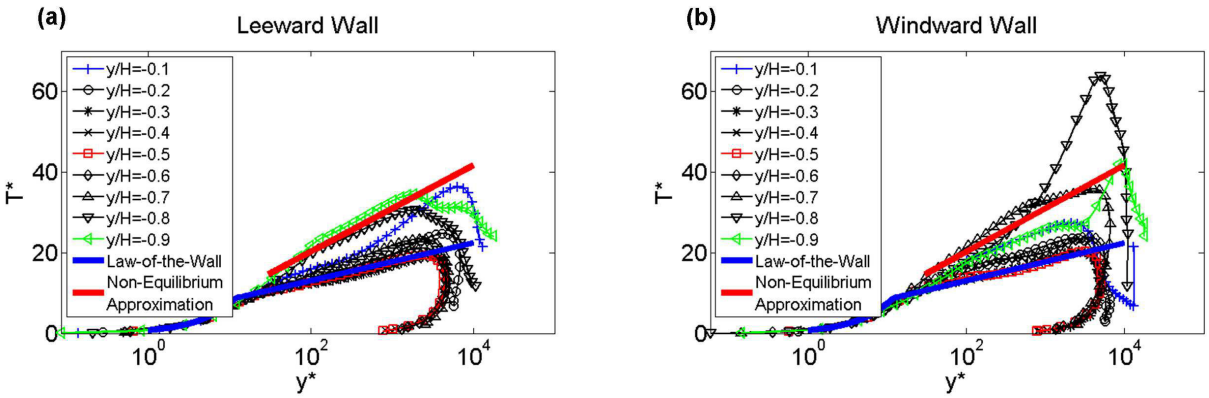

Figure 3.17: Dimensionless temperature profiles as a function of the y^* value on horizontal lines at different vertical positions y/H.

3.2.3.5 Adaptive wall function

3.2.3.5.1 Concept of the adaptive wall function

As stated in the previous section, two types of temperature profiles corresponding to equilibrium and non-equilibrium boundary flows can be found in street canyons depending on the Ri. Therefore different WF types should be used at different Ri to correctly simulate the heat exchange between the surface and the fluid. A criterion is thus needed for the selection of the appropriate WF type, based on the local flow field. A local Richardson number Ri_{lo} is therefore proposed:

$$Ri_{lo} = \frac{g\beta(T_w - T_P)h}{u_P^2} \tag{3.38}$$

where T_P is the temperature in the wall-adjacent cell centre and u_P the velocity magnitude here.
This Ri_{lo} number has the advantage that it evaluates the importance of buoyancy very locally and close to the wall, i.e. where the heat exchange of the surface with the flow occurs. In contrast, the global Ri usually is defined by a free stream velocity and temperature and thus evaluates the importance of buoyancy on the street canyon or building scale. This reference temperature and velocity are not necessarily representative for the flow close to the surface, where the heat exchange takes place. Furthermore, it was found that the local Ri is quasi grid-insensitive in the y^* range, where the WFs can be applied.

In this section it is investigated for which local Ri the temperature profiles correspond to those of equilibrium and to non-equilibrium boundary layer flows respectively. From these simulations an empirical relationship for the turbulent Prandtl number Pr_t as a function of the local Ri is derived (Figure 3.18). The adaptive wall function (AWF) is built up in following way. For local Ri below 1 the SWFs are used and therefore the wall Prandtl number is equal to the default value of 0.85 (in ANSYS Fluent). For local Ri between 1 and 6 a transition from forced to mixed convection is modelled by linear interpolation. For local Ri larger than 6 the NEWF with $Pr_t = 1.95$ is used. To determine the Ri_{lo} limits ($Ri_{lo} < 1$ and $Ri_{lo} > 6$) of the mixed and forced convection cases, simulations with different Ri_{lo} limits were run. As a lower limit Ri_{lo} between 0.5 and 4 and as an upper limit Ri_{lo} between 4 and 10 were used. Based on the least-squares method the optimum was found to be 1 for the lower limit and 6 for the upper limit.

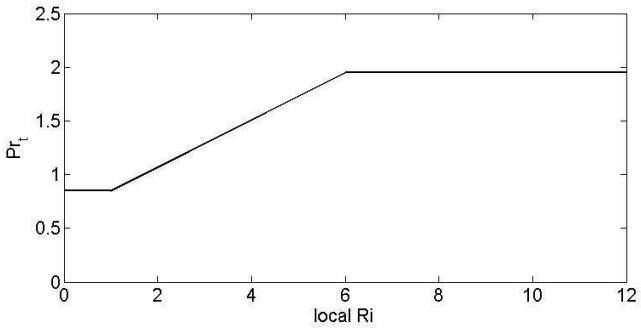

Figure 3.18: Turbulent wall Prandtl number as a function of the local Richardson number.

The local Ri is found to be quasi grid-insensitive in the y^* range, where the wall functions can be applied: Ri_{lo} is almost constant in this range, except for some special cases, where the local Ri are much higher than 6 and therefore the NEWF has to be used anyway.

In the CFD code used in this study (ANSYS Fluent 12.0), the local Ri concept was implemented by means of a user-defined function. For each wall-adjacent cell the local Ri is computed during each iteration and the wall Prandtl number is set according to the local Ri. Note that even if the wall Prandtl number changes for some cells between two iterations the simulations were found not to be prone to instabilities.

3.2.3.5.2 Results of the adaptive wall function

In Figure 3.19 the CHTCs from simulations with global $Ri = 0.38$ are given for different near-wall treatments for the leeward and the windward wall. It can be noticed that for the leeward wall the NEWF underestimates and the SWF overestimates the CHTCs. The results with the AWF with the local Ri concept show a much better agreement with the LRNM results.

For the windward wall the AWF is in better agreement with the LRNM results, except for the region close to the ground. This is due to fact that in this region the WFs and the LRNM predict different flow fields.

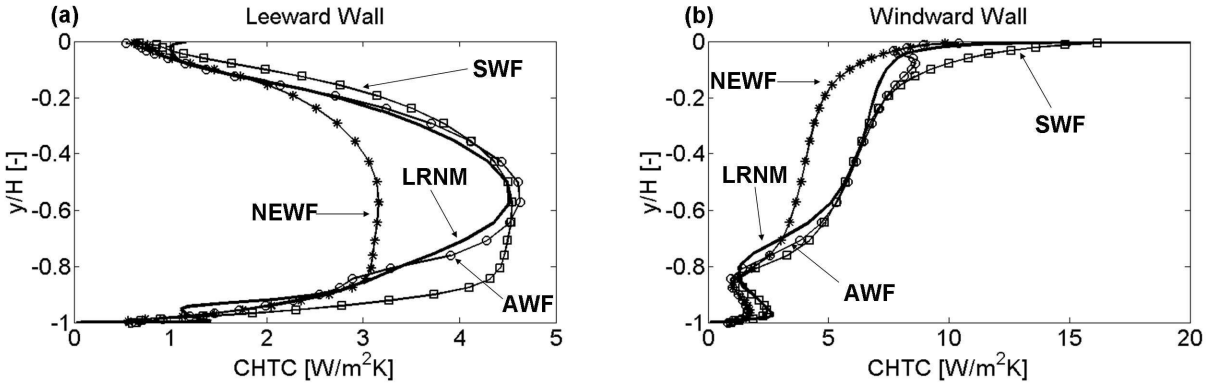

Figure 3.19: CHTC as a function of the vertical positions y/H for a simulation with global $Ri = 0.38$. Results from SWF, NEWF and AWF are compared with LRNM.

For the different combinations of wind speeds and temperatures and thus different global Ri (see Table 3.1), simulations were conducted with the three WF types presented here. The results of these simulations were compared with results of the LRNM simulations. Figure 3.20 gives the deviations from the LRNM results (total wall heat flux) for the three WF types (normalised by the LRNM results). The total wall heat flux is a conservative choice to compare the results of the simulations with different wall modelling approaches. The deviations would be even larger if the sum of the absolute value of the deviations at each location would be compared.

The SWFs overestimate the wall heat flux for all the studied cases for both walls. For cases with a global $Ri > 1$ the overestimation is between $10 - 20$ %. This overestimation is mainly due to regions at the walls, where dimensionless temperature profiles correspond to the non-equilibrium approximation. This can clearly be seen in Figure 3.13. For cases with a global $Ri < 1$ the SWFs overestimates the wall heat flux by $30 - 60$ % for both walls. For cases with a global $Ri < 1$, the NEWFs underestimate the wall heat flux up to 20 %. The new proposed AWF performs better than the SWFs and the NEWF for all the studied cases. The deviation from the LRNM is less than 10 % for almost all cases. This is a significant improvement compared to the deviation of the NEWF (up to 30 %) and the deviation of the SWFs (up to 60 %). For global $Ri = 0.68$ the accuracy of the AWF is significantly less than for all the other global Ri numbers. The reason for this higher deviation is that this case is in the transition zone between the SWFs and the

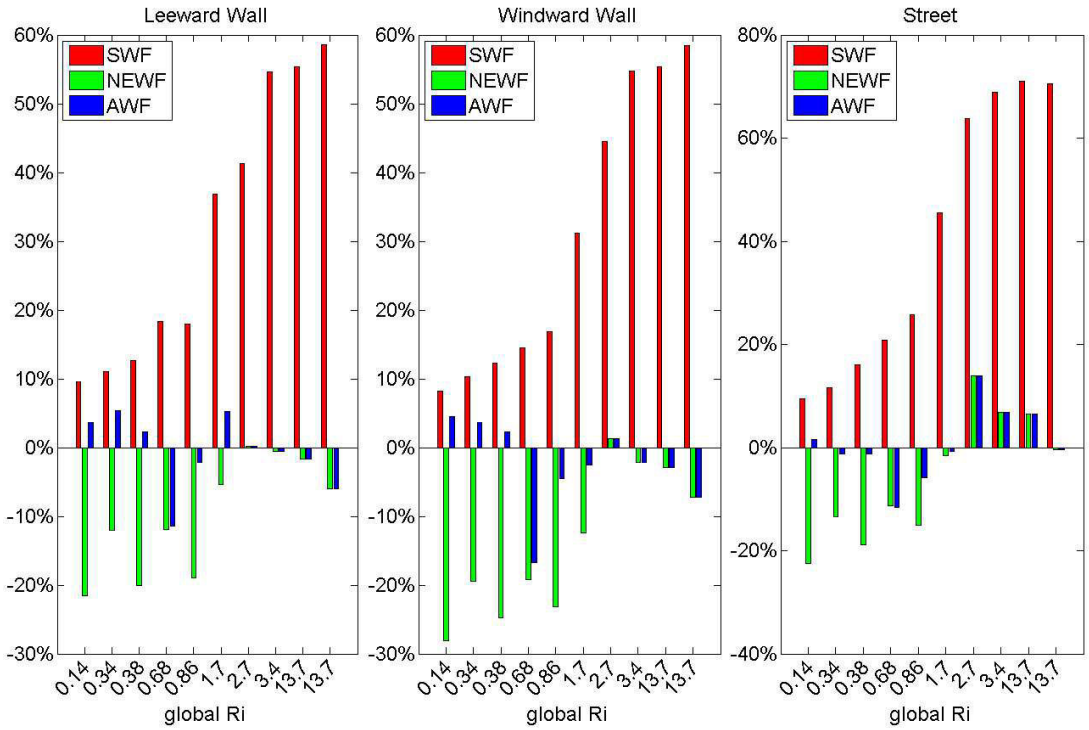

Figure 3.20: Relative differences of the total heat flux at the walls for the SWF, NEWF and the AWF compared to the LRNM for different global Ri.

NEWF (local Ri_{lo} at almost all parts of the wall are between 1 and 6) for almost the whole domain, which uses a simplified linear interpolation. In this transition zone the convective heat transfer is very sensitive to small changes in the flow field.

3.2.3.5.3 3D street canyon

The proposed AWF was also used for a 3D street canyon simulation to investigate whether the AWF also performs well for 3D geometries with oblique winds. Therefore the 2D street canyon was elongated to a 50 m long street canyon and periodic boundary conditions were used at the lateral boundaries. For the simulations, wind at a 45 ° angle to the street axis was considered. In Figure 3.21 the profiles of the CHTCs are given at the centre (normal to the x-y plane of Figure 3.9b) of the elongated street canyon. For this particular case (global $Ri = 3.4$) the AWF gives better results than the other two WFs. Further investigations have to be conducted for other 3D geometries to confirm that the AWF can be generally used for 3D street canyons.

3.2.3.6 Discussion

A new thermal WF, called adaptive wall function (AWF) was derived which varies adaptively at each location on the wall surface between two existing WF types, based on the local Ri. This methodology was developed for a 2D street canyon, but it is possible to

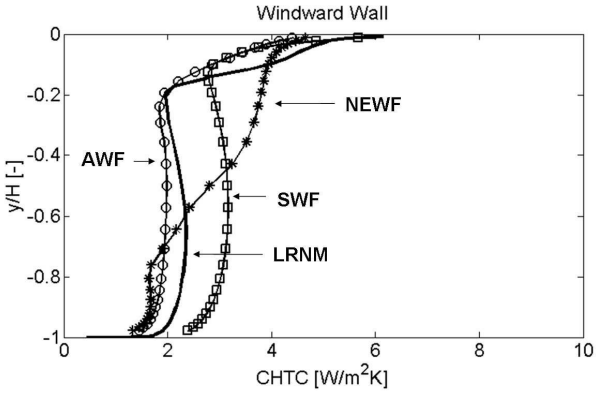

Figure 3.21: CHTC as a function of the vertical positions y for a simulation with a 3D street canyon with global $Ri = 3.4$. Results from simulations with SWF, NEWF and AWF are compared with result of a simulation with LRNM.

extend it to other (more complex) geometries. The AWF is easy to implement in existing CFD codes (for example in ANSYS Fluent). For the studied cases, the AWF results deviate less from the LRNM results than the results of the other two WF types and the AWF is applicable for both forced and mixed convection. However this new WF has some limitations, which are given here:

- This study was conducted for a two-dimensional geometry. The derived AWF is expected to be valid also for three-dimensional geometries, because the same phenomena will occur here regarding the impact of buoyancy on the profiles of the dimensionless temperature and dimensionless velocity, normal to the surfaces. The AWF was tested for one 3D street canyon with an oblique flow direction. First results indicate that the AWF is also valid for these flow fields. This conclusion has however to be confirmed by simulating a larger number of urban configurations.

- This study is performed for one specific geometric configuration, namely a symmetric street canyon, where the flow field of the WFs agrees well with the flow field of LRNM. For cases where WFs fail to predict the correct flow field on a building scale, e.g. for cylindrical buildings, it will not be possible to get the correct heat fluxes with these WFs.

- Since the NEWF is only applicable for y_P^* above about 50, this limitation holds also for the AWF, as the NEWF formulation is an integral part of the AWF.

- The AWF is based on simulations using the realizable $k-\varepsilon$ model and therefore the values of the used parameters (Pr and local Ri) should be used in combination with this turbulence model. The proposed AWF is however also expected to perform well with other similar turbulence models, such as the standard $k-\varepsilon$ model. The used parameters might have to be adjusted for other turbulence models.

- The AWF presented was derived focusing on buoyant flows in street canyons. Therefore the local Ri is used as a criterion to choose between the SWF and the NEWF.

However, the local Ri does not account for the turbulent kinetic energy which is important for the heat transfer. In future work, cases will be modelled with increased turbulence level inside the street canyon and on the building façade not only due to buoyancy but also due to advection (3D cases) or due to more detailed façade details (balconies, window sills etc.). This will have an influence on the heat transfer and thus on the selection of the WF and thus may have to be considered in future developments of AWFs.

- The results of CFD simulations using LRNM were used as a reference. As discussed in section 4.3 the results of CFD simulations using LRNM for street canyons are not yet enough validated. Here it is assumed that the errors in the flow field are caused by inaccurate prediction of the flow field at the top plane of the street canyon. Further it is assumed (based on validation studies of Defraeye et al. 2010 [134]) that with LRNM the convective heat flux can be accurately predicted.

3.2.3.7 Conclusion

Thermal boundary layers on building walls in street canyons were studied by CFD simulations accounting for buoyancy with the aim to improve the existing WFs for convective heat transfer predictions. LRNM of the transport in the boundary layer was used as a reference solution to evaluate the performance of different WF types. First the dimensionless temperature profiles and the turbulent kinetic energy profiles were analysed. Two main types of dimensionless temperature profiles could be identified. One of these dimensionless temperature profiles corresponds to the temperature law-of-the-wall as used in SWFs. The second dimensionless temperature profile corresponds to a customized temperature WF for flows with non-equilibrium boundary layers (called NEWF). Both boundary layer types can be observed in a street canyon with buoyant flow. For forced convective flows at the surfaces the SWFs provide most accurate heat transfer predictions and for mixed convective flows the simulations using NEWFs are most accurate. Based on this observation, an AWF was derived that interpolates between the two existing WF types dependent on the local Ri, proposed in this thesis. For the determination of the local Ri, the temperature and the velocity magnitude in the cell adjacent to the wall are used as reference temperature and velocity. The AWF can be used for mixed and forced convection whereas the SWFs only provides relatively accurate heat transfer results for forced convective street canyon flow and the NEWF for mixed convective street canyon flow. For the AWF, the deviations from the total heat flux of LRNM are less than 10 % for almost all cases analysed. For the SWFs these deviations are between 10 % and 60 % and for the NEWF up to 30 %. Apart from the limitations discussed above, the AWF approach has shown to be a valuable technique for the simulation of flow fields and convective heat transport in urban street canyons in cases where buoyancy plays an important role. This AWF approach shows the potential to importantly increase the accuracy of convective heat transfer predictions in CFD studies in the urban context. Even though LRNM performs better for simulations with convective heat transport, accurate WF are often the only option for large-scale urban engineering studies, where complex geometries, grid generation and computing power limitations become a limiting issue.

3.2.4 CHTC correlations for street canyons

3.2.4.1 Background and approach

As discussed in section 3.1.2, in BES models CHTCs are used to quantify the convective flow of heat at the building façades. A number of CHTC correlations for different building configurations are found in literature (overview given by Defraeye at al. 2011 [130]). For buildings in urban areas these CHTC relations are not sufficiently correct, since the global flow field and as such also the convective heat transfer is strongly influenced by the neighbouring buildings. Furthermore, buoyancy is important in urban areas, where façades and pavement are heated by the sun and where wind speeds are reduced due to wind sheltering. For example, in a street canyon with an aspect ratio (width versus height) of 1 and a wind flow direction perpendicular to the street axis, a vortex is formed in the centre of the street canyon. With increasing temperature difference between the air around buildings and the building façades, buoyancy will reinforce this vortex or other counter rotating vortices will be generated. These vortex structures have an important effect on the CHTC at the different surfaces of the street canyon. Wind tunnel experiments (e.g. Kovar-Panskus et al. 2002 [7]) and CFD simulations (e.g. Xie et al. 2007 [160]) were performed to study the influence of different surface temperatures of façades and ground on the flow field.

Due to the lack of CHTC correlation for buildings in urban environment in literature, in this thesis CHTC correlations are derived by CFD simulations as outlined below, for different building geometries, ranging from stand-alone buildings to street canyons, taking into account the effect of buoyancy. The CHTC correlations are derived for stand-alone buildings and street canyons with different lengths with or without buoyancy. Only wind directions normal to the buildings are considered. The CHTC correlations depend both on wind speed and surface temperatures when buoyancy is present. Therefore the CHTC correlations are established not only as a function of the wind speed but also as a function of the surface to air temperature difference. These CHTC correlations are in section 5 used to study the influence of wind sheltering in urban street canyons on the space cooling and heating demand of buildings.

3.2.4.2 Numerical model

For the derivation of CHTC correlations, steady 2D and 3D RANS CFD simulations using ANSYS-Fluent 12.0 [116] are conducted with a realizable $k-\varepsilon$ turbulence model. For the near-wall modelling, modified WFs discussed in section 3.2.2 [156] are used.

Seven urban geometric configurations are considered including stand-alone buildings and street canyons. For the stand-alone buildings four cases are considered: (case i) a cubical building with side dimensions H, (case ii) a rectangular building with a height H, a width W equal to H and a length L ($L = 110.5\ m$), (case iii) rectangular building with a length $2L$, (case iv) an infinite long building, which is modelled as a 2D case. The street canyon is modelled as a 2D cavity with three different aspect ratios H/W: 0.5 (case v), 1 (case vi) and 2 (case vii). H equals 14.6 m. The first 4 geometries were chosen to investigate the dependence of the CHTCs on building length. The last three cases of street canyons were chosen to analyse the influence of the aspect ratio. The dimensions

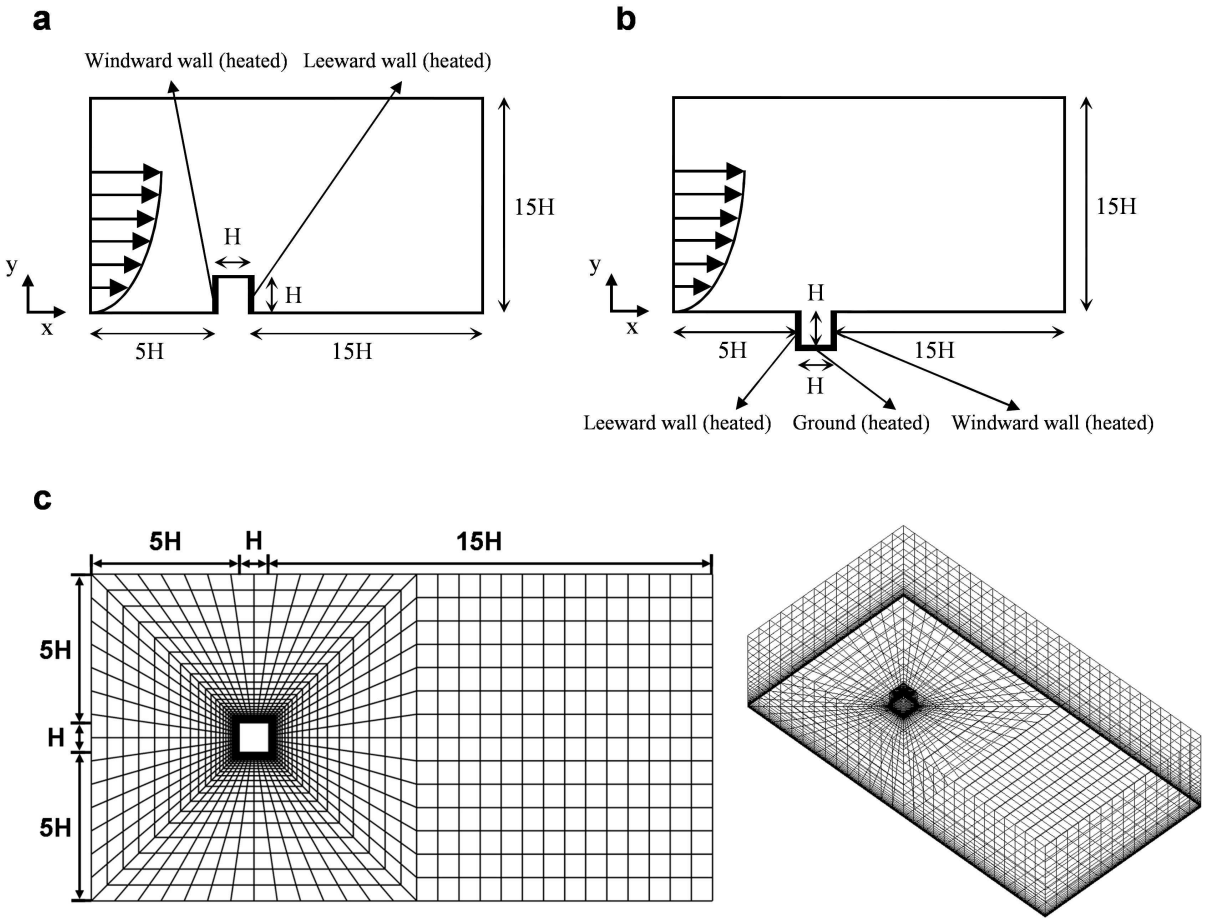

Figure 3.22: Computational domain for a 2D stand-alone building (a), a 2D street canyon (b) and a 3D cubical building (topview and 3D view) (c).

of the 2D and 3D domains are constructed according to the guidelines of Franke et al. 2007 [140]. Figure 3.22 gives as an example the domain for 2D stand-alone building and street canyon cavity and the meshed domain for the 3D cubical building (3D and topview).

At the inlet of the domain vertical profiles of the mean horizontal wind speed, turbulent kinetic energy and rate of dissipation of turbulent kinetic energy (ε) are imposed according to Richards and Hoxey 1993 [141](Equation 3.25). For z_0 a value of 0.03 m is chosen, which corresponds to a land surface with low vegetation and isolated obstacles. The same roughness length was also used for the urban geometries in order not to influence the heat transfer by the characteristics of the approach flow, but only by the building geometries itself. Because the street canyon is modelled as a cavity and therefore the longitudinal extensions of the domain are at the roof level, the used roughness length is assumed to be the roughness of the roof and not the roughness of the urban area. Eight different reference wind speeds at 10 m height are considered: 0.125, 0.25, 0.5, 1, 2, 3, 4 and 5 m/s. The incoming air temperature equals 20 $°C$. The wind direction for the 3D simulations is normal to the building. The following roughness heights were used for the simulations. The surfaces of the building and cavity have no roughness. Reason for this particular choice is that the wall functions used in this study are derived from LRNM

simulations (section 3.2.2), which allow only smooth surfaces [116]. The surfaces of the longitudinal extension of the domain in front and behind the building or the street canyon are modelled with different roughness heights, chosen in such a way that the streamwise gradients of the vertical winds speed and turbulence profiles are minimal [161]. The surface temperatures of the building and cavity walls are assumed to be uniform. Four different surface temperatures are considered: 21, 23, 25 and 30 $°C$ to mimic different solar radiation intensities. The Ri is used to quantify the amount of buoyancy. The Ri for the cases considered in this part of the thesis varies between 0.2 and 3200. The other surfaces of the domain, with exception of the building or cavity walls, are modelled as adiabatic surfaces. Symmetry boundary conditions are imposed at the top boundary and out-flow boundary conditions at the outlet. For the 3D domains symmetry boundary conditions are imposed at the lateral boundaries.

2D and 3D structured grids are built based on a grid sensitivity analysis and on the guidelines of Franke et al. 2007 [140]. The 2D grids consist of 5500 to 11500 cells. The 3D grids consist of 67000 to 155000 cells. All grids are refined towards the walls. Since a wall function approach is used, the y^+ values have a maximum of 500.

3.2.4.3 Importance of buoyancy

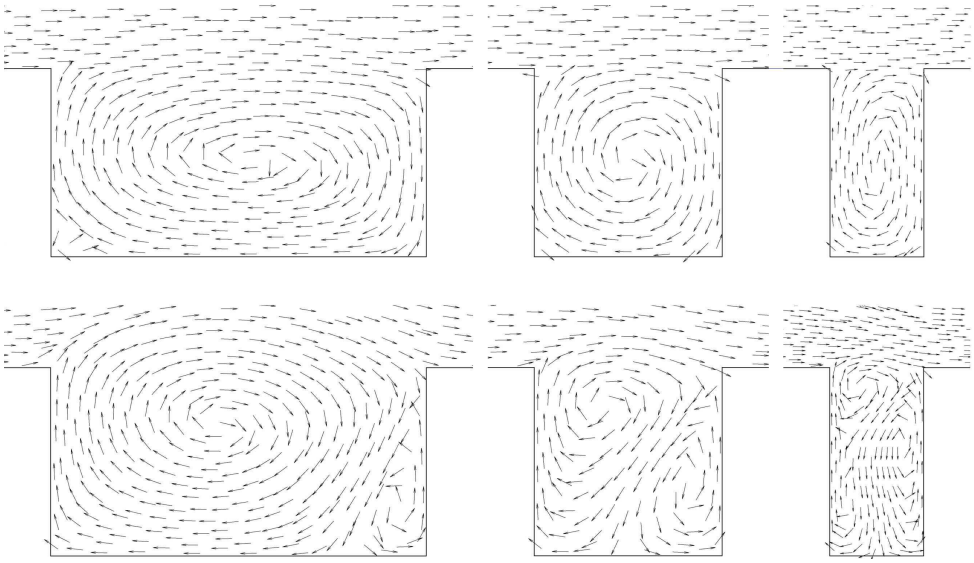

Figure 3.23: Flow fields neglecting buoyancy (top) and considering buoyancy (bottom) for aspect ratios of 0.5, 1 and 2 (left to right).

Buoyancy plays an important role in the natural and mixed convective flow regimes. The flow field in street canyons changes significantly due to buoyancy when having high surface temperatures and low wind speeds. These weather conditions are also the critical conditions for determining the building cooling demand and peak load and therefore it is important that the CHTC correlations are accurate for these conditions. In Figure 3.23 the vector flow fields obtained by CFD are shown for cases with and without buoyancy. Different aspect ratios are considered. Without buoyancy one main vortex in the centre

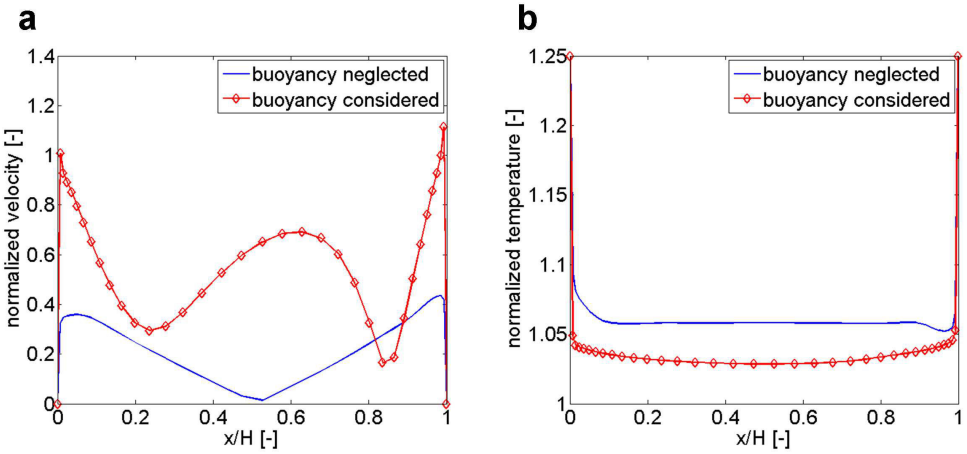

Figure 3.24: Velocity magnitude normalized by U_{10} (a) and temperature normalized by the inlet temperature (b) on the horizontal centreline in a street canyon with an aspect ratio of 2 , $U_{10} = 0.25\ m/s$, inlet temperature $20°C$ and wall and ground surface temperatures of 25 $°C$.

of the street canyon is formed. Some other small vortices in the corners of the cavity are formed. Due to the buoyancy, air rises at the heated building surfaces and two (or even more) counter rotating vortices can be formed or the vorticity can be increased in the buoyant case compared to the forced convection case. The same effects were also found with the wind tunnel tests that are discussed in section 4.2. With buoyancy, the air velocities (Figure 3.24a) and air temperatures (Figure 3.24b) at the building façades increase. As a result, the convective heat transfer and CHTCs increase in the buoyant case. It can be concluded, that buoyancy has to be taken into account for the determination of CHTC correlations when the temperature differences between air and surface is high and the wind speed low.

3.2.4.4 CHTC correlations

For the CHTC calculations the reference temperature in Equation 3.9 is defined as the temperature of the incoming air at the inlet. Surface averaged CHTCs are determined for windward and leeward façade. In Figure 3.25, the CHTC versus wind speed is shown for the 7 different geometries. Figures 3.25a-b show the results with buoyancy and Figures 3.25c-d without buoyancy. The CHTC values for the leeward façade are in general smaller than the values for the windward façade (note the lower scale in ordinate axis for leeward wall), due to lower air speeds at leeward surfaces. The CHTC increases nonlinearly with the wind speed. When buoyancy is not considered, the CHTCs decrease to zero for low wind speeds, while for buoyancy they level off to a constant value. The heat flux becomes constant for low wind speeds, because the flow inside the street canyon is mainly driven by buoyancy and not by the flow above the street canyon anymore. It can be concluded that buoyancy has to be considered for weather conditions with high surface temperatures and low wind speeds.

Different CHTC correlations are found for different geometries. First the CHTCs for the

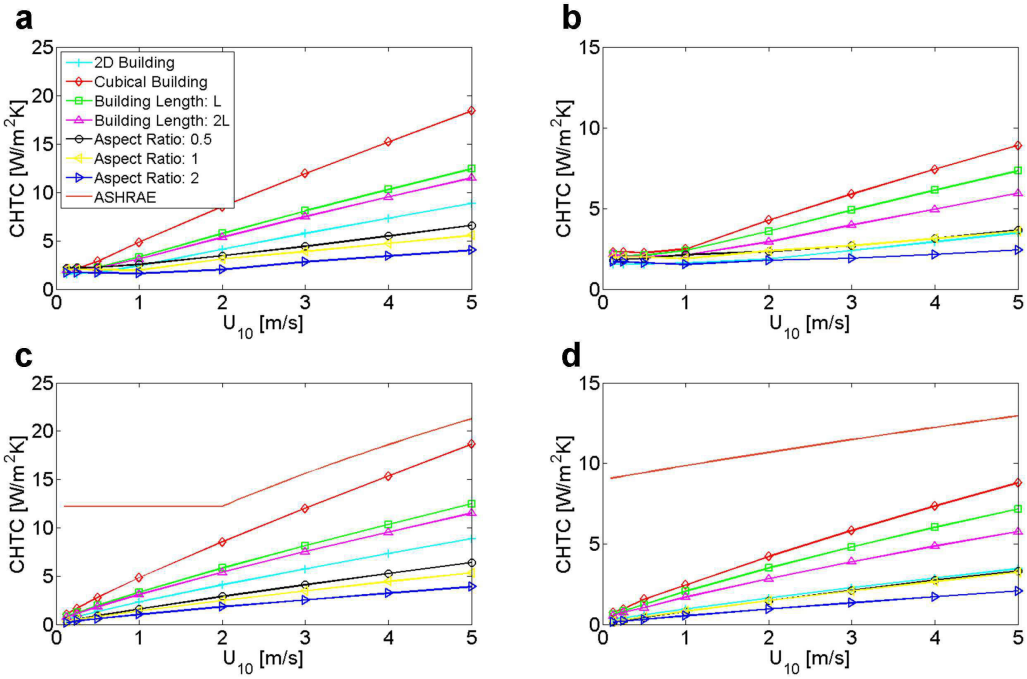

Figure 3.25: CHTC versus wind speed with a temperature of 30 $°C$ for the heated surfaces: (a) windward wall with buoyancy; (b) leeward wall with buoyancy; (c) windward wall without buoyancy; (d) leeward wall without buoyancy.

windward walls are considered. The CHTCs of stand-alone buildings are higher than the CHTCs in street canyons. The CHTCs for stand-alone buildings decrease with increasing building length starting from the cubic building towards the infinite long building. Reason is that the highest air speeds and consequently CHTCs are found for the cubical building showing an acceleration of the 3D flow around the building. With increasing building length the air speeds and CHTCs further decrease. The sensitivity of the CHTC to the wind speed, represented by the slope of the correlation, is found also to depend on the building geometry. The slope of the CHTC correlation decreases with increasing building length. The CHTCs at the windward wall in the street canyon are lower compared to the infinite long stand-alone building. This decrease is due to the wind sheltering caused by the neighbouring building. The CHTCs are lower for higher aspect ratio H/W, due to the increased wind sheltering effect in narrower street canyons.

Considering the CHTCs at the leeward wall they follow the same trend as found for the windward walls. However, the CHTCs for the wider street canyons (aspect ratios 0.5 and 1) are higher than for the infinite long stand-alone building. This observation can be explained by the existence of a vortex in the street canyon, which increases the air speed at the leeward wall compared to the leeward wall in the wake of a standalone building.

The CHTC correlations derived in this study are compared to the correlations from ASHRAE [164] in Figures 3.25c-d. The correlations from ASHRAE are commonly used for BESs and are based on measurements by Ito et al. 1972 [122]. The CHTCs determined for urban geometries studied in this section are in general much lower than the ASHRAE

correlations. Only for the windward wall of the cubical building do the ASHRAE values approximate the here established CHTC values, whereas for the leeward wall of all urban geometries the values are significantly lower, while the slope is higher.

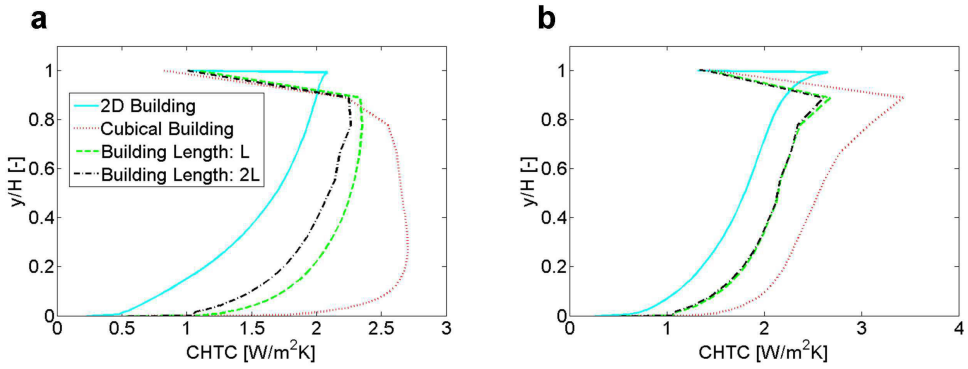

Figure 3.26: CHTC profiles on the vertical centreline of the leeward (a) and windward (b) walls of the 4 studied stand-alone buildings (simulations with 0.5 m/s and heated surface temperatures of 30 $°C$).

Profiles of the CHTCs along the vertical centreline of the leeward and windward walls are given in Figure 3.26a and 3.26b respectively for different stand-alone buildings. The profiles for these buildings are similar and the values are decreasing with increasing building length.

In Figure 3.27a the CHTC correlations for a street canyon with an aspect ratio of 1 are shown for different façade and ground surface temperatures. With increasing surface temperatures the buoyancy effect on CHTC at low wind speeds becomes more pronounced. CHTCs are higher and become function of both air speed and temperature difference between the surface and air in the street canyon. The CHTCs for wind speeds lower than 1 m/s are almost identical for leeward and windward façade, because the flow, which is mainly driven by buoyancy, is almost equal at these two façades. For higher wind speeds the CHTC correlations for the different temperature differences collapse onto one curve, because the influence of buoyancy on the flow field becomes negligible.

In Figure 3.27b the CHTC values for low wind speeds (box in Figure 3.27a) are given as a function of the temperature difference between the wall and ground surfaces and the air temperature. The CHTC values are increasing in a similar way for all geometries. Theoretically, the air speed and the CHTCs at the walls should increase linearly with the temperatures difference between the surfaces in the street canyon and the air temperature. This is because the buoyancy forces are a linear function of the air density and the air density is modelled with the Boussinesq approximation, where the air density is a linear function of the air temperature. In Figure 3.27b the increase is not linear, since the air temperature in the street canyon increases less rapidly than the façade surface temperatures. Therefore the buoyancy forces, and consequently the air speed and CHTC values, are increasing nonlinearly.

From these CFD results it becomes clear that the geometry and the temperature difference between surface and ambient air temperatures are important parameters determining

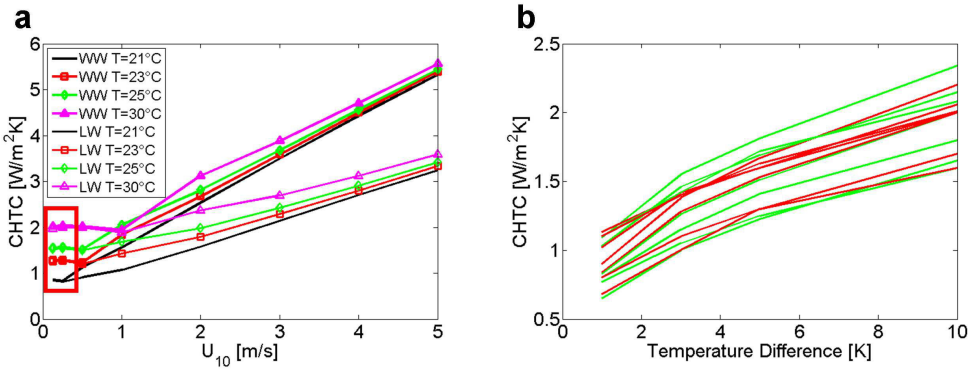

Figure 3.27: (a) CHTC versus wind speed for windward (WW) and leeward (LW) walls with different wall and ground surface temperatures for a street canyon with an aspect ratio of 1. (b) CHTC for low wind speeds (red box in Figure 3.27a) versus temperature difference between air and surfaces temperatures for all 7 geometries: windward (red) and leeward (green) walls.

the CHTC correlations. In the chapter 5 the CHTC correlations are used for BESs. For this purpose, the CHTC correlations are approximated by the following functions: (i) a constant value for wind speeds below 1 m/s (determined as the average CHTC in this low speed region); and (ii) with a power-law function for wind speeds above 1 m/s.

For all geometries it was assumed that the wind direction is normal to the buildings and street canyons. In reality the wind directions are oblique most of the time. To study the error that is introduced by assuming normal wind directions, CFD simulations for a 3D street canyon with an aspect ratio of 1 are conducted for 3 different wind directions and the CHTC correlations are compared with the correlations from the 2D simulations presented above. The following angles between the street canyon axis and the wind direction were chosen: 0 °, 45 ° and 90 °. The magnitude of the wind velocity was for all cases the same, only the wind direction was changed. The CHTC correlations for the windward and leeward walls are given in Figure 3.28. For wind directions parallel to the street canyon axis (0 °), it cannot be distinguished between windward and leeward wall. The heat transfer at both walls are the same for the here simplified symmetric geometry. Therefore the correlations in Figure 3.28 are the same for both walls.

It can also be observed that for high wind speeds the CHTCs are very similar for the different wind directions for both windward and leeward walls. The CHTC correlations for 0° correspond to the CHTC correlations at the windward wall for the other wind directions. The CHTCs in a street canyon with parallel flows are higher than for the leeward walls for cases with oblique flows. For low wind speeds buoyancy gets important. The threshold velocity, below which buoyancy starts to have an impact on the convective heat transfer, is not for all wind directions the same. Therefore some deviation of the CHTC correlations for the different wind directions can be observed. For wind speeds, where buoyancy is important, the CHTCs are again very similar for the different wind directions.

With these results it can be concluded that the error introduced by only using normal wind directions is rather low. The convective heat transfer is especially important for

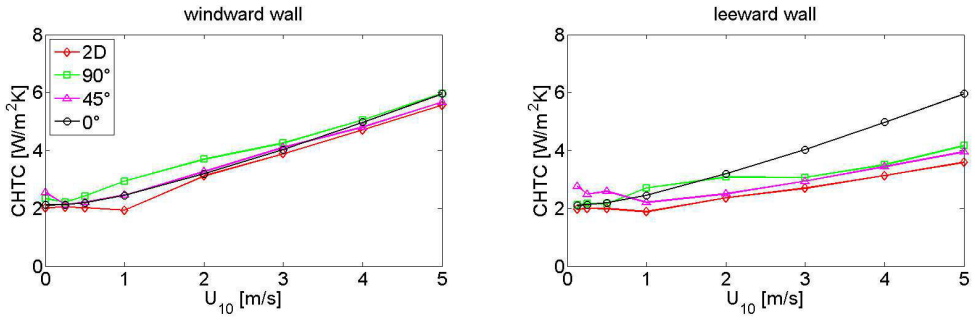

Figure 3.28: CHTC versus wind speed with a temperature of 30 °C for the heated surfaces for a 2D and a 3D street canyon (aspect ratio: 1) with different wind direction (90 °: wind normal to the street axis, 0 °: wind parallel to the street axis).

weather conditions with very high or low wind speeds and those are the ranges of wind speeds, where the CHTCs are not very sensitive to the wind directions. For low wind speeds the convective heat transfer predictions are important, because those are weather conditions with high cooling loads. And for high wind speeds it is important, because there is a strong influence of the convective heat transfer on the overall thermal behaviour of the building.

3.2.4.5 Conclusion

CHTC correlations for 7 different building geometries, ranging from a stand-alone cubical building to an infinite long narrow street canyon, were derived for windward and leeward walls. For all cases, the wind direction was normal to the buildings and street canyons. For all geometries, CHTC correlations for non-buoyant flows and for buoyant flows with different temperature differences between buildings façades and air temperatures were established. It was found that the CHTC values are decreasing from a cubical to an elongated to a building in a street canyon. Further it was found that buoyancy is important for low wind speeds especially for elongated buildings and buildings in urban street canyons. Thus CHTC correlations need not only to be a function of the wind speed, but also a function of the temperature difference between the building façades and the ambient air temperature. The convective heat transfer in urban areas is generally lower than in rural areas. Additionally a sensitivity study was conducted to investigate the effect of the wind direction of the CHTC correlation for a street canyon with an aspect ratio of 1. It was found that the influence of the wind direction is rather limited. Therefore using CHTC correlations that were established for normal wind directions to the building, does not induce large errors in BESs for space cooling demand predictions.

3.3 Summary

In this chapter the numerical models used within this thesis were presented. The UHI effect is modelled based on measurements. To study the behaviour of the building and the radiative fluxes, BESs are conducted. The convective heat transfer at the building

façades are modelled with CFD. The CFD simulations are either conducted in advance and CHTC correlations are used for the BESs or the BES model is coupled with CFD. Especially for the coupled simulations, WFs have to be used in CFD to save computational time. Therefore existing WFs were adjusted to improve the convective heat transfer predictions.

4 Experimental study and validation

The CFD models presented in the previous chapter need to be validated especially for buoyant flows, because buoyancy plays an important role in full scale street canyons. Therefore in this chapter wind tunnel measurements for a street canyon with heated surfaces are presented together with a validation study, where the measured flow fields are used for a comparison with CFD. In a first part the measurement method and the wind tunnel are described. Then the results of the wind tunnel measurements are presented and in a last part the measured flow fields are compared with CFD simulations.

4.1 ETH/Empa atmospheric boundary layer wind tunnel

The wind tunnel measurements of this thesis were conducted in the ETH/Empa atmospheric boundary layer wind tunnel localized at Empa in Dübendorf (Switzerland). The wind tunnel can be run in open and closed loop configurations. For the open loop configuration outdoor air is used for the measurements. The wind tunnel itself is built in an air-conditioned room. The air temperature inside the wind tunnel cannot be controlled. A sketch of the wind tunnel is given in Figure 4.1.

In closed loop configuration the wind tunnel has a length of 26.0 m. The flow is driven by an electric fan consisting of 8 blades. The diameter of the fan is 1.8 m. The motor of the fan has a nominal power of 110 kW and is water cooled. The speed of the fan is 25 - 1000 RPM, what results in wind speeds of $0.5 - 25$ m/s in the test section. The fan casing is mounted on silencer elements and is connected to the wind tunnel construction by flexible strips to minimize the vibrations of the wind tunnel construction. The air flows in anticlockwise direction inside the wind tunnel (looking from the top of the wind tunnel). At the four corners of the wind tunnel, turning vanes are installed to guide the flow around the corners. The turning vanes are adjustable to allow for flow optimization. The cross-section at the corners is 2.2 x 2.85 m^2. In front of the settling chamber the cross section is increased in the diffuser to 3.8 x 3.8 m^2 and therefore the wind speed is decreased. The settling chamber contains several screens (mesh size: 5.0 mm) and a honeycomb panel (tube diameter: 7.0 mm) to ensure low turbulence levels in the approach flow. In the contraction section after the settling chamber the cross section is reduced to 1.9 x 1.3 m^2 and the flow is accelerated. The following atmospheric boundary layer (ABL) development section has a length of 7.8 m and a width of 1.9 m. The height of this section is adjustable between 1.3 m and 1.6 m to allow for streamwise pressure gradient control. The ABL development section has glazed walls and a glazed roof and the walls can be opened at both sides of the wind tunnel. To create a boundary layer, spires can be installed and the roughness of the floor can be increased by using different arrangements of e.g. Lego bricks. The test section is located just after the ABL development section

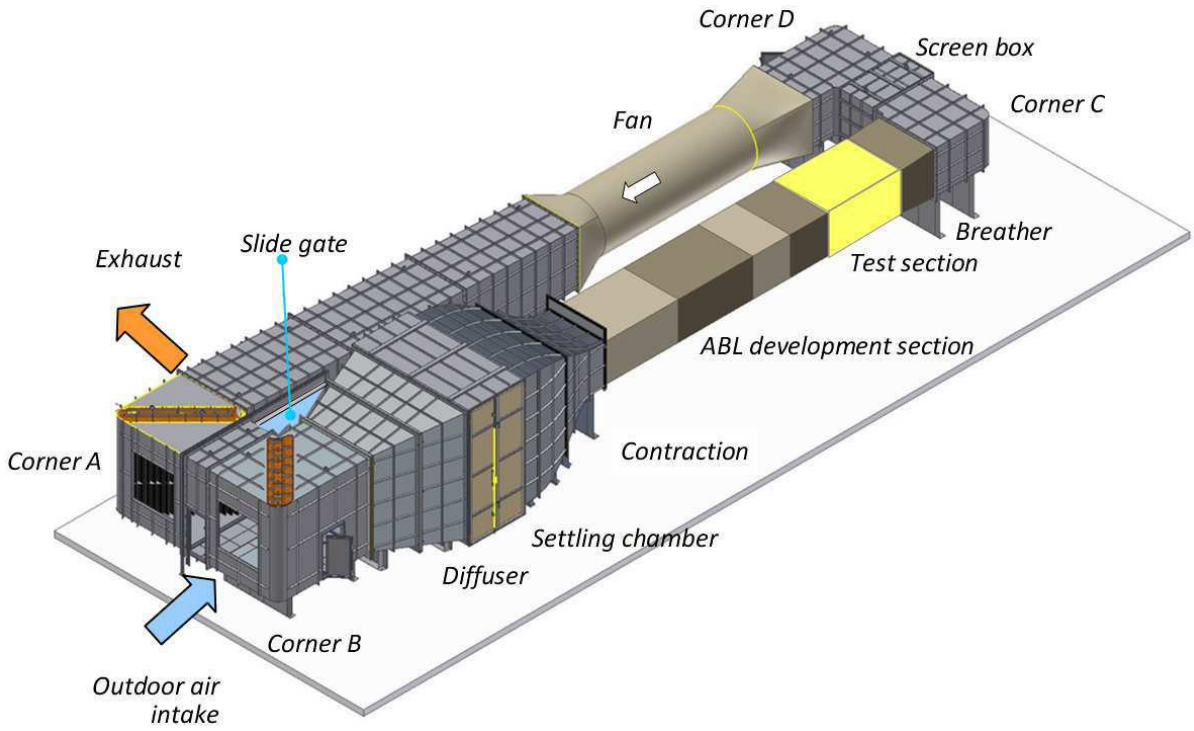

Figure 4.1: Sketch of the ETH/Empa atmospheric boundary layer wind tunnel.

and has a length of 2.6 m. It has also an adjustable roof and a therefore a cross section of 1.9 x 1.3 − 1.6 m^2. The walls and the roof are glazed to be able to guide a laser light sheet from the top of the wind tunnel into the wind tunnel and to record flow fields with high speed cameras from outside the wind tunnel. The test section is equipped with a time-resolved stereoscopic PIV (particle image velocimetry) measurement system (measurement technique is described in section 2.4.1.7). For the illumination of the flow field a Nd:YLF laser with a wavelength of 527 nm, a maximal pulse energy at 1 kHz of 30 $mJ/pulse$ and a maximal frequency of 10 kHz is installed on the top of the wind tunnel. Using different lenses (sheet optics) different sizes of laser light sheets can be generated. Two high speed cameras with a maximal resolution of 2016 x 2016 pixels and a maximal recording frequency of 4 kHz are installed. Therefore with this system all 3 components of the instantaneous flow field can be measured in a 2D plane. The two cameras and the light sheet optics are mounted on a three-axis translation stage to be able to measure at different positions inside the test section. For post-processing DaVis, implemented by LaVision GmbH, is used. A particle generator with 5 Laskin nozzles is used to produce DEHS (Di-Ethyl-Hexyl-Sebacat) particles with a diameter of about 1 μm. To run the wind tunnel in an open loop configuration, the slide gate between the corner A and corner B (Figure 4.1) can be closed and there is an air intake at corner B and an exhaust in front of corner A. The open loop configuration can either be used for measurements or to rinse the wind tunnel to remove the DEHS particles or to decrease the air temperature inside the wind tunnel.

4.2 Wind tunnel measurements: heated street canyon

4.2.1 Background

In street canyons buoyancy plays a very important role. During the day the building façades are heated by solar radiation. The heated walls induce buoyancy, what significantly affects the flow field in street canyons (e.g. [7, 160]). For a hot summer day with calm winds and high façade temperatures buoyancy has an important impact on the convective heat fluxes at the building façades and thus on the removal of heat from the building and from the street canyon. Some experimental studies have been conducted to analyse buoyant flow fields inside street canyons. Kovar-Panskus et al. 2002 [7] investigated the flow field in a street canyon by means of wind tunnel measurements. Maximum windward wall temperatures of 120 $°C$ were used in combination with wind speeds of $0.5 - 1\ m/s$ (Froude numbers: 0.27-2.03; see Equation 4.2 for the definition of the Froude number). Kovar-Panskus et al. 2002 [7] found only a very weak secondary vortex that was induced by buoyancy close to the ground of the canyon. Liu et al. 2003 [165] conducted water tank measurements of flows inside a non-symmetrical street canyon with bottom heating. Instantaneous flow field measured with PIV were analysed. The study indicated that the bottom heating can strengthen the intensity of the main vortex in the centre of the street canyon and that the flow was completely driven by buoyancy for low ambient wind speeds. Garbero et al. 2011 [8] performed wind tunnel measurements of street canyons with different aspect ratios and heated windward and leeward walls (Froude number: about 60). Only for the narrow street canyon with windward wall heating they found a significant influence of buoyancy on the vortex structure. Uehara et al. 2000 [162] conducted experiments in a wind tunnel with thermal stratification. The vortices in the street canyons were weaker for stable than for unstable stratifications. For cases with very stable stratification the wind speeds inside the street canyons almost dropped to zero. Field measurements have been carried out by Louka et al. 2002 [63] in a street canyon in Nantes (France). The flow field was visualized with non-buoyant balloons. They observed a strong upwards motion close to those walls which were heated by the sun. In contrast to the CFD simulation predictions, the effects of buoyancy were only present in a thin layer close to the walls. Besides the experimental studies, also a number of CFD studies of buoyant flows in urban street canyons can be found in literature (e.g. [54, 160]), showing mostly a stronger effect of buoyancy when compared to the experiments. Several wind tunnel studies of flows in street canyons under isothermal conditions have been conducted and reported in literature (e.g. [56–60]). For wind directions normal to the street canyon axis one main vortex in the centre of a street canyon and small corner vortices are formed. The wind velocity magnitudes inside the street canyon are strongly decreased compared to the freestream velocities.

The aim of the experimental study is to investigate by PIV the influence of wall and ground heating on the flow field inside a street canyon. To characterise the flow field a method to track the centres of the vortices inside the street canyon for different freestream velocities and surface temperatures is proposed in this chapter of the thesis. The dimensions of the street canyon were chosen to be similar to the dimension of the model used by Kovar-Panskus et al. 2002 [7] for their experiments. Compared to the study by Kovar-

Panskus et al. 2002 [7] not only the windward wall but also the leeward wall and the ground are heated and higher surface temperatures are applied. Compared to the other experimental studies on buoyant flows in street canyons mentioned above, the actual experimental set up allows for a wider range of configurations (windward wall, leeward wall and ground heating and all surface heated) and related flow fields and has the advantage that all flow fields are measured under the same conditions in the same wind tunnel. Further a PIV measurement system with a high spatial resolution is used. Therefore the measured flow fields are better resolved compared to the other experimental studies found in literature, allowing to also resolve smaller flow structures (e.g. corner vortices). A second purpose of this experimental study is to provide detailed data of flow fields that can be used for validations of CFD simulations (see section 4.3).

4.2.2 Similarity criteria

Because scaled street canyon models have to be used in the wind tunnel, some criteria have to be fulfilled to achieve a similar flow field compared to a full-scale street canyon with a similar geometry. A first similarity criterion is the Reynolds number:

$$Re = \frac{U_{FS} H}{\nu} \tag{4.1}$$

where U_{FS} is the freestream velocity and H is the street canyon height.

Due to the high scaling factors, it is not possible to reach the same Re in the wind tunnel as can be found in full-scale. However for flows around bluff bodies this is not required, the Re has to exceed a critical Re to guarantee Reynolds independent flow. Different values for the critical Re are proposed in literature for flows in atmospheric boundary layers (e.g. [162, 166–169]). For the scaled street canyon studied here, the critical Re is about 13000 (see section 4.2.4.2), while the flow fields studied have Re between 9000 and 30700 (using the kinematic viscosity at a temperature of $23°C$).

To characterise the flow in terms of buoyancy the Froude number is used in this study:

$$Fr = \frac{U_{FS}^2}{gH\frac{T_w - T_{ref}}{T_{ref}}} \tag{4.2}$$

where T_{ref} a reference temperature (here the temperature of the freestream).
Here the Froude number was used instead of the Richardson number for better comparison with the results from literature. The Fr is the inverse of the Ri that is used in the CFD part of this thesis. Small Fr correspond to buoyant flows and high Fr to forced convective flows. To be in a similar range of Fr in the wind tunnel compared to full-scale, very high surface temperatures would be needed. In wind tunnels, full Reynolds similarity cannot be realized for highly scaled building models. However, it was measured in the Reynolds independent turbulent flow regime, which is above the critical Re, where the model scale becomes unimportant. In this Reynolds independent region, it can be assumed that the flow structure is similar also for higher full-scale wind speeds. Because in the wind tunnel the Re are much lower than in full-scale it, is not possible to relate the wind speed in

the wind tunnel to a realistic full-scale wind speed. As an example, for a scaling factor of 100 and the highest freestream wind tunnel velocity used in this study (2.32 m/s), Re similarity would correspond to a very low full-scale wind speed of 0.0232 m/s. Due to the missing relation between the wind tunnel wind speed and a realistic full-scale wind speed, it is also not possible for Fr similarity to relate the temperature difference in the wind tunnel to a temperature difference at full-scale. Different combinations of wind speeds and surface to air temperature differences could lead to the specific Fr used in this study. In this experimental study the lowest Fr number is 0.65. Assuming a full-scale building height of 20 m and a wind speed of 1 m/s this Fr is achieved with a temperature difference 2.33 K at the wall.

4.2.3 Experimental setup

This study is conducted in the ETHZ/Empa atmospheric boundary layer wind tunnel described in section 4.1. To model the flow in an urban street canyon a W x H x L (W: width; H: height; L: length) of 0.2 x 0.2 x 1.8 m cavity is constructed in the wind tunnel (Figure 4.2). The flow direction is normal to the axis of the cavity. The aspect ratio H/W is 1 and the spanwise aspect ratio L/W is 9. According to [7], the highest degree of flow two-dimensionality in a section of the street canyon is achieved in their wind tunnel for a spanwise aspect ratio of 8.8. Moonen et al. 2011 [170] showed that boundary effects are negligible for street canyon geometries with spanwise aspect ratios > 10.

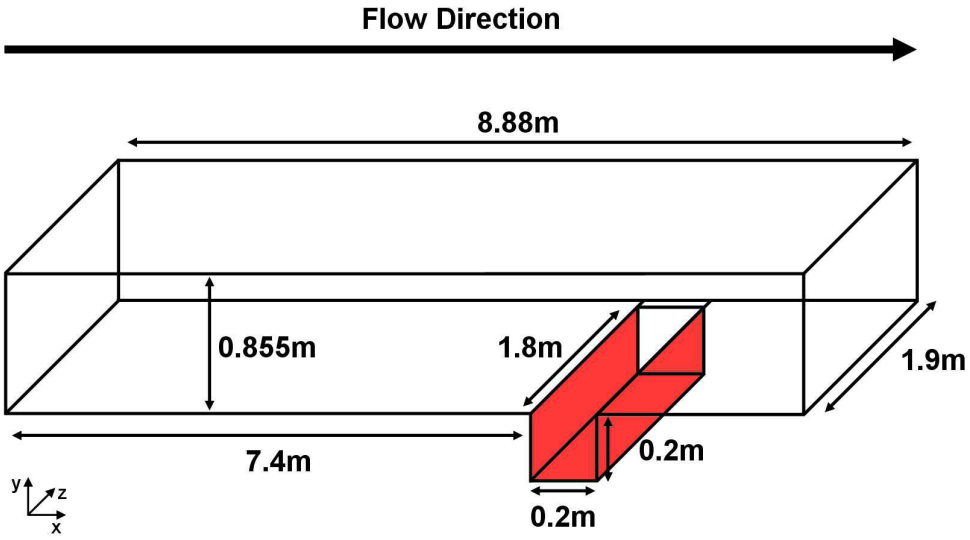

Figure 4.2: Dimensions of the wind tunnel model.

For the measurements the wind tunnel floor and the street canyon surfaces are made out of aluminium plates, thus forming a low roughness surface. With such low roughness, low-Reynolds number modelling can be applied for the validation study in section 4.3.

Heating mats with an output power of 1680 W each are attached at the back of each aluminium plate forming the street canyon to increase the surface temperatures. Due to the high thermal conductivity of aluminium, the temperature is almost uniform over the

whole heated surface. The surface temperatures are kept constant with PID controllers monitoring the surface temperatures with T-type thermocouples. Because no cooling system for non-heated surfaces is installed in the wind tunnel tests, some heating up of other surfaces due to conduction, convection and radiation cannot be avoided, but this heating effect remains limited to some degrees.

The flow field in a cross-section of the street canyon is measured with particle image velocimetry (PIV). The images are acquired with a CMOS 12 bit dual frame camera with a spatial resolution of 2016 x 2016 pixels (with a pixel size of 0.1 x 0.1 mm^2). For the illumination of the DEHS (Di-Ethyl-Hexyl-Sebacat) particles a dual cavity Nd:YLF laser is used. The size of the field of view is 19.8 x 19.8 cm^2, what is slightly smaller than the dimensions of the street canyon. The flow very close to the surfaces cannot be measured, due to laser light reflections on the surfaces, with intensities that could damage the camera sensor. These reflections are brighter than the illuminated particles and therefore no flow field can be computed in these areas.

Best practice guidelines for PIV [171–173] are taken into account to minimise the errors of the measurements. The sampling rate is estimated from the integral time-scale and is chosen to be 4 Hz to acquire statistically independent samples. To measure at least 10 rotations of the slowest vortices, 300 double frame images at 4 Hz are recorded what corresponds to a sampling time of 75 s. The separation time between the two frames is 780 μs, what is the maximum separation time that could be acquired for the used camera. The vector fields are computed by means of a standard cross-correlation function via FFT employing multigrid analysis with two refinement steps with a refinement ratio of 2 and a final interrogation window size of 32 x 32 pixels with 50 % overlapping. From the instantaneous vector fields the averaged velocities (V_{AVG}) and the root mean square velocities (V_{RMS}) are determined as follows:

$$V_{AVG} = \frac{1}{n}\sum_{i=1}^{n} V_i \tag{4.3}$$

$$V_{RMS} = \sqrt{1/\left(n-1\right)\sum_{i=1}^{n}\left(V_i - V_{AVG}\right)^2} \tag{4.4}$$

where n is the number of samples.
For the turbulent kinetic energies (k) the fluctuation of all three velocity components need to be accounted for. With PIV (unless a stereoscopic or volumetric configuration is used) only the velocity components in the plane are measured and therefore the root means square velocity V_{RMS} is only a function of these two velocity components. To account also for the out of plane component, it is assumed that this third velocity component behaves like the other two and therefore the fluctuations are similar to the fluctuations of the other two components.

$$k = \frac{1}{2}V_{RMS}^2 + \frac{1}{4}V_{RMS}^2 = \frac{3}{4}V_{RMS}^2 \tag{4.5}$$

To study the repeatability of the measurements, the measurements are repeated three

times (on different days). The results of the velocities and turbulent kinetic energies (TKE) on the horizontal and vertical centrelines of the street canyon are used for the repeatability analysis. As a criterion for the repeatability the standard deviation divided by the freestream values is used. For the velocities this value is everywhere below 1 %. For the TKE it is almost everywhere below 3 % with some extreme values of $5 - 10$ %. Therefore it can be concluded that the measurements are repeatable.

To measure the air temperatures inside the street canyon T-type thermocouples are used. The temperatures are measured for 2 min to determine the time averaged temperatures. The measurements are conducted on an equidistant grid of 10 x 10 measurement points, where the first measurement points are located at a distance of $1cm$ from the street canyon walls (the width of the street canyon is 20 cm). The uncertainty of the temperature measurements is $\pm 3\ ^{\circ}C$ originating from the radiation exchange between the thermocouple and the heated walls. The uncertainty is estimated by measuring air temperatures with different types of radiation shielding. The temperatures are not measured at the same time as the flow fields. Therefore the temperature measurements are not influenced by the PIV system and vice versa.

Table 4.1 gives the different surface temperatures and freestream velocities at which the measurements are conducted, together with the corresponding Reynolds and Froude numbers.

	70 $^{\circ}C$	90 $^{\circ}C$	110 $^{\circ}C$	130 $^{\circ}C$
$0.68m/s$ $(Re = 9000)$	1.49	1.04	0.80	0.65
$1.07m/s$ $(Re = 14200)$	3.68	2.58	1.99	1.62
$1.45m/s$ $(Re = 19200)$	6.75	4.74	3.65	2.97
$1.86m/s$ $(Re = 24600)$	11.11	7.79	6.00	4.88
$2.32m/s$ $(Re = 30700)$	17.29	12.13	9.34	7.59

Table 4.1: Surface temperatures and freestream velocities with corresponding Reynolds and Froude numbers.

The flow direction is normal to the street canyon axis, and the inflow temperature is 23 $^{\circ}C$. The inflow temperature is monitored. The heating-up of the air inside the wind tunnel is less than 1 $^{\circ}C$ during the measurements. The heating-up is slow due to the large air volume and the heavy metal construction of the wind tunnel. In addition, the wind tunnel is located in a room with air conditioning and could be flushed to maintain a constant air temperature. Due to the low roughness of the aluminium plates the boundary layer at the surfaces is rather thin and does therefore not correspond to a specific scaled atmospheric boundary layer. The approach flow boundary layer velocity and TKE profiles are measured at the centre position of the street canyon, before the street canyon is installed. Values are given in Figure 4.3 (normalized by the freestream velocity and the square of the freestream velocity). Thus these profiles are not the inlet profiles, but the developed profiles at the location of the street canyon, without the street canyon being present. A Reynolds independency can be observed for the velocity, but the TKEs are not totally Reynolds number independent. Thus some decay of the TKE might still occur.

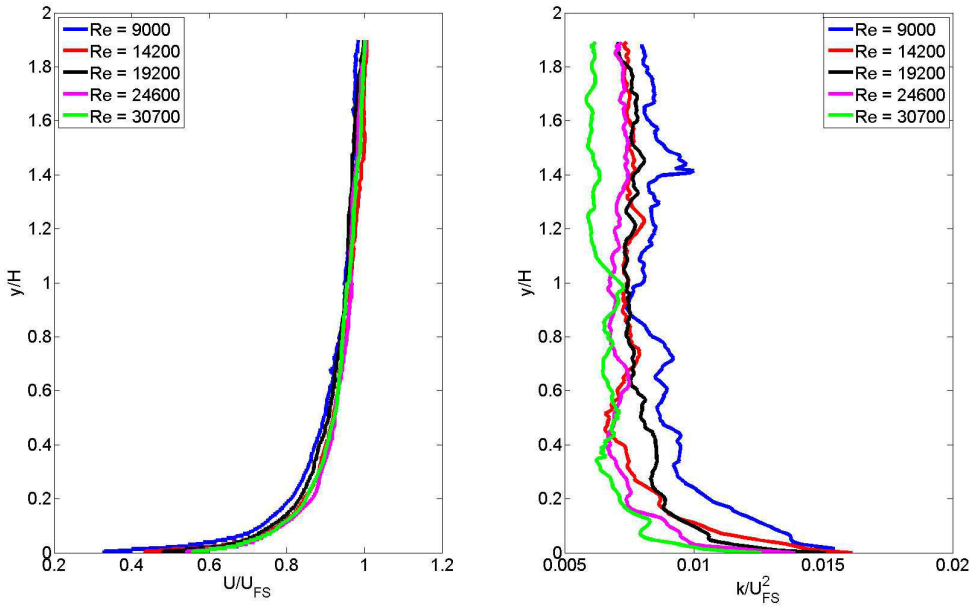

Figure 4.3: Time averaged boundary layer velocities normalised by the freestream velocity (left) and the TKE (k) normalised by the square of the freestream velocity (right).

4.2.4 Results

In this section the results of the wind tunnel measurements are given. For all results presented in this section the surface temperatures of the heated surfaces are 130°C, if not otherwise indicated.

4.2.4.1 Streamlines

To give first an overview for all studied cases with surface temperatures of 130 °C the streamlines are given in Figure 4.4 for three different Reynolds numbers. For most cases one main vortex in the centre and two small vortices in the lower corners of the street canyon are formed. Only for the cases with windward wall heating and low Reynolds numbers two counter rotating vortices of similar size can be found. Globally, buoyancy introduces three different changes in the flow field. The first change is an increase of the velocity magnitude, which can be observed at low Reynolds numbers for all cases expect for windward wall heating. The second change is a relocation of the centre of the main vortex. This is mainly observed for ground heating and for the case, where all surfaces are heated. The third change is a complete rearrangement of the vortex structures, observed for the case with windward wall heating. For all considered cases the changes are more pronounced at low Reynolds numbers (mixed convective flow regime) than at high Reynolds numbers (forced convective flow regime).

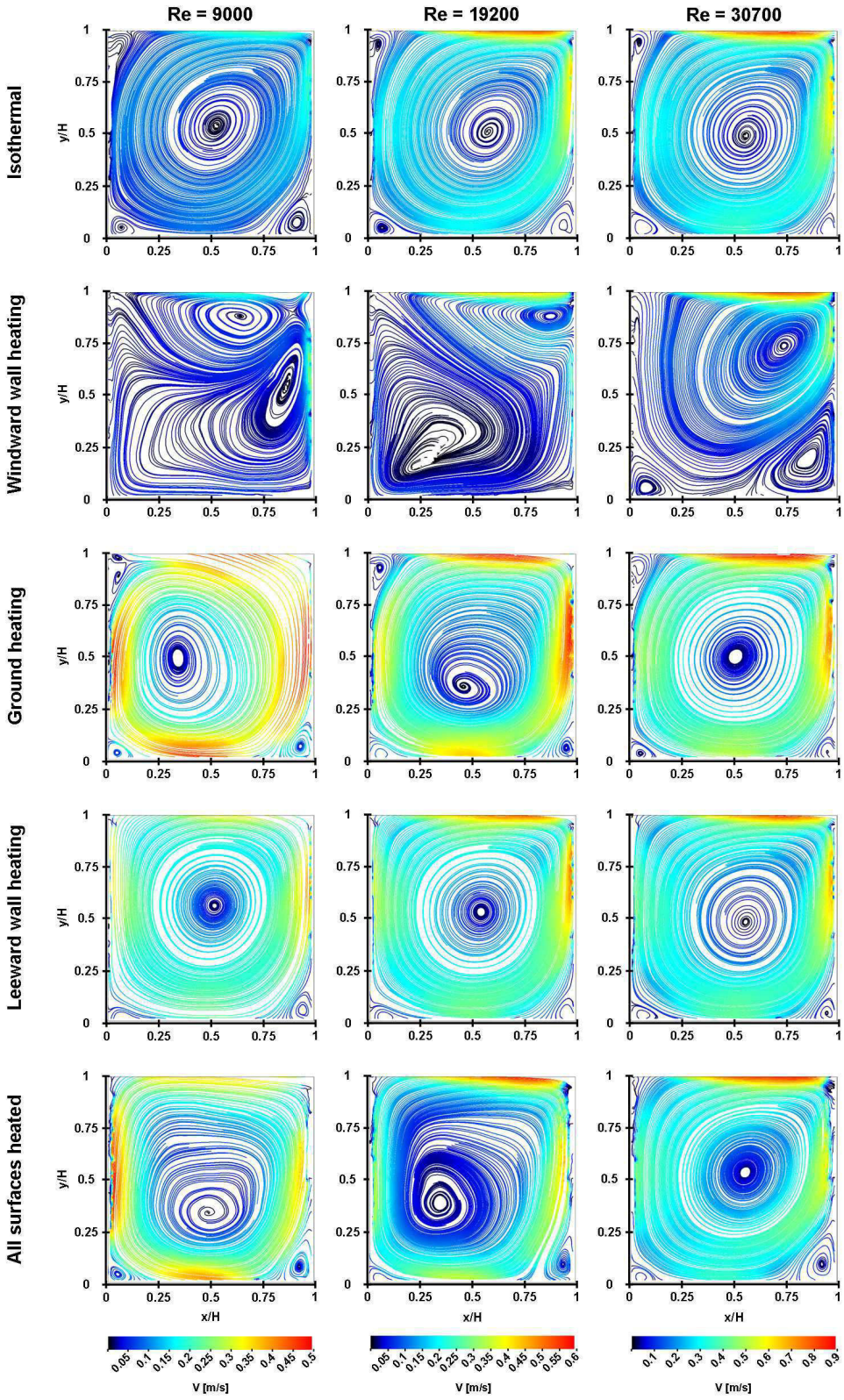

Figure 4.4: Streamlines for various configurations of heated surfaces and for three different Reynolds numbers.

4.2.4.2 Isothermal case

For the isothermal street canyon cases studied in this chapter, the normalised velocity and TKE profiles on the horizontal and vertical centrelines of the street canyon are given in Figure 4.5. The velocities are significantly lower inside the street canyon than in the freestream. The velocities are almost a linear function of x and y position. This is typical for a rotational vortex (see also Figure 4.4). The highest TKEs can be observed in the shear layer ($y/H = 1$). The second highest TKEs can be found close to the windward wall, where the air of the freestream enters the street canyon from above and hits the windward wall. The profiles are very similar for most Reynolds numbers. Only the results for the lowest Reynolds number deviate slightly from the other results. Therefore it can be concluded that for the setup used in this study the flow is Reynolds independent for Reynolds numbers above about 13000 ($U_{FS} = 1\ m/s$).

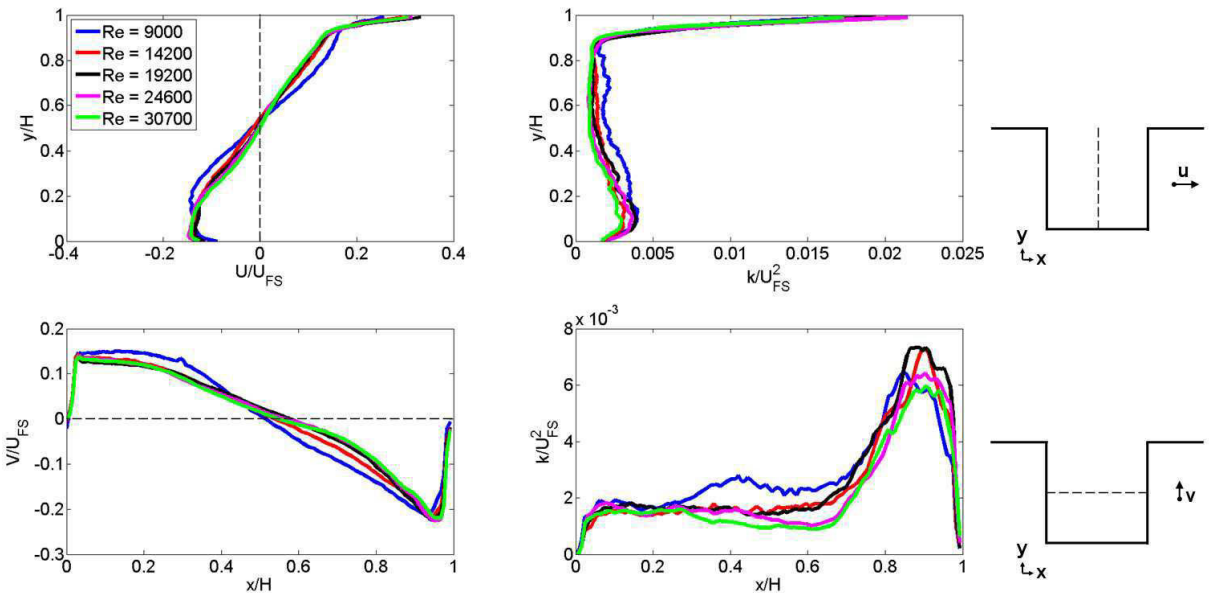

Figure 4.5: Normalised velocity (left) and TKE (right) profiles on the horizontal and vertical centrelines of the street canyon.

Figures 4.6 and 4.7 show the contour plots of the normalised velocities (by the freestream velocity) and TKEs (normalized by the square of the freestream velocity) inside the street canyon for the isothermal and heated cases at three Reynolds numbers. For the isothermal case the contour plots are very similar for the three presented Reynolds numbers. This confirms the conclusion that the flow is in a Reynolds independent regime. The velocities increase with increasing distance from the centre of the street canyon and then decrease again close to the walls. The highest velocities and TKEs can be found at the windward wall and in the shear layer at the top of the street canyon. TKE is mainly produced at the top of the windward wall and is then transported by the vortex in clockwise direction.

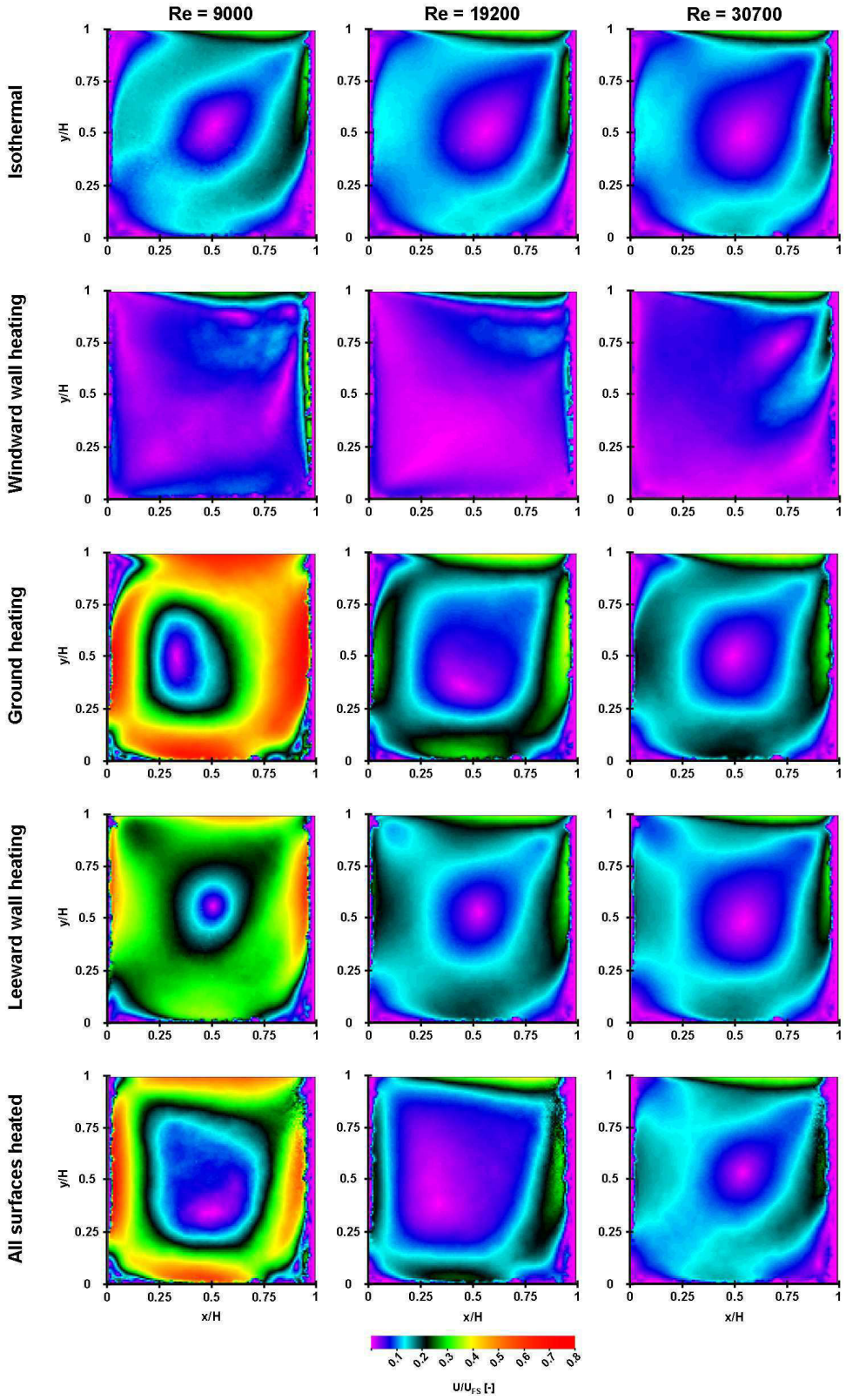

Figure 4.6: Contour plots of the normalised velocities inside the street canyon for various configurations of heated surfaces and for three different Reynolds numbers.

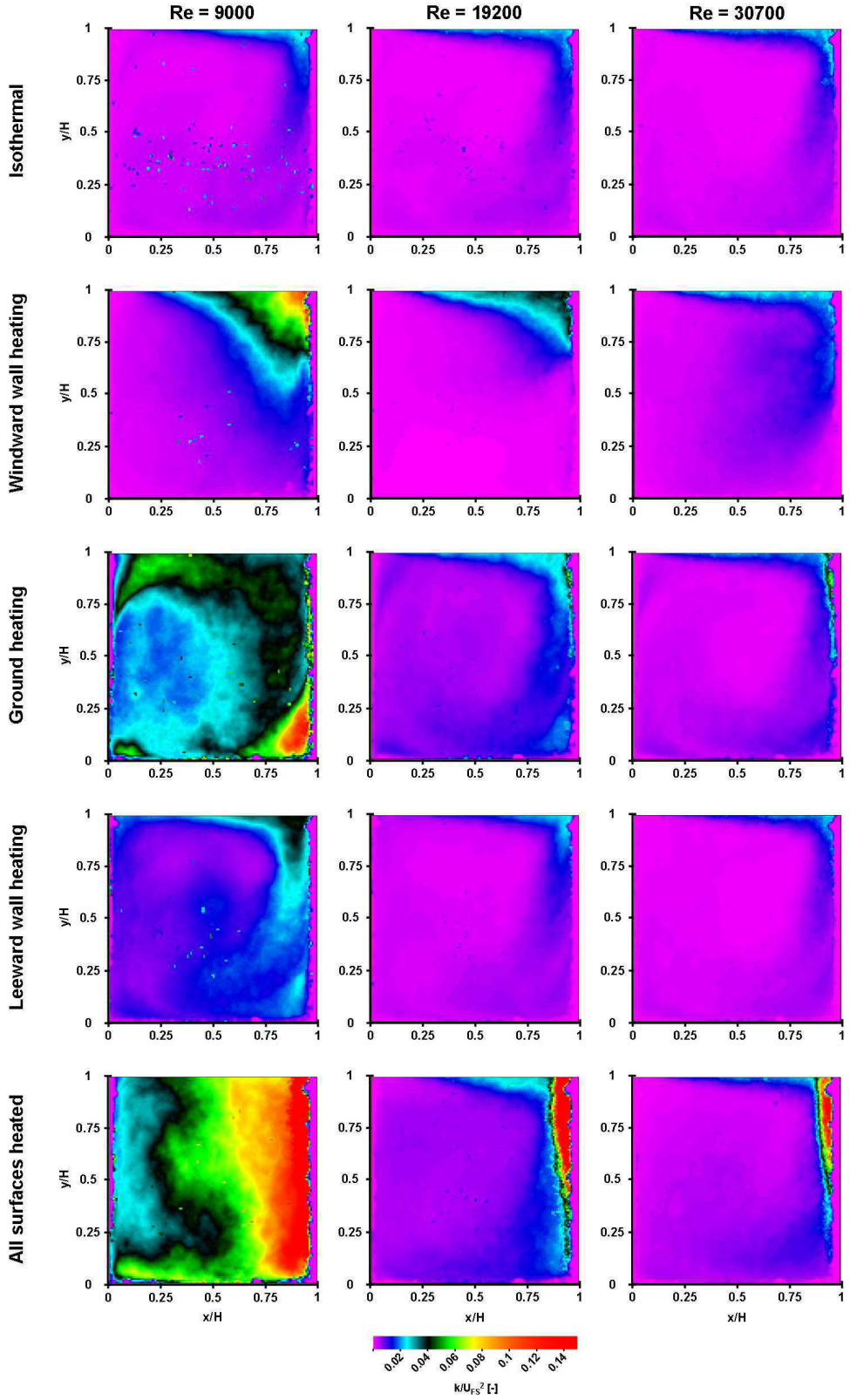

Figure 4.7: Contour plots of the normalised TKEs inside the street canyon for various configurations of heated surfaces and for three different Reynolds numbers.

4.2.4.3 Windward wall heating

For the cases with windward wall heating, buoyancy significantly changes the vortex structure. Streamlines for the five different Reynolds numbers are presented in Figure 4.8. Besides the main vortex a second counter rotating vortex is formed. This secondary vortex is located in the lower part of the street canyon and has a similar size as the main vortex at lower Reynolds numbers. For high Reynolds numbers (>24600) the size of the secondary vortex is decreased and at the highest Reynolds numbers (30700) the flow structure becomes similar to the vortex structure of the isothermal case. In Figure 4.9 the trajectories of the centre of the main and secondary vortex are given as a function of the Reynolds number for three different windward wall temperatures (trajectories for the other measured cases are similar). With increasing freestream velocities the centre of the main vortex is moving first horizontally from the top middle to the top right and then diagonally towards the centre of the street canyon, where also the centre of the vortex for the isothermal case is located. This behaviour is similar for all four windward wall temperatures. Simultaneously the centre of the secondary vortex is moving with increasing wind speed from the right side to the left and then downwards to the right bottom corner of the street canyon, where also a small corner vortex is situated in the isothermal case.

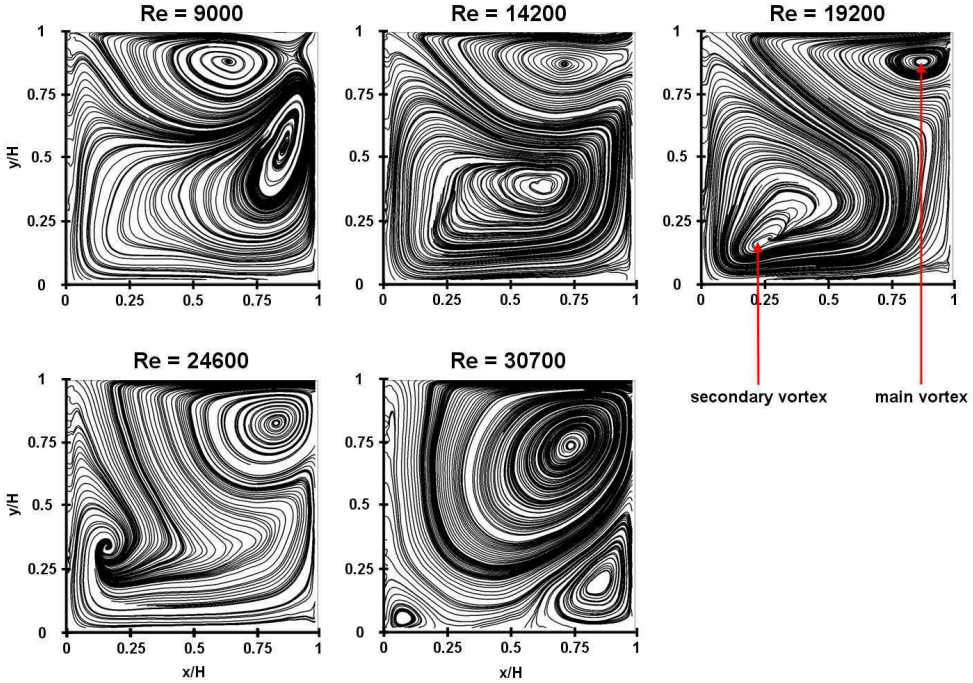

Figure 4.8: Streamlines for cases with windward wall heating and five different Reynolds numbers.

Due to the counter-rotating secondary vortex the velocities inside the street canyons are lower compared to the velocities for the isothermal case (Figure 4.6). With increasing Reynolds number, the normalised velocities do not change significantly. The TKEs however are for the two lower Reynolds numbers higher than for the isothermal case (Figure

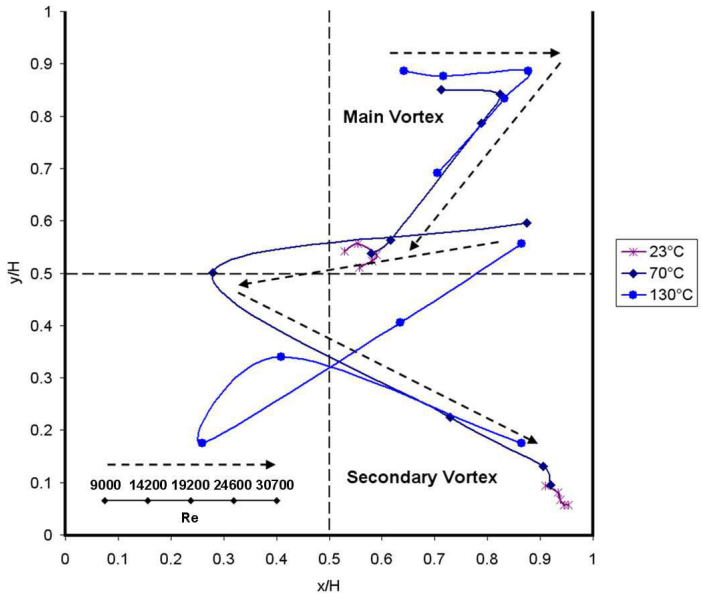

Figure 4.9: Trajectories of the centre of the main and secondary vortex as a function of the Reynolds number for three different windward wall temperatures.

4.7). The highest TKEs can be found at the top right corner of the street canyon. That is the position, where the cold air enters the street canyon and hits the air, which is rising due to buoyancy at the windward wall. The hitting of two opposite flows produces TKE. With increasing Reynolds numbers the flow evolves to a forced convective flow and therefore less TKE will be produced by buoyancy.

4.2.4.4 Ground heating

In the case of ground heating, the street canyon velocities increase strongly compared to the isothermal case (Figure 4.6). The increase of velocity is strongest for the lower Reynolds numbers. The velocity increase is much less for the two higher Reynolds number, but the velocities are still higher than for the isothermal case. The increase is caused by buoyancy which accelerates the flow especially at the leeward wall when the heated air starts to rise. The velocities are higher for this case than compared to leeward heating (see section 4.2.4.5), because in the ground heating case the air at the bottom of the leeward wall has already a high temperature, while for the latter case the air starts only to heat up when hitting the leeward wall. Comparing to all cases, ground heating results in the highest velocities inside the street canyon. There is also a strong increase of the TKE for the lowest Reynolds number (Figure 4.7). The highest TKEs can be found at the bottom corner of the windward wall, because in that corner buoyancy is acting against the main flow direction and therefore most TKE is produced.

Figure 4.10 shows the trajectory of the centre of the main vortex as a function of the ground temperature for four different Reynolds number. For low Reynolds number the main vortex is moving with increasing ground temperatures in clockwise direction around

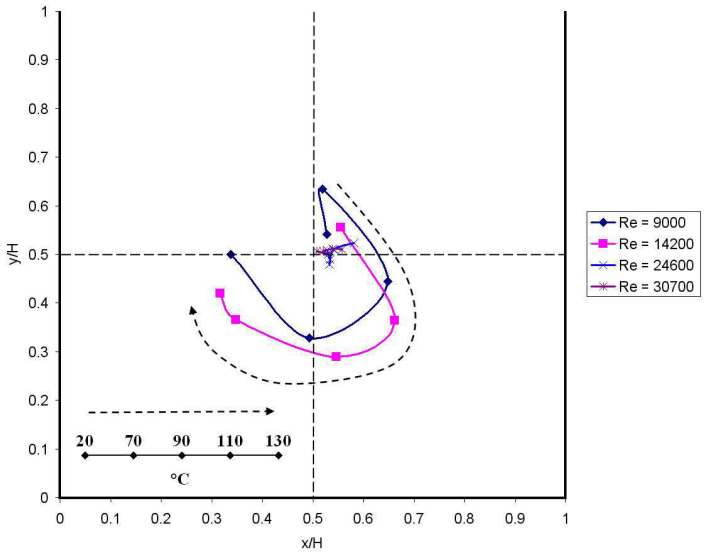

Figure 4.10: Trajectories of the centre of the main vortex as a function of the ground temperature for four different Reynolds numbers.

the centre of the street canyon. For high Reynolds number the main vortex remains at a fixed position for different ground temperatures (forced convection case).

4.2.4.5 Leeward wall heating

For leeward wall heating, the main vortex becomes also strengthened by the buoyancy effect (Figure 4.6), mainly for low Reynolds numbers. The velocities are however lower than for ground heating, because the residence time of the heated air inside the street canyon is shorter. Also the TKEs are increased but much less compared to the other cases with buoyancy, because buoyancy acts in the same direction as the main flow in the street canyon (Figure 4.7). Therefore the highest TKEs can be found at the top of the windward wall, where the air enters the street canyon.

In Figure 4.11 normalised velocity profiles are given on the vertical centreline of the street canyon for different Reynolds numbers and different leeward wall temperatures. At low Reynolds numbers a strong increase of the velocities with increasing leeward wall temperature can be observed. For a leeward wall temperature of 130 $°C$ the velocities inside the street canyon are more than doubled compared to the isothermal case. For high Reynolds numbers no strong dependency of the velocity profiles on temperature can be noticed, because the flow is in a forced convective flow regime.

4.2.4.6 All surfaces heated

In this case the main vortex is again strengthened by buoyancy for all Reynolds numbers (Figure 4.6). The velocities are lower than for the case of only ground heating, because from one side the flow is accelerated due to leeward wall and ground heating, but at the same time the velocities are decreased by windward wall heating inducing an opposite

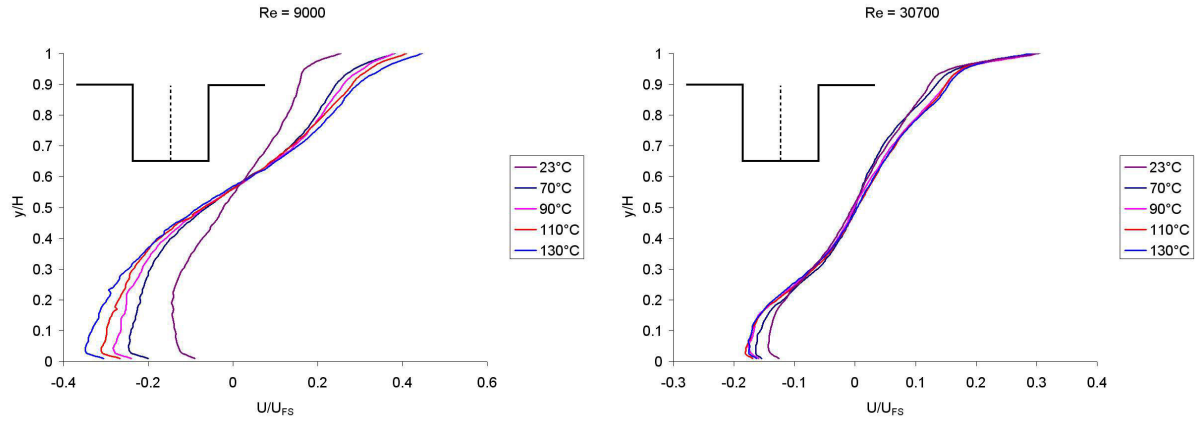

Figure 4.11: Normalised velocity profiles on the vertical centreline of the street canyon for different Reynolds numbers and different leeward wall temperatures.

flow. The highest velocities can be found close to the leeward wall, which is also explained by the observation above. For this heating case the highest TKEs of all studied cases can be observed, because of the opposite flows induced by the surface heating at different surfaces. In total also more heat is added, what causes stronger buoyancy effects (Figure 4.7). The highest TKE can be found again close to the windward wall, where buoyancy is acting against the main flow direction and therefore causes a high production of TKE.

In Figure 4.12 the trajectories of the centre of the main vortex are presented as a function of the surface temperature for five different freestream velocities. No clear trends can be observed. For high Reynolds numbers the centre of the vortices is located at similar positions as for the isothermal case, because the flow is in a forced convective regime. For low freestream velocities the flow gets strongly buoyant and the movement of the centre of the main vortex is less structured than for the other cases.

For the case with all surfaces heated the air exchange rate was also studied by analysing the vertical velocities at the top plane of the street canyon. The normalised vertical velocity profiles for different surface temperatures are given in Figure 4.13. The air exchange rate is defined as the absolute volume of air entering (or leaving the street canyon). It can be observed that the air exchange rate is strongly increased by buoyancy at low Reynolds numbers. At high Reynolds numbers the air exchange rate is not changed with increasing surface temperatures. It can be remarked that the (volume) flow rate out of the street canyon seems higher than the flow rate into the street canyon, which from a point of view of mass conservation is rather remarkable. This may be attributed to the density difference between the heated air leaving, and the colder air entering the street canyon. A second reason could be 3D flow effects, or flows out of plane of the cross section measured by PIV.

4.2.4.7 Air temperature measurements

For the case, where all surfaces are heated, the contour plots of the air temperature normalized by the surface temperatures are given for two different surface temperatures

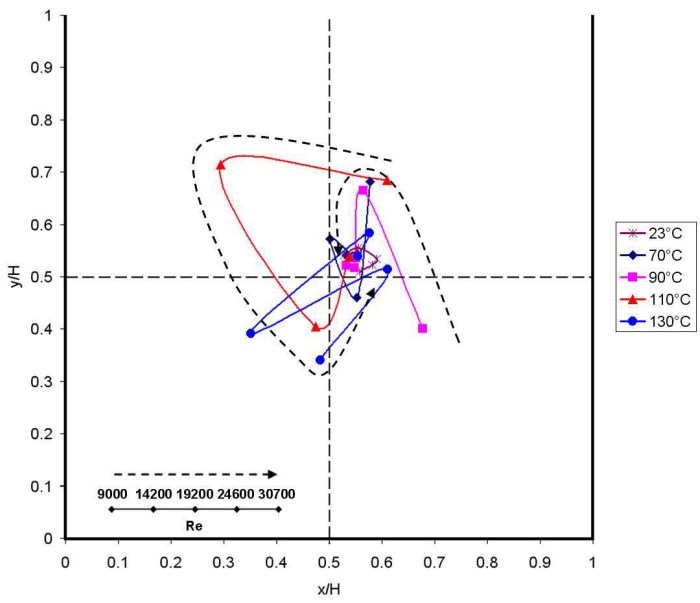

Figure 4.12: Trajectories of the centre of the main vortex as a function of the Reynolds number for five different surface temperatures.

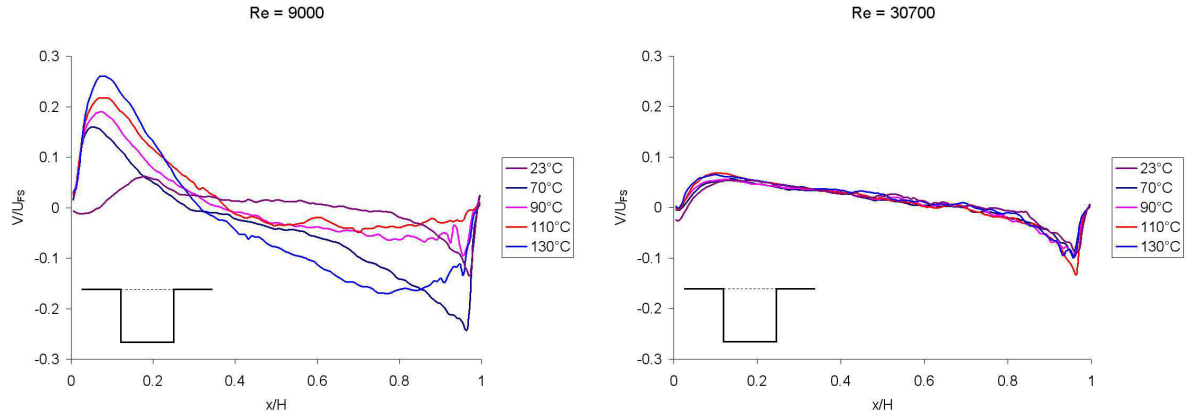

Figure 4.13: Normalised vertical velocity profiles at the top plane of the street canyon with different surface temperatures for two different Reynolds numbers.

and three different Reynolds numbers in Figure 4.14. For all cases it can be seen that the cold freestream air is entering the street canyon at the top of the windward wall. Further the vortex structure can be recognised in the temperature field. The highest temperatures are measured at the top of the leeward wall. With increasing Reynolds numbers the temperatures inside the street canyon are increasing, because the street canyon velocities and therefore also the heat fluxes from surface to air become higher. Generally the temperatures close to the heated walls are higher than in centre of the street canyon. Higher temperatures can also be found in the bottom corners, where small secondary vortices prevent the removal of heat. It can be remarked that for the case with surface temperatures of 130 $°C$ and a Reynolds number of 30700 a region of high temperatures is found at $x/H = 0.25$, no clear explanation is found. However this high temperature region is probably caused by the above mentioned 3D structure of the flow field. Another explanation could be that the inserted thermocouples influence the street canyon flow.

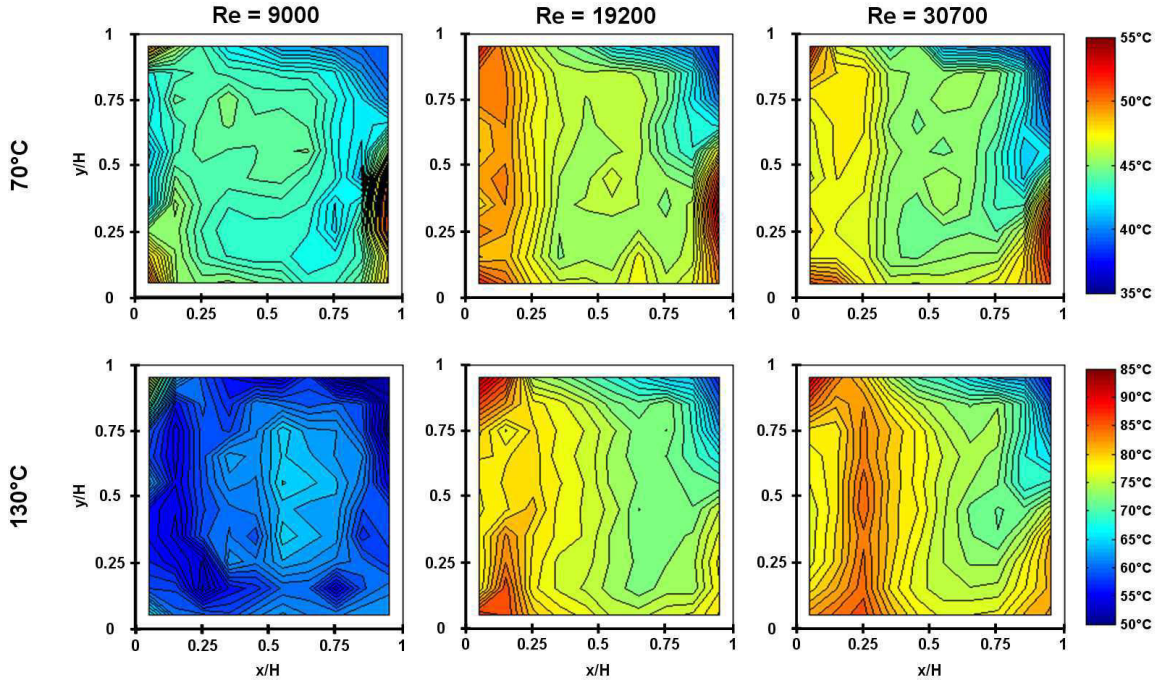

Figure 4.14: Contour plots of the air temperatures inside the street canyon for surface temperatures of 70$°C$ and 130$°C$ (all surfaces heated) and three different Reynolds numbers.

4.2.5 Discussion

Wind tunnel measurements were conducted for a cavity type street canyon. Instead of using a row of buildings, a cavity was chosen to represent an urban street canyon, because flow around this geometry can be better validated with CFD simulations (see section 4.3). For the same the reason boundary layer used for the approach flow did not represent a full-scale atmospheric boundary layer. To mimic solar irradiation, the surfaces of the

street canyon were heated to spatially uniform and constant in time surface temperatures. This is not a correct representation of the temperature distribution for real urban cases, where the sun irradiates (partly) surfaces of the street canyons. Using spatially constant temperatures has however the advantage that the surface temperatures can be better controlled and therefore the measurements are repeatable. It has to be mentioned that with the used PIV measurement technique the 3D flow effects could not be captured and therefore only 2D flow fields could be measured. The geometry of the street canyon was chosen in such a way that the flow has the highest possible two-dimensionality.

4.2.6 Conclusion

In this study the influence of buoyancy on the flow in urban street canyons was investigated by means of wind tunnel measurements. The measurements were conducted at different Reynolds numbers (9000 - 30700) and different leeward wall, windward wall and ground temperatures ($70 - 130\ ^{\circ}C$) to obtain flow fields within a wide range of Froude numbers (0.65-17.3). Significant changes of the flow fields for cases with high surface temperatures and low Reynolds numbers are found. For an isothermal street canyon a main vortex in the centre of the street canyon and two small vortices in the corner of the street canyon can be observed. When the windward wall is heated, a secondary counter-rotating vortex is formed for low Reynolds numbers. For all used surface temperatures a similar movement of the main and the secondary vortex with increasing Reynolds numbers is observed. For ground heating the main vortex is strongly strengthened. At low Reynolds numbers the centre of the main vortex changes its location in clockwise direction around the centre of the street canyon for increasing surface temperatures. With leeward wall heating the velocities inside the street canyon also increase but less compared to the case with ground heating. Reason is that in the case of ground heating the air is already heated, when it start to rise from the street canyon ground to the top and therefore buoyancy has more influence on the flow. For all cases the TKE is increased due to buoyancy, but the strongest increase can be found for the case, where all three surfaces are heated. The production of TKE is strongest for this case, because the most heat is added to the flow in this case. A second reason is that buoyancy at the windward wall is acting against the main flow direction and therefore the highest production of TKE can be found close to the windward wall. If all surfaces are heated, the main vortex is strengthened, but not as strongly as for the case with ground heating. The flow is accelerated close to the leeward wall and the ground, but slowed down close to the windward wall.

Temperature measurements for those cases show, how the cold air is entering the street canyon close to the windward wall and is heated up inside the street canyon. At low Reynolds numbers the air exchange rate of the street canyon strongly increases with increasing surface temperatures. This effect decreases strongly at higher Reynolds numbers, where the buoyancy effects are less present.

4.3 Validation

4.3.1 Background

Due to the complexity and large scale geometry of the built environment, CFD simulations are often conducted to predict the wind flow in urban areas [174]. CFD studies are e.g. used for wind comfort analysis, to access the human comfort at the pedestrian level around new buildings (e.g. [175–177]). Another research topic, where CFD is applied in urban areas, is pollution dispersion (e.g. [178–180]). In this thesis CFD is especially used to predict the convective heat transfer at building façades in urban areas (e.g. [74, 87]). To be able to rely on the CFD results, the simulations need to be validated. Because it is difficult to measure full-scale urban wind fields at a high enough resolution with controlled boundary conditions, often wind tunnel measurements are conducted for validation purposes. Today RANS simulations with a $k-\varepsilon$ turbulence model are still often applied for urban CFD simulations, due to its computational efficiency, although more advanced and more accurate CFD models exist. CFD simulations for flows in urban street canyons are not yet fully validated in literature. Especially for cases where buoyancy has an influence on the flow field, there is still a lack of validation. Buoyancy in urban street canyons originates from the increased façade temperatures due to absorbed longwave and solar radiation. Some validation studies have been conducted for flows in urban street canyons. Kovar-Panskus et al. 2002 [60] compared results of RANS CFD simulations with a standard $k-\varepsilon$ turbulence model with wind tunnel measurements for isothermal street canyons with different aspect ratios. They found a good agreement for the main flow structures, but the CFD simulations tended to underestimate the velocities inside the street canyon. The validation was based on visual comparison of streamlines and vector fields and on comparison of vertical velocity profiles inside the street canyon. Chan et al. 2002 [181] conducted CFD simulations (RANS with different $k-\varepsilon$ turbulence model) of pollutant dispersion in a 2D urban street canyon and validated their result with measurements of Meroney et al. 1996 [182]. The flow field was not validated, only the pollution concentrations were compared with the wind tunnel measurements. They found the best agreement, when using the RNG model compared to the standard and realizable $k-\varepsilon$ turbulence model. The RNG model is similar to the standard $k-\varepsilon$ model. It is based on a statistical technique and is more accurate for a wide range of flows. Further a number of validation studies have been conducted for street canyons with buoyancy. Memon et al. 2010 [183], Xie et al. 2006 [53] and Kim et al. 2001 and 2010 [184, 185] compared their CFD results with the measured data of Uehara et al. 2000 [162]. For the validation they used velocity and temperature profiles on the vertical centreline of the street canyon. On the centre line the profiles agree rather well for all studies, but a more detailed validation of the total flow field such as the exchange rate for street canyons is needed to be able to rely on the CFD simulations. Xie et al. 2007 [160] studied the pollution dispersion in a street canyon with bottom side heating. For validation purposes they compared the streamlines of the flow fields with the flow fields measured by Kovar-Panskus et al. 2002 [7]. They found that the position of the centre of the vortices agreed reasonably well. Another validation study using the results of Kovar-Panskus et al. 2002 [7] was conducted by Tablada et al. 2009 [186]. They conducted RANS simulations with a realizable $k-\varepsilon$ turbulence model

for a number of cases that were measured by Kovar-Panskus et al. 2002. Tablada et al. 2009 found an overestimation of the buoyancy effect by the CFD simulations. Garbero et al. 2011 [8] conducted a comparison study for a street canyon with windward and leeward wall heating. Due to the rather high freestream velocities there exists only one case, where buoyancy caused a significant change of the vortex structure. They found a qualitatively good agreement between the measurements and the simulations. A quantitative comparison was not possible, because their simulations were conducted for a full-scale street canyon, while the wind tunnel measurements were conducted with a scaled street canyon model. For a cube with leeward wall heating, Dimitrova et al. 2009 [187] found that CFD can be useful to predict the flow around a cube with leeward wall heating. Besides validation studies using wind tunnel measurements also studies with full-scale measurement were conducted. For example Assimakopoulos et al. 2006 [188] conducted such a study and found over- and underestimations for the CFD results compared to the measurements for the wind speeds for wind directions normal to the street canyon axis.

Although a number of validation studies have been conducted, there are still further investigations needed, especially for understanding the detailed flow structures of buoyant cases. Most studies found in literature are limited to a visual comparison or to a few profiles for a small number of cases. Therefore it is rather difficult to draw a general conclusion from the above reported studies. Here a more detailed validation study is conducted for a wider range of different flow fields. For the validation the measured flow fields, presented in section 4.2, are used. CFD simulations with different turbulence models and different near-wall treatments are conducted. The focus of this validation study is only on the flow field (velocities and turbulent kinetic energies). In this thesis CFD simulations are performed to predict the convective heat transfer at building façades. Therefore also the convective heat fluxes need to be validated. However, because in section 4.2 only the flow field was measured, the heat fluxes could not be validated. Therefore the validation study of this section is considered as a first step of a more complete validation. Correct results of the flow fields are a prerequisite to determine correct convective heat fluxes. In future in a second step, the heat fluxes itself need also to be validated.

4.3.2 Experimental data

For this validation study the buoyant flow fields in urban street canyons described in section 4.2 are used. For the isothermal cases and cases with leeward wall heating the centreline profiles of the velocities and TKE from CFD are compared with the measured results. A sketch of the centrelines is given in Figure 4.15. For the cases with windward wall heating, also the trajectories of the vortex centres are used for validation. For the cases where all surfaces are heated, in addition to the centreline profiles of the velocity and TKE, the temperature profiles and contour plots of the temperature are compared.

4.3.3 Numerical model

For this validation study 2D steady RANS CFD simulations using ANSYS Fluent 12.0 [116] are conducted. The standard and the realizable $k-\varepsilon$ models are used to model turbulence. At the near-wall regions the boundary layers are either resolved with low-

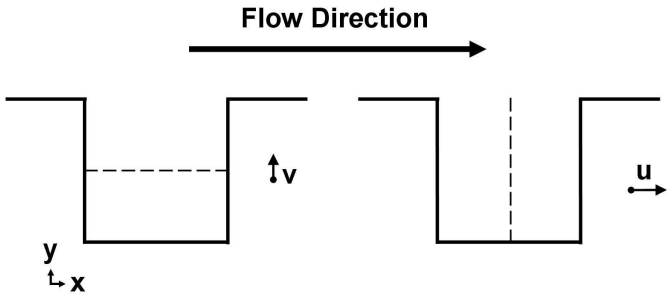

Figure 4.15: Sketch of the street canyon centrelines.

Reynolds number modelling (LRNM) or modelled with wall functions (WFs). These models are chosen for this validation study, because the same models are used for the full-scale studies in this thesis to predict the convective heat transfer coefficients.

The dimensions of the 2D computational domain are set according to the wind tunnel dimensions (Figure 4.16). The height H of the street canyon is 0.2 m. The grid is built based on a grid sensitivity analysis and on guidelines of Franke et al. 2007 [140]. The 2D grid consists of 5500 cells. It is refined towards the walls and has maximum y^+ values of 4.5. The same mesh is used for simulations with LRNM and for simulations with WFs. Therefore the y^+ values are too low for the simulations with WFs, the consequences of this selection are discussed in the following sections. A mesh with high enough y^+ values for WFs cannot be used, because the mesh would be too coarse (width of first cell: > 1 cm; street canyon width 20 cm) to resolve the global flow structures.

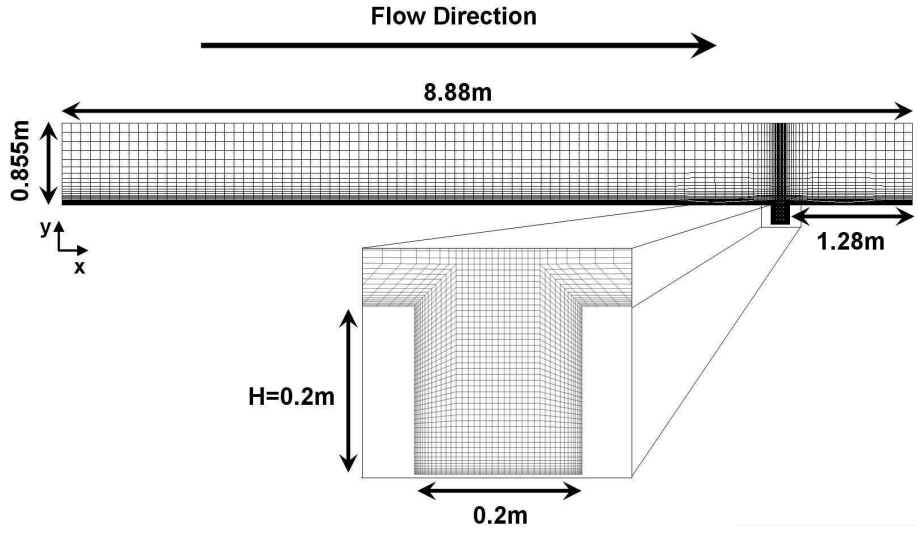

Figure 4.16: Computational domain.

At the inlet the measured boundary layer profiles for the velocity and TKE, presented in section 4.2.3, are imposed. Note that the boundary layer profiles were not measured at the beginning of the wind tunnel test section, but at the position of the centre of the street canyon, before the street canyon was installed. For the CFD simulations it is assumed that the boundary layers are fully developed and that these profiles can be used at the

inlet of the computational domain. This could lead to errors, if the profiles further develop upstream of the street canyon in CFD, or the measured profiles were not fully developed. In these cases the approach flow profiles are not the same in CFD and in the wind tunnel and therefore also the flow in the street canyon is different. The incoming air temperature is 23 $°C$, as is the air temperature measured at the inlet of the test section. All surfaces are modelled without roughness, because no roughness can be defined with LRNM. This may be justified since the wind tunnel model was made out of aluminium with a very low surface roughness. For the surfaces inside the street canyon, the surface temperatures obtained from the experiments are used as a temperature boundary conditions and it is assumed that the surface temperatures are uniformly distributed over the surfaces. The surfaces outside the street canyon are modelled adiabatic. Symmetry boundary conditions are imposed at the top boundary and outflow boundary conditions at the outlet.

To account for buoyancy the density, the specific heat, the thermal conductivity and the viscosity are approximated with polynomial functions as a function of the temperature in the Navier-Stokes equations. For all simulations the PRESTO! spatial discretization scheme is used for the pressure interpolation and second order spatial discretization schemes are used for the convection of the governing equations. Radiation is not considered directly in the CFD simulations, since constant temperature boundary conditions are imposed on the street canyon surfaces.

4.3.4 Results

4.3.4.1 Approach flow

In order to achieve a good agreement between CFD and measured flow fields inside the street canyon, also the approach flow in CFD has to match the measured approach flow profiles. In Figure 4.17 the approach flow profiles of the wind tunnel measurements and the CFD simulations at $x = 7\ m$ (0.4 m upstream of the street canyon) are given for the case with a freestream velocity of 1.45 m/s using different turbulence models and different near-wall treatments. In general the results are very similar for the two turbulence models. First the simulations are conducted with LRNM. With LRNM the boundary layer is resolved (see section 3.2.2). For both turbulence models there is a good agreement of the velocity profile using LRNM compared with the measured data. The TKEs are for both turbulence models too low. The TKE is decaying in streamwise direction in the CFD simulations. To avoid this decay in another set of simulations, shear stresses at the surfaces in front and behind the street canyon are predefined together with TKE sources in the flow in front and behind the street canyon. With this method the streamwise change of the approach flow profiles of the TKE can be decreased (dashed line). The higher TKEs have an impact on the velocity profiles. The velocities in the near-wall regions decrease and become too low, while in the freestream they are too high. In addition simulations using WFs are conducted. For the fine mesh used in this study, the first grid points are in the viscous sublayer. The flow quantities in the first grid point can be modelled with the law-of-the-wall used in the WFs. In contrast to the LRNM modelling, the damping of TKE in the viscous sublayer and the buffer layer cannot be captured. Due to this fact it is not recommended to use WFs for fine meshes. In this

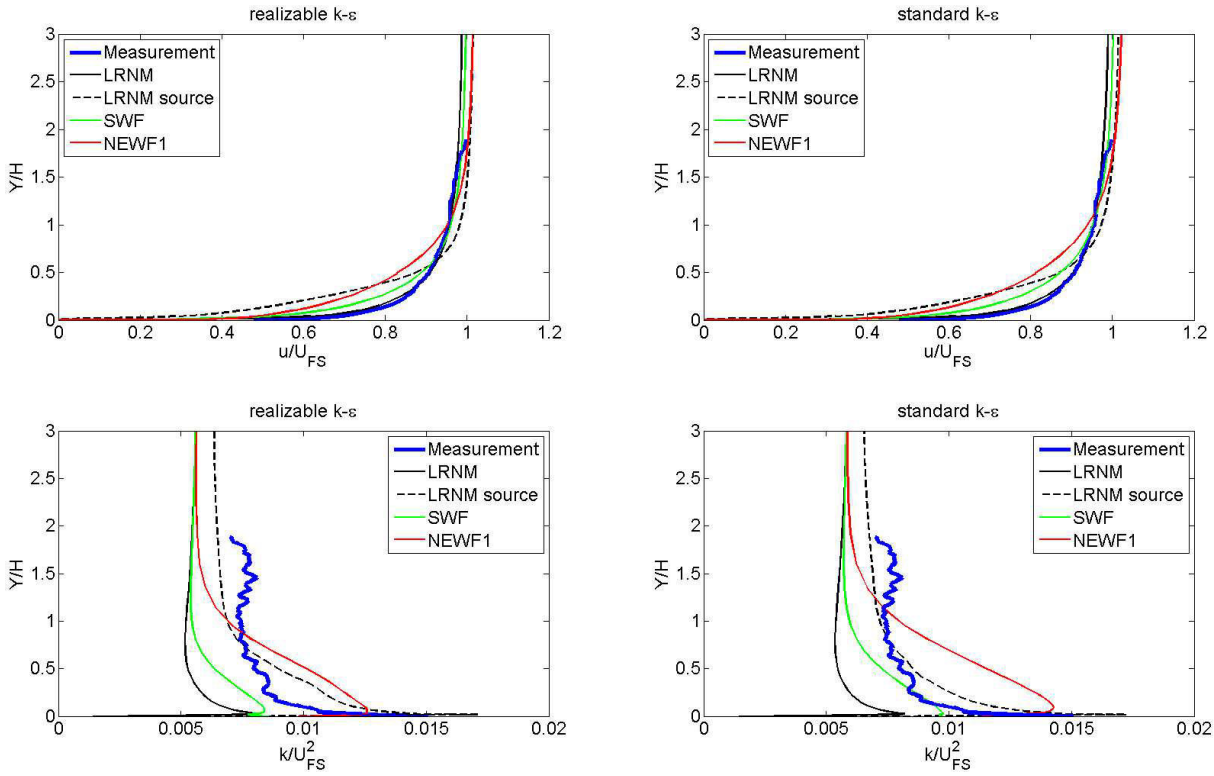

Figure 4.17: Normalised approach flow profiles of the velocity and TKE. Wind tunnel measurements and CFD simulations for the case with a freestream velocity of 1.45 m/s using two different turbulence models and different near-wall modelling approaches (LRNM: Low-Reynolds number modelling; LRNM source: LRNM with source terms for k and predefined shear stresses at the surfaces in front and behind the street canyon; NEWF1: non-equilibrium wall functions; SWF: standard wall functions).

thesis WFs are used nevertheless, since the aim was to investigate if the results can be improved using WFs. Two types of WFs are used for the validation: the standard wall functions (SWFs) and the non-equilibrium wall functions (NEWF1s) [189] (note that the NEWF1s used here for the velocity are not the same as the presented temperature WF in section 3.2.2.5). The NEWF1s can partly account for the non-equilibrium effects that are neglected in the SWFs. Therefore the NEWF1 can improve the results for complex flows involving separation, reattachment and impingement. Using the SWFs the results for the velocity profiles are slightly worse than for LRNM. The TKEs are slightly higher but still much lower compared to the measurements. As with LRNM with source terms for the TKE, the NEWF1s underestimate the velocities in the near-wall regions and overestimates the velocities in the freestream. With NEWF1s the peak of the TKE close to the ground can be captured, but the boundary layer is a thicker than in to the measurements.

Studying the approach flow profiles, it can be concluded that, with the models employed in this work, it is not possible to adjust both velocity and TKE profiles of the approach flow such that they match the measured profiles. For all simulations either the velocities

or the TKEs in the near-wall regions are underestimated. Further the standard and realizable $k - \varepsilon$ models give similar results for the approach flow.

4.3.4.2 Isothermal case

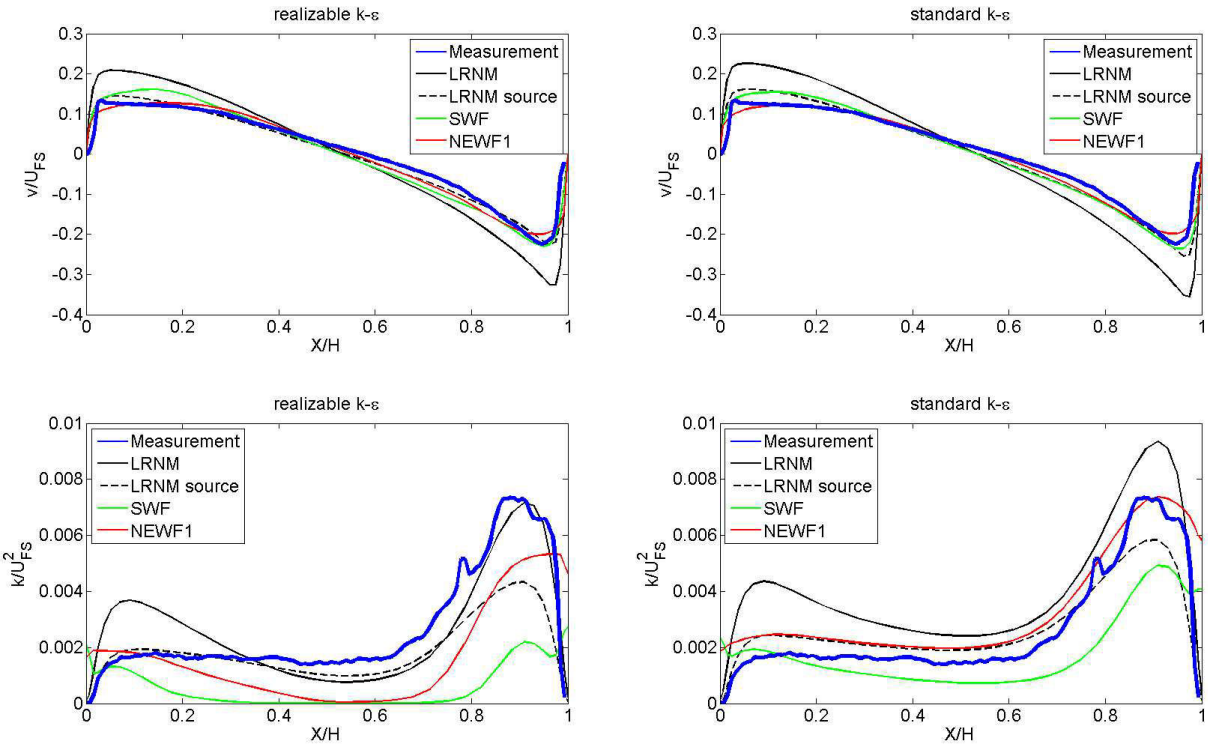

Figure 4.18: Normalised centreline profiles of the vertical velocity and TKE. Wind tunnel measurements and CFD simulations for the case with a freestream velocity of 1.45 m/s using two different turbulence models and different near-wall modelling approaches (LRNM: Low-Reynolds number modelling; LRNM source: LRNM with source terms for k and predefined shear stresses at the surfaces in front and behind the street canyon; NEWF1: non-equilibrium wall functions; SWF: standard wall functions).

For the isothermal cases the energy equation is not solved. Therefore constant values for the air properties are used instead of approximations as a function of the temperature. In Figure 4.18 the normalised horizontal centreline profiles of the velocity and TKE are given for different turbulence models and different near-wall treatments for the case of a freestream velocity of 1.45 m/s. The velocity profiles show that all models predict the vortex in the centre of the street canyon. The results of the two used turbulence models are very similar for the velocity profiles. The standard $k - \varepsilon$ model predicts slightly higher TKEs inside the street canyon than the realizable $k - \varepsilon$ model. Because the differences in TKEs do not cause a significant difference for the velocity profiles, it can be concluded that there is no strong coupling between the velocity and the TKE. The near-wall treatment has a large impact on the velocity and TKE profiles inside the

street canyon. With LRNM the velocities are overestimated especially close to the walls. The results can be improved, when using WFs (SWFs or NEWF1s) or LRNM with a source term for the TKE in the freestream. In this case the results agree rather well with the measured profiles. The CFD results differ more from the measured profiles for the TKE than for the velocities. With the realizable $k-\varepsilon$ model the TKE are too low in the centre of the street canyon for all approaches. For the WFs the TKEs are much too low in the centre of the street canyon. With LRNM a good match can be observed close to the windward wall, but the TKEs are overestimated close to the leeward wall. With the realizable $k-\varepsilon$ model the shapes of the TKE profiles are more similar to the measured profiles than with the standard $k-\varepsilon$ model. The best agreement can be found with the NEWF1s. Thus for the isothermal street canyon case with a freestream velocity of 1.45 m/s the best results can be found for the NEWF1s with a standard $k-\varepsilon$ model. Theoretically the LRNM should perform better, because it resolves the boundary layers and accounts for the damping of the TKE in the near-wall regions. Because the mesh is too fine at the walls for WFs, the NEWF1s cannot account accurately for this damping of the TKE and therefore is expected to perform worse. However it can be observed that flow fields results using NEWF1s are the most accurate. There are several possible reasons for that. For the simulations using LRNM the TKE is almost zero in the near-wall region, but for the simulations with WFs the TKEs do not drop to zero close to the walls. Therefore the higher TKEs in the near-wall regions cause a higher mixing and as a result lower velocities close to the walls. Another possible reason is that the TKE in the approach flow is higher close to the ground. Also here higher mixing causes lower velocities close to the ground. The lower velocities above the street canyon in turn cause lower velocities inside the street canyon. In the following section the influence of the approach flow profiles on the flow inside the street canyon is studied in more detail for the cases, where all the surfaces inside the street canyon are heated.

4.3.4.3 All surfaces heated

In this section three measured cases are used for the comparison: (i) surface temperatures of 70 $°C$ and a freestream velocity of 1.45 m/s; (ii) surface temperatures of 70 $°C$ and a freestream velocity of 2.32 m/s and (iii) surface temperatures of 130 $°C$ and a freestream velocity of 2.32 m/s. These three cases were chosen, because all CFD simulations and the measurements show one main vortex in the centre of the street canyon. Thus not only contour plots, but also centreline profiles can be compared.

In Figure 4.19 normalized centreline profiles of the horizontal velocity and TKE are given for three measured cases and the corresponding CFD simulations. Here the profiles are not only given inside the street canyon as for the isothermal case, but also up to $0.75H$ above the street canyon. This allows to study also the influence of the approach flow on the flow inside the street canyon. The following two CFD model combinations are used for the validation: (i) LRNM with a realizable $k-\varepsilon$ and (ii) NEWF1s with a standard $k-\varepsilon$. The first model combination is chosen, because it is used for most CFD simulations in this thesis. And the second combination of models is chosen, because it performs best for the isothermal case. Further simulations are conducted with the same models as the simulation with the NEWF1s, but the extension of the upstream

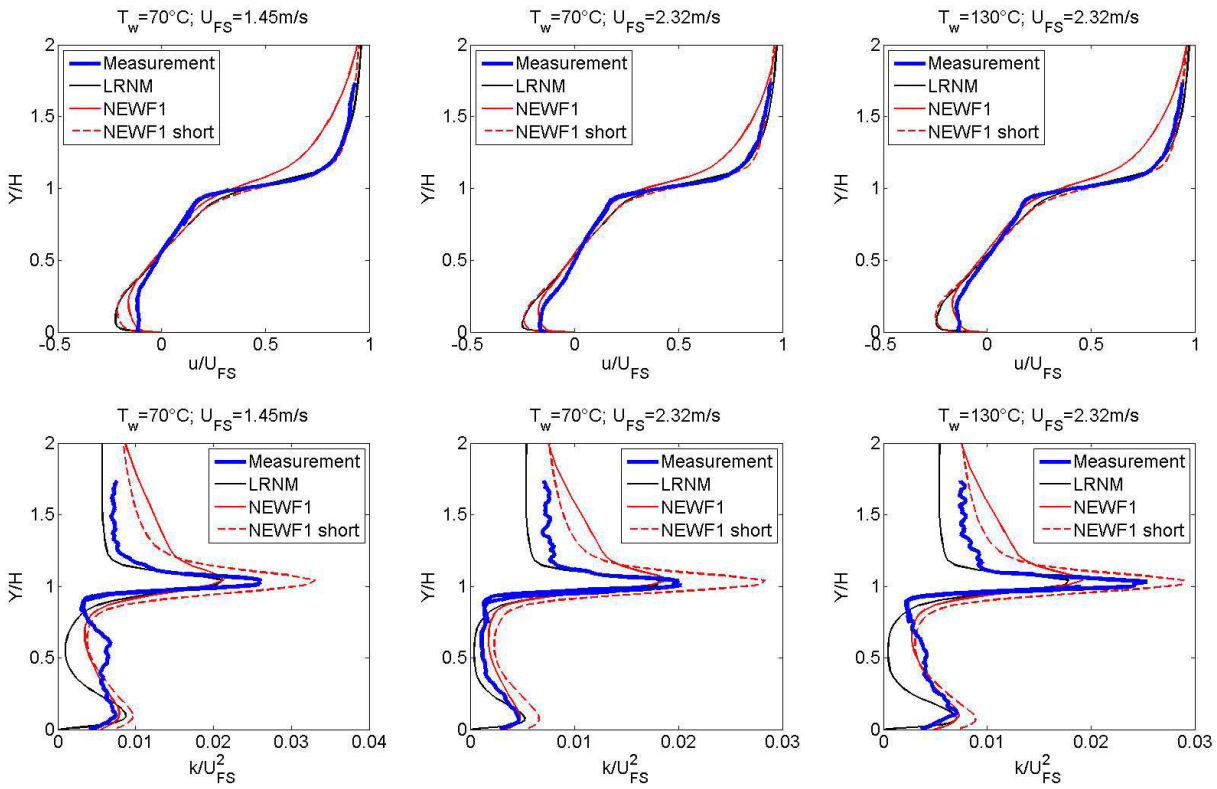

Figure 4.19: Normalised centreline profiles of the horizontal velocity and TKE. Wind tunnel measurements and CFD simulations for cases where all surfaces are heated using two different turbulence models and different near-wall modelling approaches (LRNM: Low-Reynolds number modelling with realizable $k-\varepsilon$; NEWF1: non-equilibrium wall functions with standard $k-\varepsilon$; NEWF1 short: NEWF1 with a short upstream domain).

domain in front of the street canyon is only $0.25H$ (NEWF1 short). With this short upstream domain, the boundary layer cannot develop and therefore the approach flow velocities do not decay as in the case with the long upstream domain. In this case the flow velocities at the entrance of the street canyon will be more accurate. The results for the velocities in Figure 4.19 show similar profiles for all three cases. In the boundary layer above the street canyon the simulation with NEWF1s predicts too low velocities. With LRNM and NEWF1s with the short domain a very good agreement between the simulations and the measurements can be found. In the shear layer at the top plane of the street canyon the velocities are strongly decreasing and at $H = 1$ the slope of the profiles is strongly changing. At this point the best agreement for the velocity can be found for the NEWF1s, while the other two models overestimate the velocities. Inside the street canyon the best agreement can be found for simulations using NEWF1s, while the other two models overestimate the velocities close to the ground of the street canyon. The results with LRNM and NEWF1s with the short domain show very similar results. Therefore it can be concluded that velocities inside the street canyon are mainly influenced by the velocities in the shear layer. Even with too low velocities above the street canyon

(using NEWF1s) the flow inside the street canyon can be predicted well. For the other two models the results for the velocities are worse, even though there is a better agreement for the velocities above the street canyon. For the TKE all CFD models can capture the general trend. Above the street canyon the simulations with NEWF1s overestimate the TKE and the simulations with LRNM underestimate the TKE. It can be observed that in the shear layer the two models with the long domain predict similar peak values. This

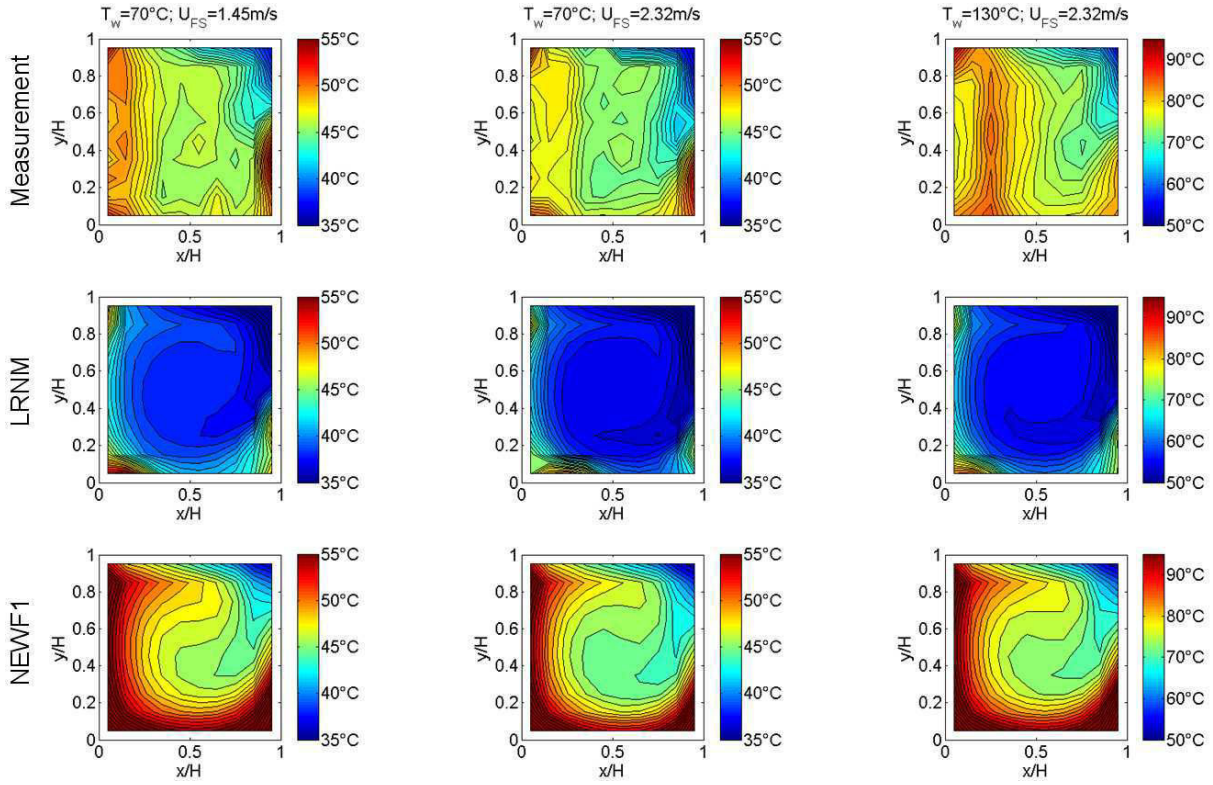

Figure 4.20: Contour plots of the air temperatures inside the street canyon. Wind tunnel measurements and CFD simulations for cases where all surfaces are heated using two different turbulence models and different near-wall modelling approaches (LRNM: Low-Reynolds number modelling with realizable $k-\varepsilon$; NEWF1: non-equilibrium wall functions with standard $k-\varepsilon$).

is remarkable, because the peak in TKE in the approach flows is significantly higher for the NEWF1s compared to the LRNM (Figure 4.17). The peaks in the shear layer are for both models lower compared to the measurements for all three cases. The simulations with the short domain overestimate the peak in TKE inside the shear layer. Inside the street canyon the NEWF1s (long and short domain) perform better than LRNM that underestimates the TKE inside the street canyon. All CFD models predict the second peak close to the ground of the street canyon. From the profiles in Figure 4.19 it can be concluded that it is important to predict correctly the flow in the shear layer in order to get accurate results inside the street canyon. With the CFD models applied in this study the measured profiles in the shear layer cannot be captured. The most accurate results inside the street canyons can be found for the simulations with NEWF1s, where

the velocities inside the boundary layer are underestimated, but the velocity at building height (H=1) is correctly predicted. It was found that the simulated profiles in the shear layer cannot be improved with a mesh that is refined in this region. Therefore, it can be concluded that the overestimation of the velocities in the shear layer for the LRNM simulations is not due to a too coarse grid. The flow structure in the shear layer seems to have a stronger impact on the flow field inside the street canyon than the near-wall treatment. This means that the error induced by not accounting for the damping of the TKE in the near-wall regions with NEWF1s leads to a smaller error for the general flow structure compared the error induced by the inaccurate velocity predictions of the LRNM in the shear layer.

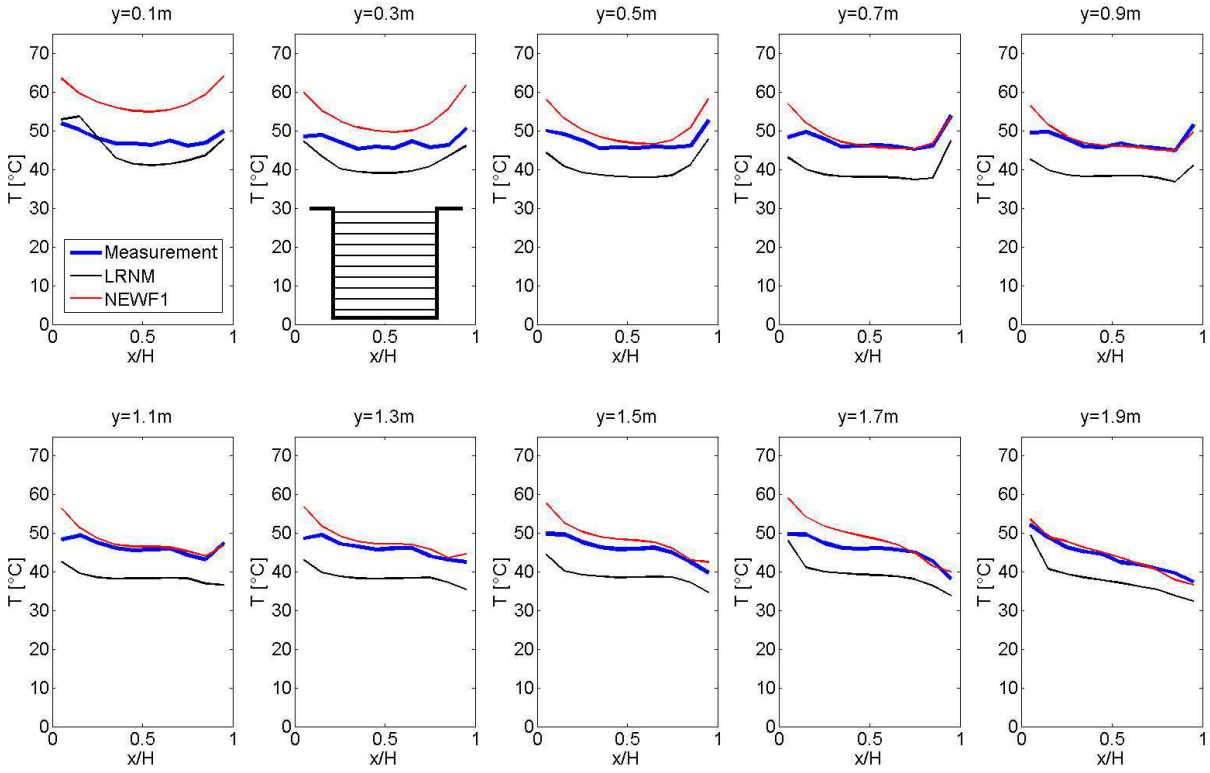

Figure 4.21: Temperature profiles on horizontals lines at different y-positions inside the street canyon. Wind tunnel measurements and CFD simulations for cases where all surfaces are heated using two different turbulence models and different near-wall modelling approaches (LRNM: Low-Reynolds number modelling with realizable $k-\varepsilon$; NEWF1: non-equilibrium wall functions with standard $k-\varepsilon$).

The shear layer is also important for the exchange of air between the street canyon and the flow above the street canyon and therefore influences the temperature distribution inside the street canyon. In Figure 4.20 the contour plots of the air temperatures inside the street canyon are given for three measured cases. Results of the measurements are compared with CFD simulations using LRNM and NEWF1s. It can be observed that the LRNM simulations underestimate the air temperatures inside the street canyon.

With NEWF1s the air temperatures in the centre of the street canyon are similar to the measured temperatures, but the thickness of the temperature boundary layers is overestimated. In Figure 4.21 additionally horizontal profiles (measured, LRNM and NEWF1s) of the temperature are given for the case with a surface temperature of 70 $°C$ and a freestream velocity of 1.45 m/s. It is expected that the most accurate results would be achieved by LRNM, where the shear layer can be accurately resolved (see section 4.3.5). With LRNM the temperatures are underestimated for all profiles by about 10 $°C$. The results can be improved by using NEWF1s. For the profiles at $y < 5$ cm and for most profiles close to the windward and leeward walls the temperatures are overestimated by NEWF1s due to the overestimated thickness of the temperature boundary layer. In the centre of the street canyon a good agreement for the temperatures with NEWF1s can be found. A reason for the better agreement of the profiles with NEWF1s compared to LRNM could be that the velocities in the shear layer correspond better to the measured velocities (see Figure 4.19). Another possible reason is that the convective heat transfer predictions are more accurate due to a different near-wall treatment.

4.3.4.4 Windward wall heating

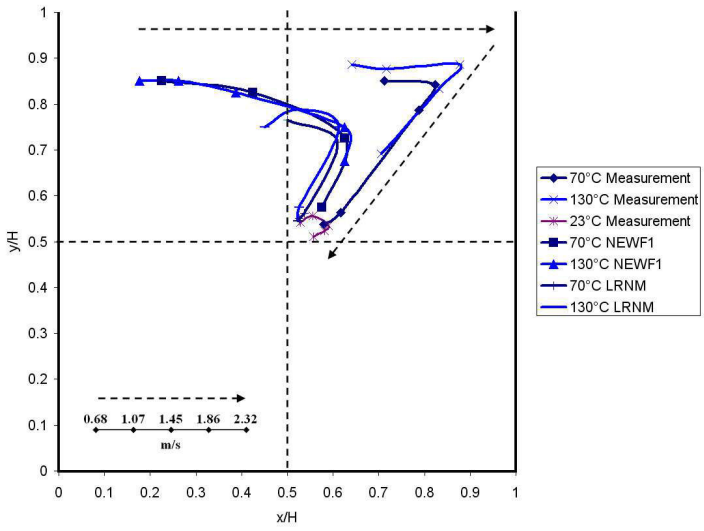

Figure 4.22: Trajectories of the centre of the main vortex as a function of the freestream velocity for different windward wall temperatures. Wind tunnel measurements and CFD simulations using two different turbulence models and different near-wall modelling approaches (LRNM: Low-Reynolds number modelling with realizable $k - \varepsilon$; NEWF1: non-equilibrium wall functions with standard $k - \varepsilon$).

For windward wall heating the vortex structure is strongly influenced by buoyancy. The information gained from comparing centreline profiles is rather limited, because already small changes of the centre of the vortices strongly change the profiles. Therefore in this section the trajectories of the centres of the main vortex are compared. Figure 4.22

shows the trajectories for the measured flow fields and the results of simulations with NEWF1 and LRNM. As for the measurements also for the CFD simulations the centre of the main vortex is moving from the leeward wall side towards the windward wall side and then to the centre of the street canyon with increasing Reynolds numbers. The trajectories are similar for the simulations with LRNM and NEWF1s. For LRNM the flow is more in the forced regime than for NEWF1s for all simulations. This can be seen in Figure 4.22, where the trajectories for the same Reynolds numbers are closer to the forced convective case for LRNM compared to NEWF1s. The more buoyant flow with NEWF1s corresponds better to the buoyant flow measured in the wind tunnel. The NEWF1s predict a higher influence of buoyancy, due to the higher predicted temperatures inside the street. Therefore it can be concluded that with CFD the general development of the vortex structure can be predicted for cases with windward wall heating. With NEWF1s the importance of buoyancy can be predicted more accurately than with LRNM. It is assumed that the higher predicted temperatures inside the street canyon correspond better to the temperatures inside the measured street canyon. However, this cannot be proofed here, because the temperatures were not measured for cases with windward wall heating.

4.3.4.5 Leeward wall heating

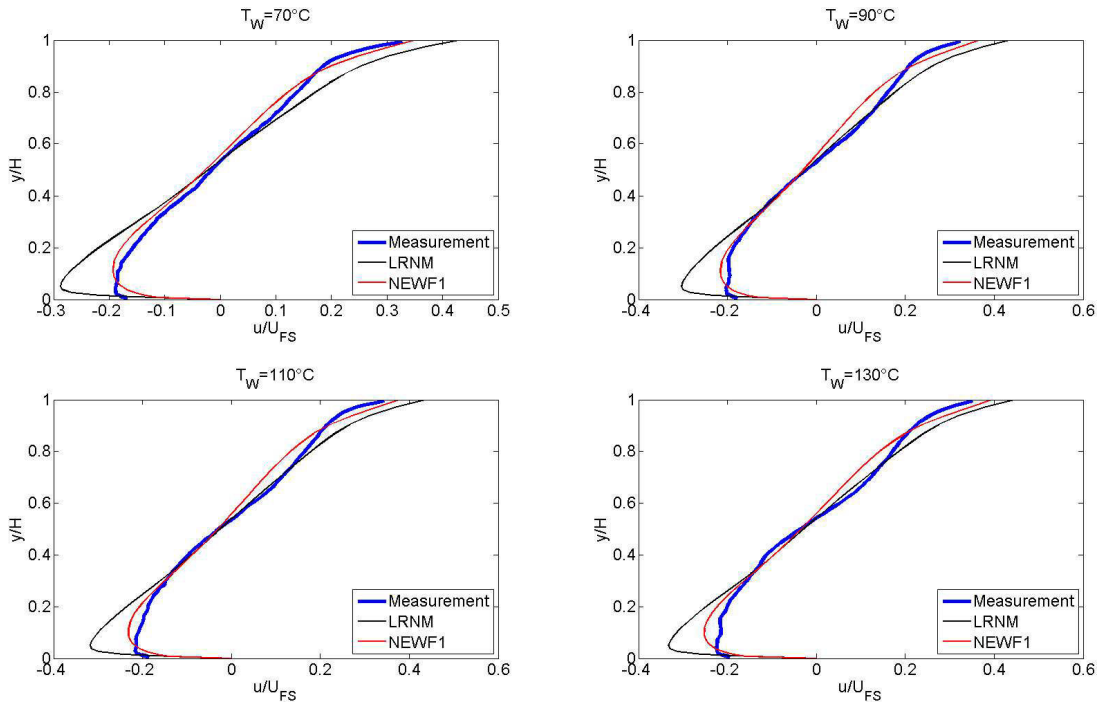

Figure 4.23: Normalised centreline profiles of the horizontal velocity. Wind tunnel measurements and CFD simulations using two different turbulence models and different near-wall modelling approaches (LRNM: Low-Reynolds number modelling with realizable $k-\varepsilon$; NEWF1: non-equilibrium wall functions with standard $k-\varepsilon$).

For the cases with leeward wall heating the validation is conducted for a freestream velocity of 1.45 m/s with different surface temperatures. The CFD results for the normalised horizontal velocities and the TKEs on the vertical centreline obtained using LRNM and NEWF1s are compared with the wind tunnel measurements (Figures 4.23 and 4.24). As for the cases, where all surfaces are heated, the velocities at the top of the street canyon are overestimated with LRNM. Therefore also the velocities at the ground of the street canyon are overestimated. The velocity profiles of the simulations using NEWF1s match the measured profiles well. Also for the TKE the results of the simulations using NEWF1s show a better agreement with the measured results than the simulations using LRNM.

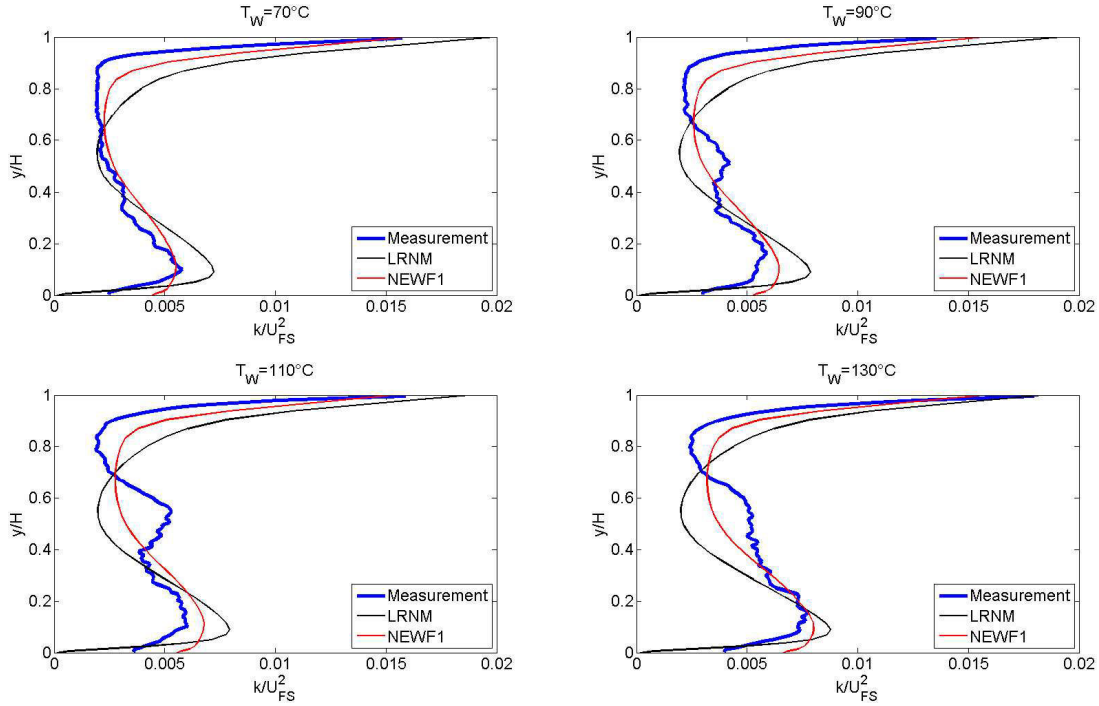

Figure 4.24: Normalised centreline profiles of the TKE. Wind tunnel measurements and CFD simulations using two different turbulence models and different near-wall modelling approaches (LRNM: Low-Reynolds number modelling with realizable $k-\varepsilon$; NEWF1: non-equilibrium wall functions with standard $k-\varepsilon$).

4.3.5 Discussion

In this chapter a study has been conducted to validate the CFD models used in this thesis by comparison with data from wind tunnel measurements. This validation study focuses on buoyant flows in a square cavity representing an urban street canyon. Buoyant flow fields have a unsteady and 3D flow characteristic. The unsteadiness and the three-dimensionality of the flow cannot be captured with the 2D steady RANS simulations that are conducted for this validation study. The strongly simplified CFD models are chosen, because they are applicable for full-scale flows in street canyons and are therefore used for the precalculations of the CHTC (convective heat transfer coefficient) correlations

(section 3.2.4) and for the coupled BES (building energy simulation)-CFD simulations (section 3.1.4). The aim of this validation study is not to find the most accurate CFD models to predict the detailed flow field inside a heated street canyon, but to study, if the most important flow phenomena in terms of heat transfer can be captured with these simplified CFD models (steady and 2D simulations) used in this thesis. It is assumed that the most accurate results can be found for time resolved 3D CFD simulations (e.g. LES: large eddy simulation). However, with today's available computational power, it is for most cases not feasible to apply these more advanced CFD models for full-scale building applications. Further in this thesis mainly the thermal behaviour of buildings is investigated and CFD is used complementary to model the convective heat transfer of the building envelope. The time scale of the heat transfer in the building envelopes is rather large compared to the time scale of the flow around buildings. Therefore not all the buoyant flow characteristics need to be captured at small time scales. It is more important to capture the correct overall heat fluxes and temperature distribution inside the street canyon.

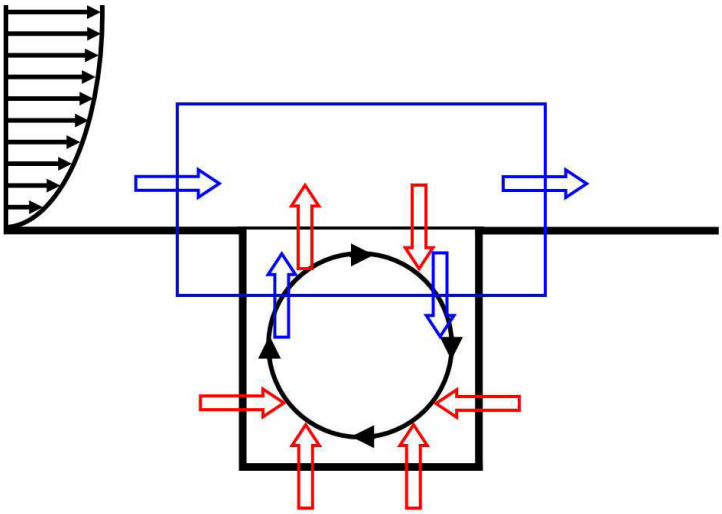

Figure 4.25: Sketch of the heat fluxes in a street canyon.

Due to buoyancy there is a strong coupling between the flow field inside the street canyon and the heat fluxes at the boundaries of the street canyon. Therefore already small errors in the prediction of the fluxes or the flow field can significantly change the results of the CFD simulations. In the case of the street canyon the important fluxes are the convective heat fluxes at the three surfaces of the street canyon, the heat flux out of the street canyon into the freestream and the heat flux into the street canyon from the freestream (red arrows in Figure 4.25). The temperature distribution inside the street canyon is strongly dependent on these heat fluxes. The main driver of all the fluxes and the resulting temperature distribution inside the street canyon is the heat exchange at the top plane of the street canyon. Theoretically there exist two extreme cases. For the first extreme case there is no heat exchange at the top plane of the street canyon. As soon as the fluxes are in equilibrium, the air temperature inside the street canyon is the same as the temperature at the (heated) surfaces and there is no convective heat

transfer at the surfaces. Due to the uniform temperature distribution, buoyancy does not influence the flow and a forced convective flow can be found inside the street canyon. The second extreme case is the case with an infinite heat exchange at the top plane. Thus all heat added to the flow by convection inside the street canyon is removed instantly. Therefore the equilibrium air temperature inside the street canyon is the temperature of the freestream above the street canyon. Also in this extreme case a uniform temperature distribution inside the street canyon can be found and buoyancy does not influence the (forced convective) flow. In reality the heat exchange at the top plane of the street canyon is between these two extreme values. Therefore also the temperatures are between the two extremes and the temperature distribution is not uniform anymore. For a case with one main vortex in the centre of the street canyon, the temperature at the windward wall, where the cold air of the freestream is entering the street canyon, is lower compared to the temperature at the leeward wall, where a part of the heated air is leaving the street canyon. Due to this non-uniform temperature distribution, buoyancy starts to play an important role and the flow structure becomes dependent on the temperature distribution. The heat exchange at the top plane is driven by the flow structure at the top plane, because it is caused by the air exchange. The air exchange is driven by convection or turbulence. On the other hand the flow structure is strongly influenced by the heat exchange at the top plane, because this exchange has an impact on the temperature distribution and therefore on the buoyancy effects. This explains the strong coupling between the heat fluxes and the flow structures inside a street canyon. For example an increase of the leeward wall temperature can increase the heat exchange at the top plane due to increased buoyancy effects. This increased heat exchange can lead to lower air temperatures at the windward wall and a significant change in the whole flow structure inside the street canyon. This change in the flow structure has an impact on all the heat fluxes and due to the coupling the flow structure will further change. This leads to the conclusion that for a validation of the flow inside a street canyon in addition to the flow characteristics also the heat fluxes need to be studied. Only if the flow structures and the heat fluxes are analysed a complete validation of the important physical phenomena can be conducted. The focus of such a validation study should be on the heat exchange at the top plane of the street canyon, because (as explained above) this heat exchange drives all physical phenomena inside the street canyon. The heat exchange at the top plane is strongly connected to the air exchange at the top plane. Analysing only the vertical velocities at the top plane is not sufficient to find the air exchange rate of the street canyon. Air leaving the street canyon at one position at the top plane, could reenter the street canyon at a different position and air entering the street canyon could leave the street canyon again without being mixed with the air inside the street canyon. For example if there is one main vortex in the centre of the street canyon and the diameter of this vortex is larger than the height of the street canyon, most of the air leaving the street canyon at the leeward wall, is reentering the street canyon at the windward wall again. And if the diameter is smaller than the height of the street canyon, most of the air entering the street canyon at the leeward wall, is leaving the street canyon again at the windward wall (Figure 4.26). Further above the top plane of the street canyon the air of the approach flow is mixing with the air leaving the street canyon and therefore the temperature of the air entering the street canyon does for most cases not correspond to the approach flow air temperature. Therefore for most

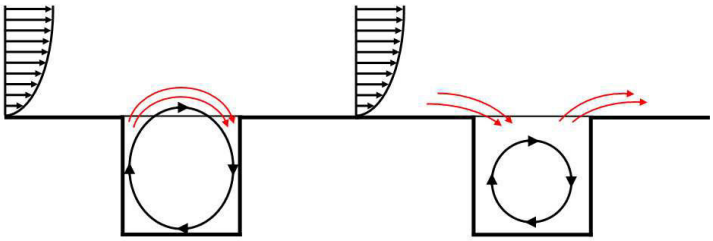

Figure 4.26: Sketch of the flow in a street canyons with a main vortex with a diameter larger than the street canyon height (left) and smaller than the street canyon height (right).

cases no surface can be defined, where the heat exchange can be studied by analysing only the wind velocities. This leads to the conclusion that the heat fluxes itself have to be analysed. For this validation study only the detailed flow fields were measured inside the street canyon. To be able to determine heat fluxes also the detailed temperature fields with a high resolution need to be known. Here only for few cases the temperature fields were measured, but at a too low resolution to determine heat fluxes. Further to determine the heat balance of the street canyon the convective heat fluxes at the surfaces of the street canyon have to be measured. In addition to the flow field inside the street canyon also the flow field above the street canyon and especially the flow field in the shear layer have to be known for the validation. As discussed here, this region is important for the heat exchange at the top plane and it is also important for the velocity prediction with CFD as discussed in the sections above. Therefore it is suggested to conduct additional wind tunnel measurements in future, focusing on the region indicated with the blue box in Figure 4.25. In this volume the important transport phenomena can be found that drive the ventilation of the street canyon. Determining a heat balance for this control volume allows to study the heat fluxes in more detail, which not only influence the heat exchange at the surfaces of the street canyon, but also the flow field inside the street canyon. To be able to measure a detailed temperature field with a high resolution inside the street canyon the existing temperature measurement techniques need to be improved. The temperature needs to be measured with a high resolution without disturbing the flow field and the measurement equipment needs to be shielded against the longwave radiation of the heated surfaces or this additional heat flux must be subtracted during post processing. Further also the convective heat fluxes at the street canyon surfaces need to be measured to determine the heat balance of the street canyon. For cases where only the heat fluxes at the walls and not the temperatures inside and above the street canyon can be measured, ventilation efficiency indices can be used to determine the ventilation of the street canyon [190].

Above it is discussed, why it is important to get accurate flow predictions in the shear layer to be able to accurately predict the heat exchange and the flow field and fluxes inside the street canyon. As concluded in the validation part of this chapter, the RANS CFD simulations with $k-\varepsilon$ turbulence models used in this thesis do not accurately predict the flow in the shear layer. However the results for the flow in this region could be improved by using more advanced turbulence models. Further, by conducting unsteady LES sim-

ulations, unsteady flushing events could be captured that have a strong impact on the heat exchange between the street canyon and the flow above the street canyon. Moonen et al. 2011 [170] showed that LES predict higher ventilation potentials for courtyards and street canyons than RANS.

In this study the same mesh was used for LRNM and WFs. The mesh was optimised for LRNM and was therefore too fine at the surfaces for WFs, because the first grid point was inside the viscous sublayer. Therefore for the simulations with WFs the damping of the TKE in the boundary layer was not considered. This leads to an error in the simulated flow fields. The results in this study show that the error that is introduced by using a not appropriated mesh is smaller than the error introduced due to the wrong prediction of the velocities at the top plane of the street canyon with LRNM. This can be seen in Figure 4.19, where the profiles for simulations using NEWF1s and LRNM give similar profiles for the velocity, when the velocity profile at the top plane of the street canyon and above the street canyon are almost the same. The most accurate results are therefore expected for CFD simulations with LRNM, where the shear layer can be accurately modelled.

4.3.6 Conclusion

A validation study was conducted for buoyant flows in street canyons. For the validation the CFD results were compared with the measurements described in section 4.2. 2D RANS simulations were conducted with $k-\varepsilon$ turbulence models and different near-wall treatments. LRNM and WFs were applied on the same mesh that is optimized for LRNM. When using WFs on that mesh in the near-wall region, damping of TKE cannot be accounted for. Therefore an error is introduced by using WFs on a mesh optimized for LRNM. It was found that the general flow structures can be captured with all applied CFD models. Differences between the different CFD models and between CFD and measurement results can be observed, when comparing detailed profiles of the flow. Already in the approach flow the profiles of the velocity and TKE cannot be captured correctly in the same simulation. Either the velocity profile can be captured correctly but with a too strong streamwise decay of the TKE (using LRNM) or the TKE profiles can be captured correctly with the velocities in the near-wall regions decreasing in streamwise direction (using NEWF1). Using LRNM the velocities in the near-wall regions are overestimated for all studied cases, while with NEWF1s a significantly better agreement can be observed. A possible reason for the better agreement are the lower (too low compared to the measurements) velocities in the boundary layer above the street canyon. Due to these lower velocities, the velocities in the top plane of the street canyon agree better with the measured velocities, while with LRNM these velocities are overestimated. This overestimation in the top plane could cause the overall overestimation of the velocities inside the street canyon. This is to a certain extend confirmed by simulations with NEWF1s using a very short domain, where the boundary layer cannot develop in front of the street canyon. For this case the velocity profile of the approach flow is the same for LRNM and NEWF1s and also the velocities inside the street canyon are comparable. These results lead to the conclusion that the error introduced by not considering the damping of TKE in the near-wall region with NEWF1s is lower than the error introduced due to the error in the prediction of the velocity at the top plane of the street canyon with LRNM.

Similar shapes of the TKE profiles can be observed for the measurements and the CFD simulations using NEWF1s. The standard $k-\varepsilon$ turbulence model predicts higher TKEs than the realizable $k-\varepsilon$ model. Mostly the best results for the TKE can be found with the realizable $k-\varepsilon$, if LRNM is applied and with the standard $k-\varepsilon$, when NEWF1s are used. Inside the street canyon the turbulence model has no strong influence on the velocities.

For the buoyant cases the use of NEWF1s gives better results for the trajectories of the main vortex than using LRNM. Simulations using LRNM underestimate the temperatures inside the street canyon, while a good agreement can be observed with NEWF1s in the centre of the street canyon. NEWF1s overestimate however the thickness of the temperature boundary layer. This better agreement for the temperatures could be caused by the better agreement of the flow at the top plane of the street canyon or due to differences in the modelling approach of the thermal boundary layer.

This study shows that CFD can be useful to predict flows in buoyant urban street canyons and that the general flow structure can be captured. But to analyse the detailed flow structures and heat fluxes a validation study with more detailed temperature and flow measurements at the top plane of the street canyon needs to be conducted.

5 BES: energy impact results

In the previous chapters all the relevant modelling approaches needed to study the impact of the urban microclimate on the building energy demand were discussed. Finally in this chapter the impact of the urban microclimate on the energy demand of buildings for space cooling and space heating is analysed. First the urban configurations and buildings, used in this study, are presented. Then the importance of correctly accounting for wind sheltering with respect to the convective heat transfer at the building façades is shown in a sensitivity study. In a next step the importance of correctly taking into account the radiation exchange between buildings as well as the urban heat island (UHI) effect on the energy demand is studied. The used approach is finally applied for different climates.

5.1 Configurations

The aim of this chapter is to quantify the influence of the urban microclimate on the energy demand for space cooling and heating in buildings using a more detailed approach accounting for multiple radiative reflections, reduced convective heat losses and the UHI. A street canyon geometry is chosen as a case of a typical urban configuration of a city. With the geometry of a street canyon two of the three most important aspect of the urban microclimate can be captured, namely the radiation exchange between buildings and the wind sheltering of neighbouring buildings. The UHI effect cannot be modelled at the street canyon scale. To simulate the UHI effect the whole urban area of a city need to be modelled. This is computationally not feasible with the level of detail applied in this study. Three office building types with different building envelopes are considered. The first building type corresponds to a new well insulated building designed for a moderate European climate, the second to an old less insulated building and the third to a retrofitted building. These three building types represent a majority of buildings that can be found in urban areas in central Europe. The following approach is chosen for this study. Multizone BESs (building energy simulations) are conducted for different stand-alone buildings and for buildings located in street canyons with different aspect ratios. Daily UHI intensity schedules based on measured data for the Swiss city of Basel are used to account for the UHI effect (see section 3.1.3). Basel has a moderate European climate. Therefore for the buildings analysed the energy demand for space heating in winter is much higher than the space cooling demand in summer. Generally the space cooling demands are rather low and only become important for example in urban areas or during heat waves in summer. Two different approaches to model the convective heat fluxes at the building façades are chosen in this study. First, CHTC (convective heat transfer coefficient) correlations derived for specific street canyon configurations and stand-alone buildings [74] (see section 3.2.4) are used to model the convective heat transfer at the building façades. In a second step, the

BES model is coupled with CFD (see section 3.1.4) for the determination of the CHTCs. In the last step the air temperature values used for modelling of the ventilation of the buildings are also taken from the CFD simulation instead of using meteorological data. The radiative exchange of longwave and solar radiation in the different street canyons are computed considering multiple reflections as implemented in the BES model. In a first part of this study the sensitivity of the space cooling demand of buildings in a street canyon on the used CHTC correlation is investigated. Then the influence of all three important aspects of the urban microclimate (wind sheltering, radiation exchange between buildings, UHI effect) is quantified. Next a study is conducted to quantify the sensitivity of the energy demand on different parameters such as UHI intensity, internal heat gain, ventilation concept and solar absorption coefficient of the building façade. As a last step different modelling approaches, including the coupled BES-CFD simulations, are compared.

5.2 Building description

In this study three-storey office and residential buildings are studied. A sketch of the buildings is given in Figure 5.1. The building studied is the building in the middle. This building is surrounded by two other rows of buildings, which have the same properties as the studied buildings. The energy demands of these two (neighbouring) buildings are not evaluated. They are needed to solve the radiation balances of the middle building. All the studied buildings and therefore also the street canyons have a length of 110.5 m (L), to minimize lateral boundary effects in the radiation model. This corresponds to a row of a few houses in a street canyon. The height of the buildings is 13.5 m (H_B) and the height of each storey 4.5 m (H_{Fl}). Buildings with two different glazing fractions (25 % and 50 %) are studied. On each façade there are three windows per floor with a size of 27.5 m x 1.5 m and 27.5 m x 3 m respectively. The distance between the windows is 7 m and they are placed centred on the façades.

The simulations are performed for stand-alone buildings in an open field and for the same buildings with street canyons in front and behind the buildings. Street canyons with aspect ratios of 0.5, 1 and 2 are considered. Different orientations Θ between 0° (showing a north and a south façade) and 90 ° (showing an east and a west façade) are used with steps of 15 °. The orientation is defined as the angle between geographical north and the direction perpendicular to the street axes (see Figure 5.1). Due to the symmetric arrangement of the buildings no new information is gained by using orientations > 90 °.

Three building types with different building envelopes are analysed. The first corresponds to a new well insulated building with a high glazing fraction of 50 %. The second building is less insulated and has a smaller glazing fraction of 25 % representing an old building as it can be found in existing urban areas. The third building represents a retrofitted building. It has the same low glazing fraction as the old building, but is as well insulated as the new building. The U-values (and g-values for windows) of the different building envelopes are given in Table 5.1.

The interior walls, the floors and the properties of the street pavements are the same for all building types and given in Table 5.2. On each floor there are 10 walls with an

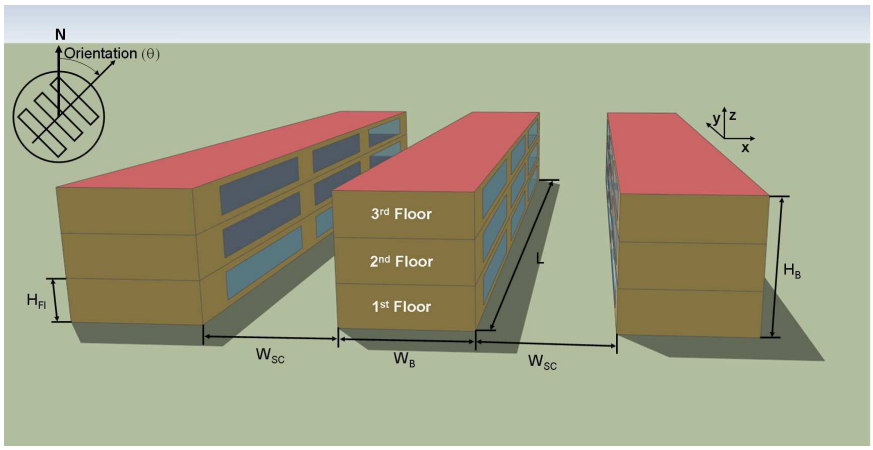

Figure 5.1: Studied building surrounded by street canyons with aspect ratios of 1 (H/W).

		Materials	Thickness	U-value	g-value
New Building	Walls	Plaster, Brick, Insulation	0.372 m	0.259 W/m^2K	
	Roof	Plaster, Concrete, Insulation, Gravel	0.530 m	0.151 W/m^2K	
	Ground floor	Carpet, Screed, Insulation, Concrete	0.376 m	0.295 W/m^2K	
	Windows			1.4 W/m^2K	0.589
Old Building	Walls	Plaster, Brick, Insulation	0.340 m	0.497 W/m^2K	
	Roof	Plaster, Concrete, Insulation, Gravel	0.305 m	0.511 W/m^2K	
	Ground floor	Carpet, Screed, Insulation, Concrete	0.376 m	0.295 W/m^2K	
	Windows			2.83 W/m^2K	0.755

Table 5.1: Building envelope properties.

area of 60.75 m^2 and one wall with an area of 497.25 m^2. The floors separate the different storeys.

	Materials	Thickness	U-value
Interior wall	Plaster, Mineral Rock Wool, Plaster	0.126 m	0.358 W/m^2K
Floor	Plaster, Concrete, Mineral Rock Wool, Screed, Carpet	0.260 m	0.896 W/m^2K
Street	Asphalt, Gravel	0.33 m	1.991 W/m^2K

Table 5.2: Properties of interior walls, ceilings and street

The lateral walls of the buildings are modelled adiabatic assuming that they are connected to other buildings. The properties of these walls are the same as the interior walls. The buildings that surround the studied building are modelled adiabatic at the backside. The later boundaries of the streets are infinitely thin walls with ambient temperature. The top boundary of the street canyon is modelled as window that transmits all radiation and has the same temperature as the sky. The ground temperature is modelled as a function of the time and the depth z. It is assumed that the building is in contact with the ground at the depth z.

$$T_{Gr} = T_m + T_0 e^{-z\sqrt{\frac{\pi}{aT}}} cos\left(\frac{2\pi}{T}t - z\sqrt{\frac{\pi}{aT}}\right) \tag{5.1}$$

where T_{Gr} is the ground temperature, T_m is the average yearly temperature, T_0 is the amplitude of the temperature fluctuations at the surface, z is the distance from the surface, a is the thermal diffusivity, T is the time period and t is the time.
For Basel the following values are used:

- $T_m = 11°C$
- $T_0 = 4°C$
- $z = 2m$
- $a = 2.398 \cdot 10^{-3} m^2/s$
- $T = 8760h$

External shading devices are used to protect the buildings from solar gains. They are closed when solar radiation on the corresponding façade is $> 120\ W/m^2$ or there is direct solar radiation on the façade (to avoid glare). The shading factor of the external shading devices is 0.8. The artificial light control is as follows: lights are on when the building is occupied and the total solar radiation on the corresponding façade is $< 70\ W/m^2$. The building is divided into two parts, where the artificial lights are controlled individually depending on the corresponding façade. A mechanical ventilation system is used with a heat recovery system with efficiency of 80 %:

$$T_{vent} = \eta_{HRV}(T_{in} - T_{amb}) + T_{amb} \tag{5.2}$$

where T_{vent} is the incoming air temperature, η_{HRV} is the efficiency of the heat recovery system, T_{in} is the indoor air temperature and T_{amb} is the ambient air temperature.
The ventilation rate at day-times is $30\ m^3/h.person$. At night-times an air change of $1\ h^{-1}$ is assumed, but only if the building needs to be cooled. This rather low air change rate is chosen, because mechanical ventilation systems are usually dimensioned for demand air flow rates based on air quality criteria. Thus air change rates higher than $1\ h^{-1}$ would require a larger ventilation system. This is usually not installed due to space and cost reasons. With natural ventilation different air change rates could be achieved. With the increased temperatures in urban areas, the natural ventilation rates would be reduced compared to the natural ventilation in rural areas. The moving average of ambient air temperature is computed for the last 24 hours. If this average is $> 15°C$ the night ventilation is switched on for operative room temperatures $> 21\ °C$ and switched off again for temperatures $< 19\ °C$. For averaged ambient air temperatures $> 18\ °C$ the night ventilation is switched on for operative room temperatures $> 20\ °C$ and switched off again for temperatures $< 17\ °C$.

Internal gains caused by lights, devices and persons and the occupancy and utilization schedules are set according to [191] for office and residential buildings and are given in Figures 5.2 and 5.3 and Table 5.3. The given schedules are schedules for weekdays. For weekends it is assumed that for the office buildings the occupancy is 0 % and the utilization of the devices 10 %. No artificial light is used during the weekends.

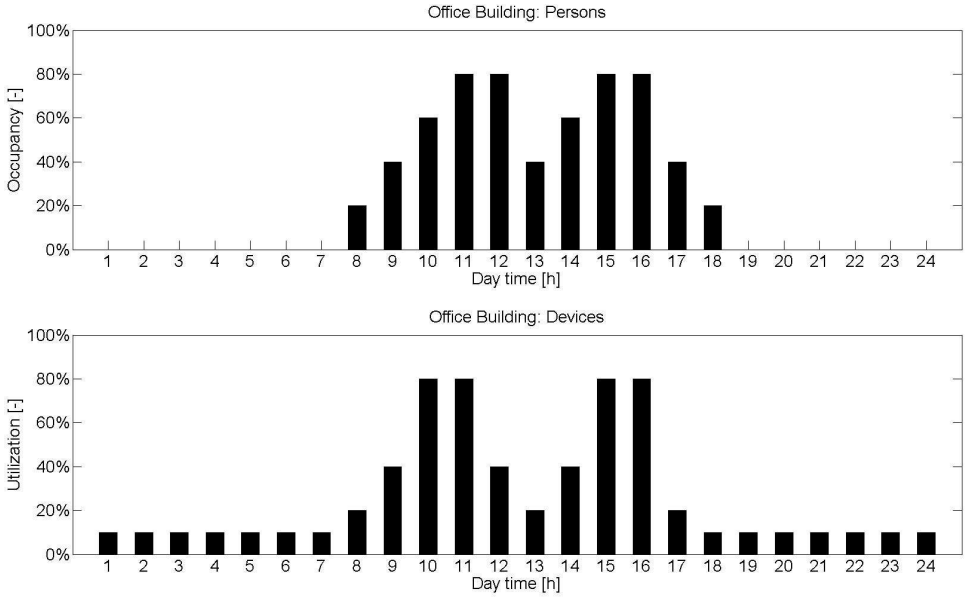

Figure 5.2: Utilization and occupancy schedules for office buildings.

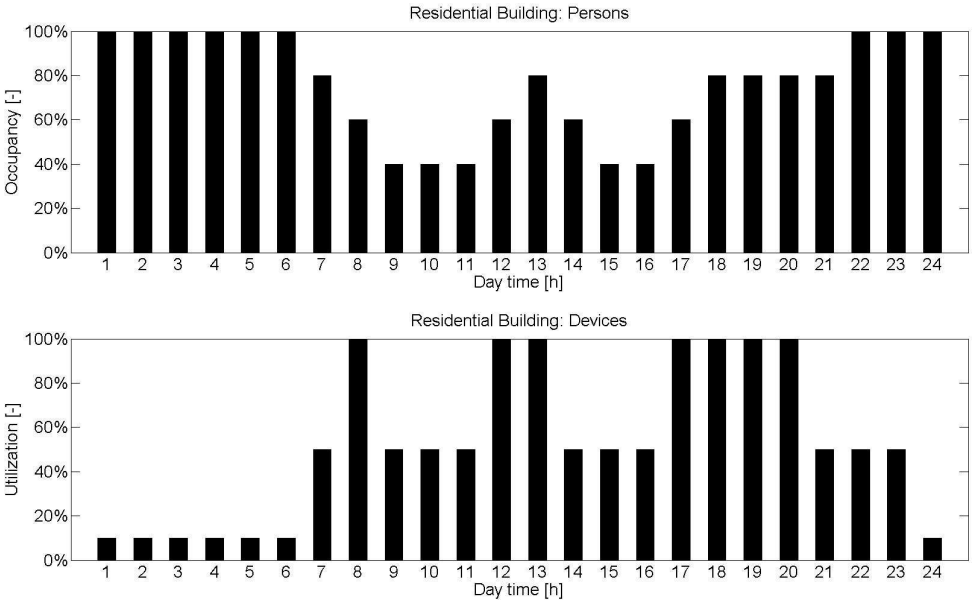

Figure 5.3: Utilization and occupancy schedules for residential buildings.

		Persons	Devices	Lights
Office	radiative	3 W/m^2	2 W/m^2	6.25 W/m^2
	convective	4.2 W/m^2	8 W/m^2	6.25 W/m^2
Residential	radiative	0.6 W/m^2	0.4 W/m^2	6.58 W/m^2
	convective	0.9 W/m^2	1.6 W/m^2	2.82 W/m^2

Table 5.3: Internal gains.

5.3 Results

5.3.1 Effect of CHTC correlations

In this section the influence of the different CHTC correlations on the space cooling demand of a building in an urban street canyon is analysed. This study is limited to one BES model of a building in an urban street canyon with an aspect ratio of 1. No urban heat island effect is considered and no night ventilation is modelled. The new office building type is used with an orientation of 0 °. The CHTC correlations as derived in section 3.2.4.4 for the different geometries are used. The CHTC values are adjusted to the hourly value of the wind speed. For simplicity the CHTC value are not adjusted for every time step to the surface temperature, but the sensitivity of the results to the CHTC correlations for different temperature differences is studied (i.e. the temperature difference between the air and surfaces are assumed to be constant in time).

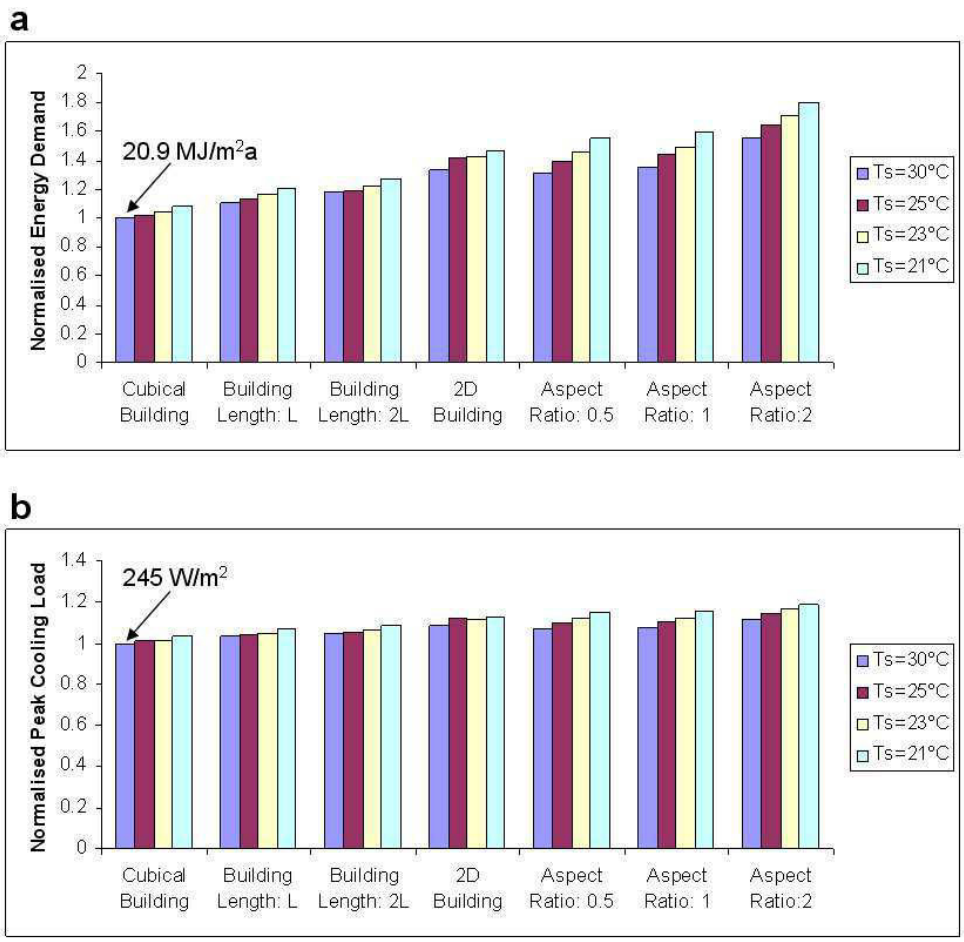

Figure 5.4: Total annual space cooling demands (a) and annual peak cooling loads (b) normalised by the results for the cubical building with $T_s = 30\ °C$ for a street canyon with an aspect ratio of 1 using CHTC correlations developed for different geometries and temperature differences between building façades (T_s) and ambient air (here 20 $°C$).

In Figure 5.4a the normalised annual energy demand for space cooling is given using the different CHTC correlations. The space cooling demand significantly depends on the CHTCs for the given geometries. The cooling demand increases by 80 % for a building situated in an infinite long narrow street canyon compared to a cubical building. Buoyancy has a less important influence on the cooling demand. The cooling demand increases with 17 % comparing the CHTC correlations for the two extreme wall temperatures (21 $°C$ and 30 $°C$) for a street canyon with an aspect ratio of 2. BESs can also be used to accurately predict accurately the peak cooling loads, as these are important for the dimensioning of HVAC systems. In Figure 5.4b normalised peak cooling loads are given for a building in a street canyon with an aspect ratio of 1, using different CHTC correlations. The same trend as for the annual demand can be found. The differences for the peak cooling loads are however much smaller than for the annual energy demands. The peak cooling loads can occur for weather conditions with high ambient air temperatures, high solar irradiation and low wind speeds. The convective heat fluxes are relatively small compared to the radiative fluxes for these weather conditions, due to the low winds speeds. Therefore the differences for the peak cooling loads are here smaller than for the annual energy demands. In this section only the effect of using different CHTC correlations is investigated. In reality however the influence of the radiation exchange between neighbouring buildings would be more important than the convective heat transfer and therefore also the differences in peak cooling loads would be larger between the different geometries.

In the next part of this study two typical weeks are extracted from the one year simulations for further analysis. One week is characterised by rather high wind speeds, while the other week is characterised by low wind speeds (Figure 5.5a). The temperatures are comparable for the two weeks (Figure 5.5b).

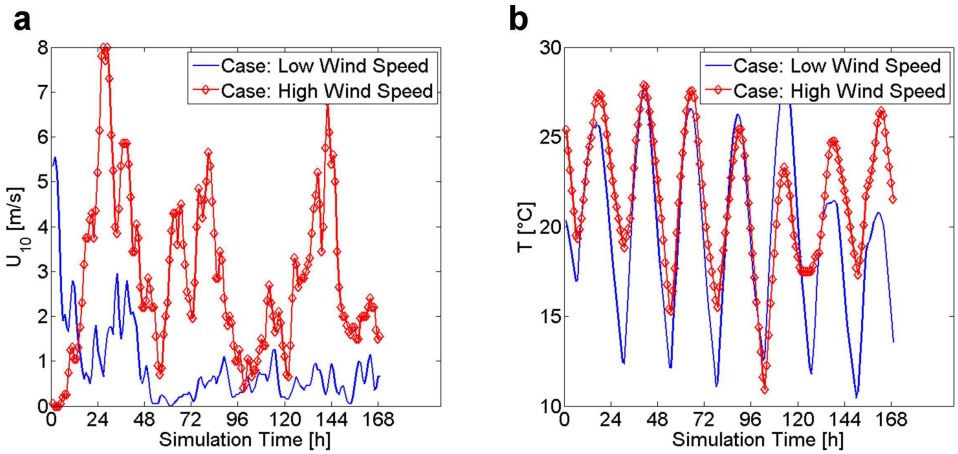

Figure 5.5: Wind speeds (a) and air temperatures (b) for the two studied weeks.

Figure 5.6 shows the normalised weekly space cooling energy demand using different CHTC correlations. In general the dependencies are very similar to the annual predictions. For both weeks the influence of the geometry is lower than for the one year simulations. For the week with the high wind speeds the influence of buoyancy on cooling demand is much lower than for the week with low wind speeds. This is due to the fact that for

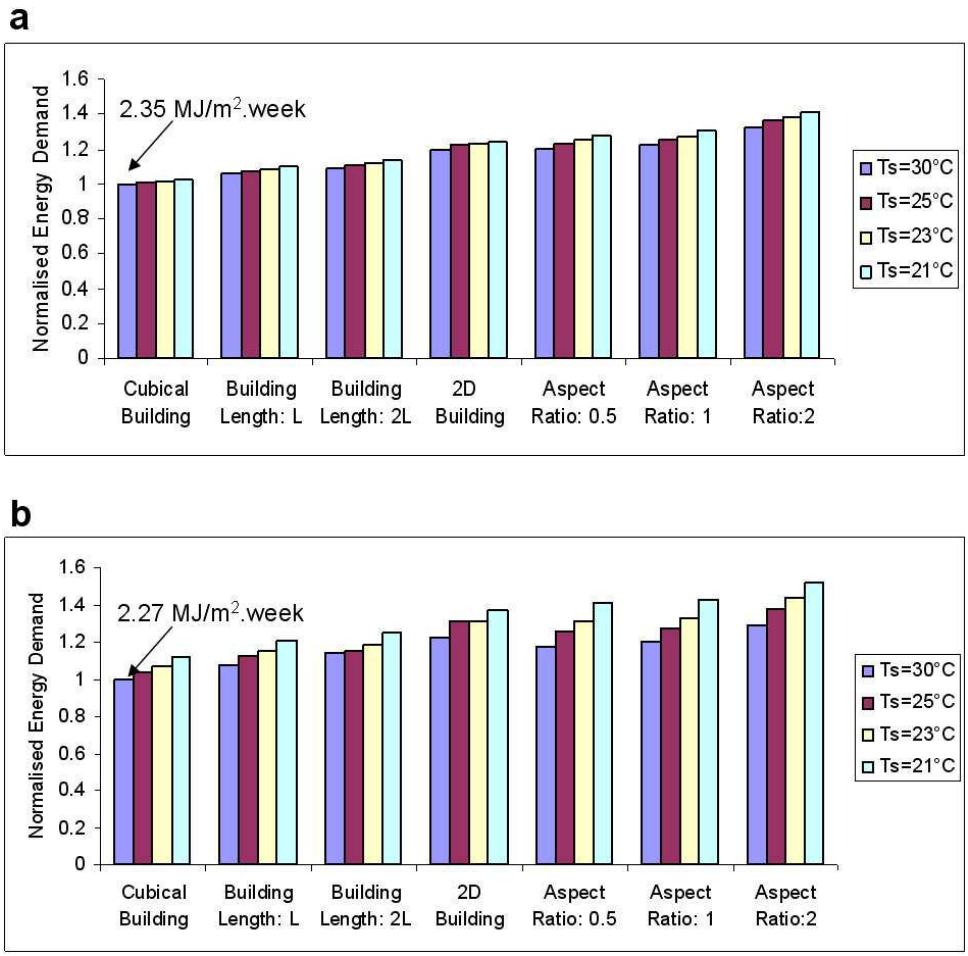

Figure 5.6: Weekly space cooling demands for a week with high wind speeds (a) and a week with low wind speeds (b) normalised by the results for the cubical building with $T_s = 30\ °C$ for a street canyon with an aspect ratio of 1 using CHTC correlations developed for different geometries and temperature differences between building façades (T_s) and ambient air (here 20 $°C$).

most of the time the wind speed is in a range where the influence of buoyancy is quite low (see section 3.2.4.3). For the week with low wind speeds the impact of buoyancy on the space cooling demand is much more pronounced, because the wind speed is mostly $< 1\ m/s$, where the CHTC is a function of the surface temperatures and independent on wind speed.

The results from this section show that it is important to use the appropriate CHTC correlations in order to get accurate predictions for the annual space cooling demands, weekly space cooling demands and the peak cooling loads. Most important is that the geometry and the neighbouring buildings are accounted for when choosing a CHTC correlation for BESs. Also buoyancy needs to be considered for weather conditions with low wind speeds and high surface temperatures especially for buildings in urban areas.

5.3.2 Space heating and cooling demands

In this section the space heating and cooling demands for the three building types in the street canyon configuration are compared with the demands for stand-alone building. The building orientation in this study is $\Theta = 0\ °$ (see Figure 5.1) or the building façades are oriented north - south. For the stand-alone building air temperatures from the rural measurement station "Basel-Binningen" are used, while the air temperature in the street canyon configuration is corrected using the UHI intensity schedules as described in section 3.1.3.

The space heating and cooling demands given in Figure 5.7 are normalized by the respective heating and cooling demand of the stand-alone New Building type (56 MJ/m^2a and 1.7 MJ/m^2a respectively). Note the difference in scales of the ordinate axes for heating and cooling demand. The results for the stand-alone building are compared with the same building in street canyon configuration for the three different building types (NewB, RetroB and OldB). Also the ratio in building energy demand between street canyon and stand-alone building configuration (SC/SA) is given (in green).

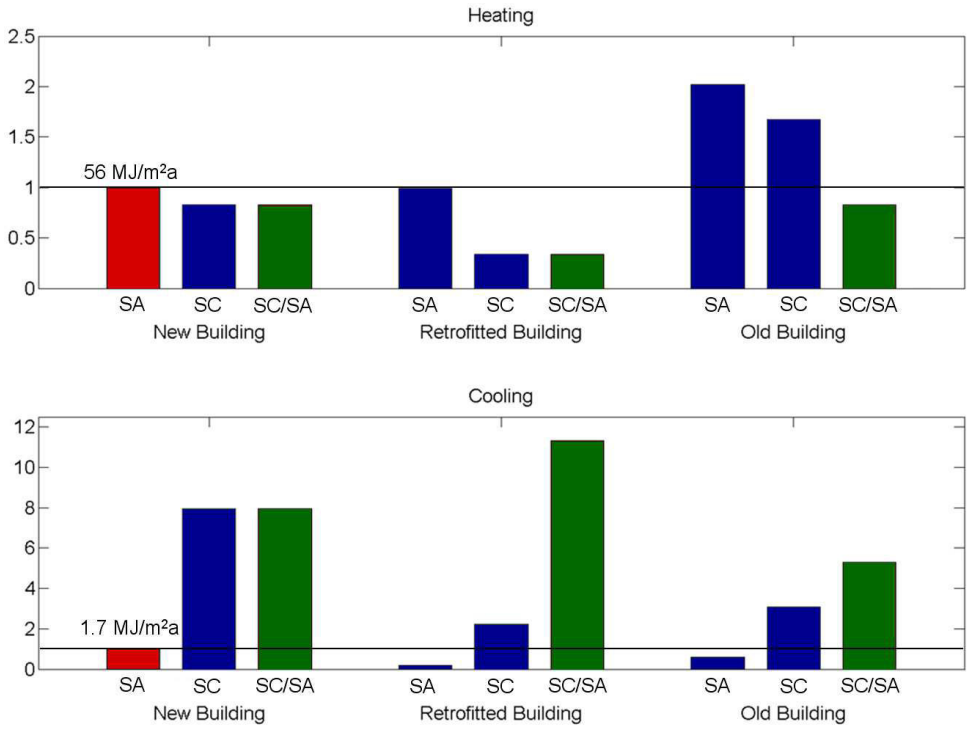

Figure 5.7: Annual space cooling and heating demands for three building types normalized by demands of the New stand-alone Building. Comparison between stand-alone buildings (SA) and buildings in street canyons (SC) with an aspect ratio of 1.

First the heating and cooling demands in the stand-alone configuration are discussed. The stand-alone configuration is considered as the reference. The Old Building type shows a higher heating demand than the New and Retrofitted Buildings, which can be explained by the lower insulation quality of the Old Building type compared to the New

and Retrofitted buildings. Remarkable is that the New and Retrofitted Buildings in stand-alone configuration have approximately the same heating demand although their glazing fraction is quite different (respectively 50 and 25 %). For these types of buildings, it can be observed that the convective heat losses through the glazed areas are largely compensated by the solar gains through the glazing, and as a consequence both building types show the same heating demand. However, the higher glazing fraction of the New Building type leads to a higher cooling demand attributed to the higher solar gains through the glazing. Reduction of the glazing fraction, like for the Retrofitted and Old Building, results in lower cooling demands. The Retrofitted Building, which is well insulated, shows the lowest cooling demand, which can be explained by the lower heat gains through the insulated walls.

Comparing stand-alone and street canyon building configurations, a reduction of heating demand and an important increase of cooling demand for the buildings in street canyon configuration can be observed. Several urban phenomena explain these observations. A first reason is that solar radiation becomes entrapped inside street canyons, leading to higher building façade temperatures, and thus to lower heating and higher cooling demands in the street canyon configuration. The solar radiation is entrapped in the following way: solar radiation heats up the sunlit urban surfaces that in return emit longwave radiation heating up other surfaces that are not sunlit. The solar radiation is then reflected multiple times between neighbouring buildings instead of being preferably reflected back to the environment as is the case for the stand-alone configuration. During summer the solar angles are higher and more solar radiation is entrapped compared to the winter. This means that the solar radiation entrapment relatively has a more important effect on the cooling (in summer) than on the heating demand (in winter). A second reason for lower heating and higher cooling demands in a street canyon configuration is that at night-times the building façades cool less compared to a stand-alone configuration, because the longwave radiation to the cold sky is partially blocked by the other buildings in a street canyon configuration. In winter, the reduction of longwave heat losses during night-time leads to a lower heating demand in street canyon configuration compared to stand-alone buildings, while in summer it leads to a higher cooling demand. A third reason for the difference in energy demand between stand-alone and street canyon configuration is that in the street canyon configuration the convective heat losses and the removal of heat from the street canyon is much lower due to the lower local wind speeds inside the street canyons and the lower ventilation potential in a street canyon setting. A fourth reason is that due to the UHI phenomenon higher air temperatures occur in the city and thus also in the street canyons. The UHI effect thus further contributes to the reduction of the heating demand during winter and the increase of the cooling demand during summer. The UHI effect also decreases the night ventilation potential and possible night-time passive cooling, which will be analysed in more detail in section 5.3.4.

Comparing the building heating demand in stand-alone and street canyon building configurations in more detail, it can be observed that the heating demand of the Retrofitted Building in street canyon configuration is relatively more reduced (SC/SA ratio of 0.3) compared to the New Building type with higher glazing fraction (SC/SA ratio of 0.8). This difference can mainly be attributed to the balance between heat gains by radiation and the convective heat losses through the glazing. For the Retrofitted Building in street

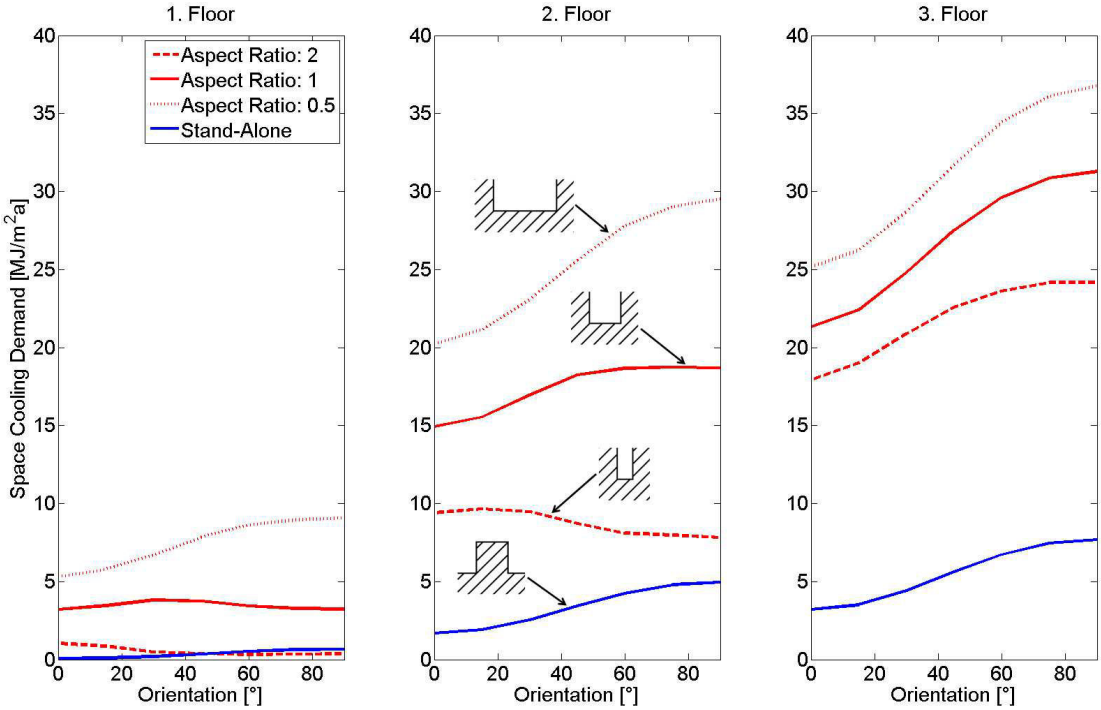

Figure 5.8: Annual space cooling demands for the three floors as a function of the street canyon orientation, for the three street canyon aspect ratios and the stand-alone building (New Building type).

canyon configuration this balance is more positive towards lower heating demand than for the New Building, especially due to the increase in longwave radiative gains. For cooling, the relative difference between the energy demand in street canyon and stand-alone configuration is very high, with SC/SA ratios of 10. This indicates the high sensitivity of space cooling to urban configurations for moderate climates. It should be noted that these large differences are due to the fact that the space cooling demand for stand-alone buildings of this type is rather low for a climate like Basel. Therefore small changes in cooling demand may result in rather high relative differences (see section 5.3.6).

Figure 5.8 shows the annual space cooling demands for the New Building type in street canyon and stand-alone configuration. The results are given as function of the building orientation Θ for different street canyon aspect ratios. Different storeys of the building are considered: ground (1), middle (2) and top floor (3). In general the building cooling demand is higher for wide street canyons than for buildings in narrow street canyon configuration (or for the stand-alone building). Reason is that more solar radiation can enter wide street canyons and becoming entrapped inside. For all cases the space cooling demand is increasing from the first to the third floor. This can be explained by the fact that the lower floors are for a longer time period protected from the sun at day-time due to shadowing by neighbouring buildings. This shadowing effect is more important for narrow street canyons than wide street canyons. The first floor is additionally cooled by the contact to the colder soil underneath the building, while the upper floor level is additionally heated by the solar radiation absorbed by the building roof. For a building

orientation 0 ° (north - south façades) the cooling demand is lower than for 90 ° (east - west façades), with exception for the lower floors in the narrower street canyons ($H/W < 1$). In general east - west façades (90 ° orientation) are sunlit for a longer period during day-time leading to higher cooling demands. However, east - west façades of the lower floors in a narrow street canyon receive less direct solar radiation, because of the smaller solar angles during the morning and evening than for north - south façades during the afternoon, leading to lower cooling demands for this case.

5.3.3 Radiative fluxes at the surfaces

In this section the radiative heat fluxes and surface temperatures are analysed in more detail for a 48 h time period during summer. The stand-alone and street canyon configuration for the New Building type with an orientation of 0 ° (north - south oriented façades) are considered.

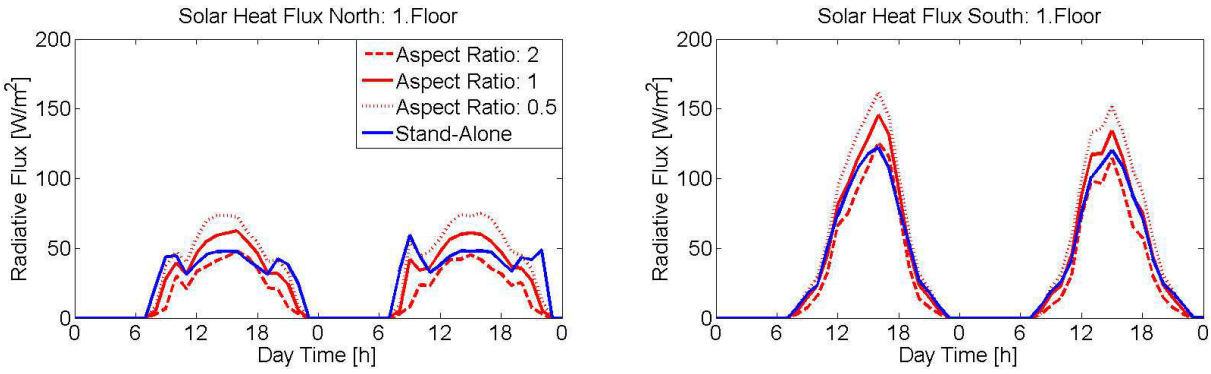

Figure 5.9: Absorbed solar radiation on the south and north façades of the first floor for a stand-alone building and buildings surrounded by street canyons with different aspect ratios (0.5, 1 and 2).

In Figure 5.9 the total solar radiation on the building façade (sum of the direct, diffuse and reflected radiation) is given for the north and south orientation. Results for the first building floor are given for street canyons with different aspect ratios. The first floor is selected, because here the influence of the neighbouring buildings on radiation is highest. As known, more solar radiation is absorbed on the south façade that is sunlit for a longer part of the day compared to the not sunlit north façade. The solar radiation on the south façade follows a classical daily pattern: increasing during the morning, reaching a peak in the afternoon and decreasing during the evening. The solar radiation on the north façade is on the contrary much more constant over day-time showing three smaller peaks, one in the morning, a second in the afternoon and a third in the evening. The peaks in the morning and evening are due to the direct solar radiation, while the peak in the afternoon is mainly due to the diffuse solar radiation. For the street canyon configuration with aspect ratio 0.5, the afternoon peak becomes more important due to the reflection of the direct solar radiation hitting the south façade of the neighbouring buildings in the street canyon.

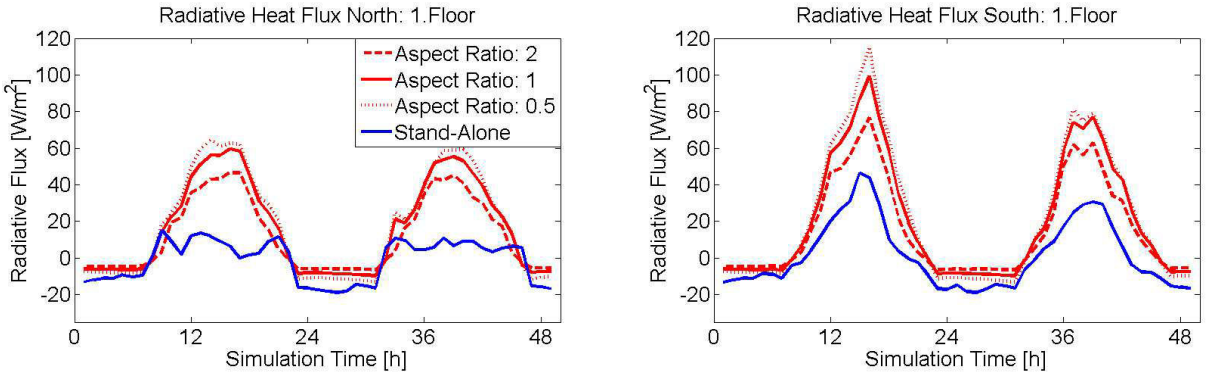

Figure 5.10: Absorbed radiation (longwave plus solar) on the south and north façades of the first floor for a stand-alone building and buildings surrounded by street canyons with different aspect ratios (0.5, 1 and 2).

In wider street canyons (aspect ratio 0.5) more solar radiation is absorbed by the building façades, because more solar radiation can enter the street canyon and is entrapped due to multiple reflections in wider street canyons. This explains why a façade of a stand-alone building receives less radiation, since in this case the façade does not receive additional radiation by reflection from other surrounding building façades. Exception is the case of the narrowest street canyon (aspect ratio of 2), where the solar radiation entering the street canyon is strongly reduced due to shadowing by neighbouring buildings. The solar radiation on a south façade is less sensitive to the street canyon aspect ratio, because here the direct solar radiation overpasses substantially the contribution by reflection from neighbouring building façades.

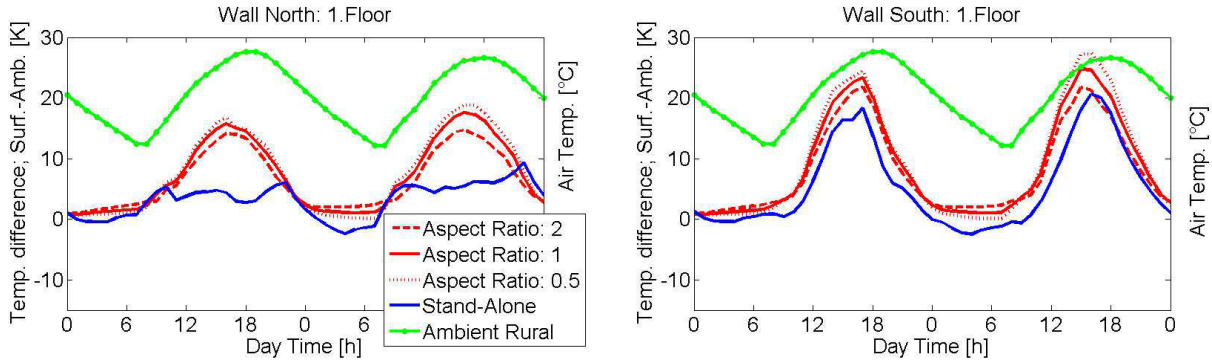

Figure 5.11: Differences between the wall surface temperature and the ambient air temperature for the north and south façades of the first floor for a stand-alone building and buildings surrounded by street canyons with different aspect ratios (0.5, 1 and 2).

In Figure 5.10 the total radiation, sum of longwave and solar radiation, is given for south and north façade of the first building floor. As for the solar radiation, more total radiation is absorbed on the south than on the north façade due to higher solar irradiation values. Comparing Figures 5.10 and 5.9, it can be observed that the total radiation on the

south façade is lower than the received solar radiation, while on the north façade these values are quite similar. A south façade heats up due to absorption of solar radiation and then emits longwave radiation to the cold sky and the neighbouring building façades, leading to lower total (net) values of radiation. During night-time negative values of total radiation are observed, which can be explained by the longwave radiation to the cold sky. On both façades (but more pronounced on the north façade) the total radiation is much higher for buildings in street canyon than in stand-alone configuration, since the stand-alone building receives no longwave radiation reflected from the neighbouring buildings and radiates much more heat to the cold sky. The total radiation on façades increases with the width of the street canyons. Wider street canyons receive more total radiation, leading to the higher entrance values and more entrapment of solar radiation. In the street canyon configuration, at night-times the radiation to the cold sky is much reduced due to the blockage by neighbouring buildings. The blockage effect is more important for narrow than for wide street canyons.

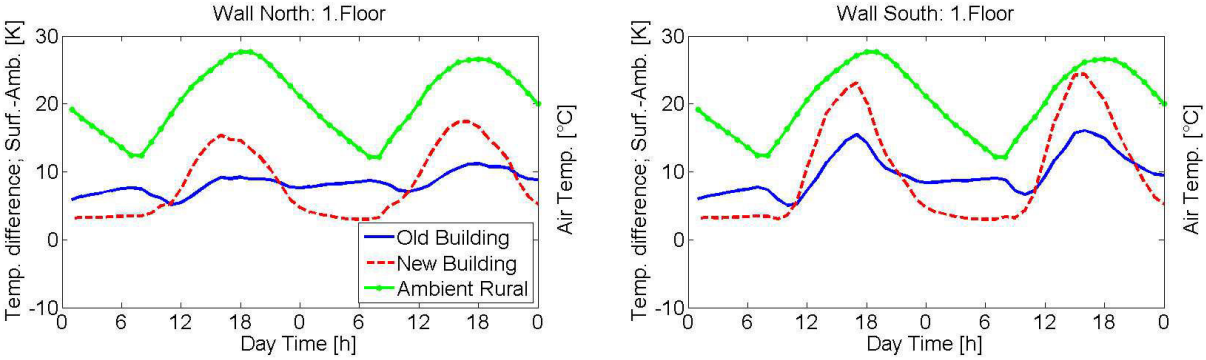

Figure 5.12: Differences between the wall surface temperature and ambient air temperature for the north and south façades of the first floor for the New and the Old Building with an aspect ratio of 1.

In Figure 5.11 the wall excess surface temperature (EST), defined here as the difference between wall surface temperature and the ambient air temperature, is given for the north and south façades of the first building floor. In the case of a stand-alone building, the ambient temperature represents the temperature at the meteorological station. In the street canyon case, it represents the air temperature at a location close to the façade, which accounts for the UHI and urban microclimate effect. The ESTs are generally positive with exception for the stand-alone building at night-times. Comparing Figure 5.10 and 5.11, it can be observed that the ESTs follow the same tendencies as the total radiation, since the surface temperature is strongly linked to the net radiative heat flux. A second influencing factor is the convective heat transfer at the surface, but their influence is found to be much smaller than the influence of the radiation. A more detailed analysis of the influence of the CHTC correlations on the space cooling demand is conducted in section 5.3.1. The ESTs are for all cases higher on the south than on the north façade due to higher total net radiative heat fluxes on south façades. Especially on the north façade the ESTs are significantly higher for the street canyon buildings during the day. The lowest ESTs are found for the stand-alone building. The highest ESTs are found at

day-time for the widest street canyon, while at night-time the highest excess temperatures occur in the narrowest street canyon.

In Figure 5.12 the excess surface temperatures of the façade of the first floor for the New and Old Building are compared (street canyon aspect ratio of 1). The ESTs for the New Building are higher during the day and are lower during night than for the respective ESTs of the Old Building. This different behaviour is mainly caused by the higher thermal mass available in the Old Building façade leading to more damping of the extremes in EST.

5.3.4 Sensitivity study

In this section, a sensitivity study of the space cooling demand is presented. The influence of UHI effect, the use of night ventilation for passive cooling, the solar absorption coefficient of the façade and internal gains are considered. For the internal gains two cases are considered: offices and residential buildings, which show lower gains (see Table 5.3). For the solar absorption coefficients of the façades, standard values of 0.5 for the reference case and values of 0.25 considering white paints are used. For the sensitivity study, the street canyon has an aspect ratio of 1 and an orientation of 0°. The New building case is considered. For the street canyons the results are normalized to the cooling demand of the case with UHI, night ventilation, solar absorption coefficients of 0.5 and internal gains of the office building (reference case). For the stand-alone building, the reference case is the one without UHI effect.

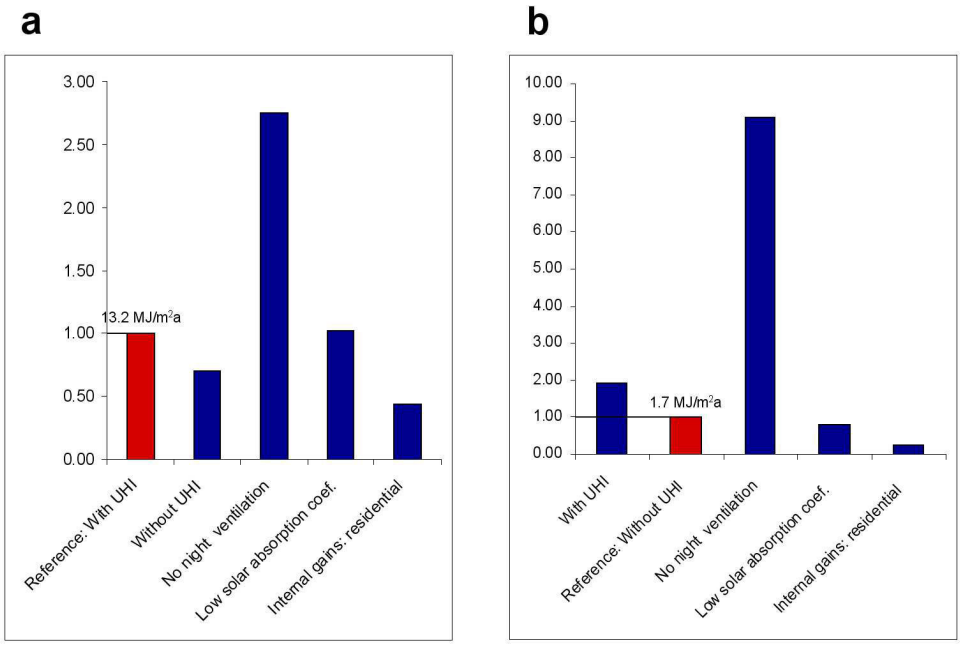

Figure 5.13: Annual space cooling demand for the New Building type and an orientation of 0°. (a) Building surrounded by street canyons with an aspect ratio of 1, normalized by the case with UHI intensity; (b) stand-alone building, normalized by the case without UHI intensity.

In Figure 5.13 the results of this sensitivity study are given for the street canyon configuration (Figure 5.13a) and the stand-alone building (Figure 5.13b). The cooling demand for the street canyon case decreases when no UHI effect is considered indicating the need for considering UHI for cooling demand simulations. For the street canyon configuration the space cooling increases significantly (by a factor of 2.7) when no passive cooling by night ventilation is considered. The effect of cooling by night ventilation is much more significant for the stand-alone building (Figure 5.13b), where the cooling demand increases by a factor 9 compared to operation without night ventilation. The lower influence of night ventilation on the cooling demand in the street canyon case, compared to the stand-alone setting, can be attributed to the higher temperature of the air, which is used for ventilation at night-time. The higher air temperature for ventilation is due to the UHI effect in the street canyon case. However it has to be remarked that even in the street canyon case for Basel, passive cooling by night ventilation can significantly reduce the building energy demands and has to be considered as a valuable approach to save energy for cooling. The application of white paints for the stand-alone building leads to a small decrease in cooling demand (90 %) due to the reduction of heat gains by increasing the reflection of radiation. For the street canyon building, the lower solar absorption coefficients (0.25 instead of 0.5) of the façades have almost no impact on the space cooling demand. Reason is that the use of white paints leads to an increase of radiation entrapment due to the multiple reflections. The solar radiation becomes more often reflected between the buildings, until it is absorbed. For residential buildings showing lower internal gains less energy for cooling is needed both for street canyon and stand-alone building.

5.3.5 Different approaches

In the sections above the important influence of the urban microclimate on energy demands in buildings was discussed. Most of the today used BES models do not account for the urban microclimate and therefore cannot accurately predict the space cooling heating demands for buildings in urban areas. In this section a sensitivity analysis is conducted with the aim to identify the influence of the urban microclimate modelling with different degrees of complexity on the predicted space cooling and heating demands in a building. All simulations in this section are conducted with the intention to predict the energy demands for a New office building in a street canyon with an aspect ratio of 1 and an orientation of $\Theta = 0$ °. In this section not only CHTC correlations are used for the convective heat transfer but also coupled BES-CFD simulations are conducted. Because the coupled BES-CFD simulations are computationally expensive, simulations for a time period of one week are run (instead of 1 year). First, simulation are run for one week with rather high air temperatures ($12-28\ °C$) and wind speeds ($0-8\ m/s$), representing weather conditions, where space cooling is important. Then the same simulations are run for a week with rather low temperatures ($-9-10\ °C$) and high wind speeds ($0-11\ m/s$), where space heating is important. The incoming solar radiation is similar for these two weeks. The different used modelling approaches are described in Table 5.4 and the results for the weekly space cooling and heating demands are given in Figure 5.14.

For the first simulations the building was modelled as a stand-alone building using CHTC correlations from ASHRAE [164] and not considering the UHI effect. In most

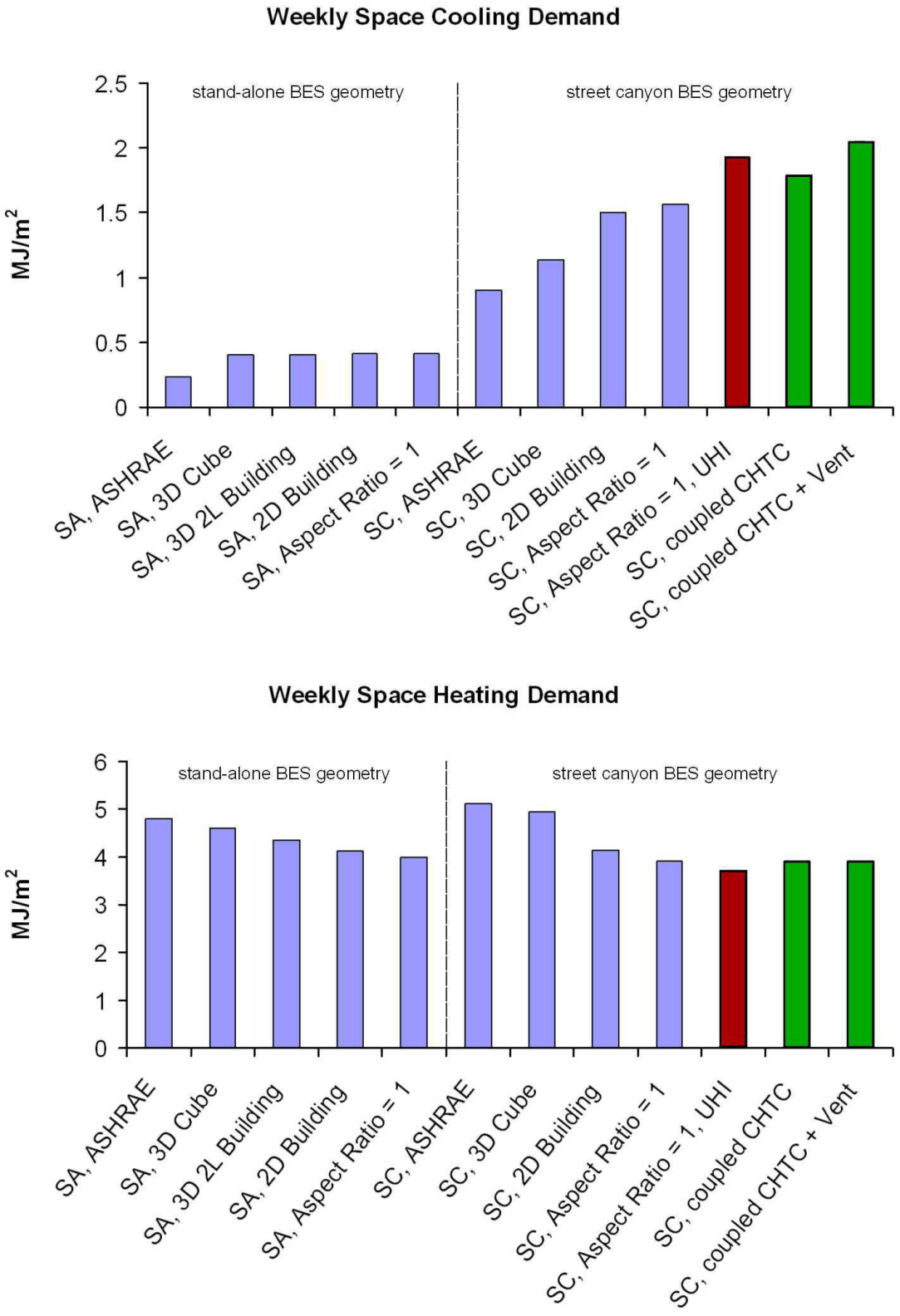

Figure 5.14: Weekly energy demand for space cooling and heating with different modelling approaches (Table 5.4).

Name	BES geometry	CHTC correlation	UHI	Ventilation
SA,ASHRAE	stand-alone	ASHRAE	no	T_{amb}
SA, 3D Cube	stand-alone	CFD cubical building	no	T_{amb}
SA, 3D 2L Building	stand-alone	CFD building length: 2L	no	T_{amb}
SA, 2D Building	stand-alone	2D building	no	T_{amb}
SA, Aspect Ratio = 1	stand-alone	aspect ratio: 1	no	T_{amb}
SC,ASHRAE	street canyon	ASHRAE	no	T_{amb}
SC, 3D Cube	street canyon	CFD cubical building	no	T_{amb}
SC, 2D Building	street canyon	2D building	no	T_{amb}
SC, Aspect Ratio = 1	street canyon	aspect ratio: 1	no	T_{amb}
SC, Aspect Ratio = 1, UHI	street canyon	aspect ratio: 1	yes	T_{amb}
SC, Coupled CHTC	street canyon	coupled	yes	T_{amb}
SC, Coupled CHTC + Vent	street canyon	coupled	yes	coupled

Table 5.4: Different simulation cases; Results are given in Figure 5.14.

BES models a building would be modelled in this way, even if the building, for which the simulations are conducted, is located in an urban area. With this simulation approach the lowest space cooling demands and rather high space heating demands are predicted compared to the other simulation approaches. Using CHTC correlations from CFD the predicted space cooling demands increase, because they predict a lower convective heat loss, when the wind speeds are lower compared to the CHTC correlations from AHSRAE. There are only very small differences for simulations using different CHTC correlations from section 3.2.4. For the space heating demand the difference between the CHTC correlation from ASHARE and from CFD is smaller but the decrease of the predicted space heating demand for the different correlations from CFD is larger.

As a next step the geometries in the BESs were modified to account for the radiation exchange between neighbouring buildings. Accounting for the radiation exchange has a significant impact on the predicted space cooling and heating demands. Using different CHTC correlations for BESs with a street canyon geometry has a bigger impact on the predicted space cooling demands than for the BESs with the stand-alone building geometry. For the street canyon geometries also CHTC correlations for stand-alone buildings are used here. This is done, to evaluate the theoretical error that is induced by using not appropriated CHTC correlations. For street canyons the convective heat transfer becomes relatively more important, because the heat loss to the cold sky by radiation is smaller. Using the UHI intensity schedules further increases the predicted space cooling demands and decreases the space heating demands. In a last step coupled BES-CFD simulations (described in section 3.1.4) are conducted to more accurately resolve the convective heat transfer at the building façades.

Figure 5.15 shows the CHTCs determined by correlations and coupled simulations for a week with rather high air temperatures ($12 - 28\ °C$) and wind speeds ($0 - 8\ m/s$). It can be observed that both CHTCs follow a similar trend. Reason is that the CHTC in the considered case are mainly determined forced convection related to the wind speed (Figure 5.15). To account for buoyancy, uniform temperatures inside the street canyon are used for the derivation of the CHTC correlation. Note that in a real street canyon there

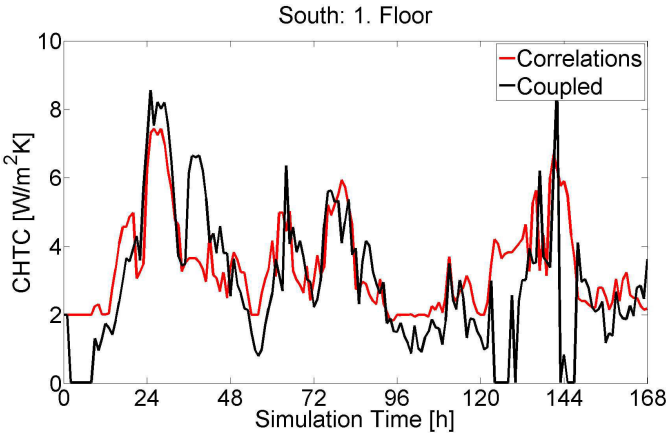

Figure 5.15: Comparison between CHTCs from correlations and coupled BES-CFD simulations.

will be temperature differences between the different surfaces in street canyons, which for simplicity is not accounted for in this study. With the coupled simulations these temperature distributions and the buoyancy effect can be accurately captured. This explains the differences that can be found in Figure 5.15 (note that for the times, when the CHTCs are 0 for the coupled simulations, there is no heat transfer, because the surface temperatures are equal to the ambient air temperatures). Figure 5.16 gives the corresponding space cooling demands. With the coupled BES-CFD simulations the predicted space cooling demand for the simulated week is 8 % lower than with the BES using CHTC correlations. The differences for the CHTCs in Figure 5.15 are large, while the differences for the

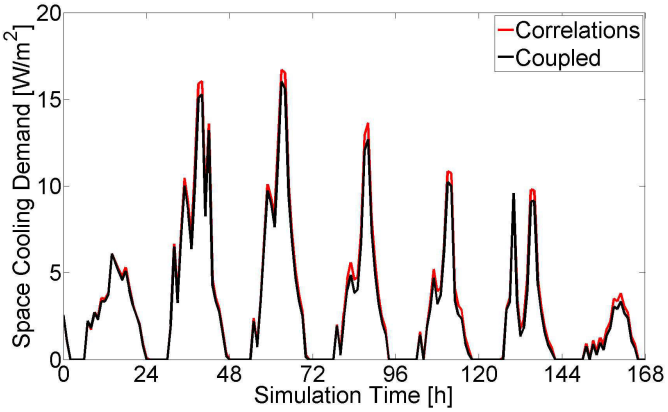

Figure 5.16: Space cooling demands for coupled and uncoupled BES simulations for a time period of a week.

space cooling demands become smaller between the coupled simulations and the CHTC correlation approach. This is due to the fact that the convective heat transfer is only a part of the total heat transfer at the building façades. For the street canyons considered here the differences between the two types of simulations are rather small, because the CHTC correlations were derived for this specific geometry. Note that the determination

of a CHTC correlation for specific geometry is computationally expensive due to the large number of CFD simulations that have to be conducted. Therefore the coupled BES-CFD simulations are also compared to simulations, where CHTC correlations from literature are used. Comparing the simulations, where the CHTC correlations from ASHRAE are used (SC, ASHRAE in Figure 5.14) with the coupled BES-CFD simulations in Figure 5.15, a significant improvement of the predicted space cooling demands can be observed. The coupled simulation predicts a 2.2 times higher space cooling demand than the simulation using the CHTC correlations from ASHRAE. When the air temperatures from the CFD simulations are used as the intake air temperatures for ventilation instead of the ambient air temperature, the predictions are further improved. The predicted space cooling demand of the simulation that uses the air temperatures from the CFD simulations, are with a factor of 1.14 higher, compared of the simulation using the ambient air temperature.

From the results of this section it can be concluded that it is important to use accurate models for the BESs, when the space cooling or space heating demands for a building in an urban area is predicted. Using not appropriated models can lead to large errors (here up to a factor of 8.8) in the energy demand predictions.

5.3.6 Different climates

So far, the impact of the urban microclimate on the energy demand in buildings is studied for the moderate European climate of Basel (Switzerland) in this thesis. Therefore the space cooling demands are, especially for the stand-alone buildings, rather low. As a consequence small changes in the space cooling demand cause rather high relative differences between the different modelling approaches. In this section the annual space cooling demands predicted with different modelling approaches are analysed for three different climates. Additionally to the climate of Basel the BESs are conducted for the climate of Madrid (Spain) and the climate of New Delhi (India). In Figure 5.17 one year air temperature profiles are given for the three climates. The air temperatures for Madrid are for the whole one year period some degrees higher compared to Basel. New Delhi has, throughout the whole year, significantly higher air temperatures than the two other climates. For the incoming solar radiation the trend is very similar with similar relative differences as for the temperatures.

For all BESs in this section the New building type is used for all simulations and the orientation is $\Theta = 0\ ^\circ$. For Basel the UHI schedules are used to consider the UHI effect. No measured data were found that could be used to derive UHI intensity schedules for Madrid and New Delhi.

The annual space cooling demand for buildings in Basel, Madrid and New Delhi are given in Figure 5.18 for different modelling cases. In the first step the space cooling demand is determined only considering the radiation exchange between buildings, using CHTC correlations for a stand-alone building (see section 3.2.4) for all geometries and not considering the UHI effect ("Base Case"). For the second step corresponding sets of CHTC correlations are used for each street canyon, as determined in section 3.2.4 (case: "CHTC"). For the last step the above described UHI intensity approximations are used for the street canyon cases (case: "UHI"). Due to the higher ambient air temperatures

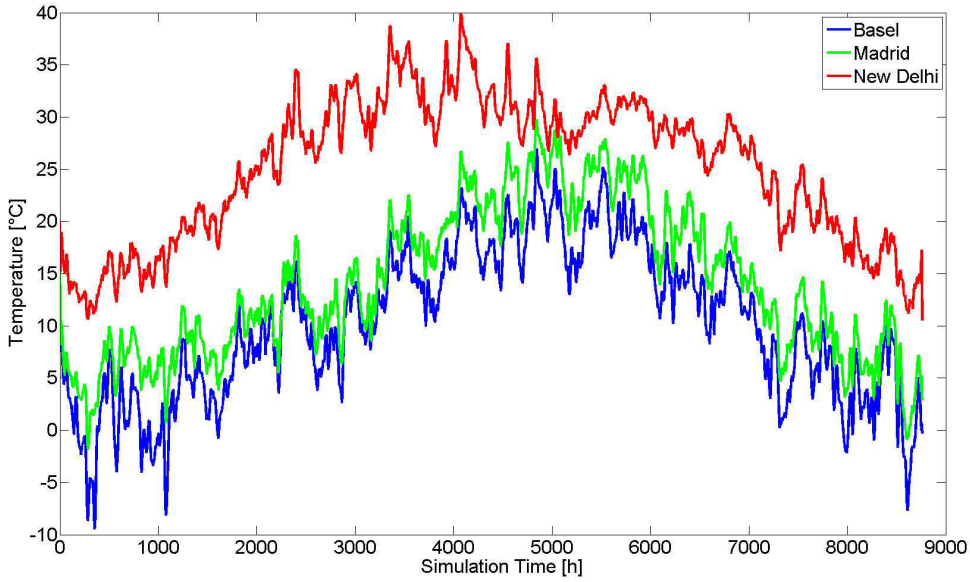

Figure 5.17: Air temperatures for Basel, Madrid and New Delhi (typical meteorological year TMY) for one year.

more energy is needed for space cooling in Madrid and New Delhi than in Basel for all modelling approaches. However when comparing the results for the different approaches for each location, the trend is the same. The space cooling demand for the stand-alone building is much lower than for the building situated in a street canyon. The largest differences are due to the radiation effect. While the trend for the different approaches is the same, the differences between the different approaches are highest for Basel and lowest for New Delhi. The differences between the different cases are smaller for the hotter climate. Reason is that the cooling demand that is very sensitive to the high ambient air temperatures, and therefore the additional heat gains due to the radiation interaction, lower convective heat transfer and UHI effect have a smaller impact on the overall demands. For Basel a building in an urban street canyon with an aspect ratio of 0.5 has a 7.7 times higher space cooling demand than the same stand-alone building, solely due to the radiation exchange with the neighbouring buildings. This value is decreasing to 2.6 for Madrid and 1.5 for New Delhi. This confirms the assumption (see section 5.3.2) that the differences in space cooling demands are rather high in Basel due to the fact that the space cooling demands for stand-alone buildings are low and therefore already moderate changes of the absolute values cause rather high relative differences. Not only the differences between the stand-alone buildings and buildings in street canyons are lower for hotter climates, but also the differences between street canyons with different aspect ratios.

Comparing the results for different climates, it can be observed that the general conclusions for the moderate European climate of Basel are also valid for other climates, but the relative differences are decreasing with increasing ambient air temperatures.

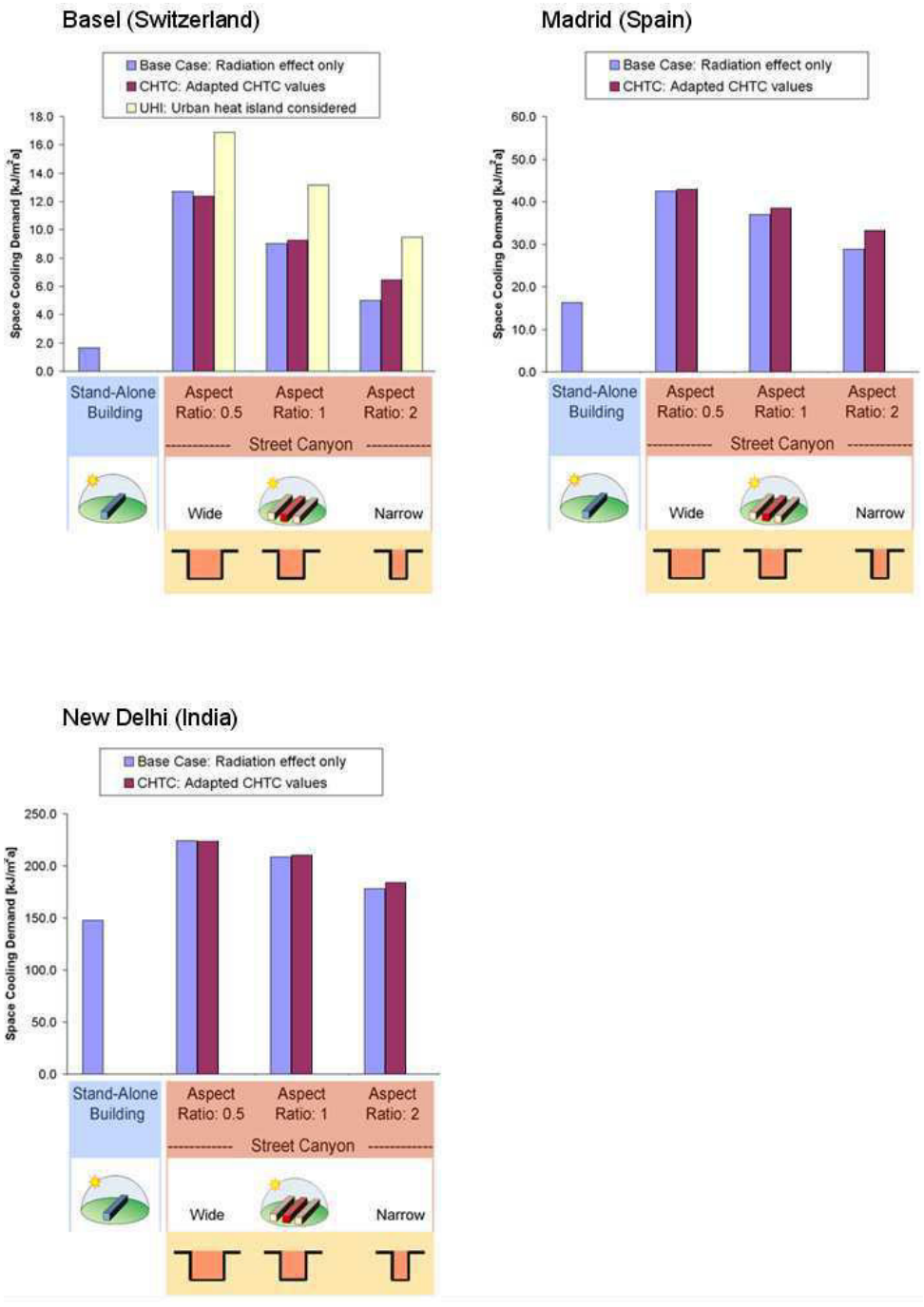

Figure 5.18: Annual space cooling demand for different climates and different modelling cases.

5.4 Discussion

The influence of the urban microclimate on the space cooling and space heating demand of buildings was investigated. This study was conducted for idealized stand-alone buildings and urban street canyons. Since the focus of this study is more on the methodology and on the analysis of the importance of the different aspects of the microclimate, more realistic geometries like street intersections, buildings with pitched roofs or balconies etc. are not considered. However the same approach can be used for other (more complex) urban geometries. Urban street canyons were chosen as they are the most generic elements a city is composed of. Street canyons are also critical in terms of space cooling demand, due to the important effect of entrapment of the solar radiation and the wind sheltering by neighbouring buildings. Further this approach can be used for a wide range of different building types.

This study was mainly conducted for the Swiss city of Basel. Cooling demand values are quite different for cities in other (e.g. hotter) climate zones (see section 5.3.6). However the radiation exchange between urban surfaces, the UHI effect and the reduction in convective heat transfer are also here the most important phenomena to be considered in the assessment of the impact of urban microclimate on energy demand. In this study the UHI intensity schedules were determined from field measurements. For most simulations no feedback mechanisms, such as heat gains/losses from building façades or building waste energy that influence the air temperature inside the street canyon were considered, nor the influence of these increased temperatures on the convective heat transfer and night ventilation cooling potential. An option to account for these feedback mechanisms is to directly couple the BES model with CFD. Such coupled simulations are however computationally expensive and therefore not yet practically feasible for annual building energy predictions. However this approach was demonstrated for a period of one week in section 5.3.5. For the case simulated in this section, there was no significant difference between the results using CHTC correlations and the coupled simulations. The results were compared with simulations, where precalculated CHTC correlations from CFD were used instead of CHTC correlations from literature. For the precalculated correlations the microclimate in the street canyons is already modelled to a certain extent.

It was found that the exchange of longwave radiation with neighbouring buildings has a determining impact on the net radiative heat exchange at the building façade. An example with typical longwave radiation values is included here to illustrate the importance of this urban microclimatic phenomenon. The geometry considered for this example is a stand-alone building and a building in street canyon configuration as given in Figure 5.19. Typical surface temperatures and surface properties used in this example are given in Table 5.5. For simplification, they are considered to be constant over the surface. The air temperature is 25 $°C$ and the temperature of the sky is 15 $°C$. The surfaces 4 and 6, and the ground surface for the street canyon case, are assumed to be heated by the sun to temperatures higher than the ambient air temperature.

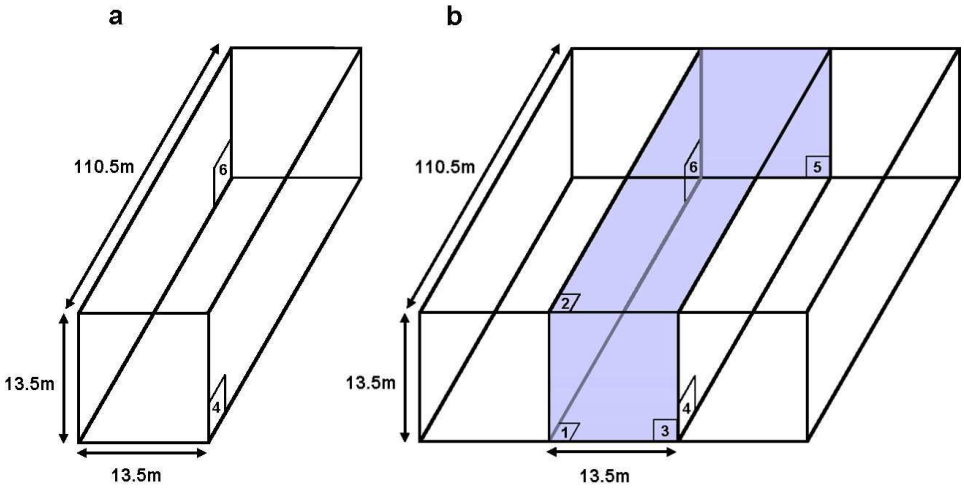

Figure 5.19: Stand-alone building (a) and the street canyon (b) geometries of the radiation example.

Surface	Temperature [°C]	Emissivity [-]
1	28	0.9
2	15	1
3	25	0.9
4	40	0.9
5	25	0.9
6	30	0.9

Table 5.5: Surface temperatures and longwave emissivities of the surfaces in Figure 5.19.

The longwave radiative flux q at the surfaces of the stand-alone building is calculated using the Stefan-Boltzmann law:

$$q = \sigma\varepsilon \left(0.5 \left(T_{Surf}^4 - T_{Sky}^4\right) + 0.5 \left(T_{Surf}^4 - T_{Gr}^4\right)\right) \tag{5.3}$$

where T_{Surf} is the surface temperature and T_{Gr} is the temperature of the ground (here $25°C$).

For the street canyon configuration the simplified approach by Glück 1997 [192] with Gebhart factors is applied to compute the longwave radiative heat fluxes. The radiative heat fluxes for the stand-alone building are respectively 114 W/m^2 for surface 4 and 54 W/m^2 for surface 6. The radiative heat fluxes for the street canyon configuration are respectively 87 W/m^2 for surface 4 and 7.6 W/m^2 for surface 6. The stand-alone building shows a total heat loss due to longwave radiation to the environment of 250 kW, while this reduces to 141 kW for the street canyon building. This example with typical radiative heat fluxes at the façades shows that a building in a street canyon has only 56 % of the longwave heat losses compared to a stand-alone building. This illustrates the importance of accounting for the longwave radiation exchange between neighbouring buildings in

urban areas.

5.5 Conclusion

The space cooling and heating demands for a stand-alone building and buildings in an urban street canyon are compared mainly for the moderate European climate of Basel (Switzerland). The three main influencing mechanisms of an urban microclimate are considered: (i) the radiation exchange between neighbouring buildings, (ii) the urban heat island (UHI) effect and (iii) the reduced convective heat transfer due to wind sheltering. This study was conducted for three different building types: a New, an Old and a Retrofitted Building.

It is found for all building types that the annual space cooling demand is higher and the space heating demand lower for buildings in a street canyon configuration than for the same stand-alone building. For the considered climate of Basel in Switzerland, the difference between rural and urban areas is higher for space cooling than for heating. All three mechanisms of the urban microclimate contribute to the observed trend. The most important mechanism is the radiation exchange between urban surfaces. In street canyons the net radiation on the building façades, being the sum of longwave and solar radiation including multiple reflections, is higher than for façades of stand-alone buildings. Additionally, for buildings in street canyons, the longwave radiation to the cold sky, and respective cooling down of the façades, is partially blocked. Therefore higher façade surface temperatures can be found in urban than in rural areas. These higher temperatures of the building façades directly cause higher space cooling and lower space heating demands. The aspect ratio of the street canyon plays an important role: in wider street canyons more solar radiation may enter leading to more radiation entrapment. In narrow street canyons radiation entrance is decreased during day-time due to shadowing, while during night-time the blockage of longwave radiation to the sky increases. North oriented façades in a street canyon configuration receive much more longwave and solar radiation compared to stand-alone buildings due to the radiation entrapment. The urban heat island effect increases the air temperature in street canyons. Neglecting the urban heat island effect leads to an important underestimation of the cooling demand. The cooling potential by night ventilation is significantly reduced in urban areas by the urban heat island effect, but for moderate climates night ventilation is found to be an important measure to reduce the space cooling demand. Related to the radiation effects in street canyons, it was found that the cooling demand increases at higher floor levels, and is higher for façades with east - west orientation. Use of white surfaces in street canyons is found to have only a minimal effect on the cooling demand, since the positive effect of higher reflections of radiation is minimized, as white paints also lead to an increase of the radiation entrapment effect. This study further shows the importance of choosing carefully the CHTC correlations for building energy simulation, especially for buildings in urban areas. For the street canyon building studied, the space cooling demand is by factor of 1.8 larger when considering CHTC correlations corresponding to an infinite long street canyon with low buoyancy, compared to the case with CHTC correlations according to a cubical stand-alone building with strong buoyancy. Most accurate results can be

achieved by using coupled BES-CFD simulations. Such simulations are computationally expensive. By establishing accurate CHTC correlation for the studied geometries, the errors of simulations using CHTC correlations can however be limited. For hotter climates than Basel in general the same trends can be found, but the importance of the different aspects of the urban microclimate is different.

This study shows the importance of accounting for the local urban microclimate, when predicting the energy demands for buildings in urban areas.

6 Conclusion and outlook

6.1 Conclusion

The aim of this thesis is to quantify the influence of the urban microclimate on the building energy demand for space cooling and heating using a more detailed and holistic approach. To capture the thermal effects of the urban microclimate a building energy simulation (BES) model was adapted to account for the thermal and solar radiation exchange between neighbouring buildings, the urban heat island (UHI) effect and the reduced convective heat transfer due to wind sheltering.

6.1.1 Modelling of convective heat transfer

In a first part of this thesis the convective heat transfer at the building façades is studied with steady RANS (Reynolds-averaged Navier-Stokes) CFD (computational fluid dynamics) simulations. Commonly correlations for convective heat transfer coefficients (CHTCs) obtained from field experiments are applied in BESs for a wide range of building geometries, even though these correlations are only accurate for the studied buildings. On the contrary, CFD allows to predict the convective heat transfer for (complex) building geometry. Building façades may be heated by the sun at day-times showing significantly higher surface temperatures than the surrounding air. Therefore buoyancy, which strongly influences the convective heat transfer, has to be considered in CFD simulations, especially during summery weather conditions with calm winds. Buoyancy is known to produce a lot turbulent kinetic energy (TKE). TKE, especially inside the thermal boundary layer, influences the convective heat transfer at surfaces. Therefore the near-wall region has to be modelled in such a way that the effect of buoyancy inside the thermal boundary layer is correctly accounted for. This effect can be resolved using low-Reynolds number modelling (LRNM). In LRNM the mesh has to be refined substantially in the near-wall region and as a consequence CFD simulations with LRNM are computationally expensive. Therefore, for CFD simulations of large urban areas, the air flow near surfaces is preferentially modelled using wall functions (WFs). It is shown that CFD simulations of, for example, street canyon configurations with standard wall functions may show errors in the convective wall heat fluxes up to 60% compared to LRNM. To improve the accuracy of WFs in terms of heat transfer predictions, the turbulent boundary layer at heated building surfaces in a street canyon is analysed in detail with LRNM. Two extreme types of normalized temperature profiles could be identified in the thermal boundary layer dependent on the Richardson number (Ri). One extreme at low Ri number could be attributed to forced convective flow, which is adequately described by the existing standard WFs. The second extreme at $Ri > 1$ could be attributed to mixed convective flows, where WFs have to adapted for non-equilibrium flows. Based on these two extremes, an adaptive

temperature wall function (AWF) was derived that varies between the two existing WFs dependent on a local Ri. In contrast to the global Ri, the local Ri is based on the local flow field and is therefore a better measure for evaluating the strength of the local buoyancy effects. The AWF can properly account for the co-occurrence of forced and mixed convective flow regimes at a single surface. With the proposed AWF, the errors in wall heat flux predictions were reduced to less than 10% for the majority over the whole range of Ri numbers of the cases studied.

CHTC correlations (CHTC as a function of the wind speed) are commonly used in BES models to determine the convective heat fluxes at building façades. As mentioned above, these CHTC correlations are commonly based on measurements at façades of stand-alone buildings. For buildings in urban areas the flow and therefore also the convective heat transfer is strongly influenced by neighbouring buildings. In this thesis, CHTC correlations are determined using CFD for seven different urban geometries, including stand-alone buildings and street canyons with different length and with different aspect ratios. The convective heat transfer is higher for stand-alone buildings than for buildings in urban street canyons. There are mainly two reasons for this difference: (i) for wind directions normal to the street canyon axis the main flow is quasi two-dimensional and therefore the local wind speeds are strongly decreased, compared to cubical buildings and (ii) due to wind sheltering of neighbouring buildings the local wind speed is further decreased. For low wind speeds the flow around buildings is mainly driven by buoyancy and the CHTCs have to be formulated as a function of the surface to air temperature difference instead of the wind speed.

6.1.2 Wind tunnel measurements

Wind tunnel measurements are conducted to study the influence of buoyancy on the flow in a scaled urban street canyon with heated surfaces. The two wall surfaces and the bottom surface of the street canyon were heated either individually or all together. The velocity and TKE fields were analysed in a cross-section of the street canyon. For most cases one main vortex is formed in the centre of the street canyon. This main vortex is strengthened, and the TKE inside the street canyon increased, by heating of (in order of importance) the ground, the leeward wall and all three surfaces for low freestream velocities. For windward wall heating a second counter-rotating vortex is formed due to buoyancy and the flow direction close to the windward wall changes from a downward to an upward motion. The centres of the main and secondary vortex change their position for constant windward wall temperatures with increasing freestream velocities. The trajectories of the vortex centres as a function of the freestream velocity are similar for all different windward wall temperatures.

The results of the wind tunnel measurements were subsequently used to validate the CFD models applied within this thesis. 2D steady RANS simulations with the standard and the realizable $k-\varepsilon$ turbulence models were performed with LRNM and WFs on the same, for LRNM optimized, mesh. For the simulations with WFs, this approach induces an error, because WFs cannot account for the damping of TKE in the near-wall regions. The general vortex structure can be predicted with all applied approaches, but the detailed flow field predictions differ significantly between the different CFD approaches. A

streamwise gradient of the approach flow profiles upstream of the street canyon cannot be avoided. The approach flow profiles of the velocity agree well with the measured profiles using LRNM, but there is a strong decay of the TKE. For the WFs on the other hand the TKE decays less, but the velocities are too low in the near-wall regions. In the shear layer at the top plane of the street canyon a better agreement can be observed when using WFs instead of LRNM. The velocities in the shear layer and inside the street canyon are overestimated with LRNM, while a good agreement of the velocities in the shear layer and inside the street canyon can be found with WFs. It is assumed that the reason for the velocity overestimation inside the street canyon with LRNM is caused by the overestimation of the velocity in the shear layer. To verify this assumption, a simulation with a computational domain with a short upstream extension was conducted with WFs. Using the short computational domain, the approach flow profiles cannot evolve and they are similar to the profiles of the simulations using LRNM. For this simulation the velocities inside the street canyon are similar to the velocities of the LRNM simulations. The simulations using WFs perform better for all isothermal and buoyant cases. With LRNM the temperatures inside the street canyon are underestimated and therefore also the induced buoyancy effects.

6.1.3 Energy impact

In a second part of this thesis the impact of the three main aspects of the urban microclimate on the building energy demand was studied with BESs for the moderate European climate of Basel (Switzerland). The radiation model, implemented in the BES model, was applied to consider the multiple reflections of the longwave and solar radiation between neighbouring buildings and to account for shadowing effects. To model the UHI effect, a diurnal schedule of the temperature difference between the rural and the urban air temperatures was specified for each month, based on measured data. The CHTC correlations, established in the first part of this thesis, were used to determine the convective heat transfer at the building façades. Three building types with different building envelopes (corresponding to a new, an old and a retrofitted building) and occupancies according to the standards and standard solar protection control were considered. All these aspects of the urban microclimate lead to an increase in space cooling and a decrease in space heating demands. The most important aspect for the studied cases is the radiation exchange between neighbouring buildings. At day-times the solar radiation is entrapped inside the street canyon due to multiple reflections and at night-times the longwave radiation to the cold sky is partially block by neighbouring buildings. These effects cause higher surface and building mass temperatures in urban street canyons compared to stand-alone buildings. Due to the UHI effect the convective heat transfer at the building façades and the passive cooling potential by night ventilation are decreased in urban compared to rural areas. The convective heat transfer is further reduced by the lower CHTCs caused by wind sheltering. Besides for the climate of Basel, the BESs were also conducted for the hotter climates of Madrid (Spain) and New Delhi (India). The same general trends were observed for the different climates. Therefore it is assumed that the general conclusions of this study are also relevant for other, here not studied, climates. No significant reduction in space cooling demands was observed by using façade paints with low solar absorption

coefficients, because the solar radiation is still entrapped inside the street canyon and only a small part of the radiation can be reflected out of the street canyon. Besides using precalculated CHTC correlations also coupled BES-CFD simulations were conducted. With coupled simulations buoyancy effects can be captured more accurately and a wide range of geometries can be studied in BES models without previously establishing CHTC correlations. However, no significant improvement in terms of building energy demand predictions could be found with the coupled simulations for the street canyon geometries of this thesis, because already the precalculated CHTC correlations were optimized for these geometries. It was shown that the convective heat transfer can be accurately captured with the proposed coupling method.

To conclude, in this thesis an approach of accounting for the urban microclimate, when conducting BESs for buildings in urban areas, is presented. With this approach it has been demonstrated that the urban microclimate has to be considered in sufficient detail to accurately predict building energy demands for space cooling and heating of buildings in urban areas.

6.2 Outlook

The approach of accounting for the urban microclimate in BESs, as presented in this study, has still to be further developed to be applied for a wide range of research topics and applications. Recommendations for future improvements and future research are given below.

6.2.1 Geometries

The studies in this thesis were mostly conducted for street canyon geometries with a wind direction normal to the street canyon axis. In reality for most weather conditions the wind flow is oblique to the street canyon axis. It was shown that the wind direction becomes mainly important for mixed convective flow regimes. The convective heat transfer predictions could be improved for these conditions by using three-dimensional street canyon geometries with oblique flow directions in CFD. For three-dimensional geometries the CHTC correlations are a function of the wind speed and the wind directions. This leads to a strong increase in computational costs to precalculate the CHTC correlations. Also for the coupled BES-CFD simulations using three-dimensional geometries could lead to improved results, but also to higher computational costs. Wind tunnel measurements with oblique wind directions need to be conducted for the validation of the three-dimensional CFD simulations. Already for the wind tunnel measurements with wind directions normal to the street canyon axis, measurements of 3D effects could lead to a better understanding of the flow structures. 3D effects could be measured with a stereoscopic PIV (particle image velocimetry) setup or with a horizontal light sheet (to measure the wind velocities in the direction of the street canyon axis). The AWF was developed for 2D street canyons. First tests indicated that the AWF is also valid for 3D street canyons. This however has to be further confirmed.

A next step could be to apply the proposed BES approach for more detailed building

geometries. Here it was assumed that the building façades have low or no roughness and all the buildings have flat roofs. To determine the building energy demands for more realistic building geometries, balconies, window sills, pitched roofs, the roughness of the building surfaces etc. could be considered more accurately. These building details could be modelled in the BESs, in the CFD simulations and for the wind tunnel studies. To study more realistic flow fields in the wind tunnel, a scaled atmospheric boundary layer could be generated by using spires and roughness elements for the approach flow. Another option to model an atmospheric boundary layer would be to install a row of street canyons inside the wind tunnel to allow the atmospheric boundary layer to develop upstream of the studied street canyon. Further the complexity of the geometries could be increased from street canyons to street intersections to a group of buildings. These more complex geometries could mainly be used for the CFD and BESs. CHTC correlations could be established or BESs could be coupled with CFD to simulate the thermal behaviour of a specific building located in a more complex neighbourhood. In CFD the AWF has first to be validated with LRNM results, before it can be applied to complex geometries. Also the BES models have to be further developed to account for more than one building.

In this thesis meteorological data were adapted to account for the UHI effect and were used as boundary conditions for the simulations. For more realistic boundary conditions the CFD and BESs could be coupled with large-scale models (e.g. mesoscale climatic models) to predict more accurately the UHI.

6.2.2 Fluid flows

Rather simplified CFD models (2D steady RANS with a $k-\varepsilon$ turbulence model) were chosen to save computational cost. The results of the CFD simulations could be improved by using for example more accurate turbulence models. The AWF would have to be adjusted for other turbulence models, because it was developed for the realizable $k-\varepsilon$ model. More complex turbulence models might significantly improve the CFD simulations of the validation study. Especially time resolved LES (large eddy simulation) or URANS (unsteady RANS) simulations are expected to predict more accurate air exchange rates between the street canyon and the freestream flow, because flushing events could be captured with these models. The AWF, developed in this thesis, can account for the production of TKE by buoyancy, using the local Ri number as a criterion. A second criterion could be defined to account for increased turbulence levels due to advection or separation at edges of bluff bodies. The highest degree of complexity for the CFD simulations could be reached, when also accounting for the TKE produced by traffic, the vegetation in urban areas and the moisture transport.

The validation study could be improved, if additional wind tunnel measurements are carried out. Heat flux measurements at the heated surfaces and spatially high resolved temperature measurements in the flow would allow to validate the heat fluxes inside and at the top plane of the street canyon. A temperature measurement technique needs to be developed, to be able to measure the temperature field in the air with a high resolution. The requirements for such a measurement technique are that it does not disturb the flow field and that it is not influenced by longwave radiation from the heated surfaces. The main focus of additional flow measurements should be on the top plane of the street

canyon, where heated air is leaving and fresh air is entering the street canyon and on the flow above the street canyon. Therefore in these regions additional flow and temperature measurements should be conducted. The temperatures at the heated surfaces were here uniformly distributed. In reality, due to for example shadowing, the temperatures will be not uniformly distributed at building surfaces. To get a realistic temperature distribution at the surfaces, they could for example be heated by infrared lamps, representing the sun, instead of using heating mats. A wide range of forced and mixed convective street canyon flows were measured within this thesis. Additionally natural convective flows (no freestream velocity) could be measured. In full-scale street canyons the flow is turbulent for natural convection. However, it is difficult to achieve the corresponding turbulence level for natural convective flows in wind tunnels. Therefore the transition from laminar to turbulent flows has to be studied in wind tunnels, before modelling natural convection in urban street canyons. In this thesis time averaged flow field were measured and used for the validation of steady CFD simulations. Time resolved flow measurements could be conducted to study the buoyant flow structures in more detail. The POD (proper orthogonal decomposition) method could be applied to detect coherent structures. POD could also be used to compare time resolved measurements with LES results.

6.2.3 Energy impact

In this thesis the influence of the UHI effect on the building energy demands was investigated. The UHI intensity is, amongst others, dependent on the surface temperatures in urban areas. The impact of the façade temperatures on the UHI intensity was not studied. To study this interaction between the UHI effect and the thermal behaviour of buildings, coupled BES-CFD simulations have to be conducted. Lower façade temperatures lead in coupled simulations to lower air temperatures and therefore lower UHI intensities. Strategies to mitigate the UHI effect could be developed based on coupled simulations, because the effects of different wind flow patterns and different surface temperatures could be captured in a coupled form. The radiation model, integrated in the BES model, was used to determine the radiation distribution. This radiation model has strong limitations. It can only be applied for strongly simplified geometries. Therefore it is recommended to apply a more advanced stand-alone radiation model (e.g. Solene or the radiation model implemented in CitySim) for future research. Only with a more advanced radiation model, it is possible to follow the recommendation of applying the approach, proposed in this thesis, for more complex geometries. Besides for determination of heat fluxes, the radiation model could also be used to consider changes in electricity demands due to changed artificial lighting demands due to shadowing. In this thesis the ventilation of the buildings was assumed to be driven with mechanical ventilation systems. With detailed natural ventilation models (e.g. TRNSFlow) the natural ventilation potential of buildings in urban areas could be studied. Here the research focus was on one building that was either located on an open field or between street canyons. The buildings of the street canyons had all the same height and only 3 different aspect ratios were studied. In real urban areas a much wider range of different building arrangements can be found. A future research topic could be to simulate the building energy demands for different building arrangements or a larger number of buildings with different building

envelopes and internal gains in an urban neighbourhood to predict energy demands of whole city quarters or urban areas. With most BES models only one building can be simulated. Therefore either a BES model has to be chosen that was developed to determine the energy demand of groups of buildings (e.g. CitySim) or a number of BES models for single buildings have to be coupled. Here the UHI intensities were modelled based on measurements. Thus this model is only valid for the location, where the temperature measurements were made. A new UHI model has to be developed or an existing model has to be applied to conduct the same analysis as presented in this thesis for any urban area. It is recommended to conduct similar studies for other cities than Basel to further enhance the understanding on the coupling of the thermal effects between the urban microclimate and the buildings in urban areas. Also the impact of the climate change or heat waves on space cooling and heating demands could be studied with the here proposed approach.

References

[1] European Commission Energy, "Market observatory: Annual report 2009," 2009. http://ec.europa.eu/energy/observatory/annual_reports/annual_reports_en.htm (accessed 15.10.2012).

[2] UN, "World urbanization prospects: The 2007 revision population database.," 2007. http://esa.un.org/unup/ (accessed 15.10.2012).

[3] T. Oke, *Boundary Layer Climates*. Cambridge University Press, Cambridge, UK, 1987.

[4] C. Schär, P. L. Vidale, D. Luthi, C. Frei, C. Haberli, M. A. Liniger, and C. Appenzeller, "The role of increasing temperature variability in European summer heatwaves," *Nature*, vol. 427, pp. 332–336, Jan. 2004.

[5] E. Fischer and C. Schär, "Future changes in daily summer temperature variability: driving processes and role for temperature extremes," *Climate Dynamics*, vol. 33, pp. 917–935, 2009.

[6] J. Hensen and R. Lamberts, *Building Performance Simulation for Design and Operation*. Spon Press, Oxon, UK, 2011.

[7] A. Kovar-Panskus, L. Moulinneuf, E. Savory, A. Abdelqari, J.-F. Sini, J.-M. Rosant, A. Robins, and N. Toy, "A wind tunnel investigation of the influence of solar-induced wall-heating on the flow regime within a simulated urban street canyon," *Water, Air, & Soil Pollution: Focus*, vol. 2, pp. 555–571, 2002.

[8] V. Garbero, P. Salizzoni, M. Marro, S. Berrone, and L. Soulhac, "Influence of heat fluxes on the flow within a two-dimensional street canyon: a comparison between wind tunnel measurements and CFD simulations," 13th International Conference on Wind Engineering, Amsterdam, Netherlands, 2011.

[9] M. W. Rotach, R. Vogt, C. Bernhofer, E. Batchvarova, A. Christen, A. Clappier, B. Feddersen, S.-E. Gryning, G. Martucci, H. Mayer, V. Mitev, T. R. Oke, E. Parlow, H. Richner, M. Roth, Y.-A. Roulet, D. Ruffieux, J. A. Salmond, M. Schatzmann, and J. A. Voogt, "BUBBLE - an urban boundary layer meteorology project," *Theoretical and Applied Climatology*, vol. 81, pp. 231–261, 2005.

[10] M. Santamouris, *Energy and climate in the urban built enivronment*. James & James, London, UK, 2001.

[11] J. Hafner and S. Q. Kidder, "Urban heat island modeling in conjunction with satellite-derived surface/soil parameters," *Journal of Applied Meteorology*, vol. 38, pp. 448–465, 1999.

[12] K. Hage, "Nocturnal temperatures in Edmonton, Alberta," *Journal of Applied Meteorology*, vol. 11, pp. 123–129, 1972.

[13] N. Magee, J. Curtis, and G. Wendler, "The urban heat island effect at Fairbanks, Alaska," *Theoretical and Applied Climatology*, vol. 64, pp. 39–47, 1999.

[14] T. R. Oke and C. East, "The urban boundary layer in Montreal," *Boundary-Layer Meteorology*, vol. 1, pp. 411–437, 1971.

[15] T. Holt and J. Pullen, "Urban canopy modeling of the new york city metropolitan area: A comparison and validation of single- and multilayer parameterizations," *Monthly Weather Review*, vol. 135, pp. 1906–1930, 2006.

[16] D. Hartz, L. Prashad, B. Hedquist, J. Golden, and A. Brazel, "Linking satellite images and hand-held infrared thermography to observed neighborhood climate conditions," *Remote Sensing of Environment*, vol. 104, no. 2, pp. 190 – 200, 2006.

[17] H. Tran, D. Uchihama, S. Ochi, and Y. Yasuoka, "Assessment with satellite data of the urban heat island effects in Asian mega cities," *International Journal of Applied Earth Observation and Geoinformation*, vol. 8, no. 1, pp. 34 – 48, 2006.

[18] B. Padmanabhamurty Technical Conference in Mexico City: Urban Climatology and its Applications with Special Regard to Tropical Areas, WMO 652, 1986.

[19] R. Giridharan, S. Lau, S. Ganesan, and B. Givoni, "Urban design factors influencing heat island intensity in high-rise high-density environments of Hong Kong," *Building and Environment*, vol. 42, no. 10, pp. 3669 – 3684, 2007.

[20] S. Sani, "Urban climatology in Malaysia: An overview," *Energy and Buildings*, vol. 15, no. 1-2, pp. 105 – 117, 1990-1991.

[21] T. Saitoh, T. Shimada, and H. Hoshi, "Modeling and simulation of the Tokyo urban heat island," *Atmospheric Environment*, vol. 30, no. 20, pp. 3431 – 3442, 1996.

[22] R. Fouli, "Some aspects of the urban climates of tropical africa," Report of Technical Conference on Tropical Urban Climate, WMO, 1994.

[23] Y. Goldreich, "The structure of the ground-level heat island in a central business district," *Journal of Climate and Applied Meteorology*, vol. 24, no. 11, pp. 1237–1244, 1985.

[24] J. Oguntoyinbo, "Some aspects of the urban climates of tropical Africa," Technical Conference in Mexico City: Urban Climatology and its Applications with Special Regard to Tropical Areas, WMO 652, 1986.

[25] N. Mazzeo and I. Camilloni, "Buenos Aires urban meteorological data analysis of a five-day period," *Energy and Buildings*, vol. 15, no. 3-4, pp. 339 – 343, 1990-1991.

[26] M. Santamouris, N. Papanikolaou, I. Livada, I. Koronakis, C. Georgakis, A. Argiriou, and D. Assimakopoulos, "On the impact of urban climate on the energy consumption of buildings," *Solar Energy*, vol. 70, no. 3, pp. 201 – 216, 2001.

[27] H. Wanner and J. Hertig, "Temperature and ventilation of small cities in complex terrain (Switzerland)," *Study supported by Swiss National Science Foundation*, 1983.

[28] R. Pongracz, J. Bartholy, and Z. Dezso, "Remotely sensed thermal information applied to urban climate analysis," *Advances in Space Research*, vol. 37, no. 12, pp. 2191 – 2196, 2006.

[29] W. Nübler, "Konfiguration und Genese der Wärmeinsel der Stadt Freiburg," *Freibuger. Geographische Hefte*, 1979.

[30] I. Eliasson, "Urban nocturnal temperatures, street geometry and land use," *Atmospheric Environment*, vol. 30, no. 3, pp. 379 – 392, 1996.

[31] K. Klysik and K. Fortuniak, "Temporal and spatial characteristics of the urban heat island of Lodz, Poland," *Atmospheric Environment*, vol. 33, no. 24-25, pp. 3885 – 3895, 1999.

[32] R. Watkins, J. Palmer, M. Kolokotroni, and P. Littlefair, "The London heat island: results from summertime monitoring," *Building Services Engineering Research and Technology*, vol. 23, no. 2, pp. 97–106, 2003.

[33] A. Lemonsu and V. Masson, "Simulation of a summer urban breeze over Paris," *Boundary-Layer Meteorology*, vol. 104, pp. 463–490, 2002.

[34] R. A. Memon, D. Y. Leung, and C.-H. Liu, "An investigation of urban heat island intensity (UHII) as an indicator of urban heating," *Atmospheric Research*, vol. 94, no. 3, pp. 491 – 500, 2009.

[35] I. D. Stewart, "A systematic review and scientific critique of methodology in modern urban heat island literature," *International Journal of Climatology*, vol. 31, no. 2, pp. 200–217, 2011.

[36] E. Aguilar, I. Auer, M. Brunet, T. Peterson, and J. Wieringa, "Guidance on metadata and homogenization," WMO techincal document no. 1186, World Meteorological Organization, 2003.

[37] T. Oke, "Initial guidance to obtain representative meteorological observations at urban sites," IOM report 81, World Meteorological Organization, 2004.

[38] I. Steward and T. Oke, "Newly developed thermal climate zones for defining and measuring urban heat island magnitude in the canopy layer," T.R. Oke Symposium & Eighth Symposium on Urban Environment, Phoenix, USA, 2009.

[39] R. A. Memon, L. Y. Dennis, and C. Liu, "A review on the generation, determination and mitigation of urban heat island," *Journal of Environmental Sciences*, vol. 20, no. 1, pp. 120 – 128, 2008.

[40] A. Christen and R. Vogt, "Energy and radiation balance of a central European city," *International Journal of Climatology*, vol. 24, no. 11, pp. 1395–1421, 2004.

[41] B. Offerle, C. S. B. Grimmond, and K. Fortuniak, "Heat storage and anthropogenic heat flux in relation to the energy balance of a central European city centre," *International Journal of Climatology*, vol. 25, no. 10, pp. 1405–1419, 2005.

[42] K. Steinecke, "Urban climatological studies in the Reykjavik subarctic environment, Iceland," *Atmospheric Environment*, vol. 33, no. 24-25, pp. 4157 – 4162, 1999.

[43] T. Ichinose, K. Shimodozono, and K. Hanaki, "Impact of anthropogenic heat on urban climate in Tokyo," *Atmospheric Environment*, vol. 33, no. 24-25, pp. 3897 – 3909, 1999.

[44] H. Taha, "Urban climates and heat islands: albedo, evapotranspiration, and anthropogenic heat," *Energy and Buildings*, vol. 25, no. 2, pp. 99 – 103, 1997.

[45] H. Taha, H. Akbari, D. Sailor, and R. Ritschard, "Causes and effects of heat islands: Sensitivity to surface parameters and anthoprogenic heating," Tech. Rep. 29864, Lawrence Berkeley Laboratory, 1992.

[46] T. R. Oke, G. T. Johnson, D. G. Steyn, and I. D. Watson, "Simulation of surface urban heat islands under ideal conditions at night part 2: Diagnosis of causation," *Boundary-Layer Meteorology*, vol. 56, pp. 339–358, 1991.

[47] D. P. Gutman and K. E. Torrance, "Response of the urban boundary layer to heat addition and surface roughness," *Boundary-Layer Meteorology*, vol. 9, pp. 217–233, 1975.

[48] P. A. Mirzaei and F. Haghighat, "Approaches to study urban heat island - abilities and limitations," *Building and Environment*, vol. 45, no. 10, pp. 2192 – 2201, 2010.

[49] S. E. Nicholson, "A pollution model for street-level air," *Atmospheric Environment*, vol. 9, no. 1, pp. 19 – 31, 1975.

[50] J. C. R. Hunt, C. J. Abell, J. A. Peterka, and H. Woo, "Kinematical studies of the flows around free or surface-mounted obstacles; applying topology to flow visualization," *Journal of Fluid Mechanics*, vol. 86, no. 01, pp. 179–200, 1978.

[51] W. Beranek, "Wind environment around building configurations," *Heron*, vol. 29, no. 1, pp. 33–70, 1984.

[52] H. Chen, R. Ooka, H. Huang, and T. Tsuchiya, "Study on mitigation measures for outdoor thermal environment on present urban blocks in Tokyo using coupled simulation," *Building and Environment*, vol. 44, no. 11, pp. 2290 – 2299, 2009.

[53] X. Xie, C.-H. Liu, D. Y. Leung, and M. K. Leung, "Characteristics of air exchange in a street canyon with ground heating," *Atmospheric Environment*, vol. 40, no. 33, pp. 6396 – 6409, 2006.

[54] J.-J. Kim and J.-J. Baik, "A numerical study of the effects of ambient wind direction on flow and dispersion in urban street canyons using the RNG - turbulence model," *Atmospheric Environment*, vol. 38, no. 19, pp. 3039 – 3048, 2004.

[55] C.-H. Liu, D. Y. Leung, and M. C. Barth, "On the prediction of air and pollutant exchange rates in street canyons of different aspect ratios using large-eddy simulation," *Atmospheric Environment*, vol. 39, no. 9, pp. 1567 – 1574, 2005.

[56] P. Kastner-Klein and E. Plate, "Wind-tunnel study of concentration fields in street canyons," *Atmospheric Environment*, vol. 33, no. 24-25, pp. 3973 – 3979, 1999.

[57] C. Gromke and B. Ruck, "Influence of trees on the dispersion of pollutants in an urban street canyon - experimental investigation of the flow and concentration field," *Atmospheric Environment*, vol. 41, no. 16, pp. 3287 – 3302, 2007.

[58] R. Kellnerova, L. Kukacka, K. Jurcakova, V. Uruba, and Z. Janour, "PIV measurement of turbulent flow within a street canyon: Detection of coherent motion," *Journal of Wind Engineering and Industrial Aerodynamics*, vol. 104-106, no. 0, pp. 302 – 313, 2012.

[59] C.-H. Chang and R. N. Meroney, "Concentration and flow distributions in urban street canyons: wind tunnel and computational data," *Journal of Wind Engineering and Industrial Aerodynamics*, vol. 91, no. 9, pp. 1141 – 1154, 2003.

[60] A. Kovar-Panskus, P. Louka, J.-F. Sini, E. Savory, M. Czech, A. Abdelqari, P. G. Mestayer, and N. Toy, "Influence of geometry on the mean flow within urban street canyons- a comparison of wind tunnel experiments and numerical simulations," *Water, Air, & Soil Pollution: Focus*, vol. 2, pp. 365–380, 2002.

[61] J. Allegrini, V. Dorer, and J. Carmeliet, "Buoyant flow in a street canyon: Comparison of CFD simulations and wind tunnel mearsurements," International Workshop on Physical Modeling of Flow and Dispersion Phenomena, Hamburg, Germany, 2011.

[62] J. Allegrini, V. Dorer, and J. Carmeliet, "Wind tunnel measurements of buoyant flows in street canyons," *Building and Environment*, vol. 59, pp. 315 – 326, 2013.

[63] P. Louka, G. Vachon, J.-F. Sini, P. G. Mestayer, and J.-M. Rosant, "Thermal effects on the airflow in a street canyon - Nantes'99 experimental results and model simulations," *Water, Air, & Soil Pollution: Focus*, vol. 2, pp. 351–364, 2002.

[64] G. Vachon, J. Rosant, P. Mestayer, and J. Sini, "Measurements of dynamic and thermal field in a street canyon," 6th International Conference on Harmonisation within Atmospheric Dispersion Modelling for Regulatory Purposes, Rouen, France, 1999.

[65] T. Oke, "Street design and urban canopy layer climate," *Energy and Buildings*, vol. 11, no. 1-3, pp. 103 – 113, 1988.

[66] Y. Nakamura and T. Oke, "Wind, temperature and stability conditions in an east-west oriented urban canyon," *Atmospheric Environment*, vol. 22, no. 12, pp. 2691 – 2700, 1988.

[67] H. Akbari, S. Davis, S. Dorsano, J. Huang, and S. Winett, "Cooling our communities - a guidebook on tree planting and light colored surfacing.," tech. rep., US Enivronmental Protection Agency. Office of Policy Analysis, Climate Change Division, 1992.

[68] M. Kolokotroni, M. Davies, B. Croxford, S. Bhuiyan, and A. Mavrogianni, "A validated methodology for the prediction of heating and cooling energy demand for buildings within the urban heat island: Case-study of London," *Solar Energy*, vol. 84, no. 12, pp. 2246 – 2255, 2010.

[69] M. Kolokotroni, I. Giannitsaris, and R. Watkins, "The effect of the London urban heat island on building summer cooling demand and night ventilation strategies," *Solar Energy*, vol. 80, no. 4, pp. 383 – 392, 2006.

[70] A. Schneider and A. Maas, "Einfluss des Mikroklimas auf das energetische und thermische Verhalten von Gebäuden am Beispiel des Standortes Kassel," *Baupyhsik*, vol. 32, no. 6, pp. 348–358, 2010.

[71] Y. Hirano and M. Ohashi, "Effects of the heat island phenomenon on energy consumption in commercial and residential sectors of metropolitan Tokyo.," International Conference on Urban Climate (ICUC7), Yokohama, Japan, 2009.

[72] C. Ghiaus, F. Allard, M. Santamouris, C. Georgakis, and F. Nicol, "Urban environment influence on natural ventilation potential," *Building and Environment*, vol. 41, no. 4, pp. 395 – 406, 2006.

[73] V. Geros, M. Santamouris, S. Karatasou, A. Tsangrassoulis, and N. Papanikolaou, "On the cooling potential of night ventilation techniques in the urban environment," *Energy and Buildings*, vol. 37, no. 3, pp. 243 – 257, 2005.

[74] J. Allegrini, V. Dorer, and J. Carmeliet, "Analysis of convective heat transfer at building facades in street canyons and its influence on the predictions of space cooling demand in buildings," *Journal of Wind Engineering and Industrial Aerodynamics*, vol. 104-106, pp. 464 – 473, 2012.

[75] J. Allegrini, V. Dorer, and J. Carmeliet, "Analysis of convective heat transfer at building façades in street canyons and its influence on the space cooling demand in buildings," 13. International Conference on Wind Engineering, Amsterdam, Netherlands, 2011.

[76] J. Allegrini, V. Dorer, and J. Carmeliet, "Influence of the urban microclimate on the energy demand of office buildings," CISBAT 11, Lausanne, Switzerland, 2011.

[77] J. Allegrini, V. Dorer, and J. Carmeliet, "Influence of the urban microclimate in street canyons on the energy demand for space cooling and heating of buildings," *Energy and Buildings*, vol. 55, pp. 823 – 832, 2012.

[78] J. Allegrini, V. Dorer, and J. Carmeliet, "Impact of urban microclimate in street canyons on building cooling demand predictions," 8. international climate conference on urban climates (ICUC 8), Dublin, Ireland, 2012.

[79] J. Allegrini, V. Dorer, and J. Carmeliet, "Urban street canyon microclimate impact on energy demand of buildings," 17. Status-Seminar, Zürich, Switzerland, 2012.

[80] V. Dorer, J. Allegrini, S. Saneinejad, P. Moonen, and J. Carmeliet, "Building energy demand and urban microclimate including heat island effect and evaporative cooling," 5. International Building Physics Conference, Kyoto, Japan, 2012.

[81] H. Akbari, M. Pomerantz, and H. Taha, "Cool surfaces and shade trees to reduce energy use and improve air quality in urban areas," *Solar Energy*, vol. 70, no. 3, pp. 295 – 310, 2001.

[82] A. Scherba, D. J. Sailor, T. N. Rosenstiel, and C. C. Wamser, "Modeling impacts of roof reflectivity, integrated photovoltaic panels and green roof systems on sensible heat flux into the urban environment," *Building and Environment*, vol. 46, no. 12, pp. 2542 – 2551, 2011.

[83] A. Synnefa, M. Santamouris, and K. Apostolakis, "On the development, optical properties and thermal performance of cool colored coatings for the urban environment," *Solar Energy*, vol. 81, no. 4, pp. 488 – 497, 2007.

[84] J. Stromann-Andersen and P. Sattrup, "The urban canyon and building energy use: Urban density versus daylight and passive solar gains," *Energy and Buildings*, vol. 43, no. 8, pp. 2011 – 2020, 2011.

[85] C.-M. Hsieh, T. Aramaki, and K. Hanaki, "Managing heat rejected from air conditioning systems to save energy and improve the microclimates of residential buildings," *Computers, Environment and Urban Systems*, vol. 35, no. 5, pp. 358 – 367, 2011.

[86] R. Stupka and C. Kennedy, "Impact of neighborhood density on building energy demand and potential supply via the urban metabolsim," *ACEE Summer Study on Energy Efficiency in Buildings*, pp. 239–252, 2010.

[87] J. Bouyer, C. Inard, and M. Musy, "Microclimatic coupling as a solution to improve building energy simulation in an urban context," *Energy and Buildings*, vol. 43, no. 7, pp. 1549 – 1559, 2011.

[88] R. Ooka, "Recent development of assessment tools for urban climate and heat-island investigation especially based on experiences in Japan," *International Journal of Climatology*, vol. 27, no. 14, pp. 1919–1930, 2007.

[89] A. Rasheed, *Multiscale Modelling of Urban Climate*. Phd thesis, EPFL, Lausanne, Switzerland, 2009.

[90] S. B. Pope, *Turbulent Flows*. Cambridge University Press, Cambridge, UK, first ed., 2009.

[91] *Transient System Simulation Program*. SEL, University of Wisconsin / TRANSSOLAR, Stuttgart, Germany, 2010.

[92] D. B. Crawley, J. W. Hand, M. Kummert, and B. T. Griffith, "Contrasting the capabilities of building energy performance simulation programs," *Building and Environment*, vol. 43, no. 4, pp. 661 – 673, 2008.

[93] *COMIS 3.0 - Users Guide*. Berkeley, California, USA, 1997.

[94] J. Clarke, *Energy simulation in building design*. Butterworth-Heinemann, Oxford, UK, 2 ed., 2001.

[95] T. Oke, "City size and the urban heat island," *Atmospheric Environment*, vol. 7, no. 8, pp. 769 – 779, 1973.

[96] T. Oke, "Overview of interactions between settlements and their enivronments," WMO experts meeting on Urban and building climatology. WCP-37, WMO, Geneva, Switzerland, 1982.

[97] T. R. Oke, "Canyon geometry and the nocturnal urban heat island: Comparison of scale model and field observations," *Journal of Climatology*, vol. 1, no. 3, pp. 237–254, 1981.

[98] F. Ludwig, "Urban temperature fields in urban climates," *WMO Techincal Note*, vol. 108, pp. 80–107, 1970.

[99] R. Bornstein, "Urban climate models: Nature, limitations and applications," Technical Conference in Mexico City: Urban Climatology and is Applications with Special Regard to Tropical Areas, WMO 652, WMO, 1986.

[100] M. C. Moreno-Garcia, "Intensity and form of the urban heat island in Barcelona," *International Journal of Climatology*, vol. 14, no. 6, pp. 705–710, 1994.

[101] J. P. Montavez, J. F. Gonzalez-Rouco, and F. Valero, "A simple model for estimating the maximum intensity of nocturnal urban heat island," *International Journal of Climatology*, vol. 28, no. 2, pp. 235–242, 2008.

[102] H. Swaid and M. E. Hoffman, "Prediction of urban air temperature variations using the analytical CTTC model," *Energy and Buildings*, vol. 14, no. 4, pp. 313 – 324, 1990.

[103] M. Elnahas and T. Williamson, "An improvement of the CTTC model for predicting urban air temperatures," *Energy and Buildings*, vol. 25, no. 1, pp. 41 – 49, 1997.

[104] E. Erell and T. Williamson, "Comments on the correct specification of the analytical CTTC model for predicting the urban canopy layer temperature," *Energy and Buildings*, vol. 38, no. 8, pp. 1015 – 1021, 2006.

[105] G. Mihalakakou, H. A. Flocas, M. Santamouris, and C. G. Helmis, "Application of neural networks to the simulation of the heat island over Athens, Greece, using synoptic types as a predictor," *Journal of Applied Meteorology*, vol. 41, pp. 519–527, 2002.

[106] Y. Ashie and T. Kono, "Urban-scale cfd analysis in support of a climate-sensitive design for the tokyo bay area," *International Journal of Climatology*, vol. 31, no. 2, pp. 174–188, 2011.

[107] H. Wanner and J.-A. Hertig, "Studies of urban climates and air pollution in Switzerland," *Journal of Climate and Applied Meteorology*, vol. 23, pp. 1614–1625, 1984.

[108] M. Bruse and H. Fleer, "Simulating surface-plant-air interactions inside urban environments with a three dimensional numerical model," *Environmental Modelling & Software*, vol. 13, no. 3-4, pp. 373 – 384, 1998.

[109] M. Bruse, *Development of a microscale model for the calculation of surface temperatures in structured terrain.* Master thesis, Universität Bochum, 1995.

[110] GEO-NET. http://www.geo-net.de/ (accessed 19.9.2012).

[111] G. W. Larsen and R. Shakespeare, *Rendering with Radiance - The Art and Science of Lighting Visualisation.* Morgan Kauffmann, San Francisco, USA, 1997.

[112] F. Miguet and D. Groleau, "A daylight simulation tool for urban and architectural spaces - application to transmitted direct and diffuse light through glazing," *Building and Environment*, vol. 37, no. 8-9, pp. 833 – 843, 2002.

[113] R. Perez, R. Seals, and J. Michalsky, "All-weather model for sky luminance distribution - preliminary configuration and validation," *Solar Energy*, vol. 50, no. 3, pp. 235 – 245, 1993.

[114] D. Robinson, F. Haldi, J. Kämpf, P. Leroux, D. Perez, A. Rasheed, and U. Wilke, "CitySim: comprehensive micro-simulation of resource flows for sustainable urban planning," 1st swiss building and urban simulation conference, Lucerne, Switzerland, 2009.

[115] D. Robinson and A. Stone, "Solar radiation modelling in the urban context," *Solar Energy*, vol. 77, no. 3, pp. 295 – 309, 2004.

[116] *Fluent 12.0 user's guide.* Lebanon-New Hampshire, USA, 2009.

[117] A. Mochida, H. Yoshino, S. Miyauchi, and T. Mitamura, "Total analysis of cooling effects of cross-ventilation affected by microclimate around a building," *Solar Energy*, vol. 80, no. 4, pp. 371 – 382, 2006.

[118] Y. Kikegawa, Y. Genchi, H. Yoshikado, and H. Kondo, "Development of a numerical simulation system toward comprehensive assessments of urban warming countermeasures including their impacts upon the urban buildings energy-demands," *Applied Energy*, vol. 76, no. 4, pp. 449 – 466, 2003.

[119] T. Defraeye, *Convective heat and mass transfer at exterior building surfaces*. PhD thesis, KU Leuven, Leuven, Belgium, 2011.

[120] B. Gebhard, *Heat Transfer*. McGraw-Hill, New York, USA, second ed., 1971.

[121] B. Gebhart, "Surface temperature calculations in radiant surroundings of arbitrary complexity - for gray, diffuse radiation," *International Journal of Heat and Mass Transfer*, vol. 3, no. 4, pp. 341 – 346, 1961.

[122] N. Ito, K. Kimura, and J. Oka, "A field experiment study on the convective heat transfer coefficient on exterior surface of a building," *ASHRAE Transactions*, vol. 78, no. 1, pp. 184–191, 1972.

[123] K. Nicol, "The energy balance of an exterior window surface, Inuvik, N.W.T., Canada," *Building and Environment*, vol. 12, no. 4, pp. 215 – 219, 1977.

[124] S. Jayamaha, N. Wijeysundera, and S. Chou, "Measurement of the heat transfer coefficient for walls," *Building and Environment*, vol. 31, no. 5, pp. 399 – 407, 1996.

[125] S. Sharples, "Full-scale measurements of convective energy losses from exterior building surfaces," *Building and Environment*, vol. 19, no. 1, pp. 31 – 39, 1984.

[126] A. Hagishima and J. Tanimoto, "Field measurements for estimating the convective heat transfer coefficient at building surfaces," *Building and Environment*, vol. 38, no. 7, pp. 873 – 881, 2003.

[127] Y. Liu and D. Harris, "Full-scale measurements of convective coefficient on external surface of a low-rise building in sheltered conditions," *Building and Environment*, vol. 42, no. 7, pp. 2718 – 2736, 2007.

[128] H. Nakamura, T. Igarashi, and T. Tsutsui, "Local heat transfer around a wall-mounted cube in the turbulent boundary layer," *International Journal of Heat and Mass Transfer*, vol. 44, no. 18, pp. 3385 – 3395, 2001.

[129] A. Hagishima, J. Tanimoto, and K.-i. Narita, "Intercomparisons of experimental convective heat transfer coefficients and mass transfer coefficients of urban surfaces," *Boundary-Layer Meteorology*, vol. 117, pp. 551–576, 2005.

[130] T. Defraeye, B. Blocken, and J. Carmeliet, "Convective heat transfer coefficients for exterior building surfaces: Existing correlations and CFD modelling," *Energy Conversion and Management*, vol. 52, no. 1, pp. 512 – 522, 2011.

[131] J. Palyvos, "A survey of wind convection coefficient correlations for building envelope energy systems' modeling," *Applied Thermal Engineering*, vol. 28, no. 8-9, pp. 801 – 808, 2008.

[132] M. G. Emmel, M. O. Abadie, and N. Mendes, "New external convective heat transfer coefficient correlations for isolated low-rise buildings," *Energy and Buildings*, vol. 39, no. 3, pp. 335 – 342, 2007.

[133] B. Blocken, T. Defraeye, D. Derome, and J. Carmeliet, "High-resolution CFD simulations for forced convective heat transfer coefficients at the facade of a low-rise building," *Building and Environment*, vol. 44, no. 12, pp. 2396 – 2412, 2009.

[134] T. Defraeye, B. Blocken, and J. Carmeliet, "CFD analysis of convective heat transfer at the surfaces of a cube immersed in a turbulent boundary layer," *International Journal of Heat and Mass Transfer*, vol. 53, no. 1-3, pp. 297 – 308, 2010.

[135] J. Allegrini, V. Dorer, T. Defraeye, and J. Carmeliet, "An adaptive temperature wall function for mixed convective flows at exterior surfaces of buildings in street canyons," *Building and Environment*, vol. 49, pp. 55 – 66, 2012.

[136] Z. Zhai, Q. Chen, P. Haves, and J. H. Klems, "On approaches to couple energy simulation and computational fluid dynamics programs," *Building and Environment*, vol. 37, pp. 857 – 864, 2002.

[137] T.-H. Shih, W. W. Liou, A. Shabbir, Z. Yang, and J. Zhu, "A new k-ϵ eddy viscosity model for high reynolds number turbulent flows," *Computers & Fluids*, vol. 24, no. 3, pp. 227 – 238, 1995.

[138] W. Jones and B. Launder, "The prediction of laminarization with a two-equation model of turbulence," *International Journal of Heat and Mass Transfer*, vol. 15, no. 2, pp. 301 – 314, 1972.

[139] B. Launder and D. Spalding, "The numerical computation of turbulent flows," *Computer Methods in Applied Mechanics and Engineering*, vol. 3, no. 2, pp. 269 – 289, 1974.

[140] J. Franke, A. Hellsten, H. Schlünzen, and B. Carissimo, *Best practice guideline for the CFD simulation of flows in the urban environment*. COST Action 732, 2007.

[141] P. Richards and R. Hoxey, "Appropriate boundary conditions for computational wind engineering models using the k-ϵ turbulence model," *Journal of Wind Engineering and Industrial Aerodynamics*, vol. 46-47, no. 0, pp. 145 – 153, 1993.

[142] M. Davies, *Building heat transfer*. John Wiley & Sons, Ltd., Chichester, UK, 1st ed., 2004.

[143] S. Chou, K. Chua, and J. Ho, "A study on the effects of double skin facades on the energy management in buildings," *Energy Conversion and Management*, vol. 50, no. 9, pp. 2275 – 2281, 2009.

[144] D. Harris and N. Helwig, "Solar chimney and building ventilation," *Applied Energy*, vol. 84, no. 2, pp. 135 – 146, 2007.

[145] S. Sharples and P. Charlesworth, "Full-scale measurements of wind-induced convective heat transfer from a roof-mounted flat plate solar collector," *Solar Energy*, vol. 62, no. 2, pp. 69 – 77, 1998.

[146] W. Tian, Y. Wang, Y. Xie, D. Wu, L. Zhu, and J. Ren, "Effect of building integrated photovoltaics on microclimate of urban canopy layer," *Building and Environment*, vol. 42, no. 5, pp. 1891 – 1901, 2007.

[147] H. Mayer, J. Holst, P. Dostal, F. Imbery, and D. Schindler, "Human thermal comfort in summer within an urban street canyon in central Europe," *Meteorologische Zeitschrift*, vol. 17, pp. 241–250, 06 2008.

[148] T. Tokairin, H. Kondo, H. Yoshikado, Y. Genchi, T. Ihara, Y. Kikegawa, Y. Hirano, and K. Asahi, "Numerical study on the effect of buildings on temperature variation in urban and suburban areas in Tokyo," *Journal of the Meteorological Society of Japan. Ser. II*, vol. 84, no. 5, pp. 921–937, 2006.

[149] F. Salamanca, A. Krpo, A. Martilli, and A. Clappier, "A new building energy model coupled with an urban canopy parameterization for urban climate simulations - part i. formulation, verification, and sensitivity analysis of the model," *Theoretical and Applied Climatology*, vol. 99, pp. 331–344, 2010.

[150] T. Defraeye and J. Carmeliet, "A methodology to assess the influence of local wind conditions and building orientation on the convective heat transfer at building surfaces," *Environmental Modelling & Software*, vol. 25, no. 12, pp. 1813 – 1824, 2010.

[151] T. van Hooff and B. Blocken, "Coupled urban wind flow and indoor natural ventilation modelling on a high-resolution grid: A case study for the Amsterdam ArenA stadium," *Environmental Modelling & Software*, vol. 25, no. 1, pp. 51 – 65, 2010.

[152] P. Moonen, C. Gromke, V. Dorer, and J. Carmeliet, "LES of dispersion in a street canyon with tree planting.," PHYSMOD, Hamburg, Germany, 2011.

[153] C. Balaji, M. Hoelling, and H. Herwig, "A temperature wall function for turbulent mixed convection from vertical, parallel plate channels," *International Journal of Thermal Sciences*, vol. 47, no. 6, pp. 723 – 729, 2008.

[154] T. J. Craft, S. E. Gant, H. Iacovides, and B. E. Launder, "A new wall function strategy for complex turbulent flows," *Numerical Heat Transfer, Part B: Fundamentals*, vol. 45, no. 4, pp. 301–318, 2004.

[155] M. Popovac and K. Hanjalic, "Compound wall treatment for RANS computation of complex turbulent flows and heat transfer," *Flow, Turbulence and Combustion*, vol. 78, pp. 177–202, 2007.

[156] T. Defraeye, B. Blocken, and J. Carmeliet, "An adjusted temperature wall function for turbulent forced convective heat transfer for bluff bodies in the atmospheric boundary layer," *Building and Environment*, vol. 46, no. 11, pp. 2130 – 2141, 2011.

[157] A. Hussain and W. Reynolds, "Measurements in fully-developed turbulent channal flow.," *Journal of Fluids Engineering*, vol. 97, pp. 568–580, 1975.

[158] E. Meinders, K. Hanjalic, and R. Martinuzzi, "Experimental study of the local convection heat transfer from a wall-mounted cube in turbulent channel flow," *Journal of Heat Transfer*, vol. 121, no. 3, pp. 564–573, 1999.

[159] M. Wolfshtein, "The velocity and temperature distribution in one-dimensional flow with turbulence augmentation and pressure gradient," *International Journal of Heat and Mass Transfer*, vol. 12, no. 3, pp. 301 – 318, 1969.

[160] X. Xie, C.-H. Liu, and D. Y. Leung, "Impact of building facades and ground heating on wind flow and pollutant transport in street canyons," *Atmospheric Environment*, vol. 41, no. 39, pp. 9030 – 9049, 2007.

[161] B. Blocken, T. Stathopoulos, and J. Carmeliet, "CFD simulation of the atmospheric boundary layer: wall function problems," *Atmospheric Environment*, vol. 41, no. 2, pp. 238 – 252, 2007.

[162] K. Uehara, S. Murakami, S. Oikawa, and S. Wakamatsu, "Wind tunnel experiments on how thermal stratification affects flow in and above urban street canyons," *Atmospheric Environment*, vol. 34, no. 10, pp. 1553 – 1562, 2000.

[163] P. Spalart, "Direct simulation of a turbulent boundary layer up to $r_\theta = 1410$," *Journal of Fluid Mechanics*, vol. 187, pp. 61–98, 1988.

[164] ASHRAE, *ASHRAE Handbook-Fundamentals*. American Society of Heating, Refrigerating and Air-Conditioning Engineers, Inc., New York, USA, si ed., 2009.

[165] L. Huizhi, L. Bin, Z. Fengrong, Z. Boyin, and S. Jianguo, "A laboratory model for the flow in urban street canyons induced by bottom heating," *Advances in Atmospheric Sciences*, vol. 20, pp. 554–564, 2003.

[166] H. C. Lim, I. P. Castro, I. P.O, and R. P. Hexey, "Bluff bodies in deep turbulent boundary layers: Reynolds-number issues," *Journal of Fluid Mechanics*, vol. 571, pp. 97–118, 2007.

[167] I. P. Castro and A. G. Robins, "The flow around a surface-mounted cube in uniform and turbulent streams," *Journal of Fluid Mechanics*, vol. 79, no. 02, pp. 307–335, 1977.

[168] W. H. Snyder, "Similarity criteria for the application of fluid models to the study of air pollution meteorology," *Boundary-Layer Meteorology*, vol. 3, pp. 113–134, 1972.

[169] W. Hoydysh, Y. Ogawa, and R. Griffiths, "A scale model study of dispersion of pollution in street canyons.," Annual Meeting of the Air Pollution Control Association, Denver, Colorado, 1974.

[170] P. Moonen, V. Dorer, and J. Carmeliet, "Evaluation of the ventilation potential of courtyards and urban street canyons using RANS and LES," *Journal of Wind Engineering and Industrial Aerodynamics*, vol. 99, no. 4, pp. 414 – 423, 2011.

[171] J. Bolinder, "On the accuracy of a digital particle image velocimetry system," tech. rep., Lund Institute of Technology, Sweden, 1999.

[172] R. D. Keane and R. J. Adrian, "Optimization of particle image velocimeters. i. double pulsed systems," *Measurement Science and Technology*, vol. 1, no. 11, p. 1202, 1990.

[173] A. Prasad, "Particle image velocimetry," *Current Science*, vol. 79, no. 1, pp. 51–60, 2002.

[174] P. Moonen, T. Defraeye, V. Dorer, B. Blocken, and J. Carmeliet, "Urban physics: Effect of the micro-climate on comfort, health and energy demand," *Frontiers of Architectural Research*, vol. 1, no. 3, pp. 197–228, 2012.

[175] T. Stathopoulos, "Pedestrian level winds and outdoor human comfort," *Journal of Wind Engineering and Industrial Aerodynamics*, vol. 94, no. 11, pp. 769 – 780, 2006.

[176] B. Blocken and J. Persoon, "Pedestrian wind comfort around a large football stadium in an urban environment: CFD simulation, validation and application of the new Dutch wind nuisance standard," *Journal of Wind Engineering and Industrial Aerodynamics*, vol. 97, no. 5-6, pp. 255 – 270, 2009.

[177] B. Blocken, W. Janssen, and T. van Hooff, "CFD simulation for pedestrian wind comfort and wind safety in urban areas: General decision framework and case study for the Eindhoven university campus," *Environmental Modelling & Software*, vol. 30, pp. 15 – 34, 2012.

[178] P. Gousseau, B. Blocken, T. Stathopoulos, and G. van Heijst, "CFD simulation of near-field pollutant dispersion on a high-resolution grid: A case study by LES and RANS for a building group in downtown Montreal," *Atmospheric Environment*, vol. 45, no. 2, pp. 428 – 438, 2011.

[179] S. D. Sabatino, R. Buccolieri, B. Pulvirenti, and R. Britter, "Simulations of pollutant dispersion within idealised urban-type geometries with CFD and integral models," *Atmospheric Environment*, vol. 41, no. 37, pp. 8316 – 8329, 2007.

[180] Y. Tominaga and T. Stathopoulos, "CFD modeling of pollution dispersion in a street canyon: Comparison between LES and RANS," *Journal of Wind Engineering and Industrial Aerodynamics*, vol. 99, no. 4, pp. 340 – 348, 2011.

[181] T. Chan, G. Dong, C. Leung, C. Cheung, and W. Hung, "Validation of a two-dimensional pollutant dispersion model in an isolated street canyon," *Atmospheric Environment*, vol. 36, no. 5, pp. 861 – 872, 2002.

[182] R. N. Meroney, M. Pavageau, S. Rafailidis, and M. Schatzmann, "Study of line source characteristics for 2-D physical modelling of pollutant dispersion in street canyons," *Journal of Wind Engineering and Industrial Aerodynamics*, vol. 62, no. 1, pp. 37 – 56, 1996.

[183] R. A. Memon, D. Y. Leung, and C.-H. Liu, "Effects of building aspect ratio and wind speed on air temperatures in urban-like street canyons," *Building and Environment*, vol. 45, no. 1, pp. 176 – 188, 2010.

[184] J.-J. Kim and J.-J. Baik, "Effects of street-bottom and building-roof heating on flow in three-dimensional street canyons," *Advances in Atmospheric Sciences*, vol. 27, pp. 513–527, 2010.

[185] J.-J. Kim and J.-J. Baik, "Urban street-canyon flows with bottom heating," *Atmospheric Environment*, vol. 35, no. 20, pp. 3395 – 3404, 2001.

[186] A. Tablada and S. Roels, "Numerical study on the influence of wind and thermal stack on street canyon airflow pattern," The 7th internatinal conference on urban climate (ICUC 7), Yokohama, Japan, 2009.

[187] R. Dimitrova, J.-F. Sini, K. Richards, M. Schatzmann, M. Weeks, E. Perez Garcia, and C. Borrego, "Influence of thermal effects on the wind field within the urban environment," *Boundary-Layer Meteorology*, vol. 131, pp. 223–243, 2009.

[188] V. Assimakopoulos, C. Georgakis, and M. Santamouris, "Experimental validation of a computational fluid dynamics code to predict the wind speed in street canyons for passive cooling purposes," *Solar Energy*, vol. 80, no. 4, pp. 423 – 434, 2006.

[189] S.-E. Kim and D. Choudhury, "A near-wall treatment using wall functions sensitized to pressure gradient.," *ASME FED*, vol. 217, 1995.

[190] M. Bady, S. Kato, and H. Huang, "Towards the application of indoor ventilation efficiency indices to evaluate the air quality of urban areas," *Building and Environment*, vol. 43, no. 12, pp. 1991 – 2004, 2008.

[191] SIA, ed., *Standard-Nutzungsbedingungen für die Energie- und Gebäudetechnik*. SIA, Swiss Association of Engenieers and Architects, Zürich, Switzerland, 2006.

[192] B. Glück, *Wärmetechnisches Raummodell, Gekoppelte Berechnungen und wärmephysiologische Untersuchungen*. C.F. Müller Verlag, Heidelberg, Germany, 1997.

Curriculum vitae

Personal information

First names	Jonas Michel
Last name	Allegrini
Nationality	Swiss
Date of birth	18.08.1983
Citizen of	Ins (BE), Switzerland

Education

2009 - present	PhD candidate at the Chair of Building Physics, Swiss Federal Institute of Technology Zürich (ETHZ), Zürich, Switzerland
2007-2009	Master degree in Mechanical Engineering, Swiss Federal Institute of Technology Zürich (ETHZ), Zürich, Switzerland
2003-2007	Bachelor degree in Mechanical Engineering, Swiss Federal Institute of Technology Zürich (ETHZ), Zürich, Switzerland
1999-2002	State High School ("Gymnasium", "Typus C"), Gymnasium Münchenstein, Münchenstein, Switzerland

Employment

2009 - present	PhD candidate at the Laboratory for Building Science and Technology, Swiss Federal Laboratories for Materials Science and Technology (Empa), Dübendorf Switzerland

Scientific publications

Journal papers

1. Allegrini J., Dorer V., Carmeliet J. (2013), Wind tunnel measurements of buoyant flows in street canyons, Building and Environment 59, 315-326.

2. Allegrini J., Dorer V., Carmeliet J. (2012), Influence of the urban microclimate in street canyons on the energy demand for space cooling and heating of buildings, Energy and Buildings 55, 823-832.

3. Allegrini J., Dorer V., Carmeliet J. (2012), Analysis of convective heat transfer at building façades in street canyons and its influence on the predictions of space cooling demand in buildings, Journal of Wind Engineering and Industrial Aerodynamics 104-106, 464-473.

4. Allegrini J., Dorer V., Carmeliet J. (2012), An adaptive temperature wall function for mixed convective flows at exterior surfaces of buildings in street canyons, Building and Environment 49, 55-66.

5. Zoller B.T., Allegrini J.M., Maas U., Jenny P. (2011), PDF model for NO calculations with radiation and consistent NO - NO_2 chemistry in non-premixed turbulent flames, Combustion and Flame 158, 1591-1601.

Conference papers

1. Allegrini J., Dorer V., Carmeliet J. (2012), Urban street canyon microclimate impact on energy demand of buildings, Proceedings of the 17. Status-Seminar "Forschen für den Bau im Kontext von Energie und Umwelt", Zürich, Switzerland

2. Allegrini J., Dorer V., Carmeliet J. (2012), Impact of urban microclimate in street canyons on building cooling demand predictions, Proceedings of the 8. International Conference on Urban Climates, Dublin, Ireland. Winner of a AMS-IAUC student award.

3. Dorer V., Allegrini J., Saneinejad S., Moonen P., Carmeliet J. (2012), Building Energy Demand and Urban Microclimate including Heat Island Effects and Evaporative Cooling, Proceedings of the 5. International Building Physics Conference, Kyoto, Japan.

4. Allegrini J., Dorer V., Carmeliet J. (2011), Influence of the urban microclimate on the energy demand of office buildings, Proceedings of CISBAT 11, Lausanne, Switzerland.

5. Allegrini J., Dorer V., Carmeliet J. (2011), Buoyant Flow in a Street Canyon: Comparison of CFD Simulations and Wind Tunnel Measurements, Proceedings of the International Workshop on Physical Modeling of Flow and Dispersion Phenomena (PHYSMOD 2011), Hamburg, Germany.

6. Allegrini J., Dorer V., Carmeliet J. (2011), Analysis of convective heat transfer at building façades in street canyons and its influence on the space cooling demand in buildings, Proceedings of the 13. International Conference on Wind Engineering, Amsterdam, Netherlands.

7. Wild M.A., Zoller B.T., Allegrini J., Jenny P. (2009), Efficient NO Calculations in Turbulent Non-Premixed Flames Using PDF Methods, Proceedings of the European Combustion Meeting 2009, Vienna, Austria.

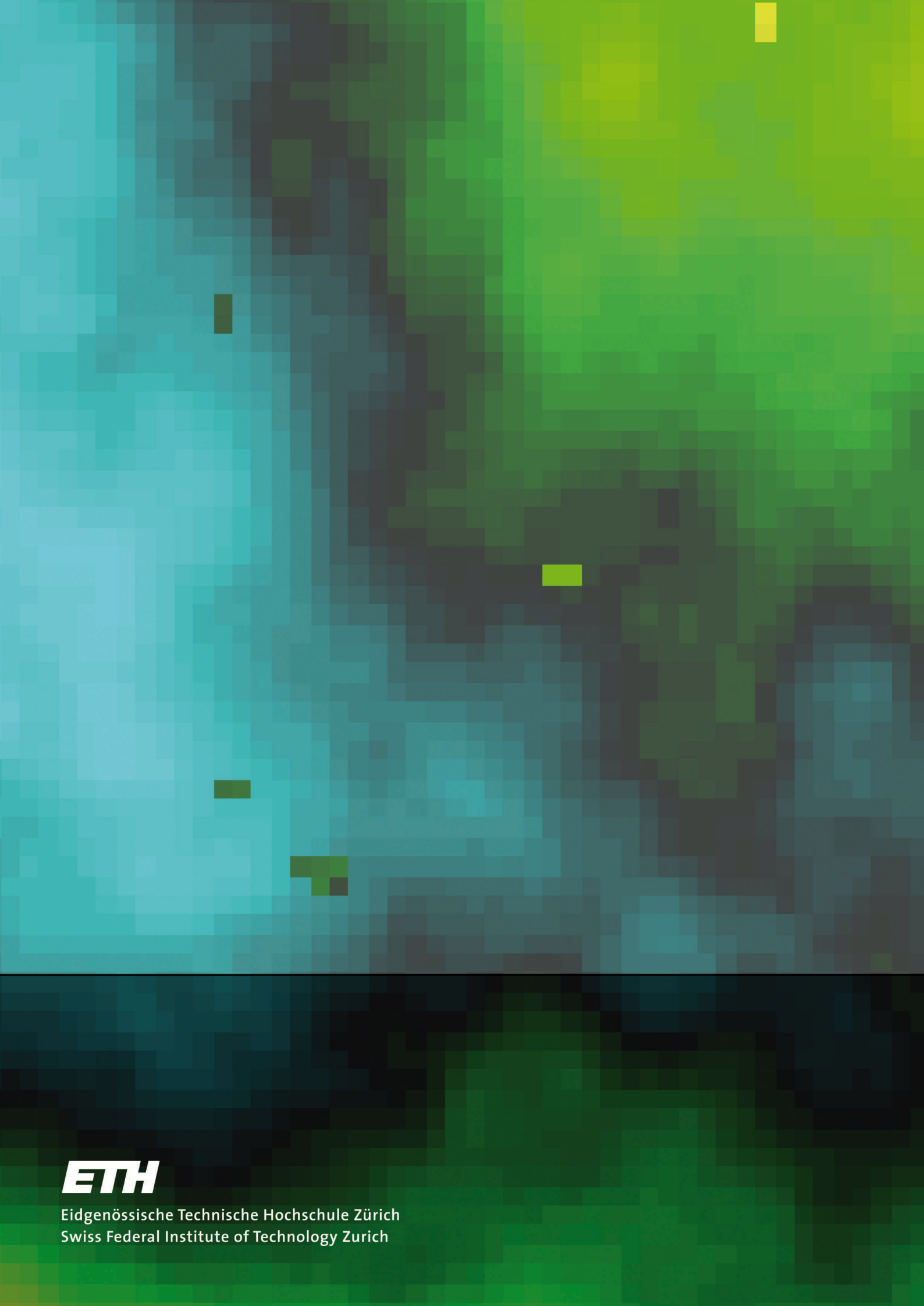

ETH

Eidgenössische Technische Hochschule Zürich
Swiss Federal Institute of Technology Zurich